2021

Metal Hydride Based Materials for Advanced Lithium Storage Applications

Yuqin Huang

UNIVERSITY
OF WOLLONGONG
AUSTRALIA

Metal Hydride Based Materials for Advanced Lithium Storage Applications

This thesis is presented as part of the requirements for the

Award of the Degree of

Doctor of Philosophy

from the

University of Wollongong

by

YUQIN HUANG

B. Sc., M. Eng.

Institute for Superconducting & Electronic Materials

Faculty of Engineering and Information Sciences

October 2021

CERTIFICATION

I, Yuqin Huang, declare that this thesis, submitted in fulfilment of the requirements for the award of Doctor of Philosophy, in the Institute for Superconducting & Electronic Materials, Faculty of Engineering, University of Wollongong, is wholly my own work unless otherwise referenced or acknowledged. The document has not been submitted for qualifications at any other academic institution.

Yuqin Huang

2021.09

ACKNOWLEDGEMENTS

Time flies, and in a blink of an eye, several years of Ph.D. career at University of Wollongong is over. During this period, I have gained a lot on both scientific research and life.

First of all, I would like to extend my sincere respect and gratitude to my supervisors, Dr. Guanglin Xia, Dr. Wei Kong Pang and Prof. Zaiping Guo for offering me the opportunity to do some research on this study. Thanks to Dr. Guanglin Xia for his professional guidance and constant encourage in scientific research. His scientific enlightenment helps me make progress and his is patient in revising manuscripts over and over again assists me to publish high quality papers. Thanks also to the Prof. Zaiping Guo for her expert guidance and valuable suggestions on my research subject and her great support and help on my study in Wollongong. My sincere gratitude to Dr. Wei Kong Pang, who gave me substantial assistance for my PhD work.

Great gratitude is also owing to Prof. Xuebin Yu (Fudan University). Thanks to his instructions and suggestions on my research project when I went to Fudan University as a visiting student. Thanks to students in his group, such as Miss. Qili Gao, Dr. Baoping Zhang, Mr. Hongyu Zhang, Mr. Wei Chen, Mrs. Qiaohuan Cheng, Dr. Long Yao, Miss. Guilei Zhu, Mr. Shunlong Ju, Miss Yanran Wang, Mr Shulin Zhong, Mrs Jiening Zheng, Dr. Yahui Sun, Dr. Hui Wu, Dr. Weili Liu, Dr. Shuang Li, Mr. Jikai Ye, Mr. Panyu Gao, Mr. Chongyang Yuan, Miss. Yongfang Lai, Miss Xiaoyue Zhang and Mr. Yang Meng. Their accompany and assistance give me great support and comfort during past four years.

Also, I want to give my appreciation to all the staffs in Prof. Guo's group, Dr. Zhijie Wang, Dr. Jing Cuan, Dr. Junnan Hao, Dr. Shilin Zhang, Dr. Yajjie Liu, Dr. Hanna He,

Dr Tengfei Zhou, and Dr Jianfeng Mao etc. are included. Thanks for their friendship and assistance.

Thanks also go to the staff members in ISEM and Fudan University. Thanks to Prof. Shixue Dou, Mrs. Joanne George (Laboratory Officer), Mrs. Crystal Login, Mrs Meiqin Zen (SEM), Dr. Hui Xu (XRD), Dr. Chang Sun (Raman), Dr. Kosta Konstantinov (TGA/DSC), Dr. Tania Silver (paper and thesis editing), Dr. Jia Wei (FTIR), etc. for their generous help and support of my study.

My deep love is dedicated to my parents for their understanding and support during my study and the whole life.

Finally, thanks to the review experts for their valuable comments and criticisms on this paper. Your comments make this paper more perfect.

ABSTRACT

The state of the art, commercial used graphite anode materials are far from meeting the increasing demand for high-energy density devices. It is necessary to develop anode materials with high energy density, low-cost and superior safety. Generally, compared with classical intercalation anodes, conversion type anodes display higher theoretical capacity have been paid widely attention. Some of the emerging metal hydrides demonstrate high specific capacity, small polarization and suitable working potential. This thesis focusing on two metal hydrides both with relatively high specific capacity, sodium alanate ($NaAlH_4$) and mageneisum hydride (MgH_2) as anodes materials in LIBs. In order to enhance the electronic conductivity of the material and relieve the volume variation, four methods of carbon doping, nano crystallization, surface modification and process modification were used to raise the lithium storage performance of metal hydride-based anode materials ($NaAlH_4$ and MgH_2). By way of self-assembly, gas-solid reaction and other synthesis methods, the multi nanostructure of metal hydride-based anode materials ($NaAlH_4$ and MgH_2) were designed, and a variety of composite materials of metal hydride and graphene with different structures were successfully prepared.

Through a facile solvent evaporation induced deposition method, $NaAlH_4$ nanoparticles with an average size of ~ 12 nm encapsulated in graphene nanosheets has been developed. The SAH@G-50 electrode exhibits an discharge capacity about 1995 mAh g^{-1} at 100 mAh g^{-1} at first cycle, with a coulombic efficiency (CE) of 85.7%. The specific discharge capacity slowly decayed and then was stabilized at ~698 mAh g^{-1} after 200 cycles. It has been founded in this thesis, graphene could act as an effective platform to tailor the metal-hydrogen bonds of $NaAlH_4$ through their favorable molecular interaction. Theoretical and experimental results confirm that graphene is

capable of weakening the Al-H bonds of $NaAlH_4$, thus facilitating the breaking and recombination of Al-H bonds towards advanced lithium storage performance. In addition, The synergistic effects of the favorable molecular interaction between graphene and $NaAlH_4$, and the noticeable decrease in particle size significantly boost the lithium storage performances of $NaAlH_4$.

An facile synthesis strategy has been reported towards the precise construction and morphology controllable of MgH_2@G for advanced performance in LIBs. A series of MgH_2 based graphene nanostructures with different morphologies (nanospheres, nanorods and nanosheets) were achieved through the self-assembly of MgH_2 growing uniformly on the graphene nanosheets Not only the shape, but also the size and loading ratio of MgH_2 could be precisely controlled via parameters regulation. Among the different morphologies, the nanospheres delivers higher capacity utilization and more stable cycling performance (a discharge capacity of 520 mAh g^{-1} at 200 mA g^{-1} after 50 cycles) than the MgH_2@G nanorods and nanosheets, as a result of the higher specific surface area and more sufficient active sites. Acted as structure director and scaffold, graphene plays a vital role in maintaining the structure stability. Additionally, the MgH_2@G could also serve as an attractive basic model for further construction of more complex structures in various applications.

Based on the nanosturcture of MHG, a series of yolk-shell-like structures, composed of porous MgH_2 nanoparticles (NPs) decorated with Mg-based composites (MHG@MBH, MHG@MS, and MHG@MNH) through *in-situ* solid-gas reaction have been fabricated and uniformly dispersed on electronically conductive graphene. The MHG@MBH electrode could keep a discharge capacity of 1629.4 mAh g^{-1} even after 380 cycles with a Coulombic efficiency of approximately 99.1%. At 2 A g^{-1}, a reversible capability around 1032 mAh g^{-1} could still be reached for the MHG@MBH

electrode after 300 cycles. More importantly, the CEs of MHG@MBH could be preserved at a level over 98.6% through the entire cycling process.

To avoid the side reactions of MHG@MBH and traditional liquid electrolyte, it has been used in solid-state battery as an anode with $LiBH_4$ as an electrolyte. The 13-MHG@MBH displays a discharge capacity of 2054 mAh g^{-1} at first cycle, with a high CE of 98%, and a high capacity of 1415 mAh g^{-1} is maintained after 150 cycles under 200 mA g^{-1}. When cycled at 2 A g^{-1}, 13MHG@MBH exhibits an admirable specific capacity of 800 mAh g^{-1} can be maintained over 300 cycles. Due to the coating layer Li_2B_6 which is double ionic-electronic transfer interface outside the MgH_2 NPs, 13MHG@MBH could not only physically alleviate the volume variation of MgH_2, but also significantly boost the transportation of electrons and ions throughout the whole electrode, which are benefit for the superior rate capability and long service life.

TABLE OF CONTENTS

LIST OF FIGURES

molecular dynamics (AIMD) simulation of MgH_2 and Li ions. (d) Cycling performances of MH@HyC, black HyC, and bulk MgH_2 electrodes at 100 mA g^{-1}. (e) Cyclic voltammetry curves of MH@HyC60 electrode at 0.05 mV s^{-1}. [83,84]

Figure 2.11 (a) Fabrication schematic of G/MgH_2@ PTh. (b) cycling capability of different marked samples. [91]

Figure 2.12 Battery configurations of MgH_2-LPS-VGCF electrode (Sample A) and MgH_2-$LiBH_4$-VGCF electrode (Sample B) working with the $80Li_2S{\cdot}20P_2S_5$ solid state electrolyte. (a) Voltage capacity profile and (b) cycling performance in the range of 0.3−2.0 V for sample A and (c) Voltage capacity profile and (d) cycling performance in the range of 0.3−1.0 V for sample B. [102]

Figure 2.13 (a) Synthetic process of $LiNa_2AlH_6$/3DG. (b) morphology characterization of $LiNa_2AlH_6$/3DG. (c) Cycling performance of $LiNa_2AlH_6$/3DG in solid-state battery with $LiBH_4$ acting as solid electrolyte: (c) potential capacity profiles at 0.2 A g^{-1}; (d) cycling properties at 0.2 A g^{-1} and (e) 1 A g^{-1}.[56]

Figure 2.14 (a) The schematic and electronic photos of the MgH_2-$LiBH_4$|$LiBH_4$|Li ASSB. (b) The voltage discharge capctiy profiles of c-MgH_2-$LiBH_4$ composite electrode at first cycle under different constant current densities increasing from 100 to 3200 mAh g^{-1}. Inset shows the average potentials and discharge capacities at corresponding current densities. (c) voltage capacity profiles of the c-MgH_2-$LiBH_4$ composite electrode at 800 mA g^{-1}. Inset shows the corresponding cyclic properties. [92]

Figure 2.15 Cyclic properties of $75MgH_2{\bullet}25CoO$-based anode with $LiBH_4$ SE at 120 ℃ (a) Discharge–charge profiles at 0.05 C rate. Inset: looped discharge/charge curve for clarity. (b) Rate capability tests of different C-rates. (c) voltage profiles corresponding to different samples at different temperature. [104, 65]

HRTEM images (d, j), STEM images (e, k), the elemental mapping (f, l). The insets of (c, i) is the SAED patterns.

Figure 7.3 PXRD patterns of the synthesized samples 50-MHG, 50-MHG@MBH, 13-MHG, and 13MHG@MBH.

Figure 7.4 Raman spectra of as-prepared (a) 13-MHG@MBH and 13MHG, (b) 50-MHG@MBH and 50MHG, and FTIR spectra of (c) MHG@MBH and MHG. Pore-size distribution of 13-MHG@MBH (d). The inset of (d) is the corresponding nitrogen adsorption/desorption isotherm.

Figure 7.5 Electrochemical performance. (a) Cycling performance of 50-MHG@MBH, 13-MHG@MBH, and MHG electrodes at 200 mA g^{-1}. (b, d) Galvanostatic charge-discharge profiles of 13-MHG@MBH, and 13-MHG at 200 mA g^{-1} at first 3 cycles, respectively. (c, e) The corresponding derivative curves (dQ/dE) of assembled half-cell. (f) Rate performance of 13-MHG@MBH and 13-MHG electrodes from 100 to 2000 mA g^{-1}. (g) Cycling performance of 13-MHG@MBH and 13-MHG electrodes at 2 A g^{-1}. (h) Nyquist plots of 13-MHG@MBH and 13-MHG electrodes in the discharged state before and after 50 cycles.

Figure 7.6 (a) Evolution of the potential (V) along with cycling time for the 13-MHG@MBH electrode at 200 mA g^{-1} in the first cycle., (b) XRD patterns of 13-MHG@MBH at different cycle states. And XPS spectra high resolution of Li 1s (c) and B 1s (d) of 13-MHG@MBH at different cycle states. (e−f) HRTEM images of 13-MHG@MBH collected at the first lithiation state and (g-h) the delithiation state. (i) TEM images and (j) the EDS line scan on a STEM image of 13-MHG@MBH at the first delithiation state. (k) STEM image and (l) the elemental mapping of 13-MHG@MBH after 200 cycles at 2 A g^{-1}.

Figure 7.7 Galvanostatic charge-discharge profiles of (a) bulk MgH_2 and $Mg(BH_4)_2$, (c) nano MBH@G, (e) amorphous B at 200 mA g^{-1} at selected cycles. Cycling performance of (b) bulk $Mg(BH_4)_2$, (d) nano MBH@G and (f) amorphous B at 200 mA g^{-1}. PXRD patterns of delithiation products of amorphous B samples (g). And XPS spectra of high resolution of Li 1s (c) and B 1s (d) of amorphous B samples at different cycle states.

Figure 7.8 Cross-sectional SEM image of electrode−electrolyte interface. SEM images of $LiBH_4$/13-MHG@MBH interface (a) after 100 cycles (a1) and 300 cycles (a2). SEM images of $LiBH_4$/13-MHG interface (b) after 100 cycles (b1) and 200 cycles (b2) at 2 A g^{-1}. Impedance measurement during the initial discharge and charge cycle for 13-MHG@MBH (c-d) and MHG electrodes (f-g). Nyquist plots of MHG@MBH (e) and MHG (h) electrodes in the charged state before and after 50,100,150, 200 cycles.

Figure 7.9 Diffusion coefficients of 13-MHG (a) and 13-MHG@MBH (a_1) extracted from high resolution PITT characterization. The particle size distributions of 13-MHG (b) and 13-MHG@MBH (b_1) after 200 cycles at 2 A g^{-1}. SEM images of 13-MHG@MBH before and after 50 cycles at 2 A g^{-1} (c-c1), SEM images of 50-MHG@MBH before and after 50 cycles at 2 A g^{-1} (d-d1), SEM images of 13-MHG (c2) and 50-MHG (d2) after 50 cycles at 2 A g^{-1}.

LIST OF TABLES

LIST OF ABBREVIATIONS

Abbreviation	Full name
LIB	Lithium-ion battery
NIB	Sodium-ion battery
ASSLIB	All solid-state battery
SSLIB	Solid-state battery
SE	Solid electrolyte
CE	Columbic efficiency
NPs	Nanoparticles
PITT	Potentiostatic intermittent titration technique
LPS	$80Li_2S$-$20P_2S_5$
3D	Three-dimensional
cm	Centimeter
FCC	Face-centered cubic
PVDF	Polyvinylidene fluoride
CV	Cyclic voltammetry
EC	Ethylene carbonate
DEC	Diethyl carbonate
DMC	Dimethyl carbonate
EDS	Energy dispersive X-ray spectroscopy
EIS	Electrochemical impedance spectroscopy
EV	Electric vehicle
FE-SEM	Field emission scanning electron microscopy
HEV	Hybrid electric vehicle
HRTEM	High-resolution transmission electron microscopy
JCPDS	Joint Committee on Powder Diffraction Standards
(h k l)	Miller indices
M	Metal element
mm	Millimeter
nm	Nanometer

Raman	Raman Spectroscopy
Li^+	Lithium ions
GNSs	Graphene nanosheets
SAED	Selected Area Electron Diffraction
SEI	Solid electrolyte interphase
SEM	Scanning Electron Microscopy
STEM	Scanning Transmission Electron Microscopy
DFT	Density Functional Theory
D	Diffusion coefficient
t	Diffusion time
TEM	Transmission Electron Microscopy
TGA	Thermogravimetric Analysis
XPS	X-ray Photoelectron Spectroscopy
XRD	X-ray Diffraction
BET	Brunauer-Emmett-Teller
MS	Mass spectrometry
HRTEM	High resolution microscopy

CHAPTER 1 INTRODUCTION

1.1 Research Background

With the rocketing progress of global economy and the further improvement of industrial modernization, the demand for energy is growing rapidly, as the indispensable resource for human survival and development. [1-3] Up to 2018, the worldwide applied energy sources are mainly derived from fossil fuels, which are typical non-renewable energy sources and will eventually face the dilemma of exhaustion. Inferred from the statistics from the International Energy Agency, all the traditional fossil energy sources in the earth can only support human life for 220 years at most, based on the current rate of energy development and consumption. [4-6] In addition, the use of fossil fuels brings about climate and environmental issues (such as the greenhouse effect, extreme weather, PM2.5, etc.) which induce a great threat to all biological groups including humans all over the world. [7] Thence, how to deal with the problem of energy shortages and environmental pollution is a huge challenge that people must face and urgently need to solve. It is significantly important to balance the sustainable economic and social development with the energy & environment, which are also becoming the cooperation direction between the industry and the industry for all countries in the world.

Therefore, renewable energy including wind energy and solar energy will become the main object of energy structure reform and development. [8-10] Despite the fact that the storage of renewable energy sources is abundant and widely distributed, it is difficult for the direct utilization, due to their discontinuous and unstable energy supply mode. Hence, the most widely used method it to store these energy sources in the form of electrical energy for application. As a result, there is a demand for an efficient and

recyclable safety and energy conversion device to achieve the effective storage, transportation and use of energy. Lithium-ion battery is an efficient system which could convert chemical energy to electrical energy reversibly. [11,12] Compared to other batteries, lithium-ion batteries have the advantages of high capacity, long service time, portability and environmental protection. From electric wearables to grid stations, Lithium-ion batteries will have broader application prospects, and simultaneously, huge difficulties and challenges are brought about in order to fulfil the increasing demand of developed battery technologies and advanced battery systems of higher energy density and longer cycling performance. [12-14]

It is urgent to explore innovative electrode materials that are smaller, lighter (higher energy densities), safer, and cheaper to satisfy the commercail usage of lithium-ion batteries (LIBs). The specific capacity of intercalation-type cathodes and graphite anodes which are generally used in commercial application are approaching their fundamental limits recently.[15-17] For instance, the relatively low gravimetric/volumetric capacity (~300 mAh g^{-1} /~735 mAh cm^{-3}) of commercial graphite anodes limits the energy densities of commercial LIBs. [18, 19] It is reported that, compared with intercalation-type and commercial anode materials, the conversion type anodes have advantages of higher theoretical lithium storage capacity and more appropriate working potential which are more likely to solve the current market problems in rechargeable batteries via improved energy densities.

Among conversion materials, metal hydrides emerges and attraced much atterntion as anode materials for LIBs owing to the excellent theoretical specific capacity and relatively small polarization. However, the intrinsic poor conductivity, volume expansion, and high chemical activity, which are easily oxidized during applications hindered its application. There are still far way to go and full of challenges to design

and develop new systems of metal hydrides based materials with outstanding discharge/charge capability and reverible properties as anode of LIBs.

1.2 Objectives of the Research

In this thesis, we focus on two kinds of metal hydrides, $NaAlH_4$ and MgH_2, which displays promising application potential when employed as electrodes in LIBs, on conditions of both liquid traditional battery and all solid-state batteries. Four modification technologies inculding carbon doping, nano crystallization, surface modification and process modification are conducted for improving lithium storage performance of the $NaAlH_4$ and MgH_2 based anodes. The modification mechanisms, and fabrication methods based on this two metal hydrides were discussed in detail in this thesis as well as electrochemical performances. The purpose of this work is to obtain high performance LIBs with enhanced rate capability and sable cycling performance. Although commercial application of these work still has a long way to go, the relevant material design, synthesis technologies, and new discoveries will be important.

1.3 Thesis Structure

This thesis concentrated on the modification of metal hydrides for advanced lithium storage performance. Four methodologies are carried out to obtain anode materials for LIBs with high specific capacity, good rate performance and long service life. This thesis is elaborated from the research background, research plan to research content and conclusions.

Chapter 1 briefly describes the background for nowadays energy crisis and the background for the LIBs.

Chapter 2 demonstrates a literature review on recent research improvements on metal hydride anodes as materials for LIBs.

Chapter 3 describes the experimental methods in detail, and related scientific research instruments for phase analysis, morphology characterization and performance testing referred in this study.

Chapter 4 presents the graphene-tailored molecular Al-H bonds of $NaAlH_4$ for advanced lithium storage performance.

Chapter 5 introduce the preparation and lithium storage performance of nano-magnesium hydride with controllable morphology.

Chapter 6 investigates porous magnesium hydride nanoparticles in-situ decorated with Mg-based composites towards advanced lithium storage performance.

Chapter 7 investigates the in-situ constructed double ionic-electronic transfer interface between MgH_2 and $LiBH_4$, which boosts the performance of the solid-state lithium ionic battery.

Chapter 8 concludes four works of this thesis and put forward some problems and prospects for the following research directions.

1.4 References

[1] S. Fleischmann, J. B. Mitchell, R. Wang, C. Zhan, D. Jiang, V. Presser and V. Augusyn, *Chem. Rev.,* **2020**, *120*, 14, 6738.

[2] H. Zhang, X. Liu, H. Li, L. Hasa, S. Passerini, *Angew.Chem. Int. Ed.,* **2021**, *60*, 598.

[3] F. Wu, N. Chen, R. J. Chen, Q. Z. Zhu, G. Q. Tan, L. Li, *Adv. Sci.*, **2016**, *3*, 1500306.

[4] X. Pu, M. M. Liu, L. X. Li, C. Zhang, Y. K. Pang, C. Y. Jiang, L. H. Shao, W. G. Hu, Z. L. Wang, *Adv. Sci.,* **2016**, *3,* 1500255.

[5] N. Zhang, Q. Li, C., et al., *Nat. Energy*, **2019**, *4*, 594.

[6] P. G. Bruce, S. A. Freunberger, L. J. Hardwickand, J. M. Tarascon, *Nat.Mater.*, **20 11**, *11*, 19.

[7] S. Kumar, G. Saeed, L. Zhu, K. N. Hui, N. H. Kim, J. H. Lee. *Chem. Eng. J.*, **2021**, *403*, 126352.

[8] X. Wang, Y. Chen, O. G. Schmidt and C. Yan, *Chem. Soc. Rev.*, **2016**, *45*, 1308.

[9] E. Pomerantseva, F. Bonaccorso, X. L. Feng, Y. Cui, Y. Gogotsi, *Science*, **2019**, *366*, 969.

[10] A.G. Olabi, M. A. Abdelkareem, T. Wilberforce, E. T. Sayed, *Renew. Sust. Energ. Rev.*, **2021**,*135*,110026.

[11] R. Schmuch, R. Wagner, G. Hörpel, T. Placke, M. Winter, *Nat. Energy*, **2018**, *3*, 267.

[12] A. Manthiram, *Nat. Commun.*, **2020**, *11*, 1.

[13] A. Gupta, A. Manthiram, *Adv. Energy Mater.*, **2020**, *10*, 2001972.

[14] J. Xiao, Q. Li, Y. Bi, *et al. Nat. Energy,* **2020,** *5*, 561

[15] Z. Jian, Z. Xing, C. Bommier, Z. Li, X. Ji, *Adv. Energy Mater.*, **2016**, *6*, 1501874.

[16] L. P. Zhang, X. Li, M.R. Yang, W. H. Chen, Energy Stor. Mater., **2021**, *41*, 522.

[17] Y. Nomura, K. Yamamoto, M. Fujii, *et al. Nat. Commun.* **2020**, *11*, 2824.

[18] F. X. Wu, J. Maier, Y. Yu, *Chem.Soc.Rev.*, **2020**, *49*, 1569.

[19] A. Ponrouch, C. Frontera, F. Bardé, M.R. Palacín, *Nat. Mater.*, **2016**, *15*, 169.

CHAPTER 2 LITERATURE REVIEW

2.1 Progress on Metal Hydrides as anodes for LIBs

With high gravimetric and volumetric energy, high energy density, and low self-discharge performance, rechargeable lithium-ion batteries (LIBs) now occupy most of the energy storage and electronic equipment markets for the replacement of fossil fuels. In particular, the wide employment of LIBs in electric vehicles (EVs) during the last few years [1-3], means that energy densities that are two to five times higher than the present LIBs technologies could offer (150 Wh/kg) are in great demand. In order to keep pace with the increasing market demand for batteries with high energy density, the investigation of high-performance LIBs is of great importance.[4]

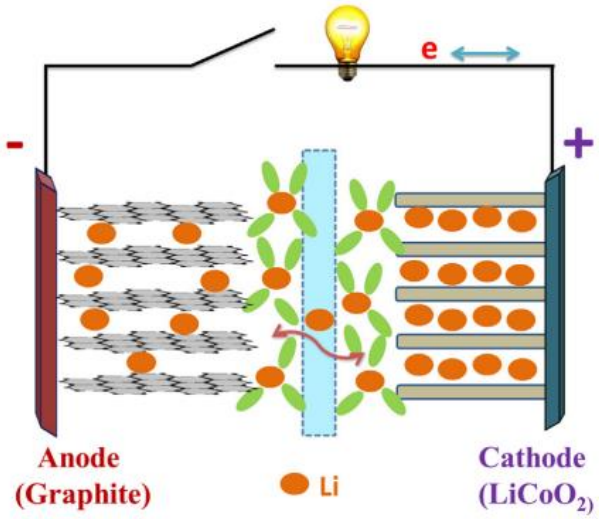

Figure 2.1 Schematic representation of lithium insertion/de-insertion mechanism for current rechargeable lithium battery. [3]

Considering the composition of a battery cell including cathode, electrolyte, separator, and anode, (**Figure 2.1**) the bottleneck of the advanced energy density of LIBs are the selected active materials with relatively high specific capacity, cathode materials with adequately high voltage, anode electrode materials with appropriate low

potential and electrolyte with wider electrochemical window stability. In terms of cathode materials, the commercial cathodes including $LiFePO_4$, $LiMn_2O_4$ and $LiCoO_2$ offer low specific capacities (<180 Ah kg^{-1}, <750 Ah L^{-1}) [4-6] and low operating potentials (<3.8 V vs. Li^+/Li). Many groups choose to explore new cathode materials with higher specific capacities (>180 Ah kg^{-1}) and/or higher average working voltages (>3.8 V vs. Li^+/Li).

In case of anode materials, **Figure 2.2** summarizes the reported widely used anode materials in LIBs, delievering their theoretical gravimetric and volumetric capacies and operating voltages. Via intercalation between the graphene planes (1 atom per 6 C), graphite (373 Ah kg^{-1}, 735 Ah L^{-1}) become the common anode material choice in the current commercial LIBs, which is apparently far from the demand of the market target. [7] In addition, lithium titanium oxides ($Li_4Ti_5O_{12}$) are also a common choice for commercial use with high-rate capability, long cycle life and no volume change, due to their "zero strain" intercalation. However, low specific capacity (373 Ah kg^{-1}, 735 Ah L^{-1}), low energy density, high working potential (1.55 V vs. Li^+/Li), and high cost of the elements Li and Ti have hindered further application [8,9].

Beyond the weak points of the mentioned insertion materials, alloy-type and conversion anode materials with multiple high specific capacity are explored to achieve the market targets of high energy densities. The alloy-type anode materials are presented to be group IV (Si, Ge, Sn, Pb) or group V (P, As, Sb, Bi) or light metals (Li, Mg, Al) in the periodic table. [10-13] For comparison, alloy-type anodes have the advantages of much higher specific capacity and lower operating potential, but the general large unavoidable volume expansion, unstable interface and low first CE of them have significantly impeded the application. For instance, Si have extremely high theoretical specific capacities of 3579 mAh g^{-1} with an average working potential of

0.4 V (vs. Li^+/Li). Unfortunately, large volume change which could reach 300% occurs during the lithiation and delithiation process, lead to huge structural destruction and deteriorating cyclic performances in LIBs systems [1,10-14].

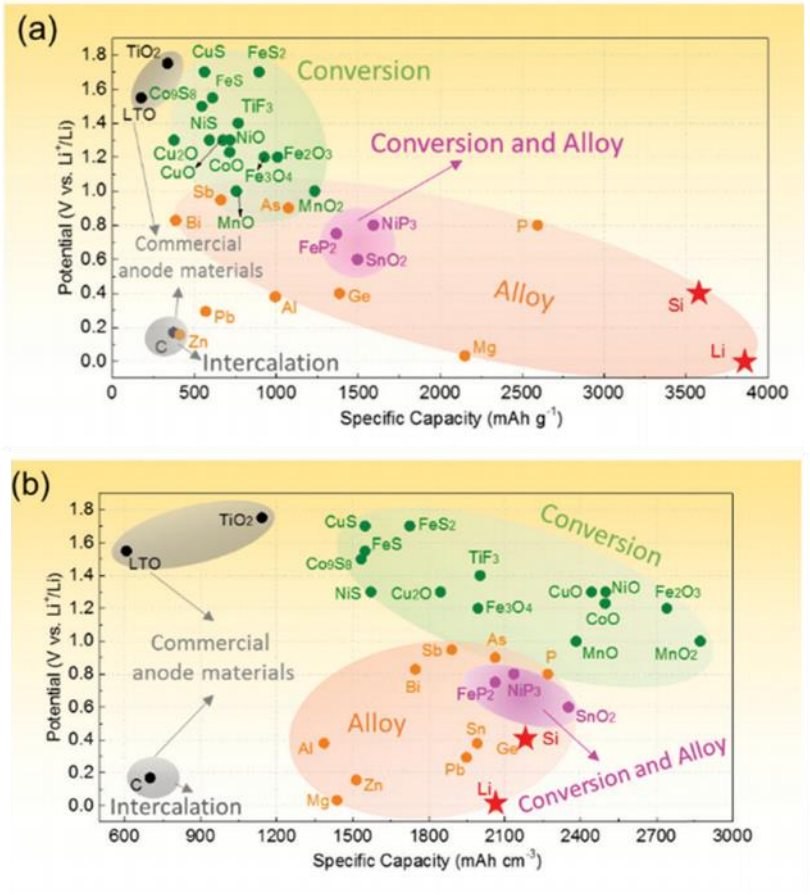

Figure 2.2 Theoretical gravimetric (a) and volumetric specific capacities (b) for these selected anode materials. [4]

As illustrated in **Figure 2.2**, conversion-type materials with high capacity including transition metal sulfides (Co_9S_8, SnS_2 etc.), oxides (MoO_6, Fe_2O_3, Fe_4O_3, etc.) and fluorides (TiF_3, FeF_2 etc.) etc. [15-20] are considered to be more promising candidates for high energy densities. The reaction mechanism is described as follow, (Eq.2.1) reacting with lithium, conversion-type materials M_aX_b transform to the transition metal M and Li_nX, where X is an anion and n is the oxidation state of X [17]:

$$M_aX_b + (b \cdot n)Li \leftrightarrow aM + bLi_nX \qquad \textbf{(2.1)}$$

This reaction implies that, every redox centre exchanging more than one electron, according to the chemical valence state of M, these reactions could involve different quantities of electrons such as one electron for Cu_2O, or four electrons for RuO_2. [21-25] Therefore, compared with graphite or insertion oxides, conversion type electrodes show better advantages of excellent theoretical specific capacity [26-30].

Nevertheless, the voltage hysteresis during discharge and charge becomes a common problem for all conversion type electrodes and would decrease the energy density and limit the application of LIBs [31-34]. Metal hydrides, emerging as a conversion LIBs anode material in 2008, have attracted much attention. Compared with the other conversion materials, metal hydrides have higher theoretical specific capacity and lower polarization. [35] The theoretical capacities of various metal hydrides are presented in **Figure 2.3**, from binary metal hydride (MgH_2, CaH_2, AlH_3 etc.) to ternary metal hydrides [36-40]. It is obvious that, the theoretical specific capacities of most of the metal hydrides are beyond thousands of mA h g^{-1}, which is several times higher than that of commercial used graphite, enough to fulfil the commercial market demand for the high energy density. The general reaction between metal hydrides and Li^+ could be written as follow (Eq 2.2):

$$MH_y + yLi^+ + ye^- = M + yLiH \qquad \textbf{(2.2)}$$

where the amorphous LiH matrix surrounding the reduced metal/alloying M. [35] The high specific capacity of the metal hydride anodes could be attributed to the participation of a high number of electrons in the conversion reactions and the light weight of the metal hydride [36].

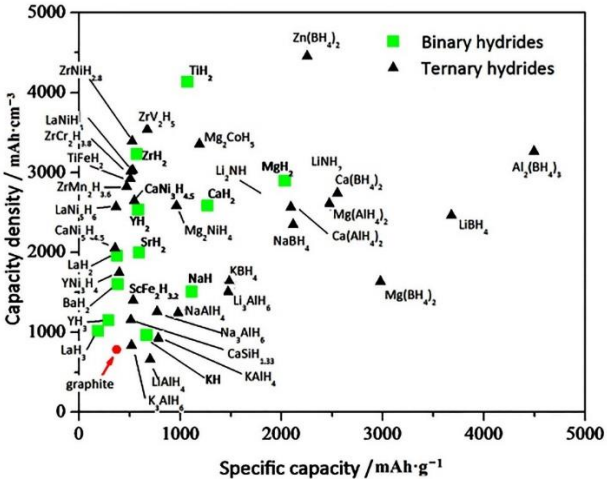

Figure 2.3 Theoretical gravimetric and volumetric specific capabilities for both binary and ternary hydrides. [40]

Based on the number of contained elements, there are two types of metal hydrides, binary and ternary hydrides. Several suitable binary metal hydrides have been widely explored. ((MH_x)-based anode materials for LIBs, M = Na, Mg, K, Ti, Cs, Y, Sr, La and Zr) **Figure 2.4** shows the equilibrium potential of the MH_x/Li cell for different hydrides. From a thermodynamics point of view, the potential is positive for Zr, Ti, Na, Cs and Mg and negative for Y, La, Ba and Ca hydrides, which means the conversion reaction is favourable for Zr, Ti, Na, Cs and Mg hydrides and not possible for Y, La, Ba, Ca. The Gibbs free enthalpy of formation of these hydrides is smaller than that of LiH (inset **Figure 2.4a**).[36] Among which, MgH_2 and TiH_2 stand out for the high specific capacity. MgH_2 has been paid much attention because of its high theoretical capacity as much as 2038 mA h g^{-1}, small polarization and wide sources storge but with poor electronic conductivity, while TiH_2 exhibits high theorecical capacities and good electronic conductivity owing to its metallic properties, which benefit for improved kinetics during the conversion process.

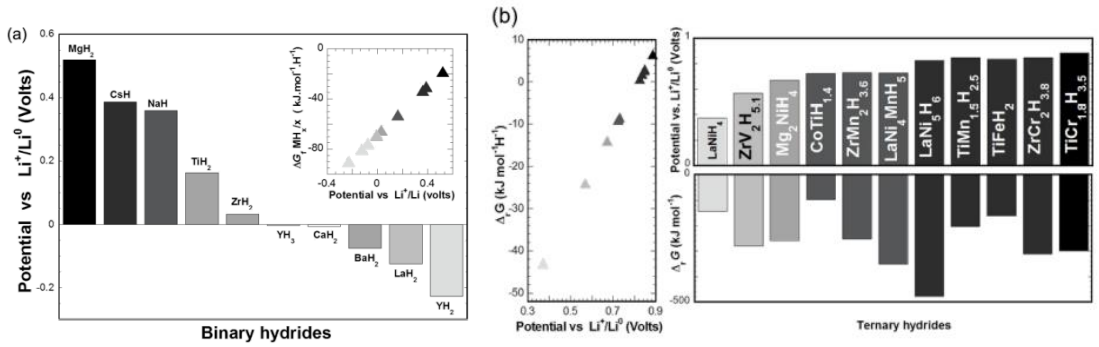

Figure 2.4 Theoretical equilibrium potential for the MH_x/Li cell vs Li^+/Li. a) For binary hydrides and b) ternary hydrides, Inset: Gibbs free formation enthalpy of these hydrides as a function of the equilibrium potential.[36]

Based on the constituent elements, ternary hydrides could be divided into many types including B-based hydrides ($LiBH_4$, $NaBH_4$, $Mg(BH_4)_2$ etc.), Al-based hydrides ($LiAlH_4$, Li_3AlH_6, $NaAlH_4$, Na_3AlH_6 etc.), and Mg-based hydrides (Mg_2CoH_5, Mg_2NiH_4 and Mg_2FeH_6 etc.) [36]. It has been shown in **Figure 2.4b** that the formation value of Gibbs free enthalpy for all these ternary hydrides is above that of LiH. The conversion reaction could be achieved if the equilibrium potential of the cell is positive. It would be favourable to be an anode electrode in LIBs, if the equilibrium potentials are in the range of 0.3–1.0 V. In the case of Al-based hydrides, the alanates has high theoretical specific capacities (e.g., 2821 mAh g^{-1} for $LiAlH_4$ and 2482 mAh g^{-1} for $NaAlH_4$), owing to the high content of hydrogen. However, their full potentials are very difficult to reach, as poor reversibility, cycling stability, and rate capability prevent alanates from practical use. Silvestri et al.[41, 42] reported that $LiAlH_4$ electrodes with $LiPF_6$-EC-DMC electrolyte can only reach a first-cycle discharge and charge specific capacity of 1150 and 460 mAh g^{-1}, respectively, which could be ascribed to bad kinetics derived from phase segregation and particle pulverization and intensive side reactions between electrolytes and highly reductive $[AlH_4]^-$ or $[AlH_6]^{3-}$ anions. A Li_3AlH_6-Al nanocomposite with fast elelctronic and Lithium ionic conductiveity (C and P63mc

$LiBH_4$) was in-situ prepared by Pang et al. [43] through pretlithiation of $LiAlH_4$. In a solid-state cell, this nanocomposite delivers a discharge capacity of 2266 mAh g^{-1} with a coulombic efficiency of 88% at first cycle, which maintains the capacity of 71% in the 100th cycle, and could realize 1429 mAh g^{-1} at 1 A g^{-1}.

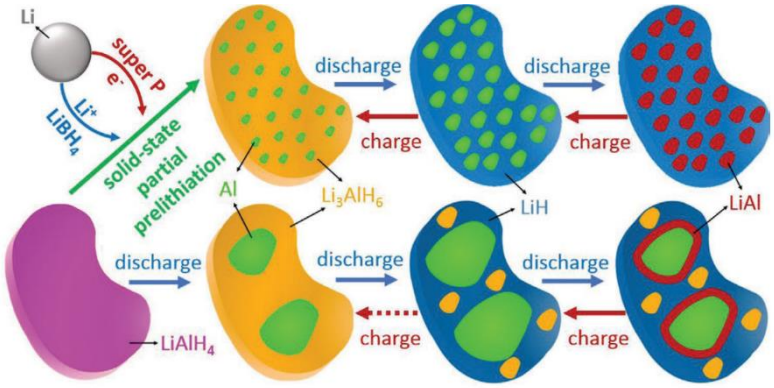

Figure 2.5 Schematic illustration of the structural evolution of the SSPP Li-Al-H anode and $LiAlH_4$ anode during cycling. [43]

As a result of the high contact area between electrode and electrolytes, LIBs system have rapid ionic diffusion with liquid electrolytes, however, it has been proved that metal hydrides electrode could gradually react with liquid electrolyte during long cycling could lead to the fast capacity fading during long cycling process. As a result, the choice of electrolyte also plays a vital role in enhancing electrochemical performances of metal hydrides. Afterwards, solid-state electrolyte with favourable ionic conductivity and appropriate operation voltage window becomes a promising tendency in the next generation of lithium-ion battery. Among all the generally used electrolytes, such as LISICON-type, Garnet-type, Perovskite-type, NASICON-type, and glassy and glass-ceramic systems made of oxides and sulphides [38], $LiBH_4$ were more suitable for the metal hydrides electrolyte due to the strong chemical reduction property. Moreover, when heated above ~390 K, $LiBH_4$ could displays superior Li^+ conductivity (~ 10^{-3} S cm^{-1}) and it still shows stable electrochemical property within

the working voltage window of 0 to 5 V vs. Li^+/Li [43-45]. Additionally, for metal hydrides-based electrode, not only $LiBH_4$, but also sulfide based solid-state electrolyte could be a favourable solid-state electrolyte. [46-48].

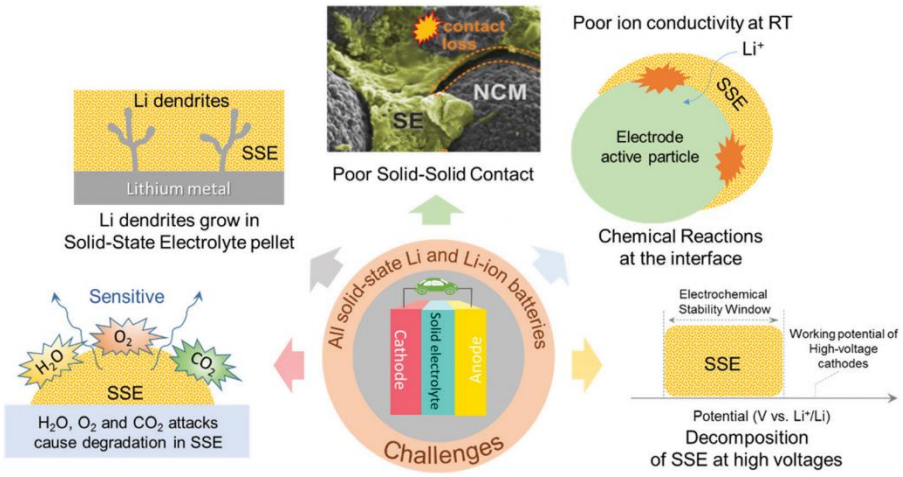

Figure 2.6 Remaining challenges of solid-state Li and Li-ion batteries. [4]

To sum up, **Figure 2.6** illustrates the existed problem that restricted the application of the general all solid-state batteries. Li-ion batteries with electrodes of metal hydrides have gone through the same challenges: (I) low ionic conductivity at room temperature, (II) the tendency of Li dendrite growth, (III) poor solid–solid contact during operation (IV) high air sensitivity of SSE, (V) unfavorable side reactions at the solid–solid interface and (VI) decomposition of SSE at high voltages. In order to solve these problems, many efforts have been devoted to enhancing the lithium storge performance of metal hydrides anodes to achieve higher specific capacity, rate capability and long cycle life. We take a representative MgH_2 and and $NaAlH_4$ as moldels from the binary and ternary materials, respectively, and conclude the modification methods and research progress in liquid lithium-ion batteries.

2.2 Metal Hydride Working with Conventional Organic Electrolyte System

2.2.1 Sodium Alanate

$NaAlH_4$ has long been regarded as a promising hydrogen storage materials because of its high weight content of H element (7.5 wt.%) and low hydrogen desorption temperature. It has been found to provide very high theoretical capacities (1985 mA h g^{-1}) ascribed to the light weight of aluminum, lithium and hydrogen element as well as the high hydrogen content. $NaAlH_4$ belongs to ionic-covalent compounds consisting of tetrahedras of $[AlH_4]^-$ or octahedras of $[AlH_6]^{3-}$. Al-H covalent bonds gathering to generate polyanions to collect negative charges which are surrounded by metal cations Na^+ [8,49,50]. Additionaly, M^+-$[AlH_4]^-$ and $3M^+$-$[AlH_6]^{3-}$ are bonded by ionic bonds [50, 51]. Their theoretical capacities (1576 mA h g^{-1} for Na_3AlH_6 [52]) is realized through exchanging 4 and 6 electrons for $NaAlH_4$ and Na_3AlH_6, respectively. Moreover, $NaAlH_4$ was reported to develop the theoretical specific capacity without any mechanochemical pre-activation [53]. The two-step conversion lithiuation reation of $NaAlH_4$ is described as follows (**Eq 2.3** and **Eq 2.4**):

$$NaAlH_4 + 3/2Li \leftrightarrow 1/2LiNa_2AlH_6 + 1/2Al + LiH \quad \textbf{(2.3)}$$

$$LiNa_2AlH_6 + 3/2Li \leftrightarrow 2Na + Al + 6LiH \quad \textbf{(2.4)}$$

As shown in **Figure 2.7**, in the discharge process of the first cycle, a slope plateau around 0.75 V should be ascribed the to the appearance of SEI layer. The plateau showing besides 0.25 V is attributed to the alloy formation process of lithium and Al. It is obvious that the lithiation reaction that occurs below 0.3 V contributes the most lithium storage capacity of the entire reaction (4.05 Li), which is closed to the potential for the lithiation of Al. The following continuous slope stretches to the low voltage

limit, suggesting the formation of AlLi occurring in parallel. The inset curves in **Figure 2.7** demonstrates cyclic voltammogram of the first cycle, the main peak in cathodic scan located at approximately 0.8 V refers to the formation of the SEI layer, below 0.25 V, following a sharp signal which corresponds to the lithiation of Al. In terms of the anodic scan, both of the delithiation of AlLi and the decomposition of LiH to reform $NaAlH_4$ could be observed. Subsequently, the electrochemical signal represents the desired hydride conversion reaction becomes weak and weak during cycling. It could be concluded that the lithiation/delithiation of Al are the primary electrochemical processes after the first cycle, which is coincidence well with the galvanostatic cycling.

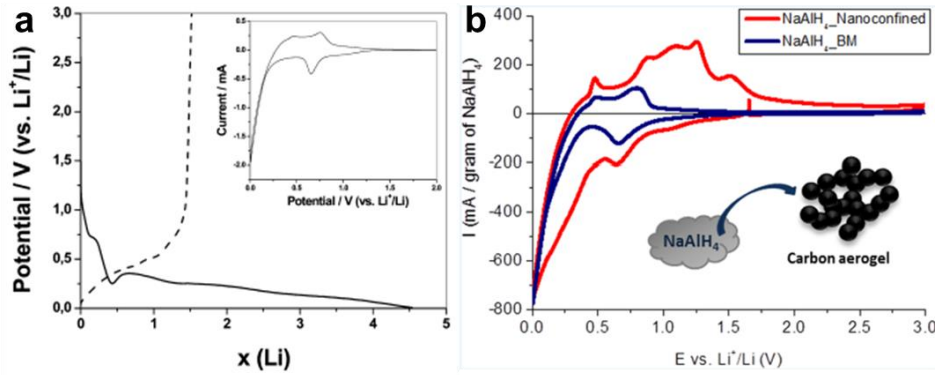

Figure 2.7 (a) Constant current cycling of the $NaAlH_4$ based anode material at a rate of 1 Li/10 h. Solid, discharge; dashed, charge. The inset shows the cyclic voltammogram of the first cycle at a scan rate of 0.1 mV/s. (b) Cyclic voltammograms of nanoconfined and ball milled $NaAlH_4$. [53, 41]

It could be inferred frrom the above, two different reaction paths could proceed simultaneously in one reaction, it is also possible to have two-intermediates coexist in one system. However, $NaAlH_4$ suffers from a rapid capacity fading at first cycle and very poor reversibility which may be ascribed to the phase separation and poor conductivity of electrode during cycling[41]. In order to advance the cycling performance of $NaAlH_4$ electorde, reducing the particle size down to nanoscale is

proved to be an effective and widely used approach [54-56]. Ball milling with carbon materials have always been an simple and effective way to develop the electronic conductivity and downsize the particle of electrode materials. [52] Silvestri et al., [53] Cirrincione et al., [54] and Wu et al. [55] have applied mechanochemical treatment with carbon on the $NaAlH_4$ active materials, which improved the reversibility of $NaAlH_4$. Silvestri et al. found that an additional ball milling with Super P carbon has a dramatic beneficial effect of the reversibility of the conversion process with a coulombic efficiency close to 70%. Cirrincione et al. reported that the conversion reaction reversibility of the sample could be dramatically improved after operating pre-treatment (ball milling for 15 h) [54]. As a consequence of the creation of a highly active carbon-hydride composite which was a kind of SEI. The first charge capacity is nearly 1250 mA h g^{-1}, with the coulombic efficiency enhanced from 30% to 70%. In addtion, the intimate mix with carbon buffers the volume change and prevents the loss of electronic contact between particles even after the large volume variations occured upon full conversion. Wu et al. [56] investigate the regeneration mechanism and the degradation mechanism of $NaAlH_4$ anode to improve its Li storage performance, as shown in **Figure 2.8**. It has been found that the cycle performance of $NaAlH_4$ benefits from decreased crystalline size. When the crystalline size decreases from 64 nm to 43 nm, the charge capacity of $NaAlH_4$ increases from 942 mAh g^{-1} to 1575 mAh g^{-1}. The ex-situ XRD patterns proved that $NaAlH_4$ with a crystalline size of 43 nm could be directly regenerated from Na and Al without any intermediate phases (such as $LiNa_2AlH_6$). However, the cycle capacity still decays quicky and only 89 mA h g^{-1} can be remained after 20 cycles (**Figure 2.8**) which is derived from the electrochemical decomposition of regenerated $NaAlH_4$ above 1.42 V. Therefore, an enhanced Li-storage performance of $NaAlH_4$ anode could be obtained by both decreasing the crystalline size and reducing

the cut-off voltage. Huen at al. [66] firstly reported the electrochemical performances of $NaAlH_4$ nanoconfined in carbon scaffolds. As shown in **Figure 2.7b**, compared to that of nonconfined $NaAlH_4$, the electrochemical reversibility of nanoconfined $NaAlH_4$ was improved from around 30 to 70% in the first cycle. The loss in the reactivity of $NaAlH_4$ could be related to inefficient diffusion of the hydride, which may limit the extent of hydride conversion.

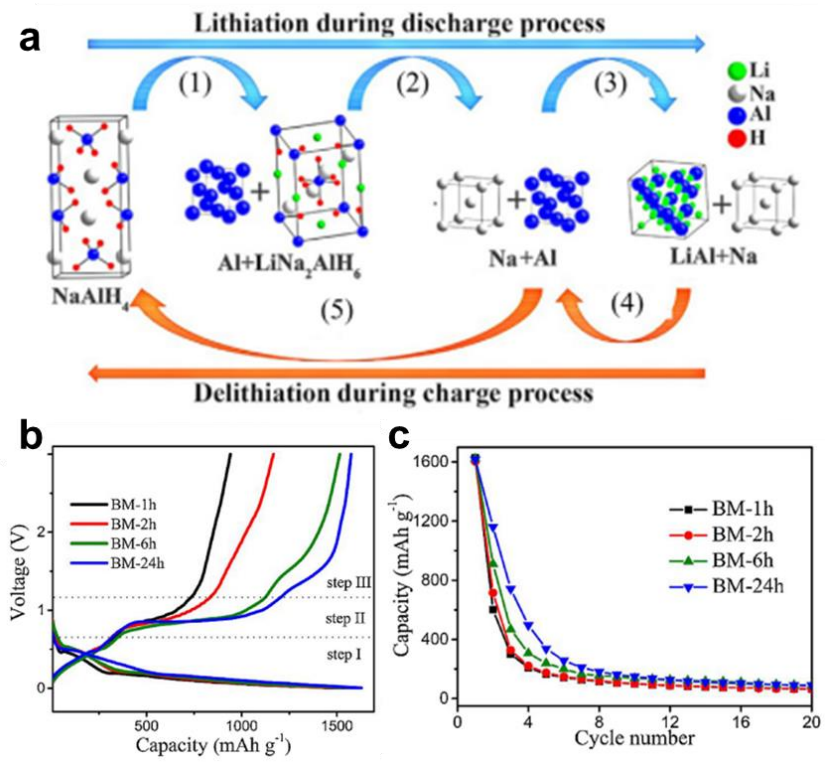

Figure 2.8 (a) Schematic diagram of lithiation and delithiation mechanisms. (b) The galvanostatic discharge-charge curves of samples at first cycle. Their cycle capacity (c) at 100 mA g^{-1}. [56]

As we can see, there are still many challenges hindered the application of nanoconfined $NaAlH_4$. To enhance the reactivity of nanoconfined hydride, it is important to maximize the loading of hydride inside the scaffold, which will also increase the material capacity. It is also interesting to study the influence of pore size and different activation methods on the electrochemical reactivity of the carbon scaffold.

A smaller pore size of the scaffold is expected to enhance the kinetics of the material and may also reduce polarization of the electrode. New electrically conductive but inert scaffolds may also need to be explored to understand the nanoconfinement effect in more detail.

2.2.2 Magnesium Hydride

When considered as an anode for LIBs, MgH_2 displays high theoretical specific capacity (2038 mA h g^{-1}, 2,878 mAh cm^{-3}), small polarization (< 0.2 V) at relatively low working voltage. With a conventional organic electrolyte, when used as an electrode for LIBs, MgH_2 could present an outstanding specific discharge capacity of 1480 mA h g^{-1} at first cycle. The operating voltage of MgH_2 is little higher than that of the lithium plating, nevertheless, much lower when compared with other conversion-type electrodes. [35]. Hence, the high working potential of an assembled full LIBs is guaranteed which lead to higher energy density LIBs systems. In addition, the magnesium resource in the earth is abundance and low cost. All these vital properties fall into the line of application of MgH_2 in future electric vehicles' batteries.

However, capacity degradation during cycling hampers the application of MgH_2 based materials when acting as an anode in LIBs. Bulk MgH_2 electrodes delivers a discharge capacity of 1,500 mAh g^{-1} with a CE of 75%. The large initial irreversible capacity (approaching 30%) and poor capacity retention limited to working less than 20 cycles, regardless of the cycling rate or voltage window. During the conversion reaction, MgH_2 can interact with 2Li, leading to the formation of 2LiH and Mg. At low cycling rate (C/100), MgH_2 can exchange up to 2.9 Li equiv during the first discharge with two plateaus at 0.44 V ($\Delta x \approx 1.8$ Li) and 0.095 V, the latter step being attributed to the formation of the hcp Mg-rich and bcc Li rich Mg−Li solid solutions. [58,59] The

delithiation of the Li_3Mg_7 phase has been found to be reversible under hydrogen pressure (2 MPa) at high temperatures (200 °C), which may be of interest for LIB MgH_2-based anodes. The most common reasons for such cycling degradation are concluded as follows, the poor electric conductivity of MgH_2, the volume variation accounts to be 85% can easily lead to contact issues and loss of conductivity, electrode surface area variation (∼2−3 times) which can affect the applied current densities per surface unit and the coarsening of the nanoparticles. [35,40,60,61].

In order to improving the lithium storage performances of MgH_2, many strategies have been used which can be divided into 4 types (catalyst/carbon doping, nanoconfinement, structure and synthetic methods optimization) [60-63]. Some cycling improvements were observed when vinylidene carbonate was added to the electrolyte mixture or when the cycling voltage was limited to values greater than 0.2 V due to the enhanced conductivity. Catalysts (carbon-based hybrids, transition metal etc.) also benefit for the high-rate capability of cycling as a result of accelerated kinetics of electrocatalytic activity of the MgH_2 [64-66]. Nanocrystallization benefit for improved reversible capacity, cycle life and rate capability, taking advantages of narrowed lithium-ion and mass transfer pathway, fast charge transfer rate and restricted volume expansion. Thus, the common problem of conversion reaction that losing of electronic percolation within the electrode induced by volume variations could be relieved somehow [67]. Meanwhile, previous studies have shown that the electrochemical performance depends on electrode morphology. Fabrication methods are of significant importance in controlling microstructure, morphology and lithium storage performance of the samples.

2.2.2.1 Catalyst

Catalyst addition contributes to effectively against kinetic limitations. It has been found that the bond energy of Mg-H could be reduced by forming new Mg–M–H compounds (M ¼ Sc, Ti) [68–70] which break the hydride thermodynamic stability of MgH_2 based materials. In terms of electronic conductivity, metal catalyst has more advantages than oxides apparently [68,69]. There are 3 wt. % of Ni was added into MgH_2 MCMB carbon mixture. The catalysed sample shows an improved reversible capability as much as 2608 mA h g^{-1} under 0.02 C and the related cut-off voltage is 0.01 V vs Li^+/Li^0. Furthermore, the addition of Ti, Co, Pt, NiTi, TiCrV and other metal catalysts significantly enhanced the charge/discharge efficiency. Additionally, some metal alloy (ZrMn, $LaNi_5$, etc.) contribute to prevent the pulverization and coarsen of particles via providing a mechanical robustness buffer [71]. As shown in **Figure 2.9**, Huang et al. [72] have recently shown that in electrochemical cells, TiH_2 addition to MgH_2 forming a $0.7MgH_2$-$0.3TiH_2$ composite which not only improves the kinetics of the conversion reaction of MgH_2 with lithium but also that the latter hydride enables the reversible conversion reaction of TiH_2. This synergetic effect is attributed to the high electronic conductivity and fast hydrogen transport of titanium hydride. Followed by Berti et al., who extend the molar ratio of TiH_2 phase over a wide composition range ($0.2 \leq y \leq 0.8$) to study the influence of the TiH_2 amount on the reaction reversibility and better understand the synergetic effects between the two hydrides on the conversion reaction mechanism. Xu et al. added TiF_3 as a catalyst the MgH_2–TiF_3@CNT anode exhibits a capacity retention of 543 mAh g^{-1} in 70 cycles at 0.2 C and outstanding rate capability in liquid electrolyte-based Li ion batteries. [73] Adding catalysts proved to be an effective way for accelerated reaction kinetics, thereby increasing the rate capability of MgH_2-based electrodes. However, more and more theoretical calculations and

laboratory results are needed to figure out the mechanism and benefit for further development. [74]

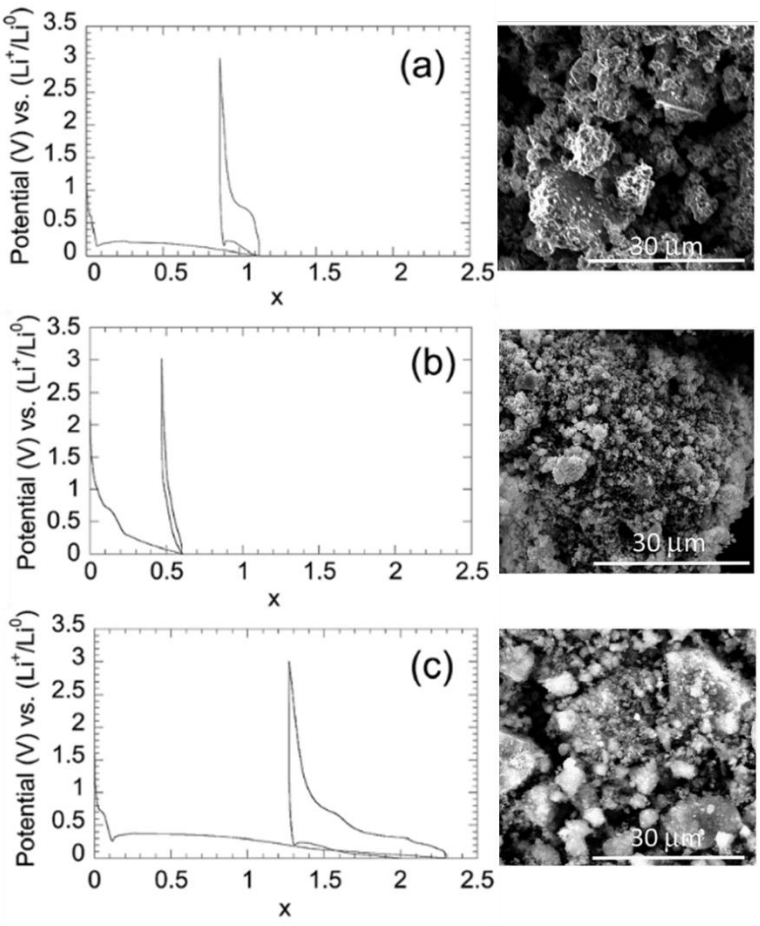

Figure 2.9 Potential composition curves (i.e. x ¼ lithium mole fraction) and the corresponding SEM images of MgH_2/Li (a), TiH_2/Li (b) and $0.7MgH_2$–$0.3TiH_2$/Li (c) cells at a current rate of 0.1Li per hour. [72]

2.2.2.2 Nanostructures

Taking the advantages of sufficient active reaction sites, shortened diffusion pathway for electronic and ionic, limited phase transfer space et al., nanostructured electrode has significant superiority in advanced lithium storage performance. Among various method for the building of nano structures, mechanochemical grinding is a widely used up-bottom strategy which is effective and facile. Nano-MgH_2 particles with a size of 10-15 nm could be easily achieved by ball milling with Super P. Through the above

post-milling operation, MgH_2 shows ~1600 mA h g^{-1} discharge capacity and an initial CE of 62.5% tested with widely used liquid electrolyte which mainly contains $LiPF_6$ in organic solvent. However, the unlimited volume variation about 200% lead to a fast capacity fading. Many other carbon materials have been added for a better cycling performance. Such as MCMB 2528 [75], $C_{7,460}$ [76], MCMB-derived carbon [77] and so on. Appropriate binders are reported to be another effective option to alleviate the volume change during cycling. a format-derivative CMC-f which is a hydrophobic polymer with less ionic properties was incorporated in MgH_2-based electrode and exhibited improved cycling performances. [78]

Compared to ball milling with carbon, chemical synthetic methods display more efficiency on suppression of agglomeration of particles during cycling which contribute to the enhanced lithium storage properties of MgH_2-carbon composites. Through magnetron sputtering and hydrogenation treatment, Peng et al. [79] have fabricated MgH_2-C films. Compared with pure MgH_2 films, the crystallite size of MgH_2-C films is smaller, which induce lower polarization effect and higher structural stability subsequently. MgH_2 particles which is only 5 nm averagely, was generated by Oumellal et al. through a bottom-up method. [80]. The prepared MgH_2 nanoparticles is uniformly dispersed into a porous carbon host. The loading rate of MgH_2 could be controlled with an up limit of 70 wt.% which is realized through adjusting the number of precursors. Among which, the composites with 50 wt% Mg content demonstrate a particle size of 5.5 nm averagely with a narrow particle size distribution (1–10 nm). Before used as electrode, the composite containing 50 wt% Mg need to ball milled under Ar. Owing to the stability and unique of the structure, the size distribution of nanoparticles could be maintained, and electronic conductivity of the whole system is enhanced which present impressively stable cycling performance with a high specific capacity around

500 mA h g^{-1}. However, the MgH_2 particles grows outside the carbon hosts leads to a dramatic capacity fading after several cycles, as a result of the lost connection between the outside MgH_2 particles and carbon scaffold. [81,82] Nowadays, nano MgH_2-graphene (GR) composite was synthesized through the similar strategy. Monodispersed MgH_2 nanoparticles around 13.8 nanometres grow uniformly on the graphene nanosheets forming a "sandwich" structure (**Figure 2.10**). The fabrication of GMH composite is illustrated in **Figure 2.10a** [48]. Comparing to the bulk MgH_2, the nanocomposites, especially with the usage of PMMA as polymer binder, demonstrate high specific capacity, stable reversibility and improved rate capability. [83] Due to the rational design of the nanostructure, the close interfacial contact and fast charge transfer rate, as well as the constrained self-aggregation and volume expansion of active material nanoparticles provide synergistic effects over the whole electrochemical cycling. After 100 cycles, the GMH composite which contains 50 wt.% MgH_2 retains a discharge specific capacity, 946 mA h g^{-1} under 100 mA g^{-1}. Moreover, the reversible capability keeps 460 mA h g^{-1} at 2 A g^{-1} could be maintained after 450 cycles (**Figure 2.10b**). Continuously, a hydrangea-shaped three-dimensional (3D) hierarchical magnesium hydride−carbon framework (MH@HyC) [84] comprising MgH_2 nanoparticles (NPs) uniformly self-assembled on hierarchical porous carbon (HyC) is fabricated for advanced lithium storage. Taking advantage of the robust 3D hierarchical porous structure and the derived interactions, MH@HyC not only provides sufficient electrochemically active sites and enhances the electronic conductivity and channels for rapid transfer of electrons/Li ions but also relieves the agglomeration and accommodates the volumetric effects during cycling, leading to high-capacity utilization, fast electrochemical kinetics, and well-sustained structural integrity. As shown in **Figure 2.10c-e**, MH@HyC delivers a high reversible capacity of 554 mAh

g^{-1} after 1000 cycles at a high current rate of 2 A g^{-1}, enabling it a potential anode candidate for LIBs.

Other synthesis method also works, attributed to ball milling and dielectric barrier discharge plasma (DBDP), unique microstructure of Ge@FLG was created [86], in which, Ge NPs uniformly distributed in few-layer graphene sheets. MgH_2-TiO_2-EG composite which was synthesized via dielectric barrier discharge plasma-assisted vibratory milling (P-milling) process, also delivers improved electrochemical performances [85]. The synthesized MgH_2-TiO_2-EG composite electrodes after 20 h ball milling retains 305.5 mA h g^{-1}, after 100 cycles, implying the enhanced reversible capability. Ascribed to the stable architecture and TiO_2 and graphite additives, the electrochemical conversion reaction between MgH_2 and lithium ion becomes much more reversible. The nanostructure of the synthesized sample contributes to relive the volume expansion and prevent self-agglomeration, while the additives help to facilitate the conductivity of electrode and accelerate the kinetics of the anode conversion reaction.

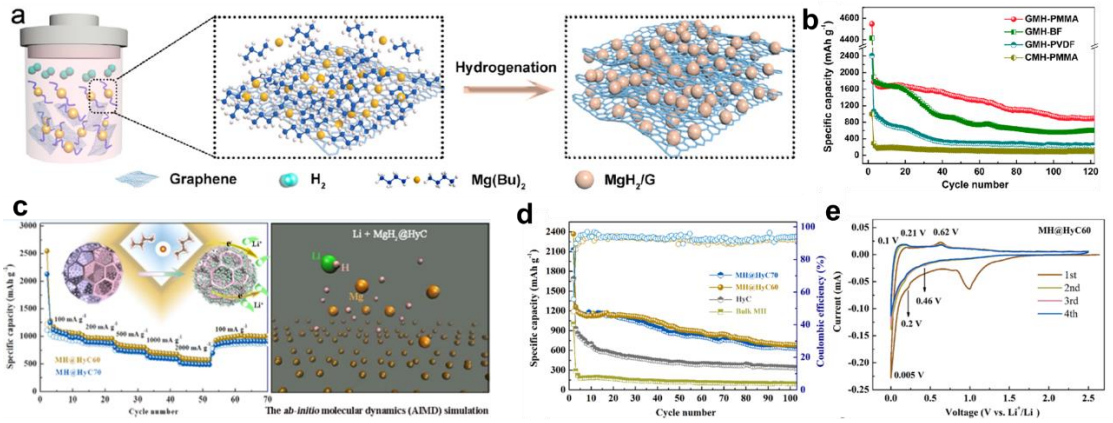

Figure 2.10 (a) Synthetic schematic of GMH composite. (b) Cycling performances of the synthesized samples at 100 mA g^{-1}. (c) Rate capabilities of MH@HyC and Ab initio molecular dynamics (AIMD) simulation of MgH_2 and Li ions. (d) Cycling

performances of MH@HyC, black HyC, and bulk MgH_2 electrodes at 100 mA g^{-1}. (e) Cyclic voltammetry curves of MH@HyC60 electrode at 0.05 mV s^{-1}. [83,84]

2.2.2.3 Surface Modification

Obviously, the nanostructure of MgH_2-based electrodes present huge imapct on its lithium storage properties. However, capacity fading is still serious that hampesrs the practical application of MgH_2 electrodes. In-situ surface coating outside the nanostructures could make up for this shortcoming. On the one hand, the coating layer act as a "shell" to confine the nanosized active materials into a restriced space, which could alleviated volume variation during the conversion reaction to some extent. On the other hand, the "core" inside the coating layer are limited to the small nanoreactors, which contributes to the mass transfer between differet phases, and effectively prevented the development of phase seperation during reversible reaction, thus, improved the rentention rate of capacity. In summery, the surface modification could be more efficient for increasing structure and performance stability of the electrode materials. Additionaly, it has been reported that core-shell architectures should be built through integration of anode materials with conductive additives, such as carbon based hybrids or conductive polymers, as a result of which, the electrial conductivity of the whole active material is also improved. With a more stable structure and reversible reacition, as well as a better conductivity, the rational designd surface modificaiton method could be beneficial for enhancing electrochemical properies of the electrode materials. Although there are many successful studies for those metal-oxide (nitride and/or sulfide)-based anode materials, [87-90] the construction of stable nanostructures is still full of challenge because of the shortage of rational design on the molecular level. Recently, A self-initiated polymerization to realize molecular-scale functionality of metal hydrides with conductive polymer, that is, polythiophene (PTh), has been

conducted, leading to the formation of MgH_2@PTh [91] core–shell nanoparticles on graphene. The nanoscale characteristics of MgH_2 not only relieve the induced stress upon volume changes but also allow fast diffusivity and high reactivity for Li-ion transport. More importantly, the conformal coating of ultrathin PTh membrane can effectively suppress the detrimental reactions between MgH_2 and electrolyte, provide enhanced performance with facile electron and Li^+ transport, and preserve its structural integrity, attributed to the strong molecular interaction between PTh and MgH_2 as well as its various products during electrochemical reactions. With this structure, a high reversible specific capacity of 1311 mAh g^{-1} at 100 mA g^{-1}, excellent rate performance of 1025 mAh g^{-1} at 2000 mA g^{-1}, and a capacity retention of 84.5% at 2000 mA g^{-1} after 500 cycles are observed for MgH_2@PTh nanoparticles as anode for LIBs.

Unfortunately, the inevitable volume expansion and irreversibility induced by the formation of LiMg alloy still hard to handle, which could take responsibility for the unsatisfied reversible capacity. The fundamental problems cannot be solved through the simple chemical modification methods mentioned above. New strategies of great effectiveness need to be furtherly investigated to solve the problem.

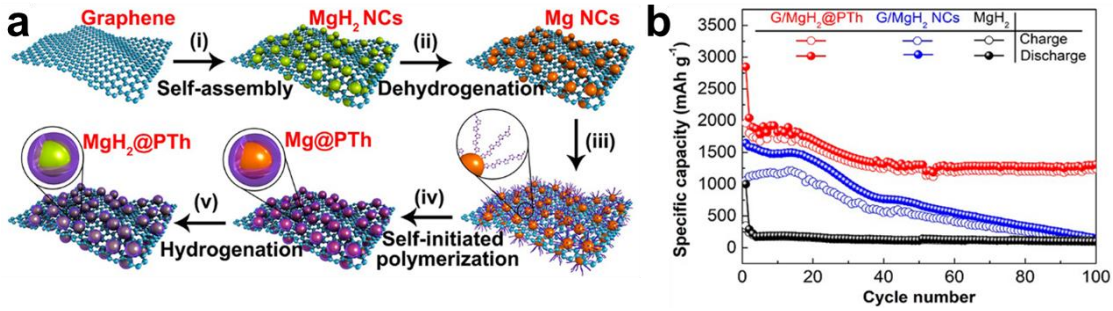

Figure 2.11 (a) Fabrication schematic of G/MgH_2@ PTh. (b) cycling capability of different marked samples. [91]

2.3 Metal Hydrides Working with Solid-state Electrolyte

Concluded from the discussion above, the side reactions between the active metal hydrides with traditional liquid organic electrolyte induced poor cycling stability and unfavorable capacity fading of the electrode are unavoidable. Although many modification methods have been employed, the main problem has not been solved. Employment of solid-state electrolyte (SE) in the batteries of metal hdyrides may be a more direct measure to break the limitations of metal hydrides-based composite electrode with better electrochemical performances. Taking into account the strong reducibility of metal hydrides-based electrode, the $LiBH_4$ based SE with high Lithium ionic conductivity and H^- mobility, and glass-ceramic sulfide based solid-state electrolyte are both the ideal alternatives. [92-94]

2.3.1 Li_2S-P_2S_5 solid-state electrolyte

Considered as promising electrolyte candidate for the practical application of ASSBs, the sulfide based solid-state electrolytes has arose wide attention for its high lithium ion conductivity and non-flammability.[95,96] Among which, Li_2S-P_2S_5 glass-ceramic material which was fabricated through mechanical milling of the mixture of Li_2S and P_2S_5, stands out for the high lithium-ion conductivity (3.2×10^{-3} S cm^{-1} at room temperature) and wide electrochemical window (>5 V vs. Li/Li^+) [97]. Along with the increasing of the crystallization and content of Li_2S, the conductivity of $80Li_2S$-$20P_2S_5$ (LPS) also escalate which could reach 2.1×10^{-4} S cm^{-1} when the Li_2S composition reaches 80 mol%. [98] The assembled ASSBs with LPS as solid-state electrolyte displayed excellent electrochemical performance, comparable to the properties of liquid batteries. For instance, In/$LiCoO_2$ ASSBs testing with the Li_2S-P_2S_5

glass-ceramic electrolytes displays excellent cycling stability, capacity fading did not occur after 500 cycles at 64 μA cm^{-1} [99].

Matched with $80Li_2S$-$20P_2S_5$, pure MgH_2 electrode showed a poor cyclability at 25 °C and barely recovered < 20% of the initial discharge capacity. The use of Nb_2O_5 as catalyst in this work significantly improved the kinetics of the electrochemical reaction at room temperature as well as high temperature by decreasing the activation energy of hydrogen ab/desorption of MgH_2. Even though this glass-type electrolyte has a good ionic conductivity, the compatibility with metal hydrides needs to be improved thus, many investigations have been made about the catalyst performance of different metal oxide on cycling capability of electrode based on MgH_2 based composites electrode. [79,80,100] For example, compared with bulk MgH_2, Al_2O_3 doped MgH_2 shows better cycling reversibility and better coulombic efficiency [80]. The pristine MgH_2 shows a constantly dropping discharge specific capacity which dramatically decreased to 200 mA h g^{-1} in the 6^{th} cycle, while the $75MgH_2$-$25Al_2O_3$ electrode still kept high capability around 580 mA h g^{-1} after 9 cycles. Additionally, the corresponding CE of the composite is positive relevant with the content of Al_2O_3. Nb_2O_5 is also a significant catalyst for MgH_2 electrode, with a more stable charge/discharge plateau. It is acknowledged that Nb_2O_5 is beneficial to reduce the H_2 ab/desorption activation energy of MgH_2, it could facilitate the mobility of the H atoms between Mg and Li phase which prompt the kinetics of the lithiation and delithiation [79]. Besides, the growing content of Nb_2O_5 in MgH_2 mixtures could also positively affect the cycling reversibility and rate capability [100]. The continuous efforts have recently been reported, such as doping active materials Nb_2O_5-MgH_2 with VGCF [101]. Unfortunately, cycling performance turns out to be poor, in the first cycle, MgH_2-LPS-VGCF electrode displays better discharge property, 1214 mA h g^{-1}, with a CE of 47.3%. However, after the 15th cycle,

it dramatically faded to below 100 mA h g^{-1} (**Figure 2.12**).[102] Surprisingly, with LPS as solid electrolyte, the MgH_2-$LiBH_4$-VGCF electrode exhibited better lithium storage performances, after 50 cycles, about 1017 mA h g^{-1} is still retained and 99.5% CE is kept (**Figure 2.12**). As a solid electrolyte, $LiBH_4$ not only promotes the reversibility of electrochemical reaction through fast Li^+ diffusion rate, but also contributes to enhance the hydride conversion reaction via accelerating the H^- transfer during the exchange process of hydrogen happened at the interfaces between the phases of MgH_2 and $LiBH_4$.

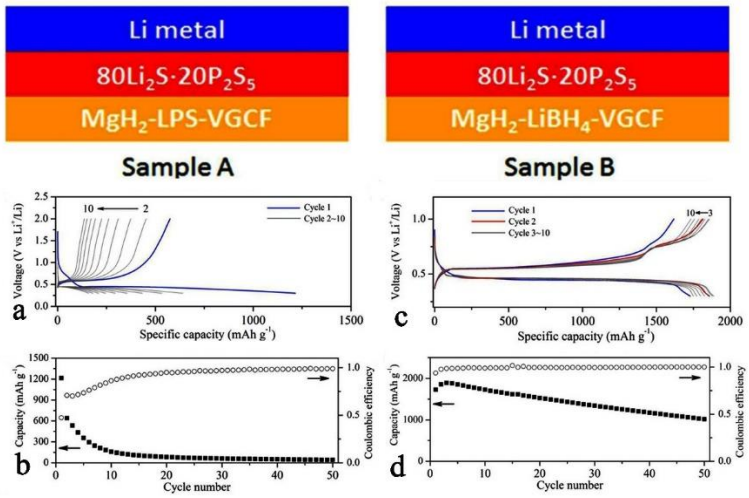

Figure 2.12 Battery configurations of MgH_2-LPS-VGCF electrode (Sample A) and MgH_2-$LiBH_4$-VGCF electrode (Sample B) working with the $80Li_2S{\cdot}20P_2S_5$ solid state electrolyte. (a) Voltage capacity profile and (b) cycling performance in the range of 0.3−2.0 V for sample A and (c) Voltage capacity profile and (d) cycling performance in the range of 0.3−1.0 V for sample B. [102]

2.3.2 $LiBH_4$ solid-state electrolyte

At the electrode/solid electrode (SE) ($80Li_2S–20P_2S_5$) interface, possible interaction between active electrode and reductive electrode is reported as a reason for the capacity fading. However, in terms of $LiBH_4$/SE, with existent of metal hydride electrode, $LiBH_4$ benefits for the significant improvement of the transfer of Lithium ions and H^-

which obviously take main responsibility during the cycling processes. $LiBH_4$ seems to be more suitable for metal hydrides electrodes compared with LPS. As a solid electrolyte, the low temperature phase of $LiBH_4$ transforms to high temperature phase above 113℃, at which the $LiBH_4$ presents highly ion-conductivity of about 1.8×10^{-3} S cm^{-1}. It has also proved to be suitable for other electrode materials with many advantages. For example, TiS_2 electrode employ $LiBH_4$ as electrolyte and Li foil as counter electrode. The batteries are tested under 393 K, exhibit discharge capacity 205 mA h g^{-1} under 0.2 C at the second cycle, compared to which, it keeps constant high reversible capability with a retention ratio of 88% at 300th cycle. Additionally, the CE is nearly 100% [103]. However, due to the dramatic reduction of the ionic conductivity of $LiBH_4$, below 115 ℃, the application of the battery is limited at lower temperature as long as employing $LiBH_4$ as SE.

Assembled with metal hydrides electrode, $LiBH_4$ could play the best role in improving the lithium storage properties. As shown in **Figure 2.13,** $LiNa_2AlH_6$/graphene composite has been synthesized by Mo et al. [56] $LiNa_2AlH_6$ nanoparticles grown on graphene nanosheets with a uniform dispersion. During synthesis process, the 2D structure of graphene and precursors transform into 3D multi hierarchical structure spontaneously, which seems like a micro flower. With $LiBH_4$ acting as a solid electrolyte, the prepared $LiNa_2AlH_6$/3DG composite demonstrates outstanding reversible cycling performance and ultra-high capability, 861 mA h g^{-1} at 5 A g^{-1} cycling for as long as 500 cycles with only 97% capacity retention. Due to the rational designed special structure, the better reversible nature and stable interface between electrode and electrolyte, the $LiNa_2AlH_6$/3DG presents best Li-storage performance among previous reports of alanates anodes in ASSLIBs.

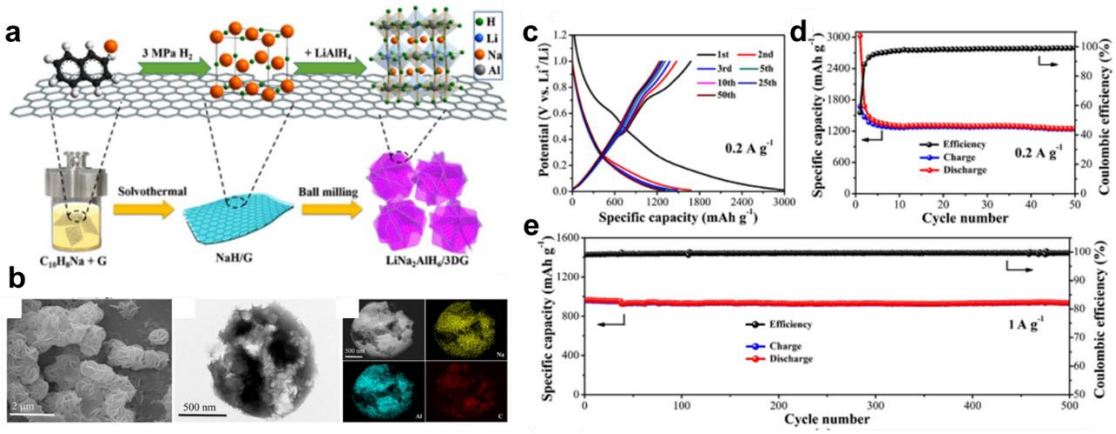

Figure 2.13 (a) Synthetic process of $LiNa_2AlH_6$/3DG. (b) morphology characterization of $LiNa_2AlH_6$/3DG. (c) Cycling performance of $LiNa_2AlH_6$/3DG in solid-state battery with $LiBH_4$ acting as solid electrolyte: (c) potential capacity profiles at 0.2 A g^{-1}; (d) cycling properties at 0.2 A g^{-1} and (e) 1 A g^{-1}.[56]

It has been revealed by Kojima and Latroche et al. that the H^- anion in MgH_2 molecular could form a stable interface with hydride-based solid-state electrolyte, such as $LiBH_4$ or $LiBH_4$-LiI. [92] Recently, much attention has been paid on the batteries with employment of MgH_2-based materials as electrode and $LiBH_4$ as electrolyte which has advantage on both Li^+ and H^- conductivity, thus induces the improved performances in SSLIBs.

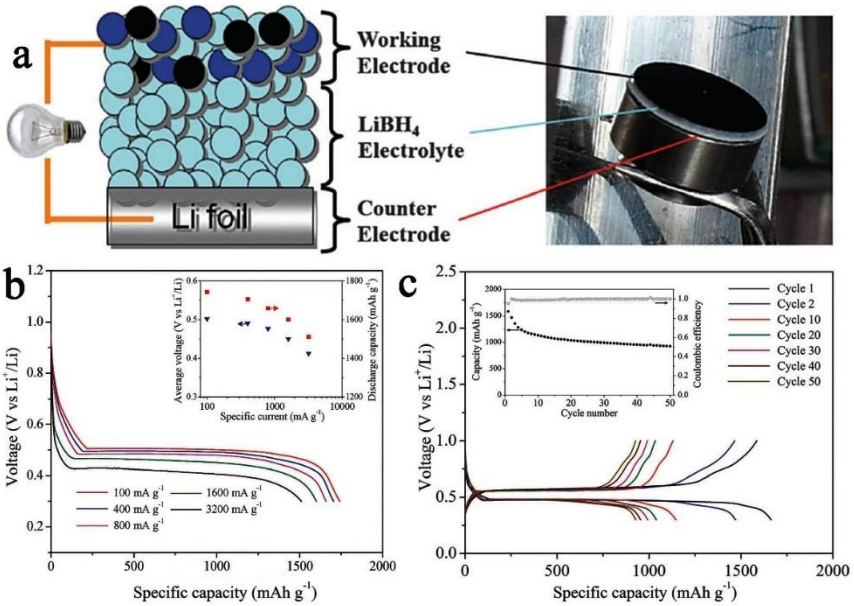

Figure 2.14 (a) The schematic and electronic photos of the MgH_2-$LiBH_4$|$LiBH_4$|Li ASSB. (b) The voltage discharge capctiy profiles of c-MgH_2-$LiBH_4$ composite electrode at first cycle under different constant current densities increasing from 100 to 3200 mAh g^{-1}. Inset shows the average potentials and discharge capacities at corresponding current densities. (c) voltage capacity profiles of the c-MgH_2-$LiBH_4$ composite electrode at 800 mA g^{-1}. Inset shows the corresponding cyclic properties. [92]

Zeng and his co-workers have tested the electrochemical performances of MgH_2-$LiBH_4$ composite materials performed as anode in LIBs (**Figure 2.14**). [92] After doping with 1 mol% Nb_2O_5, the battery cell assembled with $LiBH_4$ as electrolyte and lithium as counter electrode, the MgH_2-$LiBH_4$ composite exhibits a high discharge capacity about 1650 mAh g^{-1} with a high CE of 94.7%, at 100 mA g^{-1} for teh first cycle. The test was conducted in the potential range of 0.3 to 1.0 V at 120 ^oC. Besides, comparing with pure MgH_2-electrodes, it showed a smaller polarization of 0.05 V lower than that of 0.1 V of MgH_2-electrodes. It is the high working temperature that contributes to the raised kinetics of conversion reaction between MgH_2 and Li. $LiBH_4$ which has excellent Li^+ conductivity and H^- conductivity significantly promoted the lithium insertion and extraction process directing lower polarization and higher initial coulombic efficiency. Owing to the lower limit of testing voltage in 0.3 V, the whole lithiation/delithiation process shows better cyclability as well as rate capability resulted from avoiding the formation of LiMg alloy.

For metal hydrides, the electrochemical co-existence with metal oxide which is also conversion type anode is reported to beneficial for the reversibility of LIBs. It has been reported that CoO anode has a theoretical capacity of about 700 mAh g^{-1} and belongs to conversion type anode the same as MgH_2. Kharbachi studied the catalytic effect of CoO, adding 25 mol% electrochemically active oxide CoO, the lithium storage

performance of MgH_2 anode has been improved obviously. Indicating from the test results there is possibility that both MgH_2 and CoO co-exist synergistically and compensate mutually with each other for the mediocre reversibility of MgH_2. Separated into the MgH_2 matrix, the electrochemical incorporated CoO/Co nanoparticles is benefit for the enhancement of the cycling performance with high capacity and stable rate capability. [104]

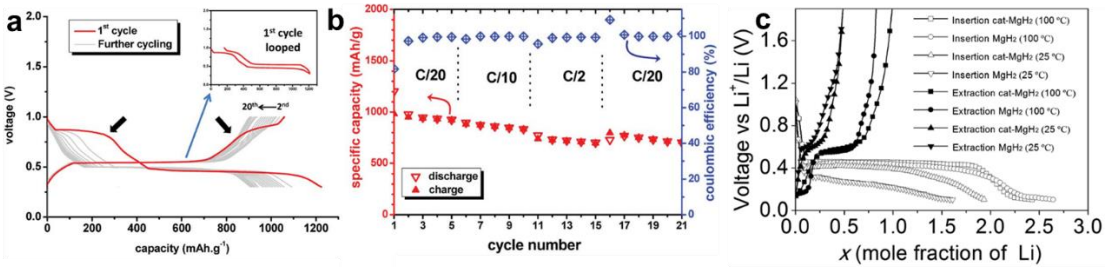

Figure 2.15 Cyclic properties of $75MgH_2$•25CoO-based anode with $LiBH_4$ SE at 120 ℃ (a) Discharge–charge profiles at 0.05 C rate. Inset: looped discharge/charge curve for clarity. (b) Rate capability tests of different C-rates. (c) voltage profiles corresponding to different samples at different temperature. [104, 65]

TiH_2 is also displays enhanced rate capability and stable reversibility when performed as an electrode material tested with $LiBH_4$ as the solid electrolyte [39]. With the help of $LiBH_4$ SE, TiH_2 electrode firstly realized the reversible reaction with lithium ion. At first cycle, discharge capability around 1223 mA h g^{-1} and a CE 86% has been achieved and the capacity retained 878 mA h g^{-1} at 50th cycle. However, the agglomeration of nanosized Ti species and the segregation of electrodes still appear as the cycling progresses, which induced the capacity fading.

Cano-Banda et al. have tested the solid-state LIBs performance of MgH_2 as the active material with different solid electrolyte at different temperatures, in order to find the all-solid-state LIBs operating at room temperature. [105] In this study, different batteries

compositions were tested for operating temperatures from 30 ℃ to 120 ℃, using $LiBH_4$, $3LiBH_4$•LiI and $80Li_2S$-$20P_2S_5$. As show in **Figure 2.16**, the cell MgH_2/$3LiBH_4$•LiI/Acetylene Black carbon|$80Li_2S$-$20P_2S_5$|Li, shown the best performance with an initial capacity of 1570 mAh g^{-1} operating at 30 ℃.

There are several $LiBH_4$ based hybride systems which could be applied on some room temperature conditions, for instance, borohydride argyrodite or $LiBH_4$+LiI+P_2S_5 and $LiBH_4$+LiCl+P_2S_5. Recently, El Kharbachi et al. have developed a solid electrolyte, $Li(BH_4)_{0.75}I_{0.25}$-($0.8Li_2S0.2P_2S_5$), [106] which could operating at room temperature. Assembled with MgH_2 as the electrode active material and $Li(BH_4)_{0.75}I_{0.25}$-($0.8Li_2S0.2P_2S_5$) as SE, the cell exhibited a better reversibility compared with the traditional liquid electrolyte, despite of the relatively lower specific capacity.

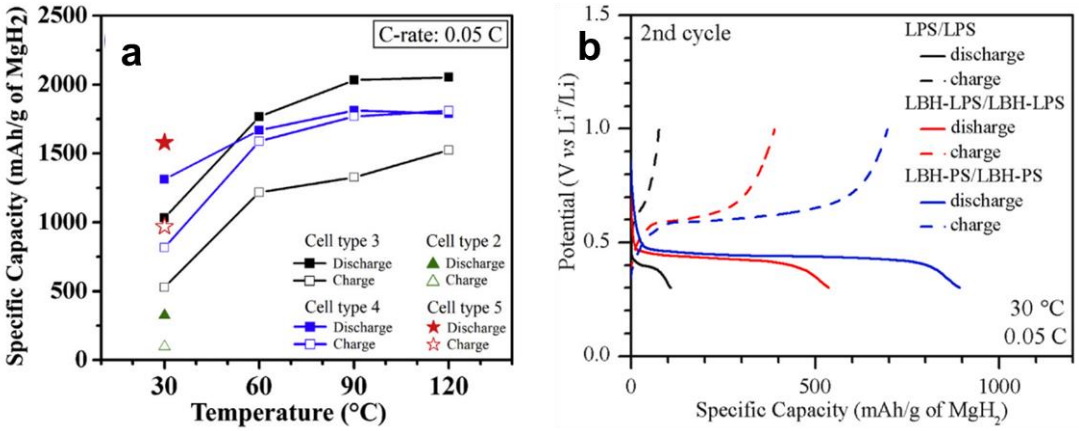

Figure 2.16 (a) specific capacity vs. Temperature. (b) potential capacity curves for cells employing different electrolyte in both layers. [105, 106]

It is important to do the research about metal hydrides-based materials used as electrode in ASSLIB, because in metal hydrides electrode system, safety problems occurred frequently which should be taken mainly responsibility by the forming of Lithium dendrite, leaking out and evaporating of liquid organic electrolytes. Especially, there are inevitable side reactions which occur between active metal hydrides and

traditional organic electrolytes. Nevertheless, in room temperature, the ionic conductivity of liquid electrolyte is still higher and more convenient than that of SE. It can be concluded that catalysts, nanostructure, and solid electrolyte are all effective methods in achieving excellent electrochemical performance for metal hydrides materials. To sum up, the realization of a system with comprehensive improved performance, only one single modification is not enough, multiple modification should be combined together. In addition, the exploration on other new solid electrolytes systems cannot be neglected.

2.4 References

[1] P. K. Nayak, L. Yang, W. Brehm, P. Adelhelm, From Lithium-Ion to Sodium-Ion Batteries: Advantages, Challenges, and Surprises, *Angew. Chem. Int. Ed.*, **2017**, *47*, 2930.

[2] Q. B. Yun, L. X. Li, Z. N. Hu, Q. P. Lu, B. Chen, H. Zhang, Layered Transition Metal Dichalcogenide-Based Nanomaterials for Electrochemical Energy Storage *Adv. Mater.*, **2020**, *32*, 1903826.

[3] S. Goriparti, E. Miele, F. D. Angelis, E. D. Fabrizio, R. P. Zaccaria, C. Capiglia, Review on Recent Progress of Nanostructured Anode Materials for Li-ion Batteries, *J. Power Sources*, **2014**, *257*, 421.

[4] F. X. Wu, J. Maier, Y. Yu, Guidelines and Trends for Next-generation Rechargeable Lithium and Lithium-ion Batteries, *Chem. Soc. Rev.*, **2020**, *49*, 1569.2.4 L. Aymard, Y. Qumellal and J. P. Bonnet, *Beilstein J. Nanotechnol.* **2015**, *6*, 1821.

[5] Q. Cheng, W. He, X. Zhang, M. Li, L. Wang, Modification of Li_2MnSiO_4 Cathode Materials for Lithium-ion Batteries: A Review, *J. Mater. Chem. A*, **2017**, *5*, 10772.

[6] S. Zhang, H. Gu, et al. A Novel Strategy to Suppress Capacity and Voltage Fading

of Li- and Mn-rich Layered Oxide Cathode Material for Lithium-ion Batteries, *Adv. Energy Mater.*, **2017**, *7*, 1601066.

[7] R. P. Fang, K. Chen, et al. The Regulating Role of Carbon Nanotubes and Graphene in Lithium-Ion and Lithium-Sulfur Batteries, *Adv. Mater.*, **2019**, *31*, 1800863.

[8] S. Brutti, S. Panero, A. Paolone, et al. Hydrides as High-Capacity Anodes in Lithium Cells: An Italian "Futuro in Riceraca di Base FIRB-2010" Project, Challenges, **2017**, 8.

[9] S. Goriparti, E. Miele, F.D. Angelis, E.D. Fabrizio, R.P. Zaccaria, C. Capiglia, Review on Recent Progress of Nanostructured Anode Materials for Li-ion Batteries, *J. Power Sources*, **2014**, *257*, 421.

[10] Y. Liu, Z. Tai, T. Zhou, V. Sencadas, J. Zhang, L. Zhang, K. Konstantinov, Z. Guo and H. K. Liu, An All-Integrated Anode via Interlinked Chemical Bonding between Double-Shelled–Yolk-Structured Silicon and Binder for Lithium-Ion Batteries, *Adv. Mater.*, **2017**, *29*, 1703028.

[11] D. Liu, Z. J. Liu et al. Group IVA Element (Si, Ge, Sn)-Based Alloying/Dealloying Anodes as Negative Electrodes for Full-Cell Lithium-Ion Batteries, *Small*, **2017**, *13*, 1702000.

[12] X. Y. Wang, L. Fan, D. Gong, J. Zhu, Q. F. Zhang, B. Lu, Core–Shell Ge@Graphene@TiO_2 Nanofibers as A High-Capacity and Cycle-Stable Anode for Lithium and Sodium Ion Battery, *Adv. Fun. Mater.*, **2016**, *7*, 1104.

[13] S. Z. Liang, Y. J. Cheng, J. Zhu, Y.G. Xia, P. M. Buschbaum, A Chronicle Review of Nonsilicon (Sn, Sb, Ge)-Based Lithium/Sodium-Ion Battery Alloying Anodes, *Small*, **2020**, *4*, 2000218.

[14] H. Zhang, L. Wang, H. Li, and X. M. He, Criterion for Identifying Anodes for Practically Accessible High-Energy-Density Lithium-Ion Batteries, *ACS Energy*

Lett., **2021**, *6*, 3719.

[15] X. Y. Li, K. Li, S. Zhu, K. Fan, et al. Fiber-in-Tube Design of Co_9S_8-Carbon/Co_9S_8: Enabling Efficient Sodium Storage, *Angew. Chem. Int. Ed.,* **2019**, *131*, 6305.

[16] H. Lin, S. L. Zhang, et al. A Cathode-Integrated Sulfur-Deficient Co_9S_8 Catalytic Interlayer for the Reutilization of "Lost" Polysulfides in Lithium–Sulfur Batteries, *ACS Nano*, **2019**, *13*, 7073.

[17] Y. Zhang, J. Huang, et al. Natural Self-Confined Structure Effectively Suppressing Volume Expansion toward Advanced Lithium Storage, *ACS Appl. Mater. Interfaces,* **2021**, *13*, 24634.

[18] L. Wu, J. Zheng, et al. PPy-encapsulated SnS_2 Nanosheets Stabilized by Defects on a TiO_2 Support as a Durable Anode Material for Lithium-Ion Batteries, *Angew. Chem. Int. Ed.,* **2019**, *131*, 6305.

[19] T. Jiang, F. X. Bu, et al. Porous Fe_2O_3 Nanoframeworks Encapsulated within Three-Dimensional Graphene as High-Performance Flexible Anode for Lithium-Ion Battery, *ACS Nano*, **2017**, *11*, 5140.

[20] H. Xu, W. J. Wang, et al. Nitrogen-Doped Carbon-Coated TiO_2/TiF_3 Heterostructure Nanoboxes with Enhanced Lithium and Sodium Storage Performance, *ACS Appl. Energy Mater.,* **2020,** *3*, 4738.

[21] Y. Wang, L.Y. Cao, J.Y. Li, et al. Cu/Cu_2O@Ppy nanowires as a long-life and high-capacity anode for lithium-ion battery, Chem. Eng. J., **2020**, *391*, 12359.

[22] W. Zhang, J. N. Li, et al. Top-Down Strategy to Synthesize Mesoporous Dual Carbon Armored MnO Nanoparticles for Lithium-Ion Battery Anodes, *ACS Appl. Energy Mater.,* **2017,** *9*, 12680.

[23] S. Kim, G. Enmenenko, et al. Thin Film RuO_2 Lithiation: Fast Lithium-Ion Diffusion along the Interface, *Adv. Fun. Mater.*, **2018**, *28*, 1805723.

[24] J. Liu, X. J. Xu, et al. Uniform Hierarchical Fe_3O_4@Polypyrrole Nanocages for Superior Lithium-Ion Battery Anodes, *Adv. Energy Mater.*, **2016**, *6*, 1600256.

[25] Y. Huang, Z. H. Xu, et al. Revisiting the Origin of Cycling Enhanced Capacity of Fe_3O_4 Based Nanostructured Electrode for Lithium-Ion Batteries, *Nano Energy*, **2017**, *41*,426.

[26] Y. Yang, Y. Liu, et al. Highly Stable Cycling of Amorphous $LiCO_3$-Coated α-Fe_2O_3 Nanocrystallines Prepared via a New Mechanochemical Strategy for Li-Ion Batteries, *Adv. Funct. Mater.*, **2017**, *27*, 1605011.

[27] P. Pietsch, D. Westhoff, J. Feinauer, et al. Quantifying Microstructural Dynamics and Electrochemical Activity of Graphite and Silicon-Graphite Lithium-Ion Battery Anodes. *Nat. Commun*, **2016**, *7*, 12909.

[28] S. J. An, J. L. Li, et al. The State of Understanding of the Lithium-Ion-Battery Graphite Solid Electrolyte Interphase (SEI) and Its Relationship to Formation Cycling, *Carbon*, **2016**, *105*,52.

[29] G. Xia, L. Zhang, General Synthesis of Transition Metal Oxide Ultrafine Nanoparticles Embedded in Hierarchically Porous Carbon Nanofibers as Advanced Electrodes for Lithium Storage, *Adv. Funct. Mater.*, **2016**, *26*, 6188.

[30] B, Ji, F. Zhang, et al. A Novel and Generalized Lithium-Ion-Battery Configuration Utilizing Al Foil as Both Anode and Current Collector for Enhanced Energy Density, *Adv. Mater.*, **2017**, *29*, 1604219.

[31] R. Hu, D. Chen, et al. Dramatically Enhanced Reversibility of Li_2O in SnO_2-Based Electrodes: The Effect of Nanostructure on High Initial Reversible Capacity, *Energy Environ. Sci.*, **2016**, *9*, 595.

[32] Y. Zhang, T. Zhou, et al. Atomic Interface Engineering and Electric-Field Effect in Ultrathin Bi_2MoO_6 Nanosheets for Superior Lithium-Ion Storage, *Adv. Mater.*,

2017, *29*, 1700396.

[33] G. Xia, Q. Gao, D. Sun, X. Yu, Porous Carbon Nanofibers Encapsulated with Peapod-Like Hematite Nanoparticles for High-Rate and Long-Life Battery Anode, *Small*, **2017**,*13*, 1701561.

[34] C. Huang, P. S. Grant, Coral-like Directional Porosity Lithium-Ion Battery Cathodes by Ice Templating, *J. Mater. Chem. A*, **2018**, *6*, 14689.

[35] Y. Oumellal, A. Rougier, G.A. Nazri, J.M. Tarascon, L. Aymard, Metal Hydrides for Lithium-Ion Batteries, *Nat. Mater.* **2008**, *7*, 916.

[36] L. Aymard, Y. Oumellal, J.P. Bonnet, Metal Hydrides: An Innovative and Challenging Conversion Reaction Anode for Lithium-Ion Batteries, *Beilstein J. Nanotechno*l., **2015**, *6*, 1821.

[37] S. Sartori, F. Cuevas, M. Latroche, Metal Hydrides Used as Negative Electrode Materials for Li-Ion Batteries, *Appl. Phys. A*, **2016**, *122*, 135.

[38] L. Zeng, K. Kawahito, T. Ichikawa, Metal Hydride-Based Materials as Negative Electrode for All-Solid-State Lithium-Ion Batteries, *Alkali-ion Batter*, InTech. **2016**, DOI: 10.5772/62866.

[39] K. Kawahito, L. Zeng, T. Ichikawa, H. Miyaoka, Y. Kojima, Electrochemical Performance of Titanium Hydride for Bulk-Type All-Solid-State Lithium-Ion Batteries, *Mater. Trans.*, **2016**, *57*, 755.

[40] S. Brutti, G. Mulas, E. Piciollo, S. Panero, P. Reale, Magnesium Hydride as a High Capacity Negative Electrode for Lithium Ion Batteries, *J. Mater. Chem.*, **2012**, *22*, 14531.

[41] P. Huen, F. Peru, G. Charalambopoulou, T.A. Steriotis, T.R. Jensen, D.B. Ravnsbæk, Nanoconfined $NaAlH_4$ Conversion Electrodes for Li Batteries, *ACS Omega*, **2017**, *2*, 1956.

[42] L. Silvestri, A. Paolone, et al. $NaAlH_4$ Nanoconfinement in a Mesoporous Carbon for Application in Lithium-Ion Batteries, *J. Electrochem. Soc.*, **2017**, *164*, A1120.

[43] Y. Pang, X. Wang, et al. Solid-State Prelithiation Enables High-Performance Li-Al-H Anode for Solid-State Batteries, *Adv. Energy Mater.*, **2020**, *10*, 1902795.

[44] M. Matsuo, S. Orimo, Lithium Fast-Ionic Conduction in Complex Hydrides: Review and Prospects, *Adv. Energy Mater.*, **2011**, *1*, 161.

[45] A. Unemoto, M. Matsuo, S. Orimo, Complex Hydrides for Electrochemical Energy Storage, *Adv. Funct. Mater.*, **2014**, *24*, 2267.

[46] J.H. Kennedy, Y. Yang, Glass-Forming Region and Structure in SiS_2-Li_2S-LiX (X = Br, I), *J. Solid State Chem.*, **1987**, *69*, 252.

[47] S. Kondo, K. Takada, Y. Yamamura, New Lithium Ion Conductors Based on Li_2S-SiS_2 System, *Solid State Ionics*, **1992**, *53*, 1183.

[48] N. Kamaya, K. Homma, A Lithium Superionic Conductor, *Nat. Mater.*, **2011**, *10*, 682.

[49] F.M. Vitucci, A. Paolone, S. Brutti, D. Munaò, L. Silvestri, S. Panero, P. Reale, H_2 Thermal Desorption and Hydride Conversion Reactions in Li Cells of TiH_2/C Amorphous Nanocompsites, *J. Alloys Compd.*, **2015**, *645*, S46.

[50] M. Hirscher, New materials for future energy storage, Chapter. In Handobook of Hydrogen Storage; Wiley-VCH: Weinheim, Germany, 2010.

[51] I.P. Jain, P. Jain, A. Jain, Novel Hydrogen Storage Materials: A Review of Lightweight Complex Hydrides, *J. Alloys Compd.*, **2010**, *503*, 303.

[52] L. Silvestri, L. Farina, D. Meggiolaro, S. Panero, F. Padella, S. Brytti, P. Reale, Reactivity of sodium alanates in lithium batteries, *J. Phys. Chem. C*, **2015**, 119, 28766.

[53] J.A.T. Jr., J. Zhang, et al. Li-Driven Electrochemical Conversion Reaction of AlH_3,

$LiAlH_4$, and $NaAlH_4$, *J. Phys. Chem. C*, **2015**, *119*, 4666.

[54] L. Cirrincione, L. Silestri, Investigation of the Effects of Mechanochemical Treatment on $NaAlH_4$ Based Anode Materials for Li-Ion Batteries, *J. Electrochem. Soc.*, **2016**, *163*, A2628.

[55] F. Wu, Z. Chen, B. Lei, J. Wang, K. Xie, Y. Song, D. Sun, F. Fang, Improved Reversibility and Cyclic Stability of $NaAlH_4$ Anode for Lithium-Ion Batteries, *Electrochim. Acta*, **2017**, *257*, 321.

[56] F. Mo, X. W. Chi, Stable Three-Dimensional Metal Hydride Anodes for Solid-State Lithium Storage, *Energy Storage Materials*, **2019**, *18*, 423.

[57] L. Silvestri, A. Paolone, L. Cirrincione, P. Stallworth, S. Greenbaum, S. Panero, S. Brutti, P. Reale, $NaAlH_4$ Nanoconfinement in a Mesoporous Carbon for Application in Lithium-Ion Batteries, *J. Electrochem. Soc.*, **2017,** *164*, A1120.

[58] S. Brutti, G. Mulas, E. Piciollo, S. Panero, P. Reale, Magnesium Hydride as a High Capacity Negative Electrode for Lithium Ion Batteries, *J. Mater. Chem.*, **2012**, *22*, 14531.

[59] D. Meggiolaro, G. Gigli, A. Paolone, F. Vitucci, S. Brutti, Incorporation of Lithium by MgH_2: An Ab Intio Study, *J. Phys. Chem. C*, **2013**, *117*, 22467.

[60] P. Vajeeston, P. Ravindran, A. Kjekshus, H. Fjellvåg, Pressure-Induced Structural Transitions in MgH_2, *Phys. Rev. Lett.*, **2002**, *89*, 175506.

[61] N. Hanada, A. Kamura, H. Siroshi, k. Takai, T. Ichikawa, Y. Kojima, Electrochemical Charge and Discharge Properties for the Formation of Magnesium and Aluminum Hydrides, *J. Alloys Compd.*, **2011**, *509*. S584.

[62] T. Moriwaki, Y. Akahama, H. Kawamura, S. Nakano, K. Takemura, Structural Phase Transition of Rutile-Type MgH_2 at High Pressures, *J. Phys. Soc. Jpn.* **2006**, *75*, 74603.

[63] C. Moysés Araújo, R. Ahuja, Electronic and Optical Properties of Pressure Induced Phases of MgH_2, *J. Alloys Compd.*, **2005**, *404*, 220.

[64] S. Sartori, F. Cuevas, M. Latroche, Metal hydrides used as negative electrode materials for Li-ion batteries, *Appl. Phys. A*, **2016**, *122*, 135.

[65] S. Ikeda, T. Ichikawa, K. Kawahito, K. Hirabayashi, H. Miyaoka, Y. Kojima, Anode Properties of Magnesium Hydride Catalyzed with Niobium Oxide for an All Solid-State Lithium-Ion Battery, *Chem. Commun.*, **2013**. *49*, 7174.

[66] S. Ikeda, T. Ichikawa, K. Goshome, S. Yamaguchi, H. Miyaoka, Y. Kojima, Anode Properties of Al_2O_3-Added MgH_2 for All-Solid-State Lithium-Ion Batteries, *J. Solid State Electrochem.,* **2015***, 19,* 3639.

[67] G. Barkhordarian,T. Klassen, R. Bormann, Fast Hydrogen Sorption Kinetics of Nanocystalline Mg Using Nb_2O_5 as Catalyst, *Scr. Mater.*, **2003**, *49*, 213.

[68] S. Srinivasan, P.C.M.M. Magusin, Nanostructures of Mg0.65Ti0.35Dx Studied with X-Ray Diffraction, Neutron Diffraction, and Magic-Angle-Spinning 2H NMR spectroscopy, *Phys. Rev. B.* **2010**, *81*, 054107.

[69] M. Ponthieu, F. Cuevas, J.F. Fernández, L. Laversenne, F. Porcher, M. Latroche, Structural Properties and Reversible Deuterium Loading of MgD_2-TiD_2 Nanocomposites, *J. Phys. Chem. C*, **2013**, *117*, 18851.

[70] M. Ponthieu, M. Calizzi, Synthesis by Reactive Ball Milling and Cycling Properties of MgH_2-TiH_2 Nanocomposites: Kinetics and Isotopic Effects, *Int. J. Hydrog. Energy*, **2014**, *39*, 9918.

[71] H. Nakayama, K. Nobuhara, M. Kon, T. Matsunaga, Electrochemical Properties of Metal Hydrides as Anode for Rechargeable Lithium-ion Batteries, *218th ECS Meeting Abstract*, **2010**, *1002*, 1052.

[72] L. Huang, L. Aymard and J. P. Bonnet. MgH_2–TiH_2 Mixture as an Anode for

Lithium-Ion Batteries: Synergic Enhancement of the Conversion Electrode Electrochemical Performance, *J. Mater. Chem. A*, **2015**, *3*, 15091.

[73] Y. L. Xu, F. M. Mulder, TiF_3 Catalyzed MgH_2 as a Li/Na Ion Battery Anode, *Int. J. Hydrog. Energy*, **2018**, *43*, 20033.

[74] K. Kawahito, L. Zeng, T. Ichikawa, H. Miyaoka, Y. Kojima, Electrochemical Performance of Titanium Hydride for Bulk-Type All-Solid-State Lithium-Ion Batteries, *Mater. Trans.* **2016**, *57*, 755.

[75] S. Brutti, G. Mulas, E. Piciollo, S. Panero, P. Reale, Magnesium Hydride as a High Capacity Negative Electrode for Lithium Ion Batteries, *J. Mater. Chem.*, **2012**, *22*, 14531.

[76] A.E. kharbachi, H.F. Andersen, Morphology Effects in MgH_2 Anode for Lithium Ion Batteries, *Int. J. Hydrog. Energy*, **2017**, *42*, 22551.

[77] J. Shu, RETRACTED: Li-Storage Performance of MgH_2-Based Materials for Lithium Ion Batteries, *Electrochim. Acta*, **2009**, *54*, 2367.

[78] W. Zaidi, Y. Oumellal, Carboxymethylcellulose and Carboxymethylcellulose-Formate as Binders in MgH_2-Carbon Composites Negative Electrode for Lithium-Ion Batteries, *J. Power Sources*, **2011**, *196*, 2854.

[79] X. Peng, H. Wang, R. Hu, L. Ouyuanf, J. Liu, M. Zhu, Electrochemical Performances of MgH_2 and MgH_2-C Films for Lithium Ion Battery Anode, *J. Alloys Compd.*, **2017**, *711*, 473.

[80] Y. Oumellal, C. Zlotea, Bottom-Up Preparation of MgH_2 Nanoparticles with Enhanced Cycle Life Stability During Electrochemical Conversion in Li-Ion Batteries, *Nanoscale*, **2014**, *6*, 14459.

[81] S. Yang, H. Wang, L. Ouyang, J. Liu, M. Zhu, Improvement in the Electrochemical Lithium Storage Performance of MgH_2, *Inorganics*, **2018**, *6*, 2.

[82] L. Ouyang, L. guo, W. Cai, Facial Synthesis of Ge@FLG Composites by Plasma Assisted Ball Milling for Lithium-ion Battery Anodes, *J. Mater. Chem. A.*, **2014**, *2*, 11280.

[83] B. Zhang, G. Xia, D. Sun, F. Fang, X. Yu, Magnesium Hydride Nanoparticles Self-Assembled on Graphene as Anode Material for High-Performance Lithium-Ion Batteries, *ACS Nano*, **2018**, *12*, 3816.

[84] B. P. Zhang, Y. S. Si, Q. F. Gu, M. Chen, X. B. Yu, Hydrangea-Shaped 3D Hierarchical Porous Magnesium Hydride−Carbon Framework with High Rate Performance for Lithium Storage, *ACS Appl. Mater. Interfaces*, **2019**, *11*, 28987.

[85] L. Ouyang, Z. Cao, H. Wang, R. Hu, M. Zhu, Application of Dielectric Barrier Discharge Plasma-Assisted Milling in Energy Storage Materials-A Review, *J. Alloys Compd.*, **2017**, *691*, 422.

[86] L. Ouyang, Z. Cao, L. Li, et al. Enhanced High-Rate Discharge Properties of $La_{11.3}Mg_{6.0}Sm_{7.4}Ni_{61}Co_{7.2}Al_{7.1}$ with added graphene synthesized by plasma milling, *Int. J. Hydrog. Energy*, **2014**, *39*, 12765.

[87] G. Q. Tan, F. Wu, Freestanding Three-Dimensional Core-Shell Nanoarrays for Lithium-Ion Battery Anodes. *Nat. Commun.*, **2016**, *7*, 11774.

[88] W. W. Zhou, J. X. Zhu, A General Strategy toward Graphene@Metal Oxide Core−Shell Nanostructures for High-Performance Lithium Storage. *Energy Environ. Sci.*, **2011**, *4*, 4954.

[89] J. Liu, X. J. Xu, Uniform Hierarchical Fe_3O_4@Polypyrrole Nanocages for Superior Lithium-Ion Battery Anode. *Adv. Energy Mater.*, **2016**, *6*, 1600256.

[90] M. Mao, F. Yan, Pipe-Wire TiO_2-Sn@Carbon Nanofibers Paper Anodes for Lithium and Sodium Ion Batteries. *Nano Lett.*, **2017**, *17*, 3830.

[91] G. L. Xia, B. P. Zhang, Molecular-Scale Functionality on Graphene To Unlock the

Energy Capabilities of Metal Hydrides for High-Capacity Lithium-Ion Batteries, *ACS Nano*, **2018**, *12*, 8177.

[92] L. Zeng, K. Kawahito, S. Ikeda, T. Ichikawa, H. Miyaoka, Y. Kojima, Metal Hydride-Based Materials towards High Performance Negative Electrodes for All-Solid-State Lithium-Ion Batteries, *Chem. Commun.*, **2015**, *51*, 9773.

[93] S. Ikeda, T. Ichikawa, et al. Anode Properties of Magnesium Hydride Catalyzed with Niobium Oxide for an All-Solid-State Lithium-Ion Battery, *Chem. Commun.*, **2013**, *49*, 7174.

[94] F. Cano-Banda, R. Singh, et al. Enhanced Performance of MgH_2 Composite Electrode Using Glass-Ceramic Electrolytes for All-Solid-State Li-Ion Batteries, *J. Alloys Compd.*, **2021**, *863*, 158729.

[95] R. Kanno, M.Murayama, Lithium Ionic Conductor Thio-LISICON: The Li_2S-GeS_2-P_2S_5 System, *J. Electrochem. Soc.*, **2001**, *148*, A742.

[96] J.H. Kennedy, Ionically Conductive Glasses Based on SiS_2, *Mater. Chem. Phys.*, **1989**, *23*, 29.

[97] A. Hayashi, S. Hama, Preparation of Li_2S-P_2S_5 Amorphous Solid Electrolytes by Mechanical Milling, *J. Am. Ceram. Soc.*, **2001**, *84*, 477.

[98] F. Mizuno, A. Hiyoharu, K. Tadanaga and M. Tatsumisago, High Lithium Ion Conducting Glass-Ceramics in the System Li_2S-P_2S_5, *Solid State Ionics*, **2006**, *177*, 2721.

[99] M. Tatsumisago, F. Mizuno, A. Hayashi, All-Solid-State Lithium Secondary Batteries Using Sulfide-Based Glass-Ceramic Electrolytes, *J. Power Sources*, **2006**, *159*, 193.

[100] S. Ikeda, T. Ichikawa, S. Yamaguchi, H. Miyaoka, Y. Kojima, Effects of Metal Oxide Additives on Anode Properties of Magnesium Hydride for All-Solid-State

Lithium-Ion Batteries, *J. Jpn. Inst. Energy*, **2014**, *93*, 926.

[101] L. Zeng, T. Ichikawa, K. Kawahito, H. Miyaoka, Y. Kojima, Bulk-Type All-Solid-State Lithium-Ion Batteries: Remarkable Performances of a Carbon Nanofiber-Supported MgH_2 Composite Electrode, *ACS Appl. Mater. Interfaces*, **2017**, *9*, 2261.

[102] L. Zeng, T. Ichikawa, K. Kawahito, Bulk-Type All-Solid-State Lithium-Ion Batteries: Remarkable Performances of a Carbon Nanofiber-Supported MgH_2 Composite Electrode, *ACS Appl. Mater. Interfaces*, **2017**, *9*, 2261.

[103] A. Unemoto, T. Ikeshoji, et al. Stable Interface Formation between TiS_2 and $LiBH_4$ in Bulk-Type All Solid-State Lithium Batteries, *Chem. Mater.*, **2015**, *27*, 5407.

[104] A. E. Kharbachi, H. Uesato, et al. MgH_2–CoO: a Conversion-Type Composite Electrode for $LiBH_4$-Based All-Solid-State Lithium-Ion Batteries, *RSC Adv.*, **2018**, *8*, 23468.

[105] F. Cano-Banda, A. Gallardo-Gutierrez, High Capacity MgH_2 Composite Electrodes for All Solid-State Li-Ion Battery Operating at Ambient Temperature, *Int. J. Hydrog. Energy*, **2021**, *46*, 1030.

[106] A. E. Kharbachi, J. Wind, Pseudo-Ternary $LiBH_4 \cdot LiCl \cdot P_2S_5$ System as Structurally Disordered Bulk Electrolyte for All-Solid-State Lithium Batteries, *Phys. Chem. Chem. Phys*., **2020**, *22*, 13872.

CHAPTER 3 EXPERIMENTAL SECTION

3.1 Overview

As described in **Figure 3.1**, the rough program of this doctoral thesis work introduces the technical route of the research briefly. Firstly, nanoconfined metal hydrides anode materials (SAH@G, MHG@MBH, MHG@MS, and MHG@MNH) were synthesized via solution infiltration and/or bottom-up self-assembly strategy and in-situ solid-gas reaction. To be identified, the as-prepared materials were analysed furtherly through a series of physical and chemical characterization techniques. Subsequently, their lithium storage performance (both with conventional organic electrolyte and solid electrolyte) was investigated by several electrochemical tests to verify the effect induced by the nanoconfinement, surface modification and interfacial modification.

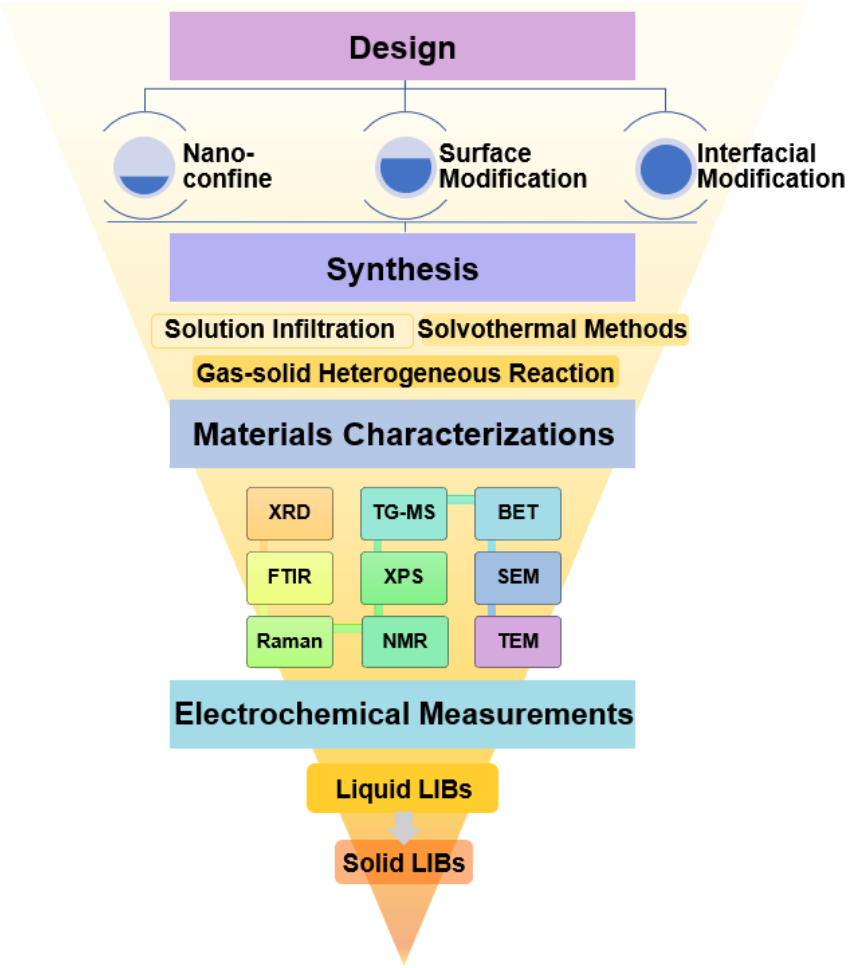

Figure 3.1 General outline of the research route which include the synthesis methods and characterization equipment covered in this doctoral thesis.

3.2 Chemicals

Table 3.1 demonstrates the details of the materials involved in the experiment in this thesis.

Table 3.1 List of the materials involved in the experiments of this thesis.

Chemicals	Formula	Purity (%)	Supplier
Lithium borohydride	$LiBH_4$	98	Sigma-Aldrich
Magnesium Hydride	MgH_2	98	Sigma-Aldrich
Di-n-butylmagnesium	$C_8H_{18}Mg$	1M	Sigma-Aldrich
Zinc chloride	$ZnCl_2$	99.99	Sigma-Aldrich
Sodium aluminium hydride	$NaAlH_4$	98	Sigma-Aldrich
Graphene	C	99.9	Simbatt Energy Technology Co.
Tetrahydrofuran (THF)	C_4H_8O	99.999	Sigma-Aldrich
Cyclohexane	C_6H_{12}	99.5	Sigma-Aldrich
Mesoporous carbon	C	Super P	Nanjing XFNANO Materials Tech
Poly(methyl methacrylate) (PMMA) M_v = 1200000	$(C_5O_2H_8)_n$	N/A	Sigma-Aldrich

N-methyl-2-pyrrolidone (NMP)	C_5H_9NO	99.5	Sigma-Aldrich
Copper foil	Cu	N/A	Canrd New Energy Technology Co.
Lithium hexafluorophosphate	$LiPF_6$	99.99%	Sigma-Aldrich
Lithium foil	Li	BG	Canrd New Energy Technology Co.
Ethylene carbonate (EC)	$C_3H_4O_3$	99^+	Sigma-Aldrich
Diethyl carbonate (DEC)	$C_5H_{10}O_3$	99^+	Sigma-Aldrich
Fluoroethylene carbonate (FEC)	$C_2H_3FO_3$	99	Sigma-Aldrich
Sulfur	S	99^+	Sigma-Aldrich
Ketjen black	C	99^+	Canrd New Energy Technology Co.

3.3 Materials Preparation

The synthetic method of the electrode materials involved in this thesis are demonstrated as shown following. Here, the XRD, FTIR, Raman, XPS, TEM and many other technologies are listed, which were adopted to characterize the morphology properties, structure changes of the materials during fabrication and electrochemical cycling. Additionally, the experimental procedures of each separated work would be introduced more specifically at the following chapters.

3.3.1 Solution Infiltration

As illustrated in Figure 3.3, nanosized metal hydrides was synthesized on the various templates (1D nanofibers, 2D nanosheets, and 3D holes) via solution infiltration. Solvent mediated infiltration dissolved the hydride to be infiltrated to form a uniform solution with a selected solvent. Firstly, the adopted templates were admixed with a solution containing metal hydrides via stirring and ultrasonication for completely infiltrating. Subsequently, the solvent removing was conducted under right temperature with constant dynamic vacuum. Finally, the This method takes the advantage to prepare nanostructure under milder conditions. It is important to note that the solvent which dissolves the hydrides to be infiltrated should be inert with the porous templates and the hydrides. Furthermore, several times of impregnation may be cycled to regulate the load rate of the hydrides that grew on the templates.

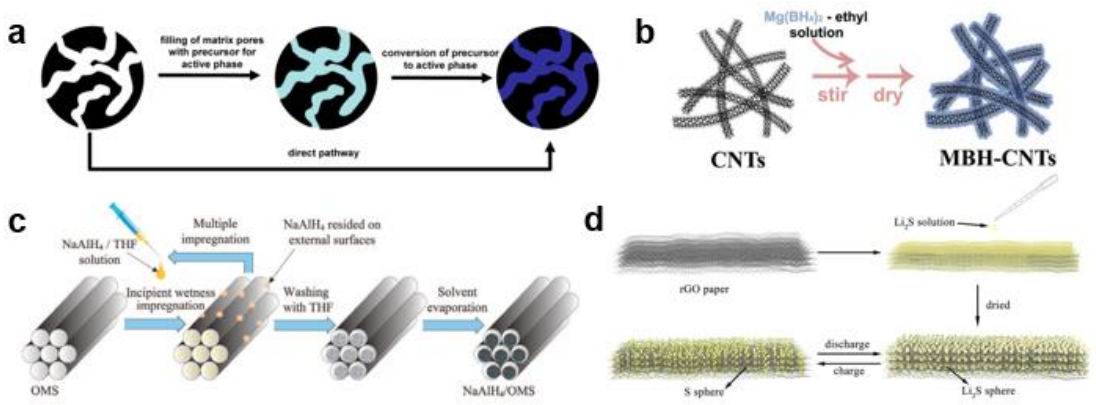

Figure 3.2 Schematic diagram of nanostructure separated on various templates via solution infiltration. a. 3D nano pore; b. carbon nano tube; c. OMS ordered mesoporous silica; d. graphene. [1-4]

3.3.2 Self-assembly Method

Self-assembly method is a powerful technique for transforming disordered building blocks into ordered microscopic structures spontaneously, either through direct

interactions, or using a template or an external field indirectly. Among the methods of nano architectonic constructions, this bottom-up approach has been widely used, ranging from energy storage to biomedicine, as a result of the precision and diversity of the products. With different building blocks and controlled reaction conditions, molecular self-assembly has several advantages in designing stable nanostructures with desired structures and unique functions, like nano-spheres, nanotubes, nanosheets, 2D molecular patterns, 3D metal organic frameworks, molecular machines, DNA origamis and so on. In this doctoral thesis, the magnesium hydride nanoparticles were synthesised through self-assembly strategy as shown in Figure 3.3. With the robust interaction between MgH_2 and graphene nanosheets, MgH_2 nanoparticles were uniformly grown on the GNs through the decomposition of dibutyl magnesium ($(C_4H_9)_2Mg$) in large cyclohexane solvent.

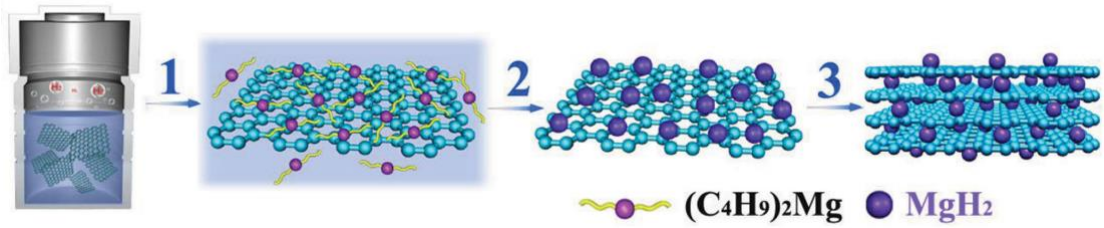

Figure 3.3 Sketch map of the MgH_2 nanoparticles self-assembly synthesis process. [5]

3.3.3 Gas-solid Reaction

Gas-solid reactions play a vital role in the synthesis technology of modern scientific research and industrial production with simple equipment and low cost. Tremendous applications of gas-solid reactions have happened in metallurgical and chemical industries, where reactants are composed of gas and solid phases that undergo chemical changes at their interfaces. The building -up process of MHG@MgX in this doctoral

thesis are illustrated in Figure 3.4. Four phenomena (external mass transfer, pore diffusion, adsorption/desorption and chemical reaction) affect the progress of reaction.

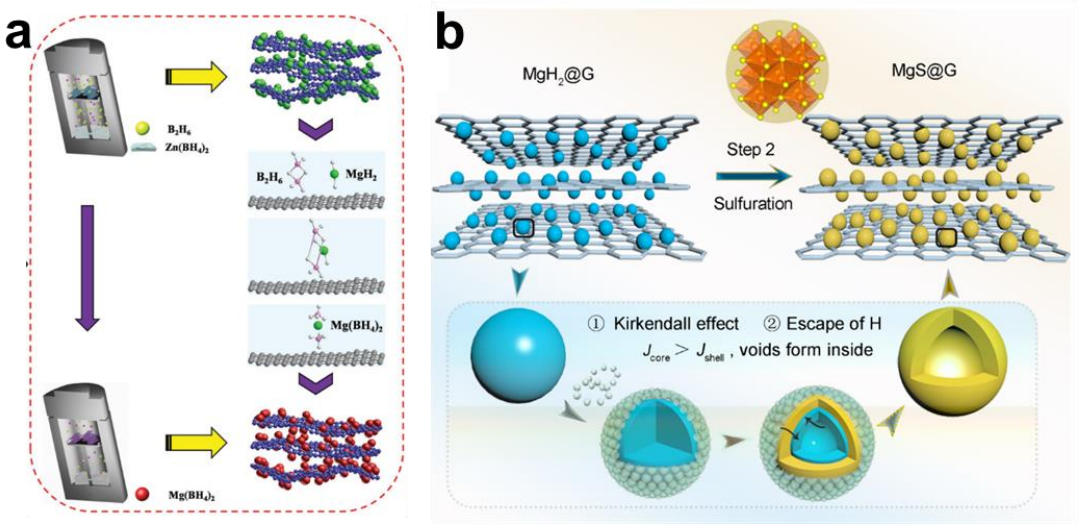

Figure 3.4 Representative synthetic process of the fabrication for MHG@MBH and MHG@MS through gas-solid reaction. [6, 7]

3.4 Characterization Techniques

3.4.1 X-ray Powder Diffraction (XRD)

XRD technology is a useful research technique for the quantitative phase analysis, determination of crystallinity and precise determination of lattice parameters through analyzing the diffraction pattern produced by monochromatic X-ray incident on the crystal. When a substance (crystalline or amorphous) is subjected to diffraction analysis, the substance is irradiated by X-rays to produce different degrees of diffraction phenomena. The composition, crystal form, intramolecular bonding method, molecular configuration, conformation, etc. determine the production of the substance unique diffraction pattern. The X-ray diffraction method has the advantages of no damage to the sample, no pollution, quickness, high measurement accuracy, and a large amount of information about the integrity of the crystal. Therefore, X-ray diffraction analysis, as a modern scientific method of material structure and composition analysis, has

gradually been widely used in the research and production of various disciplines. XRD patterns for the samples researched in the works related to this thesis were obtained using a D8 Advanc (Bruker AXS) with Cu Kα radiation. Samples were assembled into a special glass board in the Ar-filled glovebox and protected with an amorphous tape from oxidation during the XRD measurements.

3.4.2 Fourier Transform Infrared Spectroscopy (FTIR)

FTIR spectroscopy is a commonly used instrument that detects chemical bonds in molecules by generating infrared absorption spectra of solids, liquids or gases which mainly study compounds that are accompanied by dipole moment changes in vibration. Generally, the identification mechanism of the structural composition and the unknown chemical group is based on the analyze of wavelength position and the intensity of the infrared absorption band which are related to the typical characteristics of each unique molecular structure. Additionally, molecular construction and content of the chemical functional groups was reflected through the absorption intensity of the absorption band which can be used for quantitative analysis and purity identification. In this work, a Magna-IR 550 II, Nicolet, FT-IR Spectrometer was used to measure the synthesized samples with a multiple internal reflection (MIR) scan range of 500-4000 cm^{-1}. All the IR spectroscopy samples were assembled into a sealed tube in the glove box fille with inert gas to avoid oxidation.

3.4.3 Raman Spectroscopy

Raman spectroscopy is based on the Raman scattering effect discovered by the Indian scientist C.V. Raman. It analyzes the scattering spectra with different frequencies from the incident light to obtain information on molecular vibration and rotation, and is an analytical method used in molecular structure research. It is mainly used to study the

determination and confirmation of material composition. The most commonly used infrared and Raman region wavelengths are 2.5~25 μm; Raman spectrometer has distinct advantages, such as no contact with samples and no damage. It can quickly analyze and identify each of the characteristics and structure of this material and is suitable for black and water-containing sample. It can be measured at high, low temperature and high pressure as well. In this work, a XploRA Laser raman spectrometer was used to measure the synthesized samples with a spectra range of 70-9000 cm^{-1} (532 nm excitation) and a level of sensitivity above 20:1.

3.4.4 Solid State Nuclear Magnetic Resonance (SSNMR)

SSNMR is a very important analysis technique that specially focused on characterizing the properties of solid samples. By studying the absorption of radio frequency radiation by atomic nuclei, it is one of the most powerful tools for qualitative analysis of the composition and structure of various organic and inorganic substances, and sometimes quantitative analysis can also be carried out. Its working principle is that in a strong magnetic field, the atomic nucleus undergoes energy level splitting. When external electromagnetic radiation is absorbed, the nuclear energy level will undergo a transition, which is the so-called NMR phenomenon. It is very suitable for studying the microstructure and dynamic behavior of various amorphous solid material. It can also provide structural information at the atomic and molecular level. In recent years, solid-state nuclear magnetic technology has been widely used in many fields, such as batteries, catalysis, glass and membrane proteins, etc. A SSNMR was used in this doctoral thesis to analyze the structure and composition of the synthesized samples.

3.4.5 X-ray Photoelectron Spectroscopy (XPS)

XPS is an important surface analysis technique. X-rays are used to irradiate the sample to stimulate the emission of internal electrons or valence electrons in atoms or molecules. The energy level of the inner electrons is little affected by the molecular environment. As the inner electron binding energy is characteristic, the photoelectron which is excited by photons could be analyzed by the energy analyzer. The energy and quantity of photoelectrons can be measured to obtain the composition of the object under test. The main application of XPS is to measure the binding energy of electrons to identify the chemical properties and composition of the sample surface. Its characteristic is that the photoelectrons come from within 10 nm of the surface and only reveals the signals emitted from the surface layer. It takes an advantage of no damage to the sample due to the small analysis area, and shallow analysis depth. It can not only provide information on the molecular structure and atomic valence state for chemical research, but also provide information on the element composition, chemical state, molecular structure, etc. of various compounds for the study of electronic materials. It is widely used in the research of various materials such as metals, inorganic materials, catalysts, polymers, coating materials ores, etc. In this work, X-ray photoemission spectroscopy (XPS) experiments were performed on Thermo Scientific K-Alpha$^+$ with single X-ray source, using an Al Kα (1486 eV) anode.

3.4.6 Thermogravimetric Analysis and Mass Spectra (TG-MS)

TGA is an instrument that uses thermogravimetry to detect the temperature-mass change relationship of a substance. Thermogravimetry is used to study the change of the material quality along with the variation of temperature (or time) under program temperature control, while mass spectra (MS, QIC 20) are used to qualitatively and semi-quantitatively study the composition of released gas transferred from the TGA

(Netzsch STA 449 F3) instrument. In this study, TGA and the MS instrument are connected. The sample were tested under flowing argon atmosphere under a gas flowing rate of 80 ml/min and a heating rates of 5 ℃/min.

3.4.7 Brunauer-Emmett-Teller Surface Area Characterization (BET)

The BET specific surface area test is widely used in the research of particle surface adsorption performance and the data processing of related testing instruments. The BET formula based on the multi-molecular-layer adsorption model proposed by S. Brunauer, P. Emmett, and E. Teller is the most widely used method in the industry and the most reliable test results. BET test is useful for measurement of the specific surface area of particles, the pore volume, pore size distribution and nitrogen adsorption of the substances, as well as the desorption curve of particles. It contributes a lot in figuring out the properties and structure of particles. to derive the relationship equation between the single-layer adsorption capacity and the multi-layer adsorption capacity, which is the famous BET equation. In this studies, the specific surface areas were tested by a Micromeritics 2460/Quantachrome IQ3 instrument.

3.4.8 Scanning Electron Microscopy (SEM)

SEM is a large precision instrument used for high-resolution micro-area analysis. It uses a focused very narrow high-energy electron beam to scan the sample, through the interaction between the beam and the substance, various physical information is excited. After collecting, amplifying, and re-imaging of the information, the purpose of characterizing the microscopic morphology of the substance is achieved. The resolution of the new scanning electron microscope can reach 1 nm with the magnification can be 300,000 times which is continuously adjustable. Moreover, the depth and view of field are both large, and the 3D imaging effect is superb. In addition, the combination of

scanning electron microscope and other analytical instruments can be used to observe the microscopic morphology and analyze the composition of the material in the micro-region at the same time. In this thesis, the surface morphology and composition of the samples was revealed by field emission scanning electron microscopy (FE-SEM, JEOL 7500FA, Tokyo, Japan).

3.4.9 Transmission Electron Microscopy (TEM)

TEM is a very useful tool in the fields of materials, physics, chemistry, and life sciences. We often need to use TEM to obtain information on the surface (or topography) and internals of samples. Its working principle is to project an accelerated and concentrated electron beam onto a very thin sample. The electrons collide with the atoms in the sample to change direction, resulting in solid angle scattering. The size of the scattering angle is related to the density and thickness of the sample, so images with different brightness and darkness can be formed. The images will be displayed on imaging devices (such as phosphor screens, films, and photosensitive coupling components) after zooming in and focusing. The TEM measurement employed in this work comes from JEOL 2011 F, Tokyo, Japan.

3.5 Electrochemical Measurements

3.5.1 Electrode Preparation for Conventional LIBs and Coin-cell Assembly

In this thesis, the electrode slurries were achieved through mixing the prepared active materials, binder (polymethyl methacrylate, PMMA, dissolved in DMF) and conductive acetylene black according to 8:1:1 in weight. Following, the electrode was pasted onto a cupper foil at a mass loading of 0.6 mg cm^{-2} and then dried for 12 h under vacuum oven at 353 K. Finally, as shown in **Figure 3.5**, coin-type 2025 half-cells were

assembled in an Ar-filled glove box (the water and oxygen were maintained below 1 ppm), with the prepared electrodes as the working electrode, glass fibre (Celgard 2340) as separator, and lithium foil as the counter electrode. The electrolyte used in this doctoral thesis is consist of 1 M $LiPF_6$ which is dissolved in a solution consist of EC, DMC and DEC according to 1:1:1 calculated in volumetric ratio. The specific capacity of this thesis is calculated based on the mass of the active material.

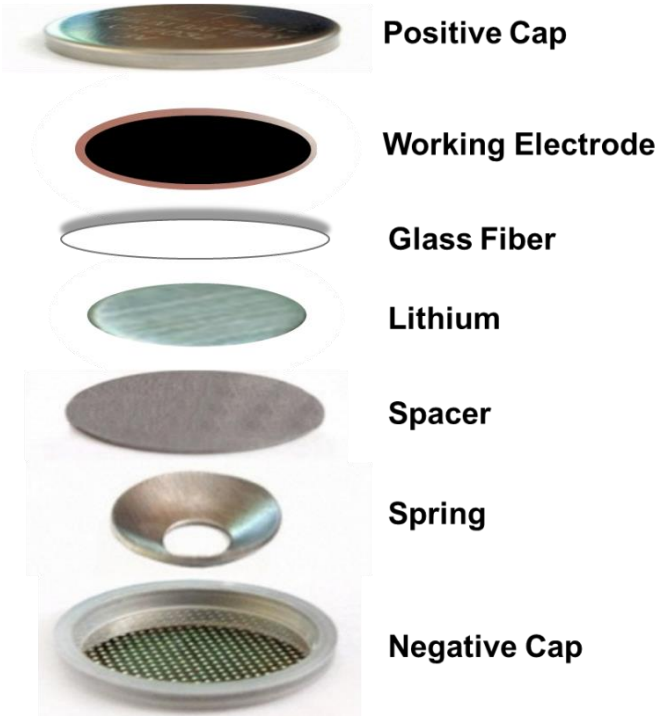

Figure 3.5 Schematic diagram showing the half-cell assembly.

3.5.2 Electrode Preparation for Solid-state LIBs and Battery Assembly

Before being used, the $LiBH_4$ and conductive carbon (Ketjen black) was heated to 423 K under a vacuum for 12 h to avoid moisture and other impurity gas. The working electrode was prepared by ball-milling of synthesized active materials, preconditioned $LiBH_4$ and Ketjen black in a weight ratio of 1:1:2.

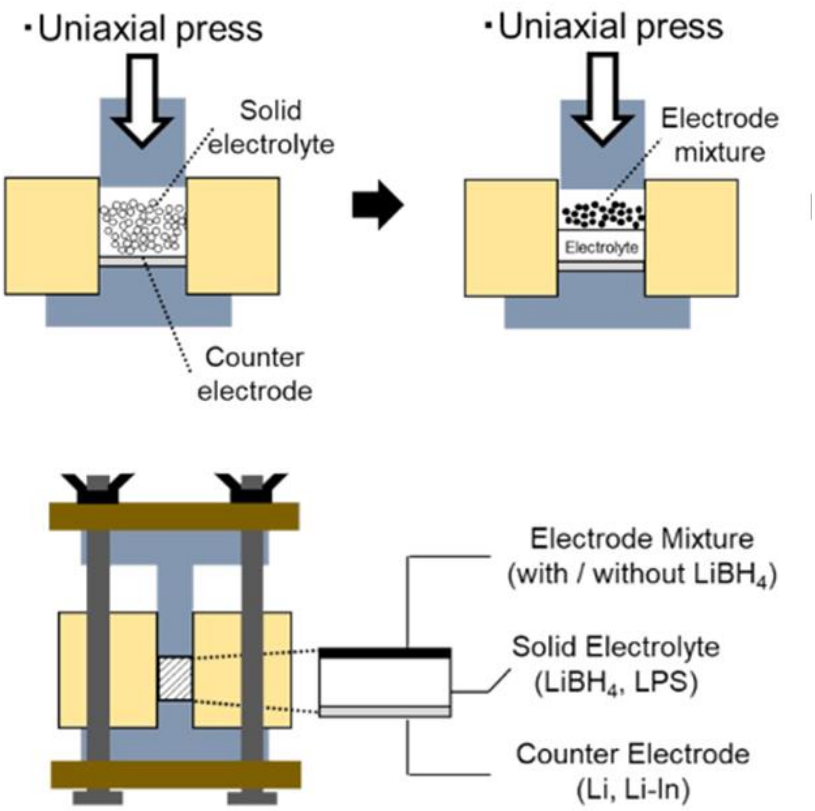

Figure 3.6 The detailed illustration of the preparation of the solid-state lithium battery electrode and cell assembly process. [8]

Next, the solid-state battery assembly process is illustrated in **Figure 3.6 and 3.7**, firstly, the solid electrolyte $LiBH_4$ (70 mg) was loaded into a sleeve made of poly (ether-ether ketone) with an inside diameter of 10 mm, pressed at 100 MPa. Secondly, the working electrode mixture with a quantity of 4 mg was placed on the upside of the $LiBH_4$ layer and pressed at 100 MPa as well, then, a lithium foil was placed on the downside of electrolyte layer as counter electrode. Finally, the whole cell was settled into a steel mould, and the screws are tightened with a torque of 10 N/cm. All the procedure were conducted in an Ar-filled glovebox with concentrations of moisture and oxygen below 1 ppm.

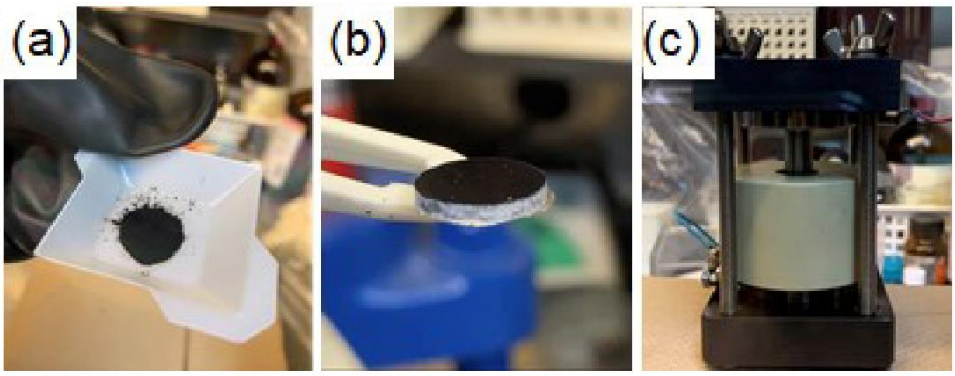

Figure 3.7 Photo images of (a) synthesized powder of electrode mixture, (b) prepared cell (Li/$LiBH_4$/MHG) and (c) assembled cell for electrochemical evaluation. [8]

3.5.3 Cyclic Voltammetry (CV)

CV is a commonly used electrochemical research method. This method controls the electrode potential to scan one or more times in a triangular waveform at different rates over time. The potential range is to allow different reduction and oxidation reactions to occur alternately on the electrode, and to record the current-potential curve. According to the shape of the curve, the degree of reversibility of the electrode reaction, the possibility of intermediates, phase boundary adsorption or new phase formation, and the nature of the coupling chemical reaction can be judged. It is a widely used physical chemistry instrument for electrochemical characterization, which is commonly used for the study of reaction mechanism and collection of kinetic parameters of electrochemical reactions. The determination of control steps, observation of reactions occurring within the entire potential scanning range and their features could also detected by the usage of this instrument. Additionally, quantitative analysis of the concentration of reactants, the coverage of the adsorbate on the electrode surface, the active area of the electrode, the electrode reaction rate constant, the exchange current density, and the transfer coefficient of the reaction could obtain through this machine. In this thesis, both

Biologic VMP-3 and CHI660E electrochemical workstation were used for the measurement of CV profiles.

3.5.4 Galvanostatic Charge/Discharge Testing

Galvanostatic charge /discharge testing is very important method for studying the electrochemical properties of materials. Perform charge and discharge operations on the measured electrode under constant current conditions, record the change rule of its potential with time, and study the rule of potential change as a function of time. It records the changing potential with time, under constant current conditions, through charging and discharging of the electrode to be measured. Thus, the lithiation and delithiation behaviors of the electrode could be studied and its actual specific capacity could also be calculated. During the constant current charge and discharge experiment, the electrochemical response signal of the control current is controlled. When the current control signal is applied, the potential is the measured response signal, and the law of potential change is a function of the main research time. In this thesis, galvanostatic charge /discharge testing were performed through an automatic battery test instrument. (LANHE, China)

3.5.5 Electrochemical Impedance Spectroscopy (EIS)

EIS is one of the most powerful tools to study the electrochemical processes occurring at the electrode/electrolyte interface, and it is widely used to study the intercalation and extraction processes of lithium ions in the active materials of lithium -ion battery intercalation electrodes. The EIS technology is an alternating current (AC) test method in which sine wave AC signals of a certain amplitude and different frequencies are applied to the electrochemical system to obtain the corresponding electrical signal feedback in the frequency domain. It can be used to characterize the

relative kinetic parameters of lithium ions in the process of insertion and extraction of positive and negative active materials, such as charge transfer resistance, electronic resistance of active materials, diffusion, and resistance of lithium ions diffusion and migration through SEI films, etc. In this thesis, both Biologic VMP-3 and CHI 660E electrochemical workstation were used for the test of EIS data.

3.5.6 Potential Intermittent Titration Technique (PITT) Method

Diffusion is an important form of mass transfer. The process of intercalation and extraction of lithium ions in the electrode material is a kind of diffusion. At this time, the chemical diffusion coefficient D of lithium ions largely determines the reaction rate and also affects the overall performance of the battery. Therefore, the determination of the chemical diffusion coefficient is of great significance to the study of the electrochemical properties of materials. PITT is a measurement method that has been widely used to characterize the diffusion coefficient D during the charge and discharge process, by changing the electrode potential instantaneously and keeping the potential value constant while recording current changes over time. In this thesis, cells were cycled in PITT from 1.5 V to 0.25 V using 10 mV step size with a current cut-off of 2 mA g^{-1} (<C/1000) of active material. The diffusion coefficient, D was calculated by measuring the linear slope of the ln(I) vs time (t) at each voltage step according to the following equation: [9]

$$\boldsymbol{D(Li^{+}) = -\frac{\mathrm{d}(\ln(I))}{dt}\frac{4L^2}{\pi^2}} \qquad \textbf{(3.1)}$$

where *I* refers to the current of the potential step, *t* is the time within the potential step, and L is the diffusion length. According to TEM images, we assume our samples are spherical particles. Then, the diffusion length is approximately the radius of the spherical particles.

3.6 References

[1] Xia. G. L.; Meng. Q. et al. Nanoconfinement Significantly Improves the Thermodynamics and Kinetics of Co-Infiltrated $2LiBH_4$-$LiA1H_4$ Composites: Stable Reversibility of Hydrogen Absorption/Resorption. *Acta Mater.* **2013**, 61, 6882.

[2] Han, M.; Zhao, Q. et al. The Enhance Hydrogen Storage of Micro-nanostructured Hybrids of $Mg(BH_4)_2$- Carbon Nanotubes. *Nanoscale*. **2015**, *7*, 18305.

[3] Zheng, S.; Fang, F.; Zhou, G.; Chen, G.; Ouyang, L.; Zhu, M.; Sun, D. Hydrogen Storage Properties of Space-Confined $NaAlH_4$ Nanoparticles in Ordered Mesoporous Silica. *Chemistry of Materials.* **2008**, *20*, 3954.

[4] Wang, C.; Wang, X. S. Slurryless Li_2S/Reduced Graphene Oxide Cathode Paper for High-Performance Lithium Sulfur Battery. *Nano Lett.* **2015**, *15*, 1796.

[5] Xia, G. L.; Tan, Y. B. et al. Uniformly Self-Assembled on Graphene. *Adv. Mater.* **2015**, *27*, 5981.

[6] Zhang, H. Y.; Xia, G. L.; Zhang, J.; Sun, D. L.; Guo, Z. P.; Yu, X. B. Graphene-Tailored Thermodynamics and Kinetics to Fabricate Metal Borohydride Nanoparticles with High Purity and Enhanced Reversibility. *Adv. Energy Mater.* **2018**, *8*, 1702975.

[7] Zhan, B. P.; Xia, G. L. et al. Controlled-Size Hollow Magnesium Sulfide Nanocrystals Anchored on Graphene for Advanced Lithium Storage. *ACS Nano.* **2018**, *12*, 12741.

[8] H. Sato, R. Sakamoto, H. Minami, H. Izumi, K. Ideta, A. Inoishi and S. Okada. The In Situ Formation of an Electrolyte via the Lithiation of $Mg(BH_4)_2$ in an All-Solid-State Lithium Battery. *Chem. Commun.* **2021**, *57*, 2605.

[9] D. Renz, M. Cronau and B. Roling. Determination of Lithium Diffusion Coefficients in Single Battery Active Material Particles by Using an AFM-Based Steady-State Diffusion Depolarization Technique. *J. Phys. Chem. C.* **2021**, *125*, 2230.

CHAPTER 4 GRAPHENE-TAILORED MOLECULAR BONDS FOR ADVANCED LITHIUM STORAGE PERFORMANCE

4.1 Introduction

The requirements of clean and renewable energy systems, along with the eagerness from a variety of industries, including large-scale alternative energy, clean transport, and portable electronics, have pushed forward the development of advanced energy storage technologies.[1-7] Due to their superior energy density, and clean and efficient energy storage mechanism, a promising strategies, electrical energy storage in lithium-ion batteries (LIBs) [8-15], have attracted enormous attention.

Sodium alanate ($NaAlH_4$) used to be considered as a highly promising hydrogen storage candidate, owing to its high gravimetric (7.5 wt.%) and volumetric capacity (94 g H_2 L^{-1}). However, $NaAlH_4$ was recently demonstrated to be a great potential candidate as a new high-energy, low-cost, and sustainable negative electrode for LIBs due to its high theoretical gravimetric capacity of 1985 mAh g^{-1} and moderately low working voltage[16]. Two different lithiation pathways were reported through the following reactions:

$$NaAlH_4 + 3/2Li \leftrightarrow 1/2LiNa_2AlH_6 + 1/2Al + LiH \quad \textbf{(4.1)}$$

$$LiNa_2AlH_6 + 3/2Li \leftrightarrow 2Na + Al + 6LiH \quad \textbf{(4.2)}$$

Or:

$$NaAlH_4 + 2Li \leftrightarrow 1/3Na_3AlH_6 + 2/3Al + 2LiH \quad \textbf{(4.3)}$$

$$Na_3AlH_6 + 6Li \leftrightarrow 3Na + Al + 6LiH \quad \textbf{(4.4)}$$

The complicated electrochemical conversions involved in the lithiation and delithiation processes mean that the $NaAlH_4$ suffers from poor reactivity and

reversibility due to its insulating nature and the presence of phase separation, significant volume changes, and the sodium stripping reaction. [17-20]

To resolve these issues, various strategies have been proposed to improve the hydrogen and lithium storage performances of $NaAlH_4$, including doping with catalysts [10, 21, 22] and/or nanostructuring [15, 18, 20, 23, 24]. Despite these numerous research efforts, the performance of $NaAlH_4$ still falls far short of the requirements for practical applications. The presence of strong ionic (Na^+ and $[AlH_4]^-$) and covalent interactions (Al-H bonds) in $NaAlH_4$ lead to high energy and kinetics barriers for breaking metal-hydrogen bonds [25]. Therefore, it has been acknowledged that, based on the reaction mechanisms for lithium storage, the strength of the metal-hydrogen bonds, *i.e.*, Al-H bonds in $NaAlH_4$, plays an important role in determining the thermodynamics and kinetics for lithiation and de-lithiation, which has been widely demonstrated by numerous experimental and theoretical studies. [26, 27] It remains a key challenge, however, to controllably tailor the strength of Al-H bonds of alanates towards advanced lithium storage performance in a way that is not only facile, but also effective.

In the present work, we demonstrate that graphene could act as an effective platform to control and tune the metal-hydrogen bonds of $NaAlH_4$ nanoparticles (NPs) through the favorable molecular interaction between them. Both theoretical calculations and experimental results validate that, owing to the intimate physical contact and the favorable molecular interaction between $NaAlH_4$ and graphene, graphene could effectively weaken the ability of Na to donate charge to the AlH_4 moiety and hence, reduce the strength of the Al–H bond, which could decrease the energy barrier for both the insertion and extraction of Li ions. Taking advantage of this favorable interaction between $NaAlH_4$ and graphene, a robust nanostructure composed of homogeneous $NaAlH_4$ NPs with an average size of ~ 12 nm encapsulated in graphene nanosheets was

fabricated via a facile solvent evaporation induced deposition (SEID) method with tunable loading and distribution. This unique nanostructure contributes for effective lithium storage in $NaAlH_4$. First, graphene could act not only as a functional support for anchoring well-dispersed $NaAlH_4$ NPs, but also to effectively prevent their aggregation and growth, thus leading to stable cycling performance for lithium storage. Moreover, the fast thermal and electronic conductivity of graphene greatly improves the transfer rate of electrons, leading to fast kinetics for lithium storage [28-30]. Moreover, the homogenous distribution of $NaAlH_4$ on graphene could provide a large surface area and large void space on the surface, which enhance the accessibility of electrolyte, and shorten the diffusion pathways for lithium ions. Owing to these advantages, the nanostructured hybrids of $NaAlH_4$-graphene could show significantly enhanced lithium storage performance.

4.2 Experimental Section

4.2.1 Material Synthesis

Fabrication of $NaAlH_4$@graphene nanostructures: All chemicals were purchased from Sigma-Aldrich and used as received without further purification. Graphene (specific surface area: 700-1000 $m^2 g^{-1}$, electrical conductivity: 700-1500 S m^{-1}) was purchased from Simbatt Energy Technology Co. Ltd.. The $NaAlH_4$ NPs grown on graphene with various mass loadings were fabricated via a facile SEID method. Firstly, 1 mol $NaAlH_4$ was dissolved into 6 mL tetrahydrofuran (THF) under ultrasonic stirring for 20 min. Secondly, 2 mL $NaAlH_4$ in the THF solution and graphene were mixed in a pressure reactor vessel and kept under ultrasonic dispersion for 1 h. A certain amount of graphene (0.156 g, 0.039 g, and 0.015 g) was added to synthesize SAH@G hybrids with different loadings of $NaAlH_4$ (SAH@G-10, SAH@G-30, and SAH@G-50). All

the above synthesis procedures were carried out in a argon-filled glove box (Mikrouna Universal) with moisture and oxygen contents below 0.1 ppm. The solvent infiltration of $NaAlH_4$ was then carried out at 120 °C under a hydrogen pressure of 50 atm for 10 h. Finally, the products were dried at room temperature via dynamic vacuum on a Schlenk line, leading to the formation of SAH@G hybrid.

4.2.2 Materials Characterizations:

The crystalline structures of samples were characterized by powder X-ray diffraction (XRD; D8 Advance, Bruker AXS) with Cu Kα radiation. To prevent any possible reactions between samples and air during the XRD measurements, amorphous tape was used to cover the samples. FTIR spectra were recorded on a Genesis II spectrophotometer (Mattson). The FTIR spectra were obtained over 32 scans in absorption mode at a resolution of 4 cm^{-1}. Thermogravimetric analysis (TG; Netzsch STA449 F3) in conjunction with mass spectrometry (MS; Hiden HPR 20) was performed under Ar flow at a ramp rate of 5 $^{o}C\ min^{-1}$. The morphology and composition of samples were determined using an FE-SEM (JEOL 7500FA, Tokyo, Japan) and a TEM (JEOL 2011 F, Tokyo, Japan) coupled with an EDX spectrometer. Samples for TEM and SEM tests were first dispersed on Cu grids and conducting resin in the glove box, respectively, and then rapidly transferred into the chambers for testing within a few seconds. The particle size distributions were calculated based on the corresponding TEM images of the samples, combine with the descriptive statistical analysis and Gaussian fitting.

4.2.3 Electrochemical Measurements

Electrochemical experiments were carried out within 2032 coin-type half-battery cells assembled with a pure lithium foil as counter electrode, and Whatman borosilicate

glass-fiber filter paper as separator. The electrolyte consisted of 1 M $LiPF_6$ in ethylene carbonate (EC)/ dimethyl carbonate (DMC)/ diethyl carbonate (DEC) (1:1:1, volume ratio) solution. The working electrodes were fabricated by grinding the active materials samples, acetylene black, and binder at a weight ratio of 8:1:1, coating the product on nickel foam, and drying it in vacuum at 60 °C for 24 h. Poly(methyl methacrylate) (PMMA) binder was dissolved in DMC. The cells were assembled in an argon-filled glove box with concentrations of moisture and oxygen kept below 0.1 ppm. CV and EIS were both performed using a CHI660D electrochemistry workstation at room temperature. CV curves were collected at a scan rate of 0.1 mV s^{-1} in the potential range of 0.01–3.0 V (vs. Li^+/Li), and EIS was carried out from 100 kHz to 0.01 Hz. The cycling performance and rate stability of cells were tested using a LANHE Battery Test System between 0.001 V and 3.0 V (vs. Li^+ /Li) at different constant current densities.

4.2.4 Theoretical Calculations

The theoretical calculations were mainly conducted according to the density functional theory (DFT) approach[31] including the DMol^3 package. Based on Perdew-Wang generalized-gradient approximation (GGA-PW91), the effects of exchange correlation interaction were performed.[32] A double numerical basis with polarized orbital (DNP) was used to expand all-electron Kohn-Sham wave functions.[33] A regular Monkhorst-Pack grid of special k-points was used for performing the Sampling of the irreducible wedge of Brillouin zone.[34] In order to obtain final structures with minimum total energy, the whole models used for DFT were first relaxed. The convergence criteria for relaxation were 1.0×10^{-5} Ha, 0.002 Ha/Å, and 0.005 Å for the energy, gradient, and atomic displacement, respectively. As shown in **Figure 4.1**, in order to simulate the adsorption of $NaAlH_4$ nanoparticles with various sizes, different $(NaAlH_4)_n$ (n = 1-6) clusters were constructed.

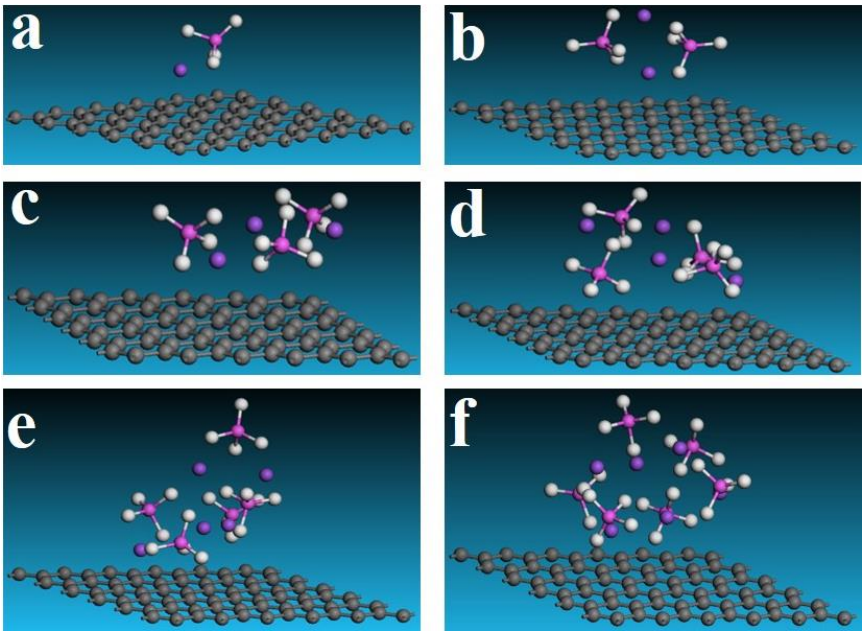

Figure 4.1 Optimized configuration of the $(NaAlH_4)_n$ on graphene (n = 1 (a), 2 (b), 3 (c), 4 (d), 5 (e), and 6 (f)).

The binding energy (E_b) of $(NaAlH_4)_n$ was calculated by subtracting the total energies of $(NaAlH_4)_n$ units and the substrate from the total energy of $(NaAlH_4)_n$-Graphene system (**Figure 4.2**), as shown in Eq. (4.5).

$$E_b = (E_{(NaAlH4)n} + E_G) - E_{total} \quad \textbf{(4.5)}$$

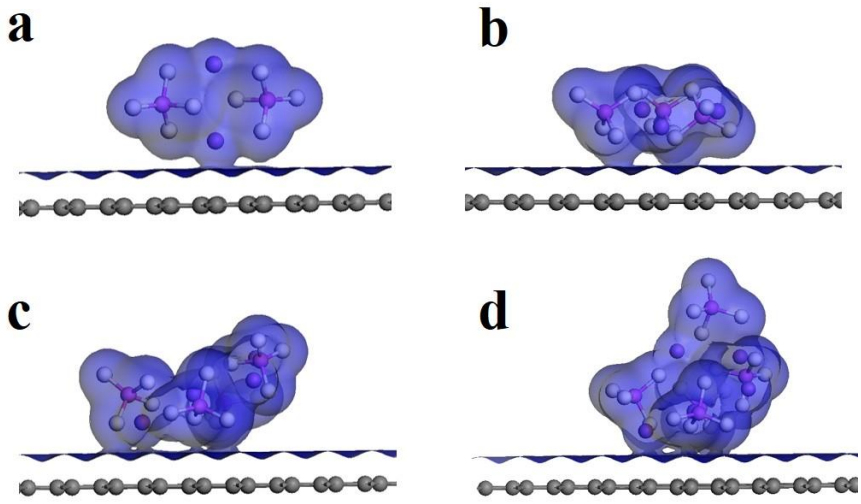

Figure 4.2 Iso-surface of electron density of the $(NaAlH_4)_n$ on graphene (n = 2 (a), 3 (b), 4 (c), and 5 (d)).

The energy (E_{re}) required for the removal of hydrogen from $NaAlH_4$ was calculated by subtracting total energies of $NaAlH_4$/Graphene from the total energies of the $NaAlH_4$ with one less hydrogen on the graphene and an isolated hydrogen (**Figure 4.3**), as shown in Eq. (4.6).

$$E_{re} = (E_{NaAlH3} + E_H) - E_{total} \quad \textbf{(4.6)}$$

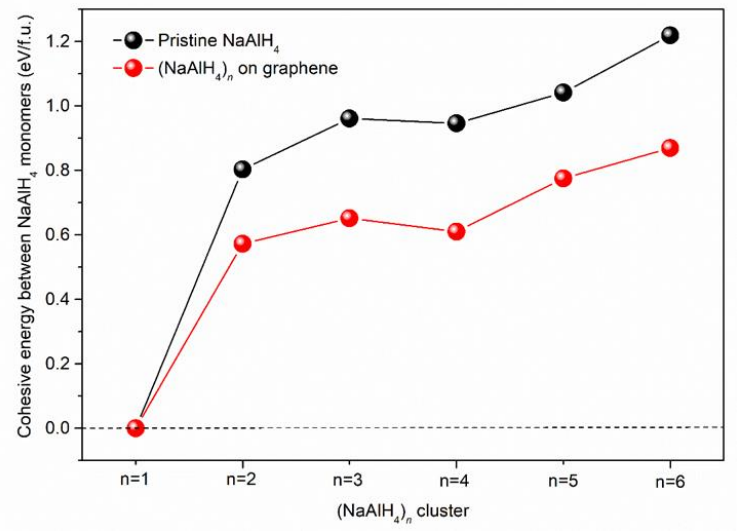

Figure 4.3 Cohesive energy of between $NaAlH_4$ monomers with and without the presence of graphene.

4.3 Results and Discussion

The $NaAlH_4$@graphene composite (denoted as SAH@G) was fabricated by a facile SEID method via infusing $NaAlH_4$ solution (in tetrahydrofuran, THF) into porous graphene nanosheets (GNs), as illustrated in **Figure 4.4**. Under the most stable adsorption configuration, density functional theory calculation results verify that the binding energy between $NaAlH_4$ and graphene approaches 0.477 eV (**Figure 4.1**), which favors the homogeneous distribution of $NaAlH_4$ on the graphene. Mulliken charge analysis demonstrated that, when $NaAlH_4$ clusters interact with graphene, a significant charge is transferred from $(NaAlH_4)_n$ to graphene, which could be verified

by the clear overlap between various $NaAlH_4$ clusters and graphene for all the $NaAlH_4$-graphene systems (**Figure 4.2** and **Figure 4.4b and c**). It underscores the strong electronic interaction between graphene and $NaAlH_4$. In addition, the energies required to form larger clusters in the presence of graphene are much smaller than that without graphene (**Figure 4.3**), which confirms that $(NaAlH_4)_n$ tends to be uniformly adsorbed on the graphene rather than forming larger clusters. To be specific, graphene could act as an electron acceptor and withdraw electrons from $NaAlH_4$ clusters, and hence, Na^+ ions are pulled toward the graphene planes in the $NaAlH_4$-graphene hybrid. This results in a large charge transfer of 0.06 e from the $NaAlH_4$ clusters to graphene, which could effectively reduce the electron donation of Na to the AlH_4 moiety and thus weaken the Al-H bonds of the AlH_4 moiety.

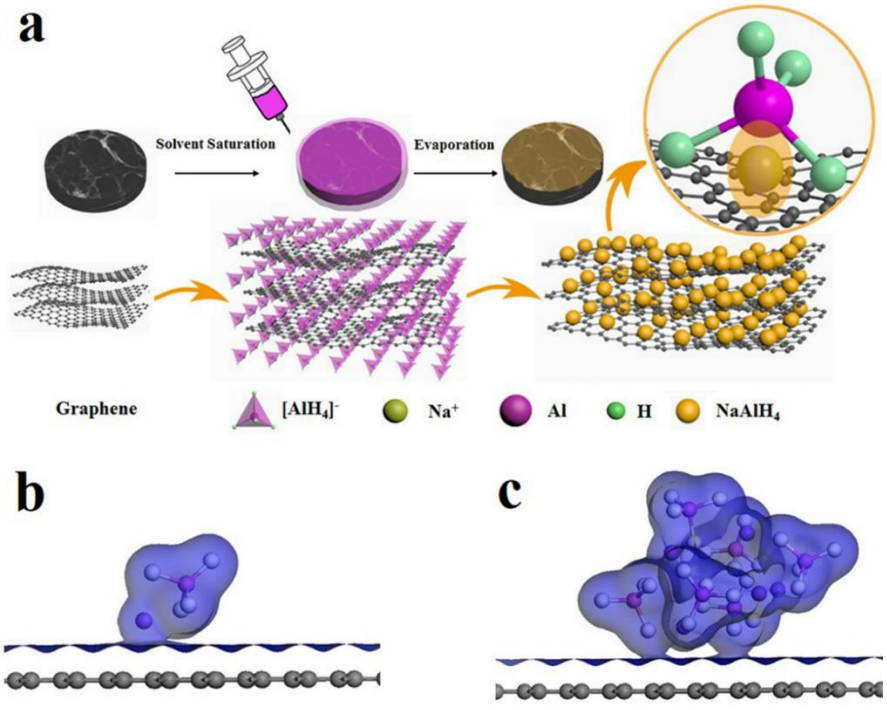

Figure 4.4 (a) Schematic illustration of the synthesis of SAH@G-50. Isosurface of electron density of the $NaAlH_4$ on graphene (b) and $(NaAlH_4)_6$ on graphene (c).

In order to unravel the morphologies of the as-prepared nanostructured composite, field-emission scanning electron microscopy (FE-SEM) was conducted. As shown in

Figure 4a, pure GNs exhibit large-sized lamellar structures with clean surfaces. After the deposition of $NaAlH_4$ on graphene via the SEID method, nanoparticles distributed on the GNs with an average particle size of ~ 10.2 nm could be clearly observed when loaded with 10 wt.% $NaAlH_4$ (sample denoted as SAH@G-10) (**Figure 4.6a and b**). More importantly, the homogenous distribution of $NaAlH_4$ NPs is well preserved when

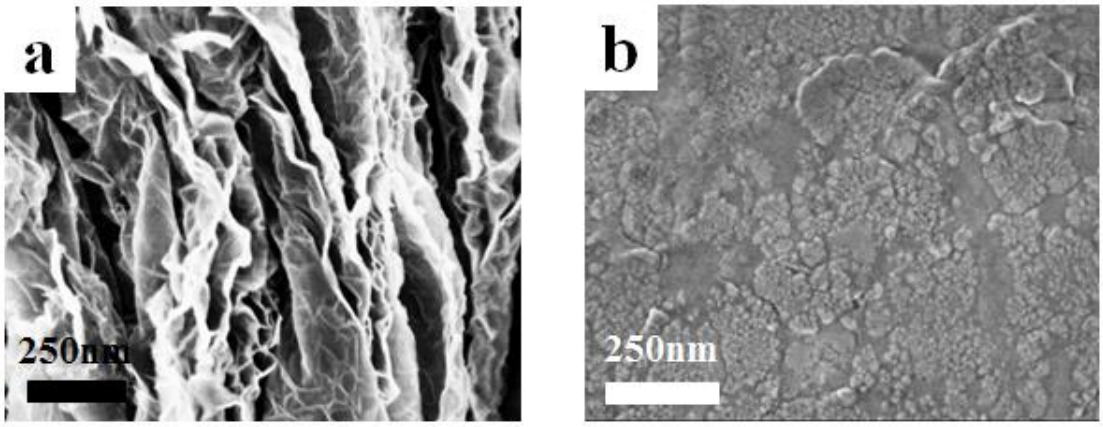

Figure 4.5 SEM images of (a) graphene and (b) $NaAlH_4$ NPs via the SEID method without the presence of graphene.

the loading rate of $NaAlH_4$ is increased from 10 wt.% to 30 and 50 wt.%, and only slight growth of particle size of the thus-formed $NaAlH_4$ NPs is observed along with the increased density (**Figure 4.6a-f**). In particular, when the proportion of $NaAlH_4$ reaches 50 wt.% (sample denoted as SAH@G-50), there is still obvious interparticle space between individual $NaAlH_4$ NPs (**Figure 4.7a** and **b**), and the average particle size of the as-synthesized $NaAlH_4$ NPs is only 12.4 nm. (**Figure 4.6e and f**). The significant decrease in the particle size could effectively shorten the diffusion pathways for lithium ions, which improves the lithium storage performance. In strong contrast, without the support and direction provided by graphene, $NaAlH_4$ particles synthesized via the SEID method show a bulk shape with serious aggregation (**Figure 4.5b**). This highlights the important role of the molecular interaction between $NaAlH_4$ and graphene in tuning the formation and distribution of $NaAlH_4$ on the graphene, which

provides an enormous number of nucleation and anchoring sites for $NaAlH_4$ NPs and prevents the aggregation of $NaAlH_4$.

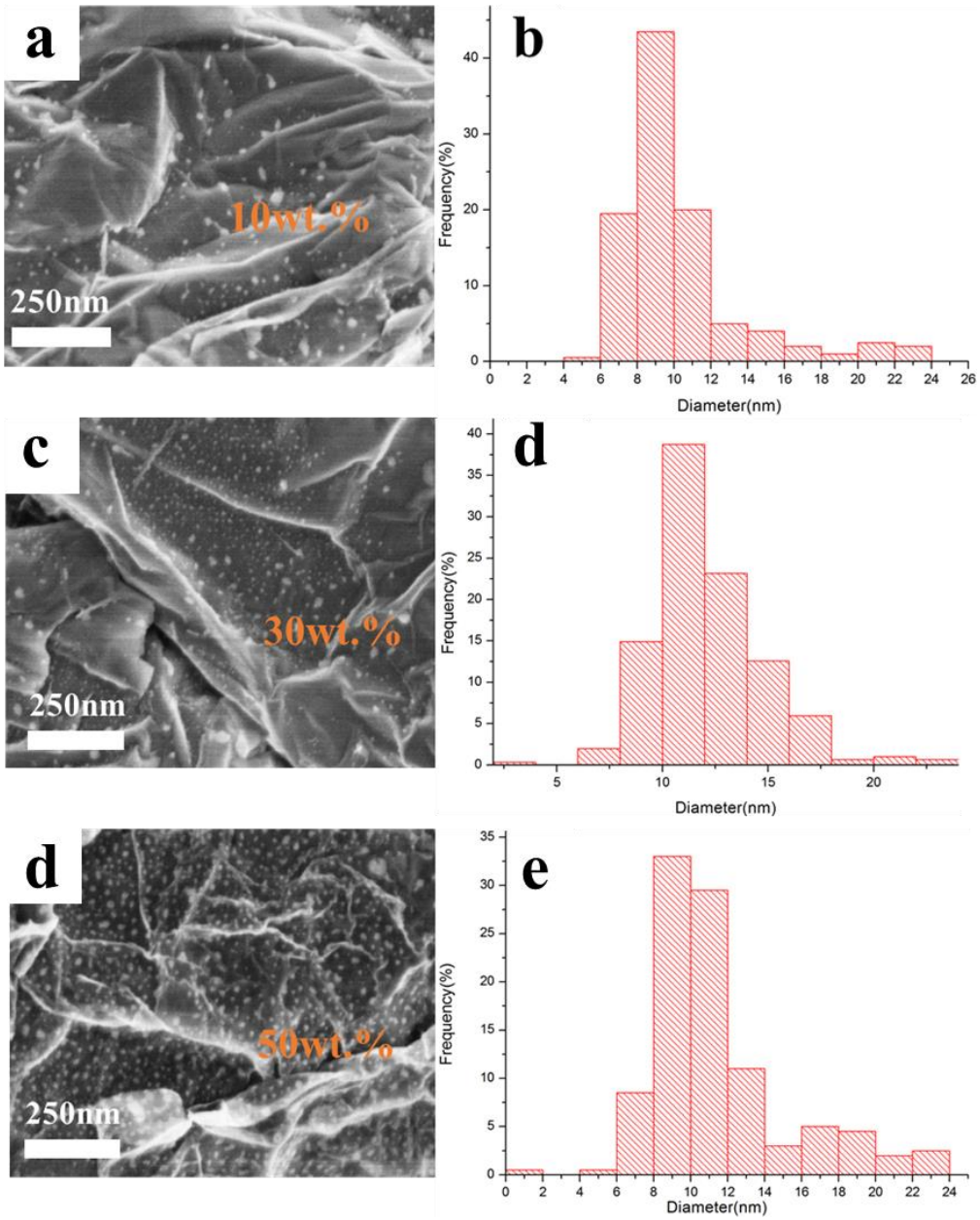

Figure 4.6 SEM image of SAH@G-10 (a), SAH@G-30 (c), SAH@G-50 (e) and the corresponding particle size distribution (b), (d), (f), respectively.

Transmission electron microscopy (TEM) image of SAH@G-50 provides additional evidence of the homogeneous distribution of $NaAlH_4$ NPs on GNs (**Figure 4.7c**). The scanning TEM (STEM) images (**Figure 4.7d-f**) further demonstrate that high-density

$NaAlH_4$ NPs are homogenously scattered throughout the surface and interleaved layers of GNs with space in between. This feature is beneficial for accommodating the volume variation and alleviating particle aggregation during lithiation and de-lithiation cycling. No isolated $NaAlH_4$ NPs were observed in the hybrid, even after ultrasonic treatment for 20 min to disperse the sample for TEM and STEM tests, indicating the strong molecular interactions between $NaAlH_4$ and GNs, which contributes to the uniform formation of $NaAlH_4$ NPs on GNs. The intimate contact between $NaAlH_4$ NPs and GNs with excellent thermal and electron conductivity could significantly improve the transfer of heat and electrons in the hybrid. Additionally, the corresponding energy dispersive X-ray spectroscopy (EDX) mapping (**Figure 4.7g-k**) of Na, Al, and C elements in the SAH@G-50 sample indicates that the maps of all three elements apparently match very well with the structure of the as-prepared SAH@G-50, which validates the argument that the $NaAlH_4$ NPs are evenly distributed on the GNs. Therefore, it is clearly established that SAH@G-50 shows a compact three-dimensional (3D) stacking nanostructure, in which $NaAlH_4$ NPs are uniformly anchored on the GNs.

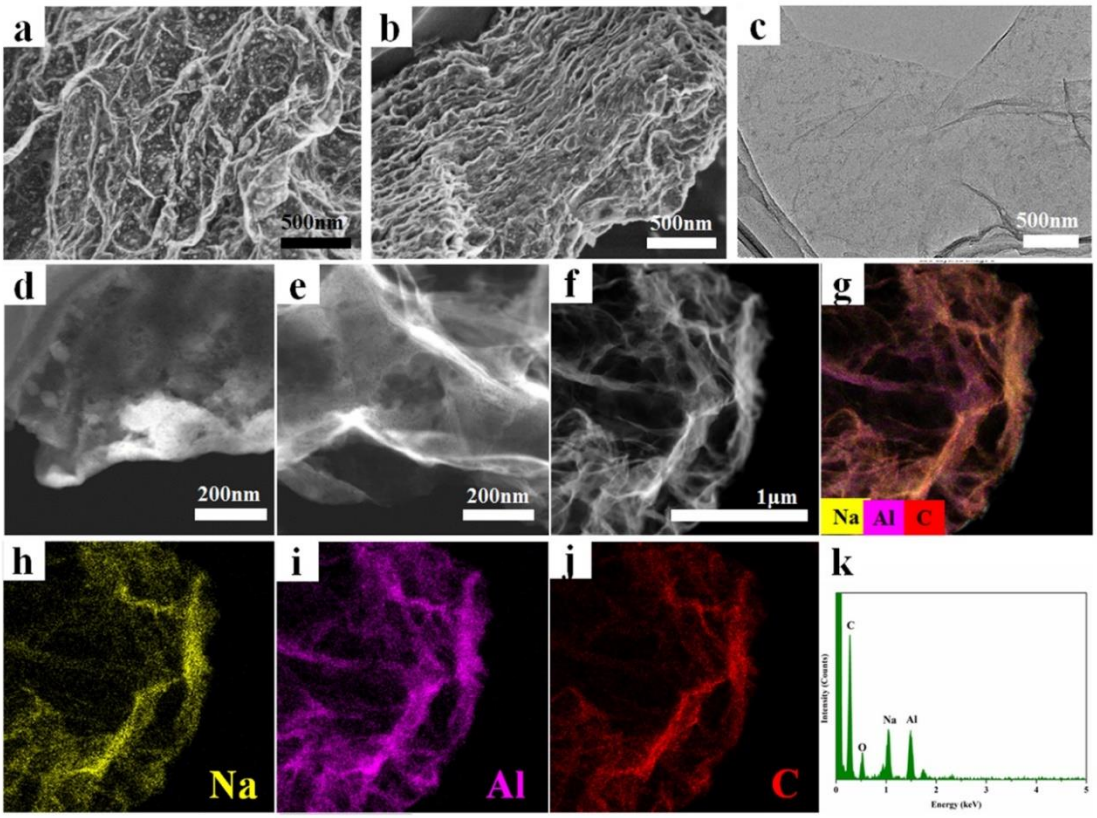

Figure 4.7 FE-SEM images (a, b), TEM images (c), and STEM images (d, e, f) of SAH@G-50. Elemental mapping (g) of SAH@G-50 composite, the corresponding elemental mapping of Na (h), Al (i), and C (j), and the EDX spectrum (k).

The formation of $NaAlH_4$ in SAH@G-50 was confirmed by powder X-ray diffraction (PXRD), and the sample exhibits clear diffraction peaks readily indexed to a pure tetragonal phase of $NaAlH_4$ (**Figure 4.8a**). Fourier transform infrared spectroscopy (FTIR) was subsequently adopted to characterize the presence of $NaAlH_4$ on the graphene in SAH@G-50. As shown in **Figure 4.8b**, the peaks of the bulk $NaAlH_4$ sample at 1676 cm^{-1} and 736 cm^{-1} correspond to the stretching mode ν_3 of the Al–H vibration and the bending mode ν_4 in the AlH_4 group, respectively. It is interesting to note that, after the homogeneous encapsulation of $NaAlH_4$ in porous GNs, both characteristic peaks of the SAH@G-50 sample obviously shift to lower wavenumbers compared with those of pure $NaAlH_4$, which indicates the weakening of Al–H bond

strength in the thus-formed $NaAlH_4$ phase when interacting with graphene. This coincides well with the theoretical calculation results and directly demonstrates the favorable molecular interactions between graphene and $NaAlH_4$.

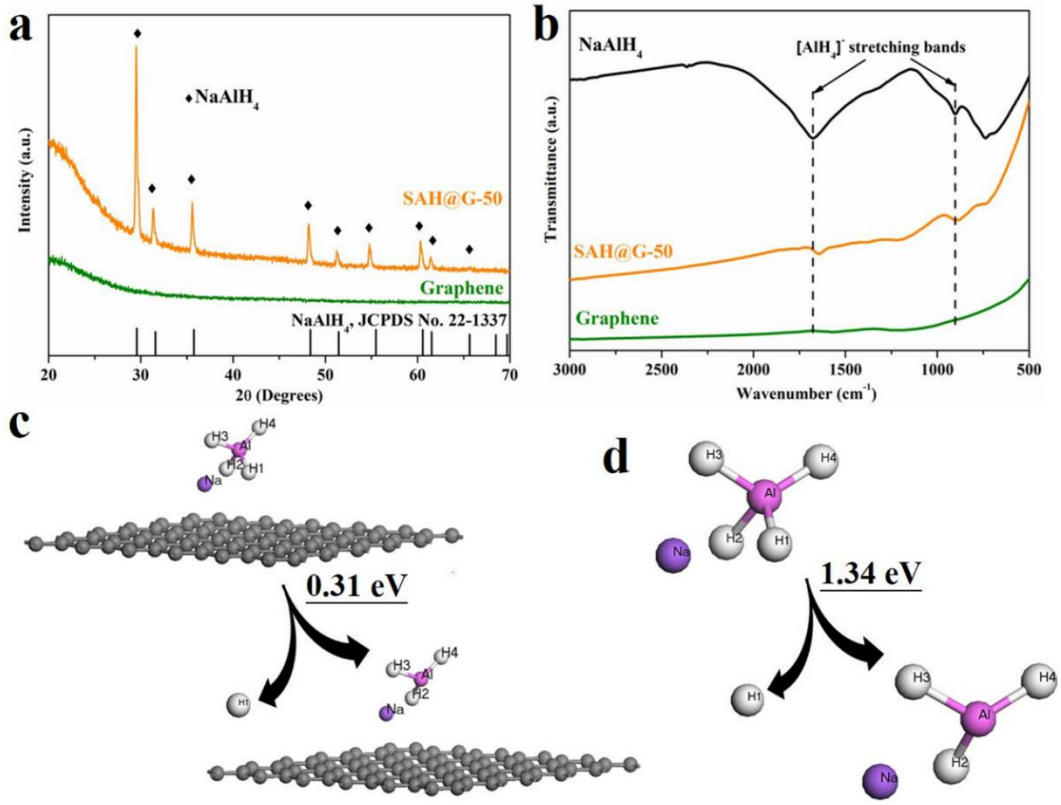

Figure 4.8 (a) PXRD patterns and (b) FTIR spectra of the as-prepared SAH@G-50, in comparison with pristine $NaAlH_4$ and graphene. Energies required for the removal of hydrogen from $NaAlH_4$ with (c) and without (d) the presence of graphene.

In order to quantitatively verify the weakening of Al-H bonds due to the intimate interaction of $NaAlH_4$ with graphene, the energies required for removing hydrogen from $NaAlH_4$ were calculated based on DFT calculations. It is revealed that the removal energy of hydrogen from $NaAlH_4$ interacting with graphene is only ~ 0.31 eV (**Figure 4.8c**), while this value approaches around 1.34 eV without the presence of graphene (**Figure 4.8d**). This result directly confirms that graphene could effectively decrease

the energy required for breaking and recombination of the Al-H bonds and thereby facilitate the lithium storage performance of $NaAlH_4$.

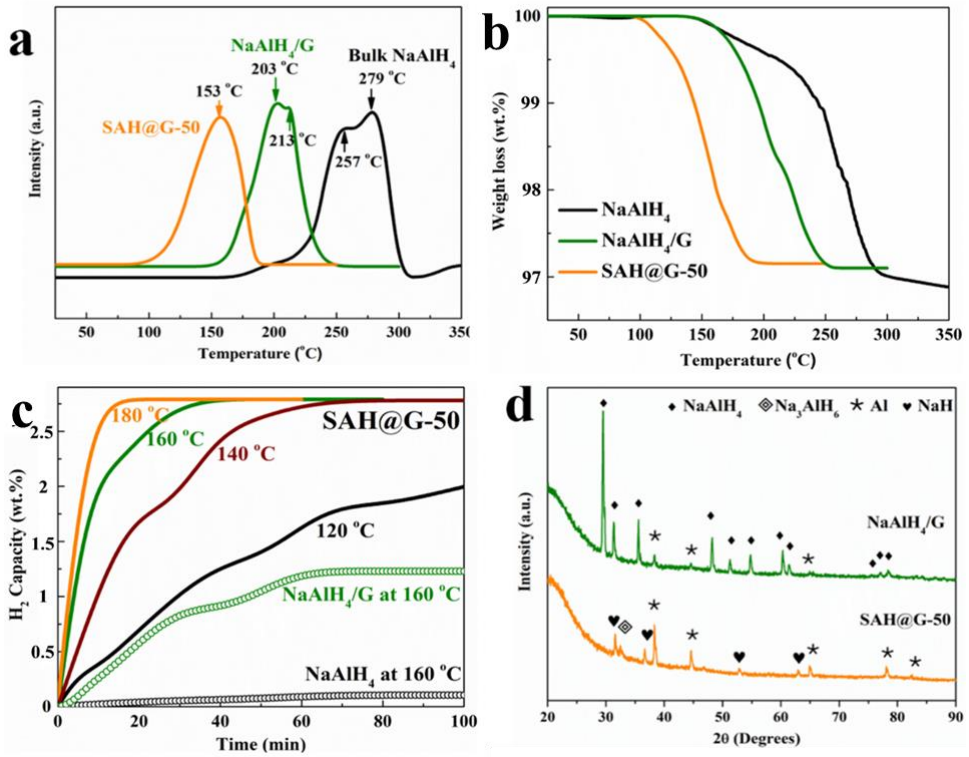

Figure 4.9 Mass spectra (a) and thermogravimetric analysis curves (b) of the as-prepared SAH@G-50 compared with bulk $NaAlH_4$ and the ball-milled composite of $NaAlH_4$ and graphene ($NaAlH_4$/G). (c) Isothermal dehydrogenation of SAH@G-50 in comparison with $NaAlH_4$ and the ball-milled $NaAlH_4$/G composite at various temperatures. (d) XRD patterns of SAH@G-50 after dehydrogenation for 40 min and the ball-milled $NaAlH_4$/G composite after dehydrogenation for 100 min at 160 ^oC.

The actual load of $NaAlH_4$ in the as-prepared SAH@G-50 was evaluated through thermogravimetric analysis in conjunction with mass spectrometry (TGA-MS) in a comparison with bulk $NaAlH_4$ and the ball-milled $NaAlH_4$/G composite. As illustrated in **Figure 4.9**. SAH@G-50 exhibits an onset temperature of 100 ^oC, which is 80 ^oC and 50 ^oC lower than for the bulk counterpart and the ball-milled composite, respectively. In addition, a maximum hydrogen capacity of ~ 2.8 wt.% could be achieved at a

temperature of less than 200 °C. Because the theoretical H_2 desorption content at the first two steps of $NaAlH_4$ is 5.6 wt%, it could be calculated that the content of $NaAlH_4$ in SAH@G-50 composite is 50%. The complete transformation of $NaAlH_4$ at this temperature was further proved by the XRD results (**Figure 4.9d**), in which the main phases of NaH and Al were observed for SAH@G-50 after dehydrogenation at 160 °C for 40 min, without oxidation or residual $NaAlH_4$. From a comprehensive point of view, compared with other very recent hydrogen storage systems (**Table 4.1**), the SAH@G-50 exhibits superior reversible hydrogen storage performance in terms of reversible temperature and cycling stability.

To evaluate the electrochemical lithium storage performance of SAH@G-50 electrode, cyclic voltammetry (CV), and galvanostatic charge-discharge cycling were conducted using CR2032 coin cells with lithium foil as counter/reference electrode. In the first cycle, the cathodic scan is dominated by the formation of the solid-electrolyte interphase (SEI), starting at approximately 0.69 V and followed with a sharp signal at a low potential (< 0.25 V vs. Li), which is attributed to the lithiation of Al resulting from the reduction of $NaAlH_4$ (**Figure 4.10a**). In the initial charge process, two peaks at 0.5 V and 0.8 V are observed, which could be ascribed to the reversible delithiation of Al and the reformation of $LiNa_2AlH_6$, respectively, which are in good agreement with previous reports [37]. It validates that the electrochemical reaction of SAH@G-50 for cycling lithium storage should be based on **Eqs. (4.3)** and **(4.4)**. In the subsequent cycles, the CV curves of SAH@G-50 are almost overlapping, demonstrating its good reversibility. By comparison, bulk $NaAlH_4$ acts differently within the same potential range, and only the peak at 0.5 V versus Li exists in the first anodic cycle, suggesting poor reversibility of these reactions (**Figure 4.11b**). **Figure 4.11c** presents the cycling

performance of SAH@G-50 at a current density of 100 mA g^{-1}, with bulk $NaAlH_4$ and pure graphene (**Figure 10**) included for comparison.

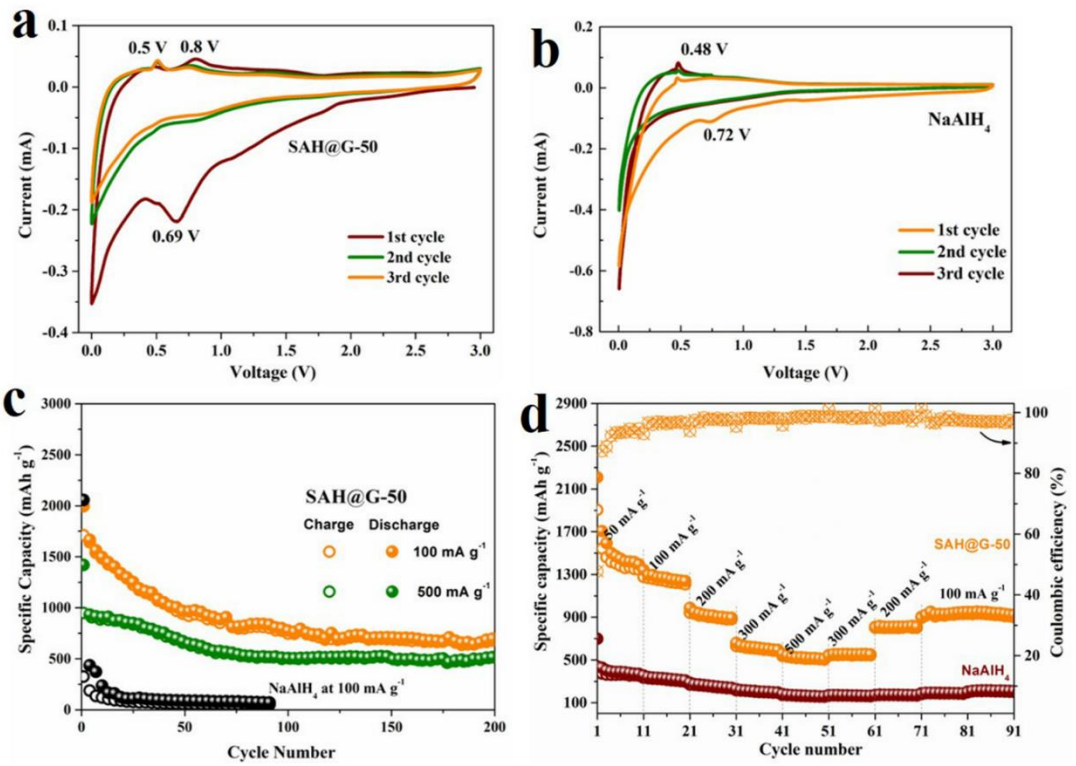

Figure 4.10 Representative CV curves for the first 3 cycles of the SAH@G-50 (a) and bulk $NaAlH_4$ (b) electrodes at a scan rate of 0.1 mV s^{-1}. (c) Comparison of the specific capacities of SAH@G-50 with bulk $NaAlH_4$ at the current densities of 100 mA g^{-1} and 500 mA g^{-1}. (d) Rate performance of SAH@G-50 electrode, with bulk $NaAlH_4$ electrode included for comparison.

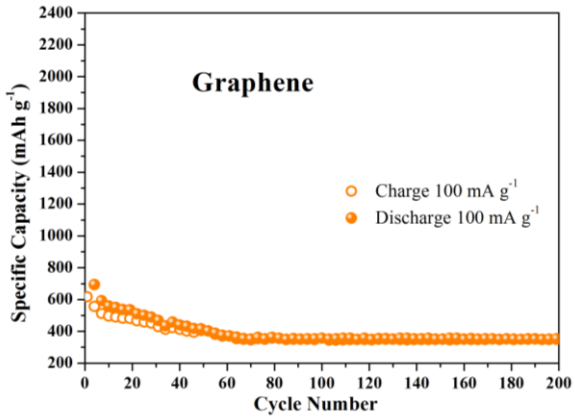

Figure 4.11 Cycling performance of graphene used in SAH@G-50 at 100 mA g^{-1}.

It should be noted that all the specific capacity is based on the mass of $NaAlH_4$ in the composite. The SAH@G-50 electrode exhibits an initial discharge and charge capacity of 1995 and 1710 mAh g^{-1}, respectively corresponding to a coulombic efficiency (CE) of 85.7%. The capacity loss can be mainly ascribed to the formation of SEI films on the electrode surface or the irreversible side reactions with electrolyte, in accordance with the CV curves. The specific discharge capacity slowly decayed and then was stabilized at ~698 mAh g^{-1} after 200 cycles. In strong contrast, although bulk $NaAlH_4$ electrode displayed an initial discharge capacity of 2057 mA h g^{-1}, the capacity rapidly decreased to less than 100 mAh g^{-1} after only 20 cycles, which is consistent with the results reported previously[16]. The rate capability test of SAH@G-50 electrode at current densities ranging from 50 to 500 mA g^{-1} demonstrates that this electrode could deliver average capacities of 1495, 1273, 924, 620, and 529 mAh g^{-1} at 50, 100, 200, 300, and 500 mA g^{-1}, respectively (**Figure 4.10d**). When switching back to 100 mA g^{-1} after the high-rate cycling, the capacity can return to 950 mA h g^{-1}. In comparison, the capacity of bulk $NaAlH_4$ electrode rapidly decreased to only 100 mAh g^{-1} at 500 mA g^{-1}. This validates the strong tolerance of SAH@G-50 electrode toward rapid lithium ion insertion and extraction. Furthermore, the SAH@G-50 electrode delivered an impressive discharge capacity of 522 mAh g^{-1} after 200 cycles at a high current density of 500 mA g^{-1}, with a high CE of around 100% through the whole cycling process, which further demonstrates its superior reversibility.

To investigate the superior electrochemical properties of SAH@G-50 electrode, electrochemical impedance spectroscopy (EIS) was carried out. As shown in **Figure 4.12**, each of the Nyquist plots contains a depressed semicircle at medium and high frequencies, corresponding to the charge-transfer impedance at the interface between the electrolyte and the working electrode, followed by a straight line with constant

inclining angle at low frequencies. It could be readily observed that the SAH@G-50 electrode displays a much smaller diameter of the semicircle as compared with $NaAlH_4$ electrode, indicating that SAH@G-50 has higher electrical conductivity and faster kinetics. The poor reversible capacity of $NaAlH_4$ is mainly due to the low conductivity, huge volume changes, and severe aggregation during the cycling process. In SAH@G-50, the presence of graphene with uniform distribution and favorable interaction with $NaAlH_4$ could significantly improve the conductivity of the composite, buffer the big volume change, and prevent the growth and aggregation of nanosized particles during the lithiation and delithiation process. TEM observations validate that SAH@G-50 maintains its original structure, with the $NaAlH_4$ NPs in SAH@G-50 still uniformly anchored on the graphene layers after 100 cycles (**Figure 4.12**). The selected area diffraction patterns (SADP) (inset of **Figure 4.12**) demonstrates the amorphous nature of SAH@G-50 after cycling, which is in good agreement with XRD results (**Figure 4.13**). This phenomenon is mainly attributed to the formation of thick SEI films and the smaller particle size due to the pulverization of $NaAlH_4$ NPs during the cycling charge and discharge process. Thereby, in comparison with the pristine $NaAlH_4$, the SAH@G-50 electrode exhibits a higher capacity and better cycling performance by taking advantage of the synergistic effects of the molecular interaction between graphene and $NaAlH_4$, and the significant decrease in the particle size.

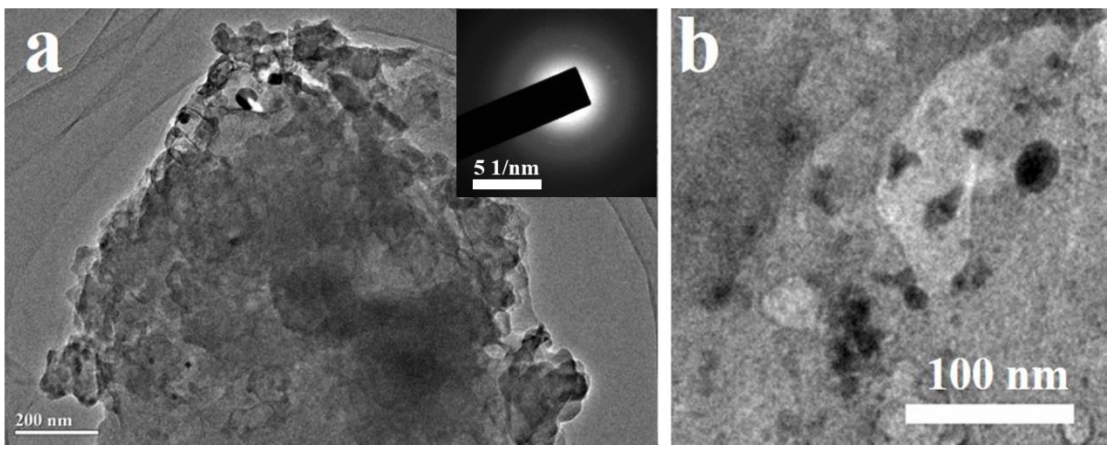

Figure 4.12 TEM images and SADP (inset of a) of charged SAH@G-50 after 100 cycles.

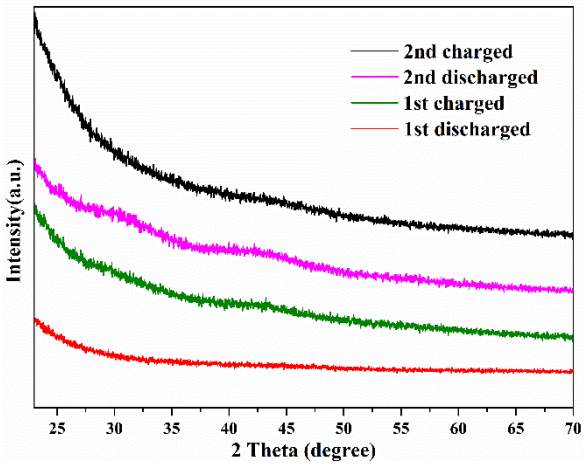

Figure 4.13 XRD patterns of SAH@G-50 at different states of charge and discharge.

Table 4.1 Comparison of different hydrogen storage systems.

	Materials	Reversible temperature	Regeneration method	Capacity retention	Cycle number	Reference
1	$LiBH_4$-MgH_2	393 °C	Direct hydrogenation	---	---	38
2	$NaBH_4$	Room temperature	Chemical regeneration	78 %	1	39
3	MgH_2/CHNBs @PCNFs	265 °C	Direct hydrogenation	100 %	1	40
4	SAH@G-50	153 °C	Direct hydrogenation	98 %	20	This work

4.4 Conclusion

In summary, we have developed a facile SEID method to realize the homogeneous distribution of $NaAlH_4$ NPs on graphene with intimate contact. This unique nanostructure contributes to the effective hydrogen and lithium storage in $NaAlH_4$, among which, graphene could not only act as a structural support for the formation of uniformly dispersed $NaAlH_4$, but also improve electron transport of the system and restrict $NaAlH_4$ NPs from growing and aggregating to a large extent during cycling, leading to the enhancement of cycling stability. Moreover, the favorable interaction between graphene and $NaAlH_4$ could effectively tailor the strength of Al-H bonds of $NaAlH_4$ and therefore promote their breaking and recombination towards advanced lithium storage performance. Additionallly, the significant reduction of particle size of $NaAlH_4$ down to only ~12 nm is also favorable for improving the kinetics for lithium storage through the reduced diffusion pathway and more active reaction sites on the surface. It is these synergistic effects that significantly enhance the lithium storage performance of $NaAlH_4$. Moreover, this strategy represents a highly novel approach based on tailoring the molecular bonds of metal hydrides with advantageous structures to promote their energy storage performance.

4.5 Reference

[1] R. Raccichini, A. Varzi, S. Passerini, B. Scrosati, Nat. Mater. **2014**, *14*, 271-279.

[2] Q. L. Zhu, Q. Xu, Energy Environ. Sci. **2015**, *8*, 478-512.

[3] L. Ouyang, W. Chen, J. Liu, M. Felderhoff, H. Wang, M. Zhu, Adv. Energy Mater. **2017**, 1700299.

[4] L. Z. Ouyang, X. S. Yang, M. Zhu, J. W. Liu, H. W. Dong, D. L. Sun, J. Zou, X.

D. Yao, J. Phys. Chem. C. **2014**, *118*, 7808-7820.

[5] R. Mohtadi, S.-i. Orimo, Nat. Rev. Mater. **2016**, *2*, 16091.

[6] Y. Sun, N. Liu, Y. Cui, Nature Energy **2016**, *1*, 16071.

[7] J. Zhang, S. Yan, H. Qu, Int. J. Hydrogen Energy **2018**, *43*, 1545-1565.

[8] Y. Pang, Y. Liu, M. Gao, L. Ouyang, J. Liu, H. Wang, M. Zhu, H. Pan, Nat. Commun. 5 (2014) 3519.

[9] M. Paskevicius, L. H. Jepsen, P. Schouwink, R. Cerny, D. B. Ravnsbaek, Y. Filinchuk, M. Dornheim, F. Besenbacher, Chem. Soc. Rev. 46 (2017) 1565-1634.

[10] X. Zhang, Y. Liu, K. Wang, Y. Li, M. Gao, H. Pan, ChemSusChem 8 (2015) 4180-4188.

[11] S. Deng, V. Tjoa, H. M. Fan, H. R. Tan, D. C. Sayle, M. Olivo, S. Mhaisalkar, J. Wei, C. H. Sow, J. Am. Chem. Soc. 134 (2012) 4905-4917.

[12] T. Mueller, G. Ceder, ACS Nano 4 (2010) 5647-5656.

[13] X. Zhang, Y. Liu, Y. Pang, M. Gao, H. Pan, J. Mater. Chem. A 2 (2014) 1847-1854.

[14] Y. Li, F. Fang, H. Fu, J. Qiu, Y. Song, Y. Li, D. Sun, Q. Zhang, L. Ouyang, M. Zhu, J. Mater. Chem. A 1 (2013) 5238-5246.

[15] X. Fan, X. Xiao, J. Shao, L. Zhang, S. Li, H. Ge, Q. Wang, L. Chen, Nano Energy 2 (2013) 995-1003.

[16] J. A. Teprovich, J. Zhang, H. Colón-Mercado, F. Cuevas, B. Peters, S. Greenway, R. Zidan, M. Latroche, J. Phys. Chem. C 119 (2015) 4666-4674.

[17] F. Wu, Z. Chen, B. Lei, J. Wang, K. Xie, Y. Song, D. Sun, F. Fang, Electrochim. Acta 257 (2017) 321-327.

[18] L. Silvestri, A. Paolone, L. Cirrincione, P. Stallworth, S. Greenbaum, S. Panero, S. Brutti, P. Reale, J. Electrochem. Soc. 164 (2017) A1120-A1125.

[19] L. Silvestri, M. A. Navarra, S. Brutti, P. Reale, Electrochim. Acta 253 (2017) 218-226.

[20] P. Huen, F. Peru, G. Charalambopoulou, T. A. Steriotis, T. R. Jensen, D. B. Ravnsbæk, ACS Omega 2 (2017) 1956-1967.

[21] W.-B. Li, L. Li, Q.-L. Ren, Y.-J. Wang, L.-F. Jiao, H.-T. Yuan, Rare Metals 34 (2015) 679-682.

[22] L. Li, F. Qiu, Y. Wang, Y. Wang, G. Liu, C. Yan, C. An, Y. Xu, D. Song, L. Jiao, H. Yuan, J. Mater. Chem. 22 (2012) 3127-3132.

[23] V. Stavila, R. K. Bhakta, T. M. Alam, E. H. Majzoub, M. D. Allendorf, ACS Nano 6 (2012) 9807-9817.

[24] Y. Li, G. Zhou, F. Fang, X. Yu, Q. Zhang, L. Ouyang, M. Zhu, D. Sun, Acta Mater. 59 (2011) 1829-1838.

[25] A. J. Du, S. C. Smith, G. Q. Lu, Phys. Rev. B 74 (2006) 193405.

[26] L. Xu, Q. Ge, Int. J. Hydrogen Energy 38 (2013) 3670-3680.

[27] Q. Li, P. Xu, W. Gao, S. Ma, G. Zhang, R. Cao, J. Cho, H.-L. Wang, G. Wu, Adv. Mater. 26 (2014) 1378-1386.

[28] L. Ouyang, Z. Cao, H. Wang, R. Hu, M. Zhu, J. Alloys Compd. 691 (2017) 422-435.

[29] L. Ouyang, L. Guo, W. Cai, J. Ye, R. Hu, J. Liu, L. Yang, M. Zhu, J. Mater. Chem. A 2(2014) 11280 -11285.

[30] L. Ouyang, Z. Cao, L. Li, H. Wang, J. Liu, D. Min, Y. Chen, F. Xiao, R. Tang, M. Zhu, Int. J. Hydrogen Energy 39 (2014) 12765-12772.

[31] P. Hohenberg, W. Kohn, Phys. Rev. 136 (1964) B 864-871.

[32] J. P. Perdew, Y. Wang, Phys. Rev. B 45 (1992) 13244-13249.

[33] B. Delley, J. Chem. Phys 94 (1991) 7245-7250.

[34] J. D. Pack, H. J. Monkhorst, Phys. Rev. B 16 (1977) 1748-1749.

[35] R. Wu, H. Du, Z. Wang, M. Gao, H. Pan, Y. Liu, J. Power Sources 327 (2016) 519-525.

[36] Q. Gao, G. Xia, X. Yu, Nanoscale 9 (2017) 14612-14619.

[37] W. Zeng, S. W. Buckner, P. A. Jelliss, ACS Omega 2 (2017) 2034-2040.

[38] X. Huang, X. Xiao, X. Wang, Z. Yao, C. Wang, X Fan, L Chen, Energy Storage Materials 13 (2018) 199–206.

[39] H. Zhong, L. Ouyang, J. Ye, J. Liu, H. Wang, X. Yao, Energy Storage Materials 7 (2017) 222–228.

[40] G. Xia, L. Zhang, X. Chen, Y. Huang, D. Sun, F. Fang, Z. Guo, X. Yu, Energy Storage Materials 14 (2018) 314–323.

CHAPTER 5 STUDY ON PREPARATION AND LITHIUM STORAGE PERFORMANCE OF NANO-MAGNESIUM HYDRIDE WITH CONTROLLABLE MORPHOLOGY

5.1 Introduction

With the rapid development of social economy and the significant improvement of people's environmental awareness, high-energy-density lithium-ion batteries with better cycling lives have received more and more attention in applications such as electric vehicles, consumer electronics, grid stations, and energy storage devices. [1-3] As one of the key components of lithium-ion batteries, commercial lithium-ion battery negative electrodes developed based on graphite materials are limited by their limited inherent capacity and can no longer fulfil the need for batteries with higher energy density. Therefore, there is an urgent need to develop new negative electrode materials and apply them to high-performance lithium-ion batteries. Among the many choices of negative electrodes, conversion-type anodes have been attracting much attentions resulting from their ultra-high specific capacities, compared to traditional oxides, [4] sulfides, [5] and phosphides-based [6] conversion-type anodes, the emerging magnesium hydride displays the lowest charge-discharge polarization and more favorable potential for lithium storage.

Since 2008, Oumellal et al. [7] has proposed magnesium hydride (MgH_2) as a particularly promising convention-type anode for LIBs, due to its high theoretical specific capacity around 2048 mAh g^{-1} and the thermodynamic Nernst potential for the corresponding hydride conversion reaction (HCR) process (Eq. 5.1) is ~ 0.5 V vs Li which is the lowest charge-discharge polarization of any tested conversion-type material. However, there are two main defects in the MgH_2 anode hinder its application. One is its inherent low conductivity, and the other is that repeated insertion and

extraction of lithium ions along with the cycling process in LIBs will cause drastic changes in the volume of the magnesium matrix, and even cause particle rupture and pulverization. Eventually lead to the destruction of the electrode structure. [8-10] As a result of which, two main challenges: the capactiy degragation after few cycles, and the poor cycle stability make it far from applications in the future batteries. After the first discharge, MgH_2 shows a reversible charge capacity of 1480 mAh g^{-1} and then the capacity fades rapidly and the reported capacity retention of bulk MgH_2 is generally less than 35% after 10 cycles. [11]

$$MgH_2 + 2Li^+ + 2e^- \leftrightarrow Mg + 2LiH \quad \textbf{(5.1)}$$

Although the origin of capacity fade of MgH_2 and exact mechanism of the conversion reaction are still lacking, many efforts have been made to solve these problem. Carbon doping is a widely used effective way to improve the composite conductivity, graphite [12], mesoporous carbon [13], carbon nanofiber [14], graphene [15], Mxene [16], and 3D hierarchical porous carbon materials [17] have been employed to form continuous electron-conducting paths in the composite electrodes to enhancing the electrical conductivity of the MgH_2 based composite. Zhu and co-workers [18] have compared the MgH_2 and MgH_2-C film electrode by magnetron sputtering hydrogenation treatment, and found that the MgH_2-C film has smaller crystallite size, lower polarization effect and structural stability, but exhibiting lower capacity and equally poor cyclic performance, thus the carbon addition could improve the conductivity and structural stability, not the cycle life of MgH_2 film electrode.

Additionally, most of the above issues can be effectively solved through reasonable design of microstructure of the materials such as multiple hierarchical nanostructures. Oumellal and co-workers found that reducing crystallite sizes to the nano-meter range and adding carbons to enhance electron conductivity are effective approaches to

improve capacity. This nano-structuring strategy has increased the capacity of MgH_2 anodes is up to 946 mA h g^{-1} at 100 mA g^{-1} after 100 cycles, although this is still far from the desired cycle life. Core–shell or yolk–shell structure is one of the most effective and widely used methods to maintain structure stability. The surface coating layers not only reducing the uncontrollable growth of the SEI film, but also relieving volume change during cycling. Recently, Yu's group has reported the formation of graphene supported MgH_2@PTh core-shell NPs, leading to a reversible capacity as high as 884 mAh g^{-1} at a current density of 2 A g^{-1}, but the coating effect and method still needs to be developed to meet the application requirements.[9]

Hence, nanostructures such as nanowires, nanotubes, nanobelts, nanoribbons, nanosheets, and nanoparticles have a wide range of significant applications in many fields, such as light-emitting diodes, transistors and energy storage. These nanostructures have been able to acquire their distinctive characteristics via modifications in the morphology, sizes, and shapes, through the fabrication process that involves the application of temperature, pressure, and chemicals such as catalysts and substrates. [10-14] In this thesis, we have developed a facile self-assembly method to build nanostructure of MgH_2@G composite with controllable morphology (nanofibers, nanoparticles, nanosheets) and size (8~50 nm). Nanoscale MgH_2 crystals with different sizes and morphologies grown on the GNS fabricated through adjusting the hydrogen pressure, types of solvents and synthesis atmosphere. Graphene contributed to the enhanced conductivity, and acted as structure director, on which the robust nanoarchitecture were built. [15, 16] Due to the nanostructure, the synthesized nanosized MgH_2@G with various morphologies are endowed with more active sites, shorter electrons/Li^+ transport channels and a spatially confined reaction space when it has been regarded as anode material for lithium-ion battery. [17-19] By comparing the

electrochemical performance of magnesium hydride with different morphologies, we have initially obtained the relationship between morphology and lithium storage performance. And it has been proved that nanoparticles have the highest specific capacity and the fastest lithium storage kinetics, which delivers a discharge capacity above 1000 mAh/g at 100 mA/g. However, the MgH_2@G nanosheets demonstrates worst cycling performance due to the pulverization and agglomeration of nanosheets after repeated lithiation/delithiation.

5.2 Experiment Section

5.2.1 Material Synthesis

All chemicals used in this chapter were purchased from Sigma-Aldrich and used as received without further purification. High purity hydrogen gas (99.999%) was used throughout the experiments. All material handling, weighing, loading and washing were performed in a glove box filled with high purity argon (O_2 and H_2O< 1 ppm) from Braun.

***Fabrication of nano-MgH_2*:** nano-MgH_2 was obtained from the hydrogenolysis of $(C_4H_9)_2Mg$. $(C_4H_9)_2Mg$ solution (1.7 ml) was placed in a sealed reactor vessel, and charged with 2 MPa H_2, and then the assembled vessel was heated at 220 ^oC for 10 h with a heating rate of 2 °C/min. Subsequently, the product was dried at 80 ^oC via dynamic vacuum on a Schlenk line overnight. Finally, the nano-MgH_2 was collected in the glove box.

Fabrication of MgH_2@G nanospheres: 1.7 mL $MgBu_2$ solution and 0.02 g graphene were mixed in a pressure reactor vessel with a volume of 5 mL. The vessel was ultrasonic for 1 h. The hydrogenolysis of $MgBu_2$ was then carried out at 220 °C under a hydrogen pressure of 2 MPa for 10 h, with a heating rate of 2 °C/min. Subsequently,

the product was dried at 80 ^{o}C via dynamic vacuum on a Schlenk line, leading to the formation of MgH_2@G nanospheres.

***Fabrication of MgH_2@G nanorods*:** 1.7 mL $MgBu_2$ solution and 0.02 g graphene were mixed in the same reactor vessel which filled with nitrogen. The slurry assembled vessel was mixed uniformly under ultrasonic for 1 h. The hydrogenolysis of $MgBu_2$ was then carried out at 220 °C for 10 h, with a heating rate of 2 °C/min. Subsequently, the product was dried at 80 ^{o}C via dynamic vacuum on a Schlenk line, leading to the formation of MgH_2@G nanorods.

***Fabrication of MgH_2@G nanosheets*:** 1.7 mL $MgBu_2$ solution and 0.02 g graphene were mixed in the pressure reactor vessel. For uniformly mixing, the vessel was ultrasonic for 1 h. And then, the vessel was heated at 80 ^{o}C overnight, under dynamic vacuum to remove solvent. 3 ml THF solvent was added to the vessel and mixing for 1 h with ultrasonic under a hydrogen pressure of 2 MPa. The hydrogenolysis of $MgBu_2$ was then carried out at 220 °C for 10 h, with a heating rate of 2 °C/min. Subsequently, the product was dried at 80 ^{o}C via dynamic vacuum on a Schlenk line, MgH_2@G nanosheets were obtained in the glove box.

5.2.2 Materials Characterization

Field emission scanning electron microscopy (FE-SEM, JEOL 7500FA, Tokyo, Japan) and TEM were applied for determination of morphologies of the synthesized samples. The crystal structure of samples was revealed through powder XRD. During XRD testing, the sample was covered by amorphous tapes to avoid oxidation. TG machine is connected to a mass spectrometer (MS; QIC 20).

5.2.3 Electrochemical Measurements

The composite of electrode consists of hand mixed 80 wt.% active material, 10 wt.% super carbon and 10 wt.% binder PMMA dissolved in DMF solutions. The electrolyte was made of 1 M $LiPF_6$ in EC/DMC/DEC (volumetric ratio of 1:1:1) solution. With pure lithium foil as counter electrode and Whatman glass fibre as separator, the coin-type 2025 half battery cell were assembled with all the parts above in an argon-filled glove box. In order to characterize the product after lithiation and delithiation and study the morphology of the electrodes after cycling, the cells were carefully opened in a glove box, and then the working electrodes were soaked in DEC for several hours to rinse any residual electrolyte, finally dried under vacuum at 120 ℃. The galvanostatic charge and discharge test were performed on LANHE CT2001A testing system under different constant current densities with the voltage rang of 0.01~3.0 V versus Li^+/Li. CV test was conducted on a CHI660D electrochemistry workstation at room temperature at 0.1 mV/s in the limited voltage scope from 0.01V to 3 V (vs Li^+/Li). Additionally, the EIS spectra were carried out on the same machine with a frequency rang of 100 kHz~ 0.01 Hz.

5.3 Results and Discussion

The synthesis process of MgH_2@G with various morphologies (nanospheres, nanorods and nanosheets) were illustrated in **Figure 5.1**. Based on the hydrogenolysis and decomposition of $(C_4H_9)_2Mg$ ($(C_4H_9)_2Mg \rightarrow 2C_4H_9(g) + MgH_2(g)$), different morphologies of nanosize MgH_2 crystals were uniformly dispersed on the graphene through adjusting the reaction parameters, such as the reaction atmosphere, solvent, and hydrogen pressure. Like other self-assembled nano-scale processes, [20-23] during the temperature-rise period and the process of heat preservation, the $(C_4H_9)_2Mg$ begins to

decompose, and the magnesium hydride nucleates and grows on the graphene. In this process, if the hydrogen pressure is controlled to 2 MPa, nano-spherical magnesium hydride can be obtained, if the reaction atmosphere is changed from hydrogen to nitrogen, nanorod-shaped magnesium hydride could be obtained, and if the solvent of the $(C_4H_9)_2Mg$ solution changed from the built-in n-hexane to THF, the product could be flake like. Taking advantage of the favorable adsorption energy between $(C_4H_9)_2Mg$ and graphene, [24, 25] the fabricated MgH_2 crystals could be firmly anchored on the graphene with well dispersion. Generally, graphene act as a structure director and substrate during the synthesis process, which plays a vital role on stabilizing of MgH_2 crystals against self-agglomeration and degradation during lithium storage process.

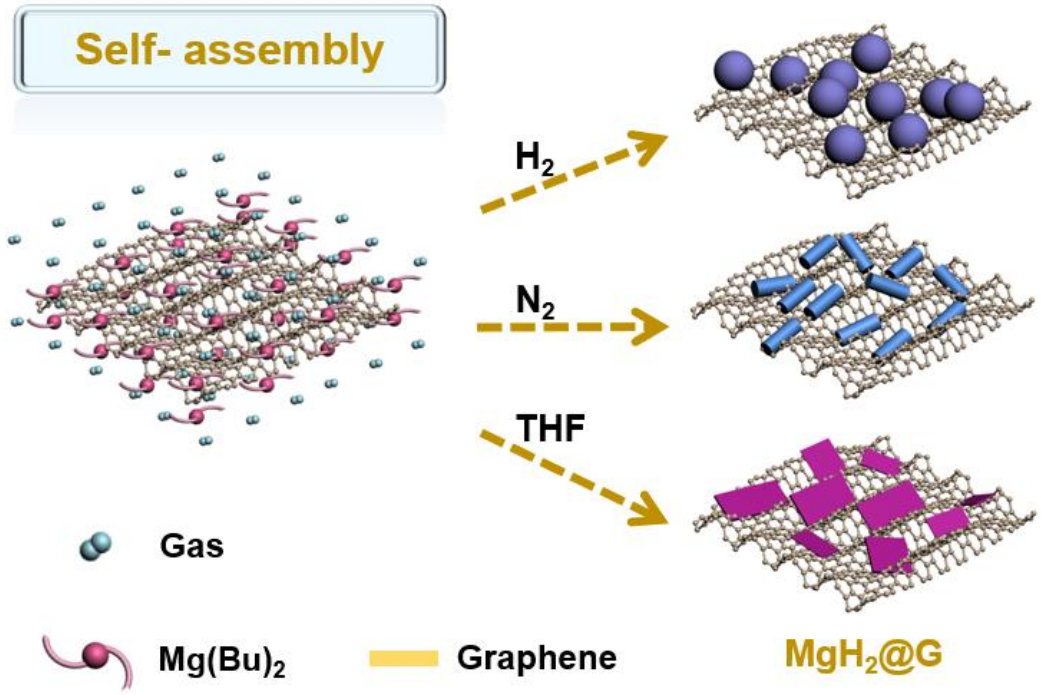

Figure 5.1 Schematic illustration of synthesis process of MgH_2@G with different morphologies (nanospheres, nanorods, and nanosheets).

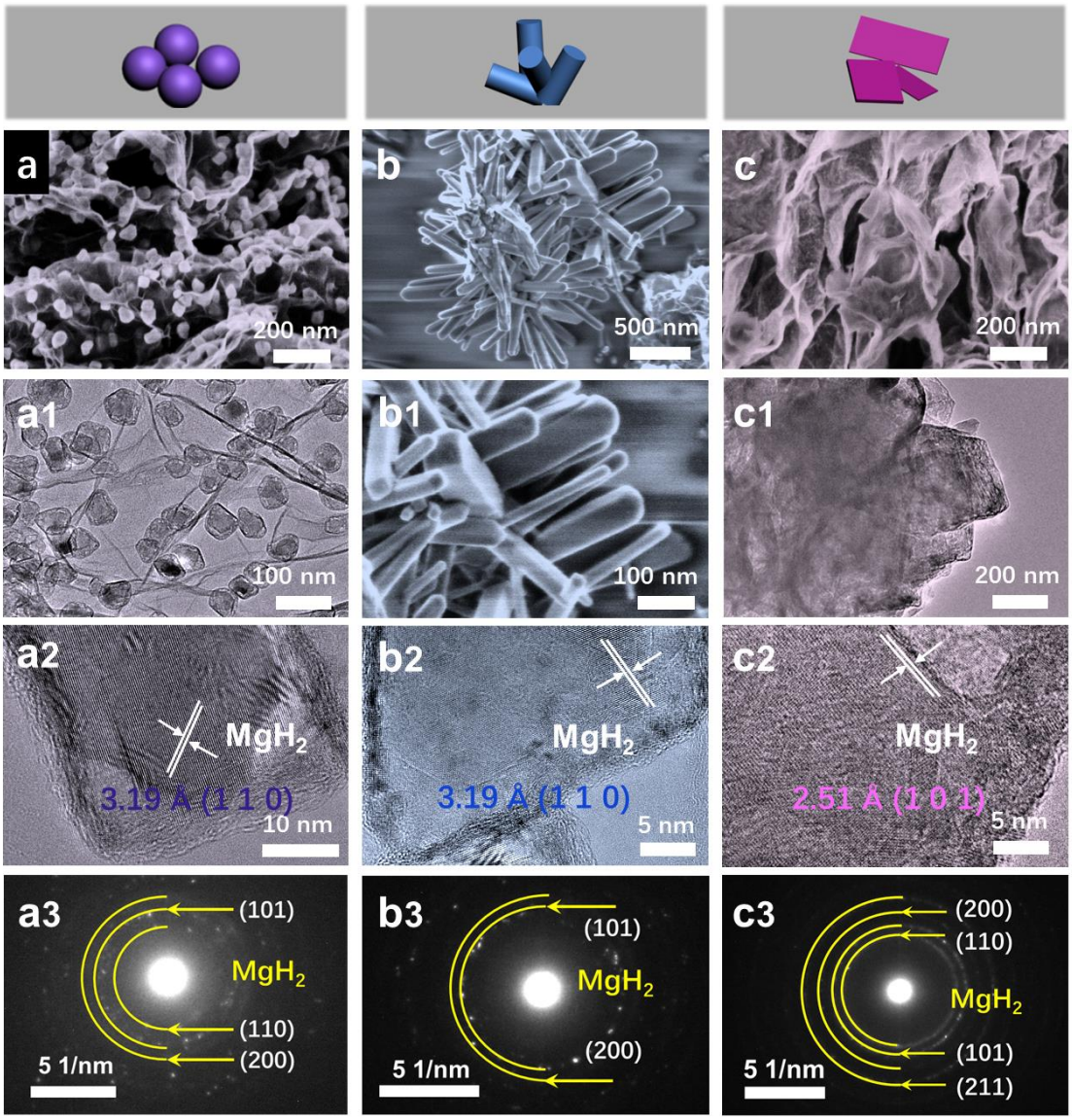

Figure 5.2 Top frame: schematic diagram of the synthesized MgH_2@G with various morphologies, purple color represents nanospheres, bule color represents nanorods and red color refers to nanosheets, and the corresponding (a-c) SEM images, (a2-c2) HRTEM images, and (a3-c3) SAED patterns. And (a1, c1) TEM images of the prepared nanospheres and nanosheets respectively, while (b1) is the SEM images of nanorods.

Figure 5.2 represents the morphological and structural characteristic of as-synthesized samples. In SEM/TEM images, the formed MgH_2@G nanospheres dispersed on graphene sheets with a diameter around 50 nm. The morphology structure

of nanocrystals is revealed through the HRTEM images, the nanospheres clearly display lattice fringes of 3.19 Å, referred to the (110) planes of MgH_2, which is also coincidence with the information come from the SEAD patterns (**Figure 5.2a3**). Simultaneously, the as synthesized nanorods were 75 nm in diameter, and the tails of rod-shaped MgH_2@G tend to gather together to form clusters, which are dispersed on graphene. According to HRTEM images, (110) planes was also observed with the measured lattice fringes of 3.19 Å. Additionally, the nanosheets of MgH_2@G are shown in **Figure 5.2c and c1-3**, the sheet shaped MgH_2 spreads out on graphene, the length and width of which could reach out 500 nm. The HRTEM images of the nanosheets demonstrate the lattice fringes of 2.51 Å, and accordingly, the SEAD patterns reveals (200), (110), (101) and (211) planes.

This synthesis method can also be used to control the size of the synthesized MgH_2 nanoparticles and the loading rate of magnesium hydride, as shown in the **Figure 5.3** below, when the loading rate of MgH_2 is limit to 60 wt.%, the size of the synthesized MgH_2 nanospheres can be controlled between 10 and 50 nanometers, (**Figure 5.3a-c)** via changing the amount of solvent added. And what's more, through adjusting the ratio of the added magnesium hydride precursor to graphene, the MgH_2 loading rates could be manipulated as well. As shown in **Figure 5.3d-f**, with the MgH_2 loading rates ranging from 45 wt.% to 75 wt.%, there is almost no change in the size of MgH_2 nanospheres, but when the loading rate of MgH_2 increased to 75 wt.%, slight agglomeration phenomenon could be observed which may be the load limit of the graphene.

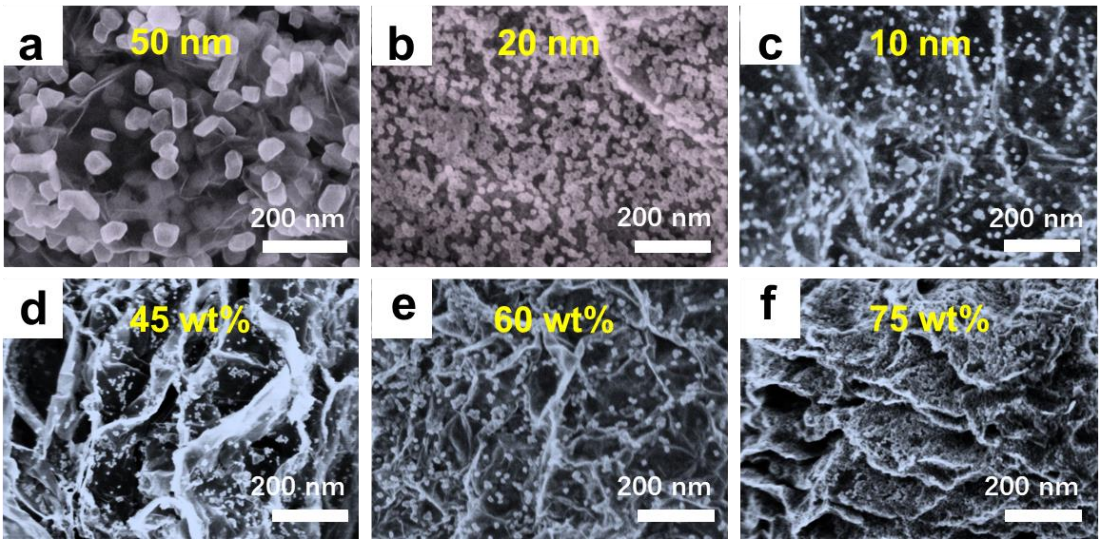

Figure 5.3 SEM images: (a-c) Morphology of the synthesized nanosphere MgH_2@G with different sizes 50 nm, 20 nm and 10 nm respectively. (d-f) Morphology of the prepared 10 nm diameter particles with different loading rates of MgH_2, 45 wt.%, 60 wt.% and 75 wt.%, respectively.

Furtherly, illustrated in **Figure 5.4,** the structure of MgH_2@G with different morphologies could be verified with the help of X-ray powder diffraction (PXRD). It could be observed that all the diffraction peaks can be matched to the tetragonal structure of β-MgH_2 (PDF 12-0697), which confirms the crystal structure of the synthesized MgH_2. As we all known, the intensity of the pattern peaks correlates to the crystallinity of the sample. It is obvious that, the high intensity and sharp peaks appears in nanorods and nanospheres MgH_2@G samples, the pattern peaks of nanosheets have the lower intensity but still obvious which may be ascribed to the thin thickness of the MgH_2 nanosheets. As the diameter of nanospheres decreases from 50 nm to 10 nm, the intensity of the diffraction peaks is also significantly reduced, when it comes to 10 nanometers, peaks are almost invisible.

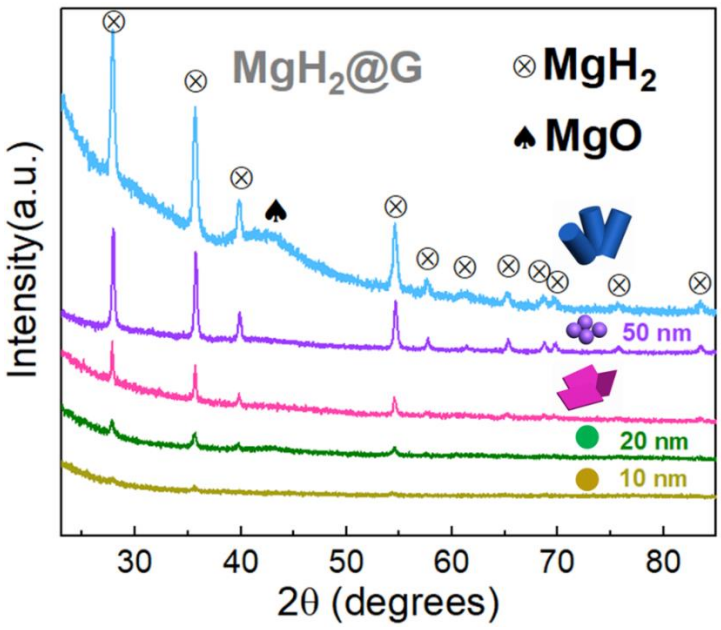

Figure 5.4 The X-ray diffraction patterns of the synthesized MgH_2@G samples: blue line represents nanorods, purple line represents nanospheres, red line refers to nanosheets, green and yellow line represents the as prepared nanospheres with diameter of 20 nm and 10 nm, respectively.

The content of MgH_2 in the composite is determined based on the maximum hydrogen desorption amount of the sample via TGA-MS. The results are presented below (**Figure 5.5**). Calculated by TG, the hydrogen release amount of the nanosized samples is all about the same with each other, which is around 4.56 wt.%. It means that, the MgH_2 loading rate of all the nanostructure composites as synthesized are 60 wt.%. In addition, as shown in MS lines, the peak temperature of hydrogen desorption in MgH_2@G nanospheres, nanorods and nanosheets are 344 ^oC, 362 ^oC and 300 ^oC, respectively. Apparently, the MgH_2@G nanosheets demonstrates the lowest hydrogen release temperature, which may be due to the smallest size in a certain dimension.

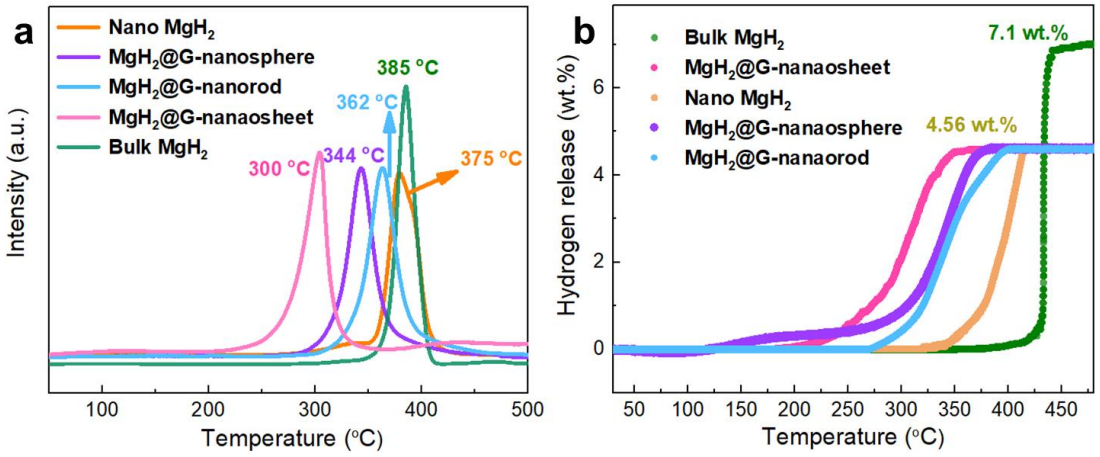

Figure 5.5 Mass spectra (a) and thermogravimetric analysis curves (b) of the as-prepared MgH_2@G samples compared with bulk MgH_2 and the nano-MgH_2 without graphene.

In the same with hydrogen storage, different structure will lead to different lithium storage performance. To appraise the electrochemical lithium storage performance of MgH_2 electrode, galvanostatic charge-discharge cycling conducted at 200 mA g^{-1}, using CR2032 coin cells with lithium foil as counter/reference electrode, as shown in **Figure 5.6**. The specific capacities in this chapter were measured by weight of active materials. As the contrast sample, nano MgH_2 electrodes displays the initial discharge capacity of 1837 mAh g^{-1}. Due to a low Coulombic efficiency of 39.7 % on first lap, the capacity fades rapidly after the first cycle, about 343 mAh g^{-1} retains in the 12th cycle. Taking advantage of outstanding conductivity of graphene, the performance of all the MgH_2@G electrodes outperform the nano MgH_2 electrodes despite of the different morphologies. The nanosheets has high discharge capacity around 1730.6 mAh g^{-1} at the first cycle, and the corrspongidng CE is 50 %. However, it also degragated fast to 414 mAh g^{-1} in 20 cycles, which may because of the pulverization tending of nanosheets and the instinct of poor conductivity of MgH_2. Since the rod-shaped structure is a one-dimensional nanostructure, which has better conductivity than a two-dimensional

lamella, it displays better performance, the capacity retains 480 mAh g^{-1} after 50 cycles, higher than that of nanosheets of 420 mAh g^{-1} of, but it is still difficult to escape the doom of capacity attenuation. After the highest initial capacity of 2181 mAh g^{-1} with a Coulombic efficiency of 44.6 %, it also faded to 546 mAh g^{-1} in 20 cycles. The capacity performance of nanospheres are most stable in the first 20 cycles for the maintained reversible capactiy of 740 mAh g^{-1}. However, it declines to 520 mAh g^{-1} after 50 cycles. Due to the fact that, the particles have the smallest size in three dimensions, so they have a shorter lithium-ion transmission path and better conductivity. Meanwhile, there is some space between particles, and support effect of graphene also makes it difficult for particles to agglomerate and grow up. Hence, MgH_2@G of nanospheres delivers the best discharge/charge performance with the highest capacity and most stable cycling. Considering the better lithium storage potential and a more easily modified morphology, spherical magnesium hydride has become the research objectives of the next chapters for this doctoral thesis.

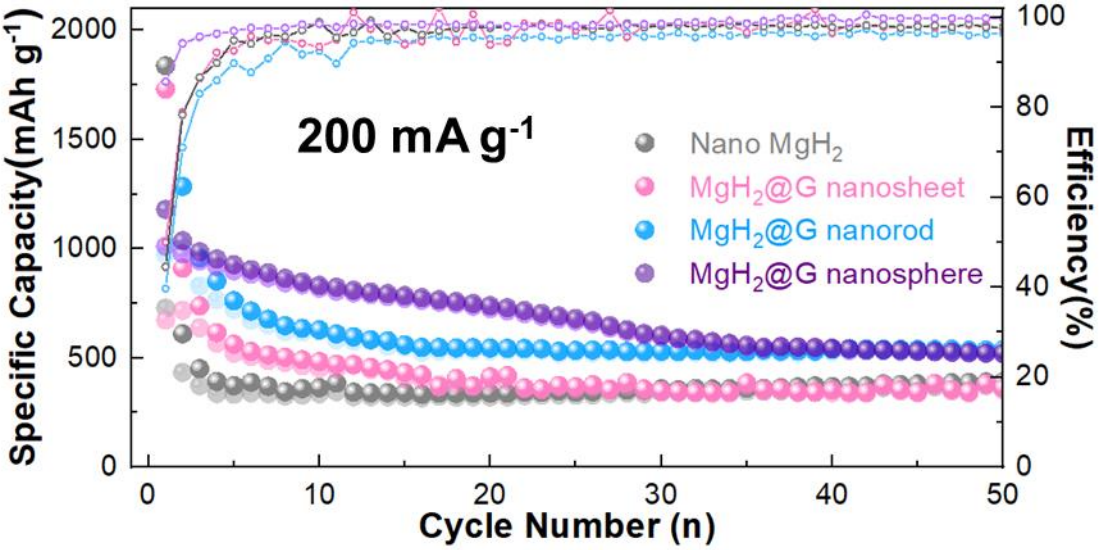

Figure 5.6 Comparison of the specific capacities of MgH_2@G samples with with bulk MgH_2 and the nano-MgH_2 without graphene at 200 mA g^{-1}.

5.4 Conclusion

To sum up, a series of magnesium hydride-graphene nanostructures with different morphologies (nanospheres, nanorods and nanosheets) were achieved through the self-assembly of MgH_2 growing uniformly on the graphene nanosheets, under the hydrogenolysis of $(C_4H_9)_2Mg$. Not only the shape, but also the size and loading ratio of MgH_2 could be precisely controlled via parameters regulation. Acted as structure director and scaffold, graphene plays a vital role in maintaining the structure stability. When regarded as an anode in lithium-ion battery, the MgH_2@G demonstrates better lithium storage performance benefiting from the graphene supported nanostrucure with better electronic conductivity, compared with the nano MgH_2. Among the different morphologies, the nanospheres delivers higher capacity utilization and more stable cycling performance (a specific capacity of 520 mAh g^{-1} at 200 mA g^{-1} after 50 cycles) than MgH_2@G nanorods and nanosheets, as a result of the higher specific surface area and more sufficient active sites. Generally, this work reports an facil synthsis strategy towards the precise construction and morphology controllable of MgH_2@G for advanced performance in LIBs. Additionally, the MgH_2@G could also serve as an attractive basic model for futher construction of more complex structures in various applications.

5.5 Reference

[1] Schmuch, R.; Wagner, R.; Horpel, G. *et al.* Performance and Cost of Materials for Lithium-Based Rechargeable Automotive Batteries. *Nat. Energy* **2018**, *3*, 267-278.

[2] Choi, J. W.; Aurbach, D. Promise and Reality of Post-Lithium-Ion Batteries with High Energy Densities. *Nat. Rev. Mater.* **2016**, *1*, 16013.

[3] Li, M.; Lu, J.; Chen, Z. W. *et al.* 30 Years of Lithium-Ion Batteries. *Adv. Mater.* **2018**, *30*, 1800561.

[4] Liu, N.; Lu, Z. D.; Zhao, J.; McDowell, M. T.; Lee, H. W; Zhao, W. T.; Cui, Y. A Pomegranate-Inspired Nanoscale Design for Large-Volume-Change Lithium Battery Anodes. *Nat. Nanotech.* **2014**, *9*, 187-192.

[5] An, W. L.; Gao, B. A.; Mei, S. X. *et al.* Scalable Synthesis of Ant-Nest-Like Bulk Porous Silicon for High-Performance Lithium-Ion Battery Anodes. *Nat. Commun.* **2019**, *10*, 1447.

[6] Jia, H. P.; Li, X. L.; Song, J. H. *et al.* Hierarchical Porous Silicon Structures with Extraordinary Mechanical Strength as High-Performance Lithium-Ion Battery Anodes. *Nat. Commun.* **2020**, *11*, 1474.

[7] Zhao, Y.; Li, X. F.; Yan, B. *et al.* Recent Developments and Understanding of Novel Mixed Transition-Metal Oxides as Anodes in Lithium-Ion Batteries. *Adv. Energy Mater.* **2016**, *6*, 1502175.

[8] Wu, L.; Zheng, J.; Wang, L. *et al.* PPy-Encapsulated SnS_2 Nanosheets Stabilized by Defects on a TiO_2 Support as a Durable Anode Material for Lithium-Ion Batteries. *Angew. Chem. Int. Ed.* **2018**, *57*, 1-6.

[9] Zhang, Y. P.; Wang, L. L.; Xu, H. *et al.* 3D Chemical Cross-Linking Structure of Black Phosphorus@CNTs Hybrid as a Promising Anode Material for Lithium-Ion Batteries. *Adv. Funct. Mater.* **2020**, *30*, 1909372.

[10] Pang, Q.; Liang, X.; Kwok, C. Y.; Nazar, L. F. Advances in Lithium–Sulfur Batteries Based on Multifunctional Cathodes and Electrolytes. Nat. Energy 2016, 1 (9), 16132.

[11] Jin, Y.; Zhu, B.; Lu, Z.; Liu, N.; Zhu, J. Challenges and Recent Progress in the Development of Si Anodes for Lithium-Ion Battery. Adv. Energy Mater. 2017, 7 (23).

[12] Li, H.-W.; Zhu, M.; Buckley, C.; Jensen, T.; Li, H.-W.; Zhu, M.; Buckley, C.; Jensen, T. R. Functional Materials Based on Metal Hydrides. Inorganics 2018, 6 (3), 91.

[13] Naguib, M.; Halim, J.; Lu, J.; Cook, K. M.; Hultman, L.; Gogotsi, Y.; Barsoum, M. W. New Two-Dimensional Niobium and Vanadium Carbides as Promising Materials for Li-Ion Batteries. J. Am. Chem. Soc. 2013, 135 (43), 15966.

[14] Anasori, B.; Lukatskaya, M. R.; Gogotsi, Y. 2D Metal Carbides and Nitrides (MXenes) for Energy Storage. Nat. Rev. Mater. 2017, 2 (2), 16098.

[15] Xu, Q.; Li, J.-Y.; Sun, J.-K.; Yin, Y.-X.; Wan, L.-J.; Guo, Y.-G. Watermelon-Inspired Si/C Microspheres with Hierarchical Buffer Structures for Densely Compacted Lithium-Ion Battery Anodes. Adv. Energy Mater. 2017, 7 (3), 1601481.

[16] Bruce, P. G.; Scrosati, B.; Tarascon, J.-M.; Bruce, P. G. Nanomaterials for Rechargeable Lithium Batteries. Angew. Chemie Int. Ed. 2008, 47, 2930.

[17] Oumellal, Y.; Zlotea, C.; Bastide, S.; Cachet-Vivier, C.; Léonel, E.; Sengmany, S.; Leroy, E.; Aymard, L.; Bonnet, J.-P.; Latroche, M. Bottom-up Preparation of MgH 2 Nanoparticles with Enhanced Cycle Life Stability during Electrochemical Conversion in Li-Ion Batteries. Nanoscale 2014, 6 (23), 14459.

[18] Li, H.-W.; Zhu, M.; Buckley, C.; Jensen, T.; Li, H.-W.; Zhu, M.; Buckley, C.; Jensen, T. R. Functional Materials Based on Metal Hydrides. Inorganics 2018, 6 (3), 91.

[19] Manthiram, A.; Yu, X.; Wang, S. Lithium Battery Chemistries Enabled by Solid-State Electrolytes. Nat. Rev. Mater. 2017, 2, 1.

[20] Yan, Y.; Li, S. B.; Yuan, B. *et al.* Flowerlike Ti-Doped MoO_3 Conductive Anode Fabricated by a Novel NiTi Dealloying Method: Greatly Enhanced Reversibility of the Conversion and Intercalation Reaction. *ACS Appl. Mater. Interfaces.* **2020**, *12*, 8240−8248.

[21] Wu, L.; Zheng, J.; Wang, L. *et al.* PPy-Encapsulated SnS_2 Nanosheets Stabilized by Defects on a TiO_2 Support as a Durable Anode Material for Lithium-Ion Batteries. *Angew. Chem. Int. Ed.* **2018**, *57*, 1-6.

[22] Oumellal, Y.; Rougier, A.; Nazri, G. A.; Tarascon, J. M.; Aymard, L. Metal Hydrides for Lithium-Ion Batteries. *Nat. Mater.* **2008**, *7*, 916-921.

[23] Deng, J. J.; Yu, X. L.; Qin, X. Y. Co-B Nanoflakes as Multifunctional Bridges in $ZnCo_2O_4$ Micro-/Nanospheres for Superior Lithium Storage with Boosted Kinetics and Stability. *Adv. Energy Mater.* **2019**, *9*, 1803612.

[24] Zhang, B. P.; Si, Y. S.; Gu, Q. F.; Chen, M.; Yu, X. B. Hydrangea-Shaped 3D Hierarchical Porous Magnesium Hydride-Carbon Framework with High-Rate Performance for Lithium Storage. *ACS Appl. Mater. Interfaces* **2019**, *11*, 28987-28995.

[25] Xia, G. L.; Tan, Y. B.; Chen, X. W.; Sun, D. L.; Guo, Z. P.; Liu, H. K.; Ouyang, Uniformly Self-Assembled on Graphene. *Adv. Mater.* **2015**, *27*, 5981-5988.

CHAPTER 6 POROUS MAGNESIUM HYDRIDE NANOPARTICLES IN-SITU DECORATED WITH MG-BASED COMPOSITES TOWARDS ADVANCED LITHIUM STORAGE PERFORMANCE

6.1 Introduction

The development of rechargeable lithium-ion batteries (LIBs) with high energy density, fast charge/discharge rate, and long cycle life has been rapidly promoted due to the urgent demand of ever-growing markets from portable electronics to grid-scale energy storage.[1-6] Consequently, tremendous efforts have been devoted to developing high-capacity anode materials for LIBs and among them, conversion-type anodes have been attracting a great deal of attention due to their high theoretical capacities.[7-12] In comparison with the traditional oxides, sulfides, and phosphides-based conversion-type anodes, the emerging magnesium hydride (MgH_2) displays the lowest charge-discharge polarization and more favourable working voltage (0.1-0.5 V vs Li^+/Li^0) for lithium storage.[13-17] More importantly, compared with the transition metal and oxygen, sulfur, or phosphorous, the much lighter molecular weights of MgH_2 leads to a theoretical specific capacity as high as 2048 mAh g^{-1}.[18-22] In spite of these attractive features, little attention has been paid to Mg-based hydrides due to multiple essential issues. The first one is the inherent poor conductivity of MgH_2, which results in low electrochemical capacity and unsatisfied rate performance. Another challenging issue for MgH_2-based electrodes is their rapid capacity fading induced by the agglomeration and even fall off and losing connection with the copper collector which induce poor electronic conductivity. The dramatic volume expansion appears along with the repeated lithium insertion and extraction process should take the responsibility. [23-26]

Nanoconfinement of MgH_2 into carbon matrix *via* physical encapsulation process, which could not only downsize the particle size to nanoscale for alleviating the volume changes but also enhance the electrical conductivity of metal hydrides, has shown potential in advancing the lithium storage performance of MgH_2-based electrodes to some extent.[18-20] Unfortunately, this strategy is severely plagued by the lack of control over the physical encapsulation process, which inevitably leads to partial agglomeration of electroactive particles, the inhomogeneous distribution, and even worse a limited loading weight owing to the massive introduction of the dead weight of carbon matrix, resulting in a low systematic capacity.[23, 27] To solve these issues, our group have developed a hydrogenation-induced solvothermal assembly method to realize the uniform distribution of MgH_2 nanoparticles (NPs) with high loading capacity on the electrically conductive graphene, which also could effectively facilitate the conductivity of the MgH_2 anode.[28] Subsequently, a core-shell protective strategy *via* the coating of polythiophene films on MgH_2 NPs has been further developed for physically alleviating the volume change of metal hydrides upon cycling charge and discharge process.[29] Despite these progresses, induced by the slow transfer of lithium ions into active MgH_2 owing to the low lithium ion conductivity of polythiophene films and the lack of void space for effectively mitigating the volume change of MgH_2, which results in the serious cracking of the shells upon cycling lithiation and delithiation process, the lithium storage performance of MgH_2 still falls short in systematic rate capabilities and cycling stability for practical applications. Furthermore, the hydrogenation-induced self-assembly process, as well as the subsequent synthesis of polythiophene films, involves the use of massive organic solvent, which has high economic and environmental cost.

To overcome these shortcomings, herein we report a facile solvent-free strategy to fabricate yolk-shell-like structure, *i.e.*, porous MgH_2 NPs coated with Mg-based composites (including MgS, $Mg(NH_2)_2$, and $Mg(BH_4)_2$) using an *in-situ* solid-gas reaction strategy.[30, 31] First, by virtue of the favourable adsorption of dibutyl-magnesium on graphene, a solvent-free strategy using the self-decomposition of dibutyl-magnesium was adopted to fabricate homogeneous MgH_2 nanoparticles which is about 50 nm in average uniformly distributed on graphene, which would effectively contribute to the enhancement of electronic conductivity of the whole electrode.[32] Subsequently, taking advantage of the inherent high chemical reactivity of MgH_2 NPs, a homogeneous shell composed of Mg-based composites are *in-situ* built on the surface of MgH_2 NPs *via* a series of solid-gas reactions using MgH_2 as both the reactant and the structural template. Interestingly, due to the Kirkendall effect upon the uniform formation of Mg-based composites, the original MgH_2 NPs inside break up into smaller clusters, beneficial for the construction of porous structure with void spaces under the physical protection of Mg-based composites, which essentially accommodates the volume expansion of MgH_2 NPs during cycling charge-discharge process. Besides, density functional theory (DFT) calculations demonstrate that, among all these Mg-based composites, $Mg(BH_4)_2$ is theoretically verified to be an effective Li-ion conductor, which contributes to the most effective effect on improving the lithium storage performance of MgH_2. Taking advantage of the synergistic improvement on electronical and ionic conductivity, the as-formed MgH_2@$Mg(BH_4)_2$/G (MHG@MBH) exhibits a stable and high capability around 1651 mAh g^{-1} at 200 mA g^{-1} even after 380 cycles.

6.2 Experimental Section

6.2.1 Material Synthesis

High purity hydrogen gas (99.999%) was used throughout the experiments. All material handling, weighing, loading and washing were performed in a glove box which is filled with high purity argon (O_2 and H_2O< 1 ppm) from Mikrouna.

Fabrication of MHG nanostructures: MgH_2 were synthesized via the hydrogenolysis of $(C_4H_9)_2Mg$. 1.6 mL $MgBu_2$ solution and 0.02 g graphene were mixed in a pressure reactor vessel with a volume of 5 mL. The vessel was stirred for 1 h with ultrasonic stirring. The hydrogenolysis of $MgBu_2$ was then carried out at 200 °C under a hydrogen pressure of 2 atm for 20 h, with a heating rate of 2 °C/min. Subsequently, the product was dried at room temperature via dynamic vacuum on a Schlenk line, leading to the formation of MHG.

***Fabrication of MHG@MBH nanostructures*:** Firstly, $Zn(BH_4)_2$ was used as a B_2H_6 source, which was synthesized through the reaction between $ZnCl_2$ and $LiBH_4$ with a molar ratio of 1:2 via ball milling at 300 rpm for 2 h. Secondly, 0.02 g of the prepared $Zn(BH_4)_2$ and MHG were placed in two different crucibles which was put into a sealed reactor vessel. The temperature is maintained at 120 ^oC and the heat treatment lasted for 24 h, $Zn(BH_4)_2$ decomposed and produced B_2H_6/H_2, and the B_2H_6 reacting with MgH_2 to form $Mg(BH_4)_2$ simultaneously. After which, the obtained MHG@MBH was collected in glove box fille with Ar.

***Fabrication of MHG@MS nanostructures*:** 0.032 g sulfur and 0.088 g MHG were mixed in a crucible which was sealed in a reactor vessel. During heat treatment at 360 ^oC for 2 h, S powder reacting with MgH_2 to form MgS. After reaction, MHG@MS was collected in a glove box.

***Fabrication of MHG@MNH nanostructures*:** MHG was placed in a sealed reactor vessel, and charged with 0.6 MPa NH_3, and the NH_3 reacting with MgH_2 to form $Mg(NH_2)_2$, during heat treatment at 200 ^oC for 24 h, the NH_3 reacting with partial MgH_2 to form $Mg(NH_2)_2$ After reaction, the MHG@MBH was obtained.

6.2.2 Materials Characterization

The definition of phase composition of MHG@MBH electrode was conducted by XRD, Raman and FT-IR. In order to avoid oxidation, all the samples were covered with amorphous tapes, in order to avoid oxidation. The morphology and microstructure on the surface of the samples was revealed by FE-SEM and TEM. The measurement of the content of MgH_2 in the composite was conducted in a dynamic argon gas flowing through the TG connecting with a mass spectrometer.

6.2.3 Electrochemical Measurements

The electrode composite consists of hand mixed active material, super carbon and binder PMMA which is dissolved in DMF solutions as a weight rate of 8:1:1. The electrolyte was made of 1 M $LiPF_6$ in EC/DMC/DEC (volumetric ratio of 1:1:1) solution. With pure lithium foil as counter electrode and Whatman glass fibre as separator, the coin-type 2025 half battery cell were assembled with all the parts above. In order to characterize the product after lithiation and delithiation and study the morphology of the electrodes after certain cycles, the active materials are collected through shaving from collectors after cell opening, all the process is conducted in a glove box, and then the working electrodes were soaked in DEC for several hours to rinse any residual electrolyte, finally dried under vacuum at 120 ℃. The galvanostatic cycling test were performed with LANHE CT2001A under different constant current densities with the voltage ranging from 0.01 V to 3.0 V versus Li^+/Li. CV test was

conducted through a CHI660D electrochemistry workstation at room temperature. The rate of scanning is 0.1 mV/s and the voltage ranges from 0.01 V to 3 V (vs Li^+/Li). Additionally, the EIS spectra were carried out on the same machine with a frequency rang of 100 kHz~ 0.01 Hz.

6.2.4 Theoretical Calculations

Computational Method: DFT calculations were conducted by usage of projector-augmented wave (PAW) method as implemented in Vienna ab initio simulation package (VASP) [33, 34, 35]. In order to introduce the exchange-correlation interaction, a generalized gradient approximation (GGA) of Perdew-Burke-Ernzerhof (PBE) functional was employed [36]. All calculations employed an energy cut off at 500 eV and same density k-points mesh. Until the forces and total energy on all atoms were converged to less than 0.05 eV $Å^{-1}$ and 1×10^{-5} eV, the calculated structures were relaxed. The climbing-image nudged elastic band (CI-NEB) method was used to simulate Li migration in $Mg(BH_4)_2$ and $Mg(NH_2)_2$ [37, 38,39].

To evaluate the complexity of Li intercalation, the formation energy (E_f) was calculated for every Li intercalated compound. E_f represents the energy difference of the Lithium ions insertion state and Lithium ions extraction state,

$$E_f = E_{Total} - E_{Li} - E_{host}$$

where E_{host} and E_{Total} are the total energy of compound before and after Li intercalated, respectively. E_{Li} is the energy per atom for the bulk Li. Therefore, a lower value of E_f indicates an easier Li intercalation process.

6.3 Results and Discussion

The fabrication of porous MgH_2 NPs decorated with Mg-based composites is presented in **Figure 6.1**. Firstly, graphene-supported MgH_2 NPs were fabricated

through a solvent-free hydrogenation-induced decomposition of $(C_4H_9)_2Mg$ according to our previous work.[32] Taking advantage of the advantageous adsorption energy between $(C_4H_9)_2Mg$ and GNs, the size of the thus-formed MgH_2 NPs is 50 nm averagely could be closed linked on the GNs with well distribution (**Figure 6.2 and 6.3**), which was subsequently adopted as the nanoreactor to support *in-situ* solid-gas reaction between MgH_2 nanoparticles and precursor gas (B_2H_6, NH_3, S). The graphene with flexible and porous structure could not only act as the structural support to inhibit the aggregation and growth of MgH_2 NPs, but also offer facile tunnels for the transportation of gases to facilitate the uniform reaction with MgH_2 NPs [28]. Based on this methodology, a series of Mg-based composites (MHG@MgX (X=BH_4, S, NH_2)) are *in-situ* coated on the surface of MgH_2 NPs distributed on graphene, including MgH_2@$Mg(BH_4)_2$/G (denoted as MHG@MBH), MgH_2@MgS/G (denoted as MHG@MS), and MgH_2@$Mg(NH_2)_2$/G (denoted as MHG@MNH) (**Figure 6.4-6.6)**.

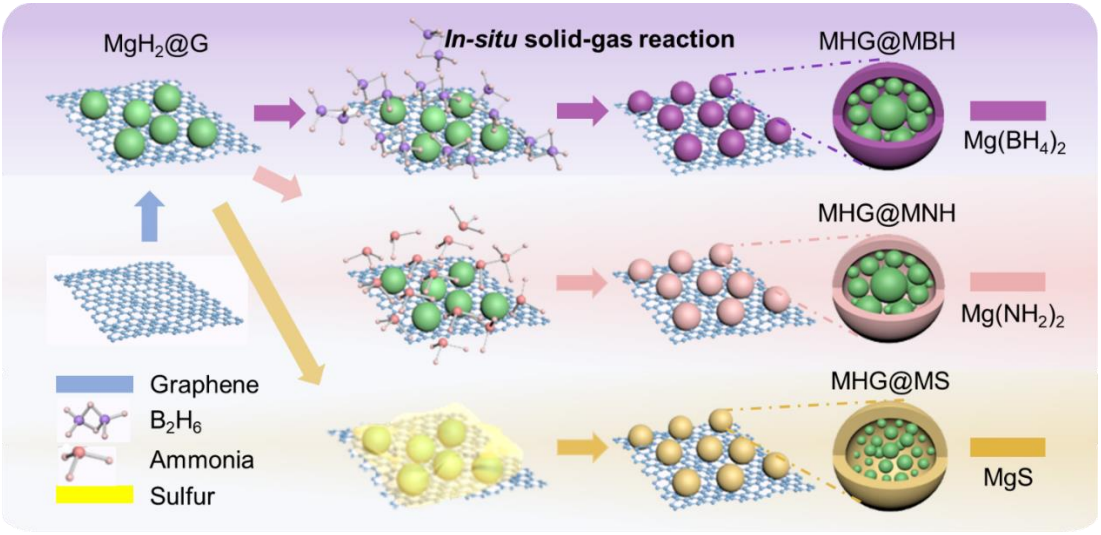

Figure 6.1 Synthetic schematic of MHG@MBH, MHG@MNH, and MHG@MS.

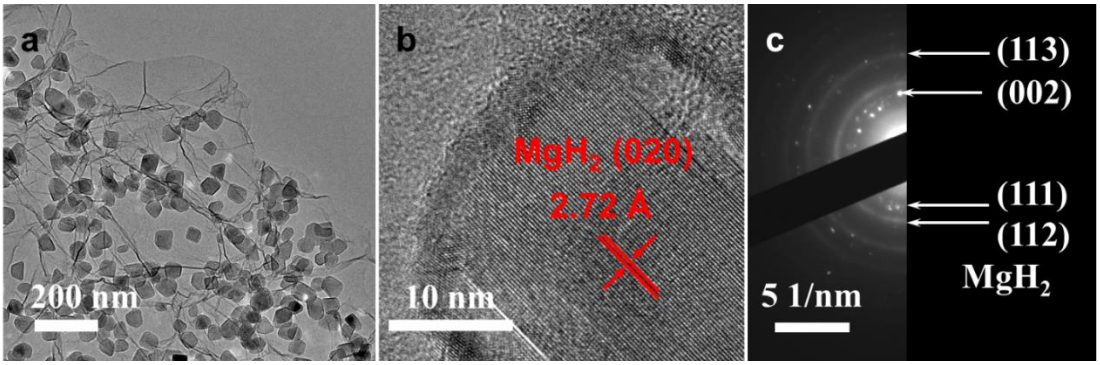

Figure 6.2 (a) TEM and (b) HRTEM images of as-prepared MHG, and (c) the corresponding selected area electron diffraction (SAED) pattern.

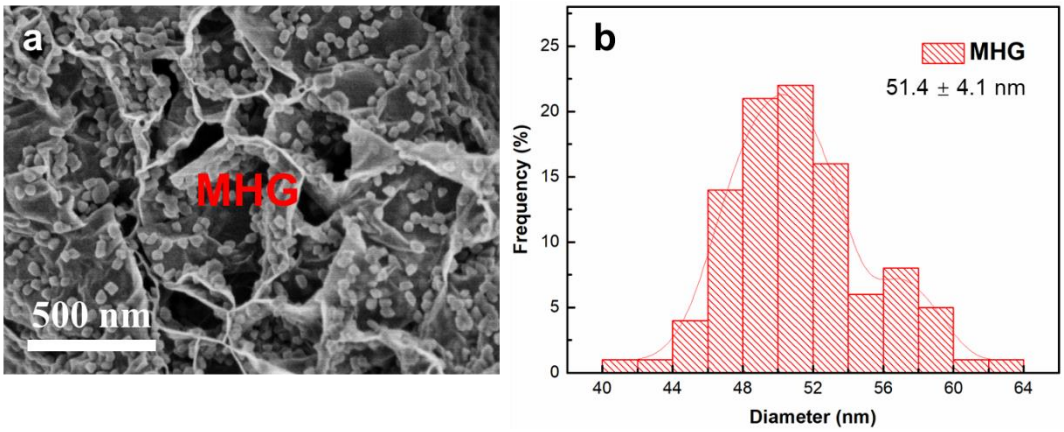

Figure 6.3 The morphology structure characterization of MHG: (a) SEM image and (b) the corresponding particle size distribution.

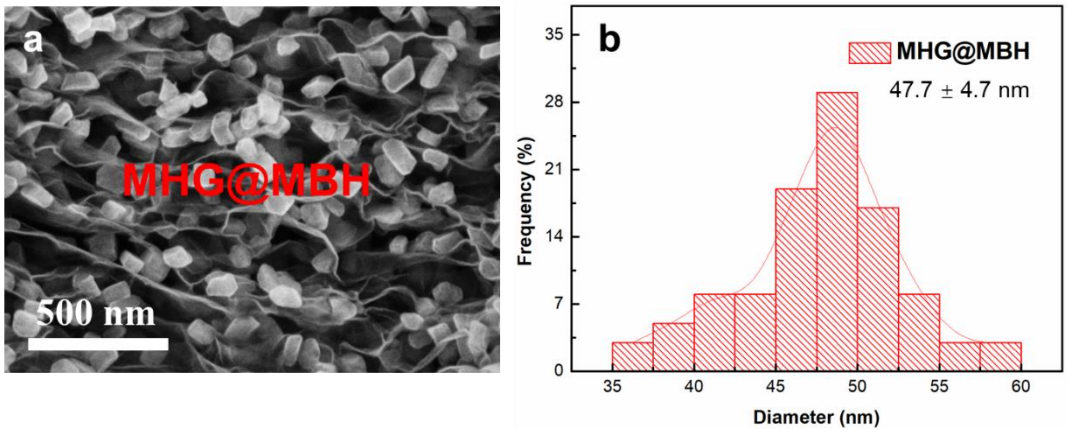

Figure 6.4 The morphology structure characterization of MHG@MBH: (a) SEM image and (b) the corresponding particle size distribution.

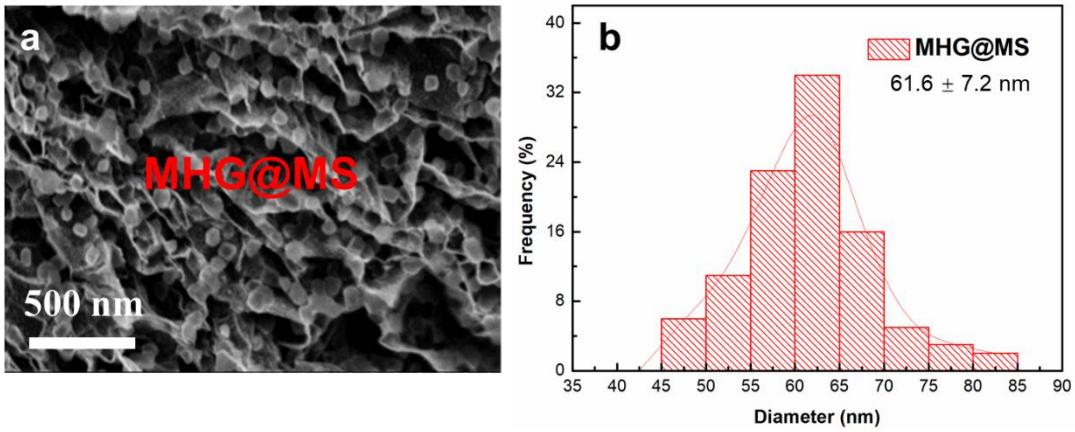

Figure 6.5 The morphology structure characterization of MHG@MS: (a) SEM image and (b) the corresponding particle size distribution.

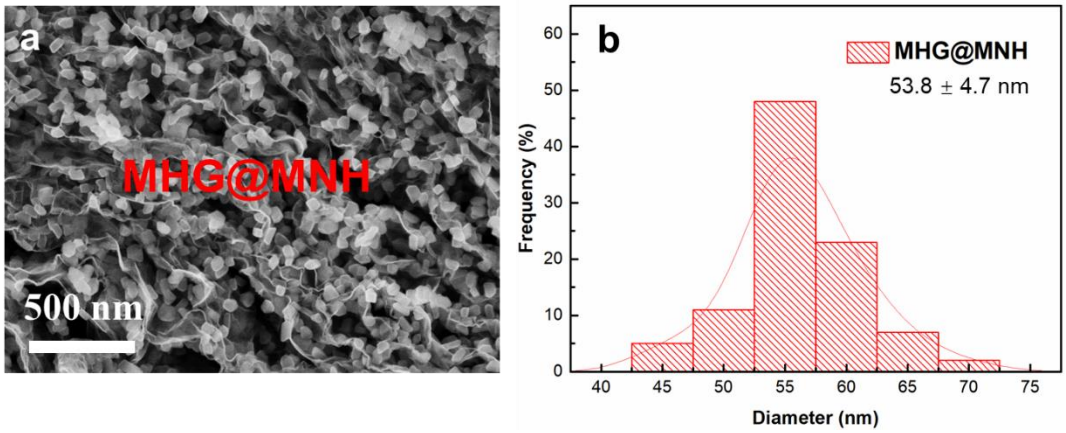

Figure 6.6 The morphology structure characterization of MHG@MNH: (a) SEM image and (b) the corresponding particle size distribution.

As shown in **Figure 6.7a and b**, the morphology of MgH_2 NPs and their homogeneous distribution on graphene could be well preserved after the *in-situ* solid-gas reaction owing to the graphene which acting as a structural support. Specifically, after the *in-situ* reaction, a uniform shell of $Mg(BH_4)_2$ with an average thickness of only 2 nm was formed on the surface of MgH_2 NPs and could be easily controlled by tuning the reaction time and the amount of reactants (**Figure 6.7e and f**). Moreover, characteristic lattice fringes of 2.13 and 2.86 Å, represents the (122) and (021) planes of the patterns of $Mg(BH_4)_2$, respectively, could be clearly observed on the surface of

MgH_2 NPs, indicating the successful formation of $Mg(BH_4)_2$ as a result of the MgH_2 NPs reacting with B_2H_6. More interestingly, scanning TEM images (**Figure 6.7c and d**) validate that, accompanied with the formation of $Mg(BH_4)_2$, original MgH_2 NPs break up into several smaller nanoparticles, which could be attributed to the Kirkendall effect induced by the different diffusion rates of Mg and B-containing species during the solid-gas reaction, inducing the simultaneous synthesis of $Mg(BH_4)_2$ as the shell and the porous structure of MgH_2 inside.[40] The void spaces between different MgH_2 crystals inside the shell provide extra spaces for accommodating the volume expansion of MgH_2 NPs during the cycling charge-discharge process. In addition, abundant spaces are present between individual MHG@MBH NPs uniformly distributed on graphene, which could further buffer the volume variation and avoid agglomeration of electroactive MgH_2 NPs, coupled with the porous structure constructed by the flexible graphene, greatly shorten the diffusion channel and accelerate the diffusion rate of electrons and lithium ions through the electrode composite. Obviously observed in elemental line-scan profile (**Figure 6.7g**), the containing of B element belonging to $Mg(BH_4)_2$ in the fringe of MgH_2 NPs is lower than that in the center area, indicating the formation of $Mg(BH_4)_2$ on the surface of MgH_2 NPs, fatherly proved The yolk-shell-like structure of MHG@MBH. Furthermore, as shown in the elemental mapping images of Mg, B, and C elements, the B comes from $Mg(BH_4)_2$ separated uniformly outside the MgH_2 NPs which provide more evidences for the define of the yolk-shell-like structure of MgH_2@$Mg(BH_4)_2$ throughout the graphene (**Figure 6.7h-l**), which could largely promote the electronic conductivity of the whole electrodes.

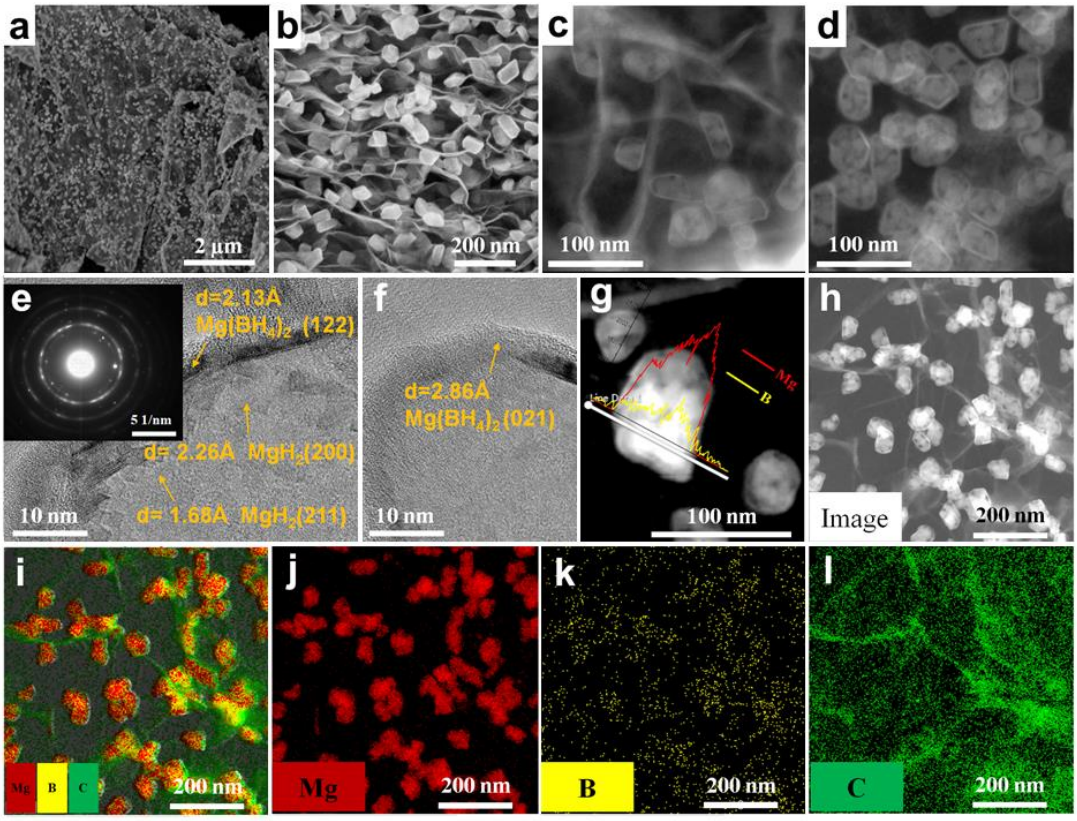

Figure 6.7 (a, b) SEM, (c, d) STEM, and (e, f) HRTEM images of MHG@MBH. (g) EDS line-scan profiles of MHG@MBH (route marked by white line). (h-l) Elemental mapping images of MHG@MBH.

Upon the adopting of MgH_2/G as the nanoreactor to react with NH_3 and S, comparable yolk-shell-like structure, composed of porous MgH_2 NPs as the core and MgS and $Mg(NH_2)_2$ as the shell, could be observed for the as-synthesized MHG@MS and MHG@MNH, respectively. As illustrated in **Figure 6.8 and 6.9**, the uniform decoration of MgS and $Mg(NH_2)_2$ shells on the surface of MgH_2 NPs homogeneously distributed on graphene could be clearly verified by the corresponding HRTEM images, the elemental line-scan profile and the elemental mapping results of MHG@MS and MHG@MNH, respectively. XRD patterns (**Figure 6.10**) demonstrate that, after *in-situ* reaction, all the diffraction peaks of MgH_2 become weaker in comparison with pure MHG, which could be attributed to the consumption of MgH_2 NPs due to the formation

of Mg-containing species as the shells. Particularly, the formation of $Mg(BH_4)_2$ in MHG@MBH, MgS in MHG@MS could be directly demonstrated by the presence of their characteristic peaks in the respective XRD patterns while no detectable diffraction patterns of $Mg(NH_2)_2$ have been detected for the MHG@MNH composite which may due to its poor crystallinity. Therefore, Fourier-transform infrared (FTIR) spectra (**Figure 6.11**) and Raman spectra (**Figure 6.12**) were subsequently conducted to characterize the chemical composition of the thus-formed Mg-based composites. It could be observed that, after the solid-gas reaction, the characteristic peaks of B-H bonds of $Mg(BH_4)_2$, N-H bonds of $Mg(NH_2)_2$, and Mg-S bonds of MgS are clearly detected by both FTIR and Raman spectra of MHG@MBH, MHG@MNH, and MHG@MS, respectively, which are strong proofs of the formation of $Mg(BH_4)_2$, $Mg(NH_2)_2$, and MgS. [41-44] Moreover, around 1338 and 1600 cm^{-1} there are two broad peaks observed in the Raman spectra of all the as-synthesized composites could be indexed to the typical D and G bands of graphene. [45] Tested by thermogravimetric analysis (TGA) and mass spectrometer (MS), the loading ratio of MgH_2 in the MHG composite, $Mg(BH_4)_2$ in the MHG@MBH composite, MgS in the MHG@MS composite and $Mg(NH_2)_2$ in the MHG@MNH composite were 60 wt.%, 7 wt.%, 12.5 wt.% and 12.5 wt.%, respectively. (**Figure 6.13 and 6.14**).

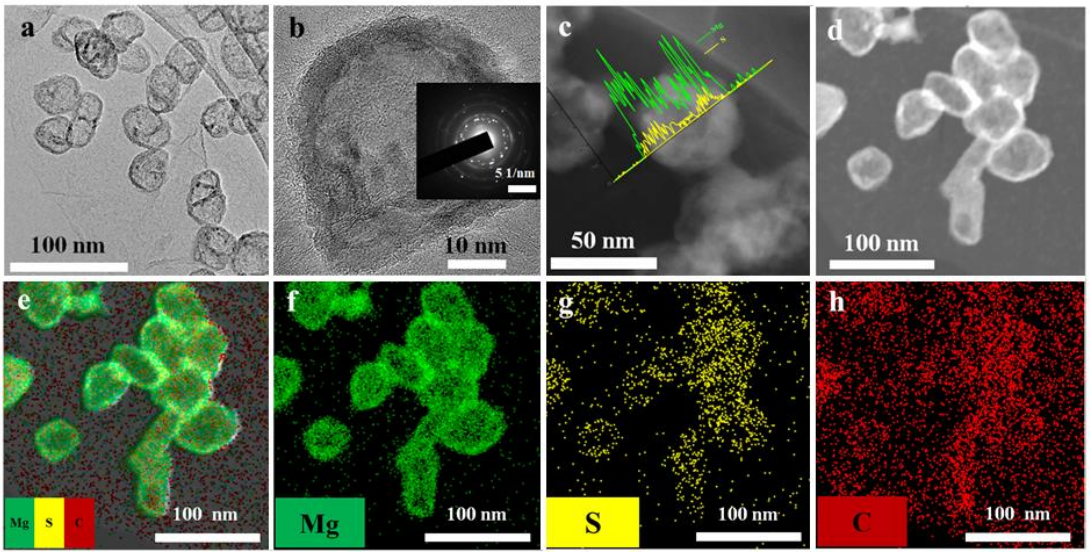

Figure 6.8 (a) TEM and (b) HRTEM images of MHG@MS. (c) EDS line-scan profiles of MHG@MS. (d-h) Elemental mapping images of MHG@MS.

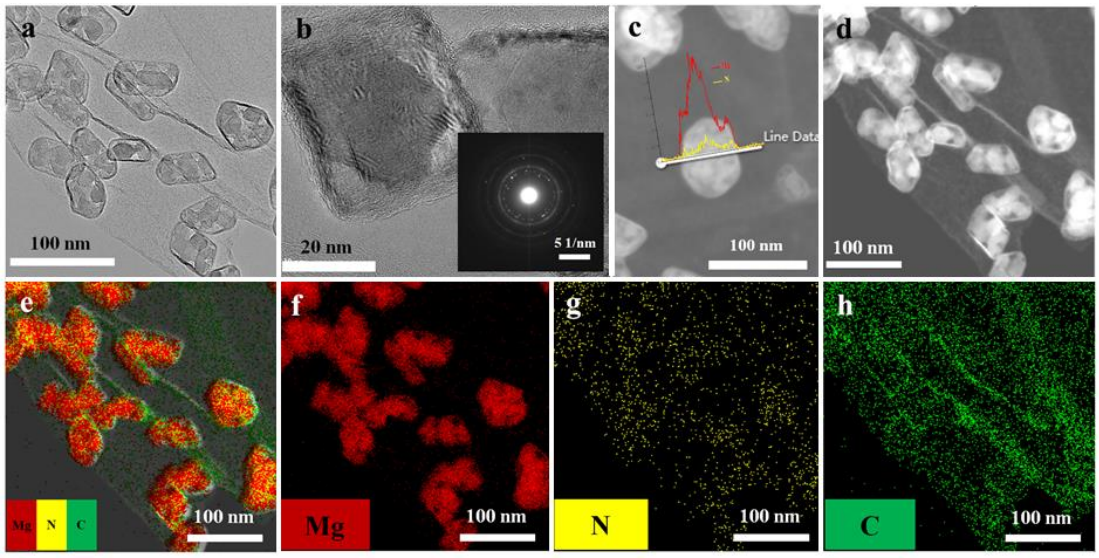

Figure 6.9 (a) TEM and (b) HRTEM images of MHG@MNH. (c) EDS line-scan profiles of MHG@MNH (route marked by white line). (d-h) Elemental mapping images of MHG@MNH.

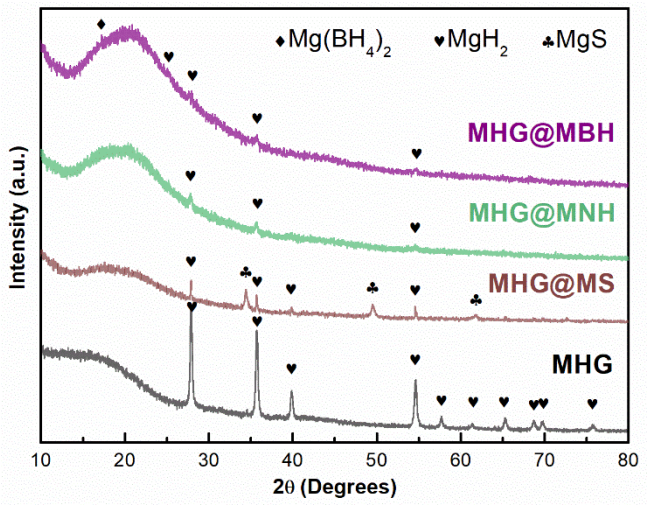

Figure 6.10 XRD patterns of the as-synthesized MHG@MBH, MHG@MNH, MHG@MS, and MHG.

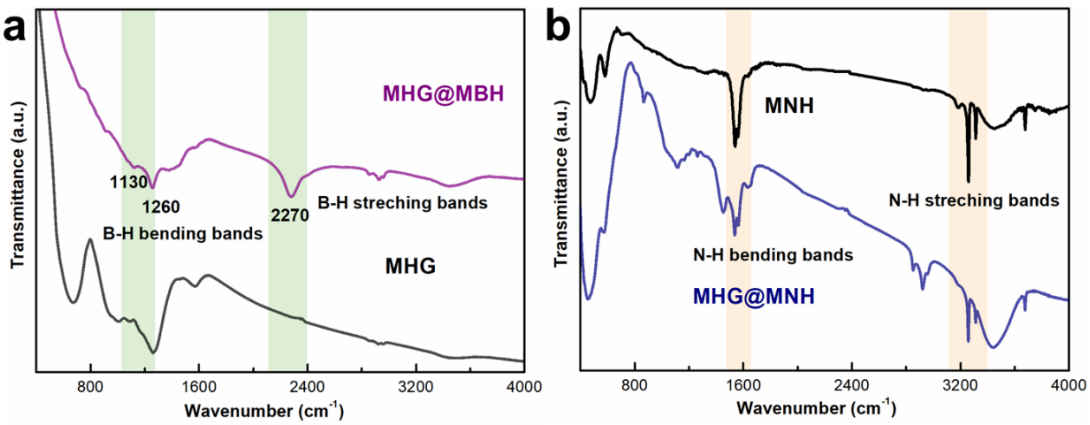

Figure 6.11 FTIR spectra of (a) MHG@MBH and (b) MHG@MNH.

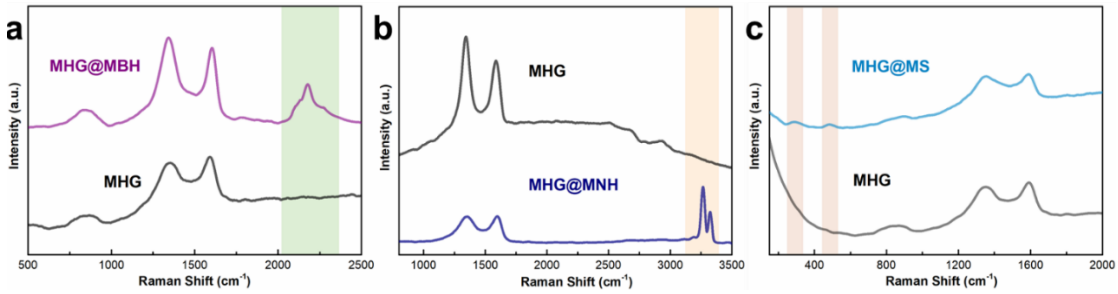

Figure 6.12 Raman spectra of as-prepared (a) MHG@MBH, (b) MHG@MNH, and (c) MHG@MS.

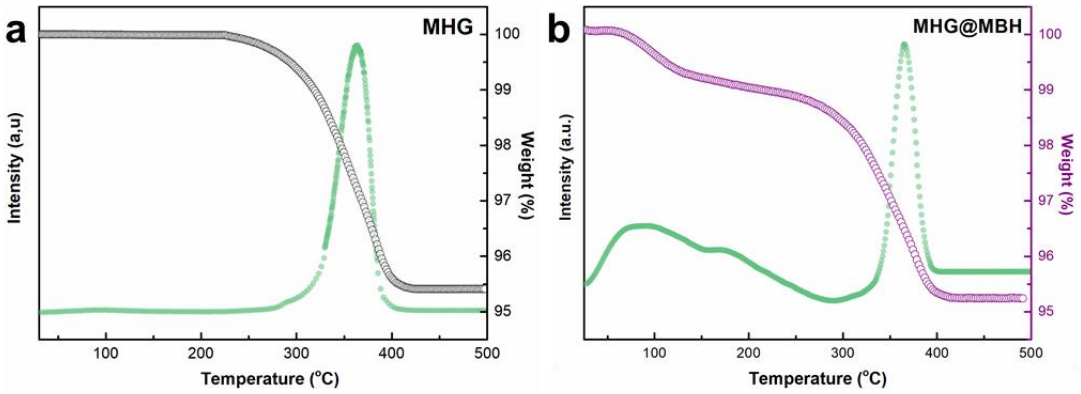

Figure 6.13 Thermogravimetric analysis and mass spectra curves of the as-prepared (a) MHG and (b) MHG@MBH.

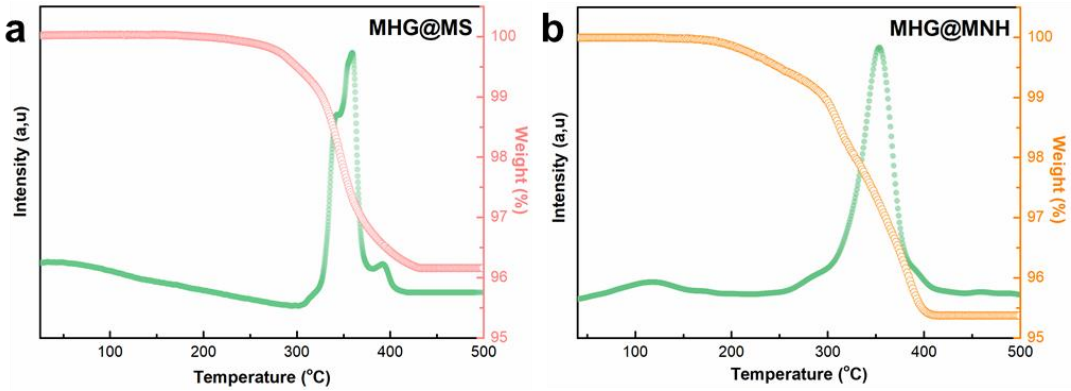

Figure 6.14 Thermogravimetric analysis and mass spectra curves of the as-prepared (a) MHG@MS and (b) MHG@MNH.

To evaluate the effect of *in-situ* decoration of Mg-based composites as the shells on improving the lithium storage performance of MgH_2, the charge-discharge performance of the as-synthesized MHG@MBH, MHG@MS, and MHG@MNH electrodes were first investigated at a current density of 200 mA g^{-1}, with pure MHG included for comparison. As shown in **Figure 6.15a**, although an initial charge capacity of 1298 mAh g^{-1} could be achieved for pure MHG, which is much higher than bulk MgH_2 or the nanoconfined MgH_2 NPs reported previously due to the structural support role of graphene with excellent electrical conductivity [25], the reversible capacity rapidly faded

to only 350 mAh g^{-1} after 30 cycles of lithiation and delithiation process induced by the large volume change. It should be noted that all specific capacities in this work are calculated based on the weight of MgH_2. In strong contrast, after *in-situ* coating of Mg-based composites as the shell, both the specific capacity and the cycling stability of MHG electrode are significantly improved. Among them, the MHG@MBH electrode exhibits highest specific capacity at first cycle, which is 1454.6 mAh g^{-1}, higher than the corresponding capacity of both MHG@MS (1186.4 mAh g^{-1}) and MHG@MNH (1195 mAh g^{-1}). More importantly, a reversible capability around 1629.4 mAh g^{-1} could be maintained for the MHG@MBH electrode even after 380 cycles with a Coulombic efficiency of approximately 99.1%, while this value is gradually decreased to be around 561 and 523 mAh g^{-1} for MHG@MS and MHG@MNH electrodes after only 200 cycles, respectively, which is comparable with pure MHG electrode.

Concluded from the above, the coating shell of Mg-based composites, especially $Mg(BH_4)_2$, could effectively enhance the cycling stability of MgH_2 and more importantly, considering their comparable structures, $Mg(BH_4)_2$ has significant impact on unlocking lithium performance of electrode MgH_2. Hence, to understand the role of Mg-based composites during the lithium storage process, the morphology and microstructures of various electrodes after 100 cycles under 200 mA g^{-1} was systematically investigated using SEM, TEM measurement and the corresponding elemental mapping (**Figure 6.15b-i**). It reveals that, after 100 cycles, MgH_2 NPs of pure MHG exhibit serious aggregation and collapse owing to the big volume expansion of MgH_2 and the lack of the physical protection upon cycling process, which corresponds well with its fast decay of specific capacities. By comparison, under the identical condition, the uniform dispersibility of MgH_2 NPs anchored on graphene could be preserved to a large extent in MHG electrodes by virtue of the coating with Mg-based

composites due to the formation of yolk-shell-like structures, which confirms that the coating of Mg-based composites could buffer the volume expansion of MgH_2 electrode upon cycling process.

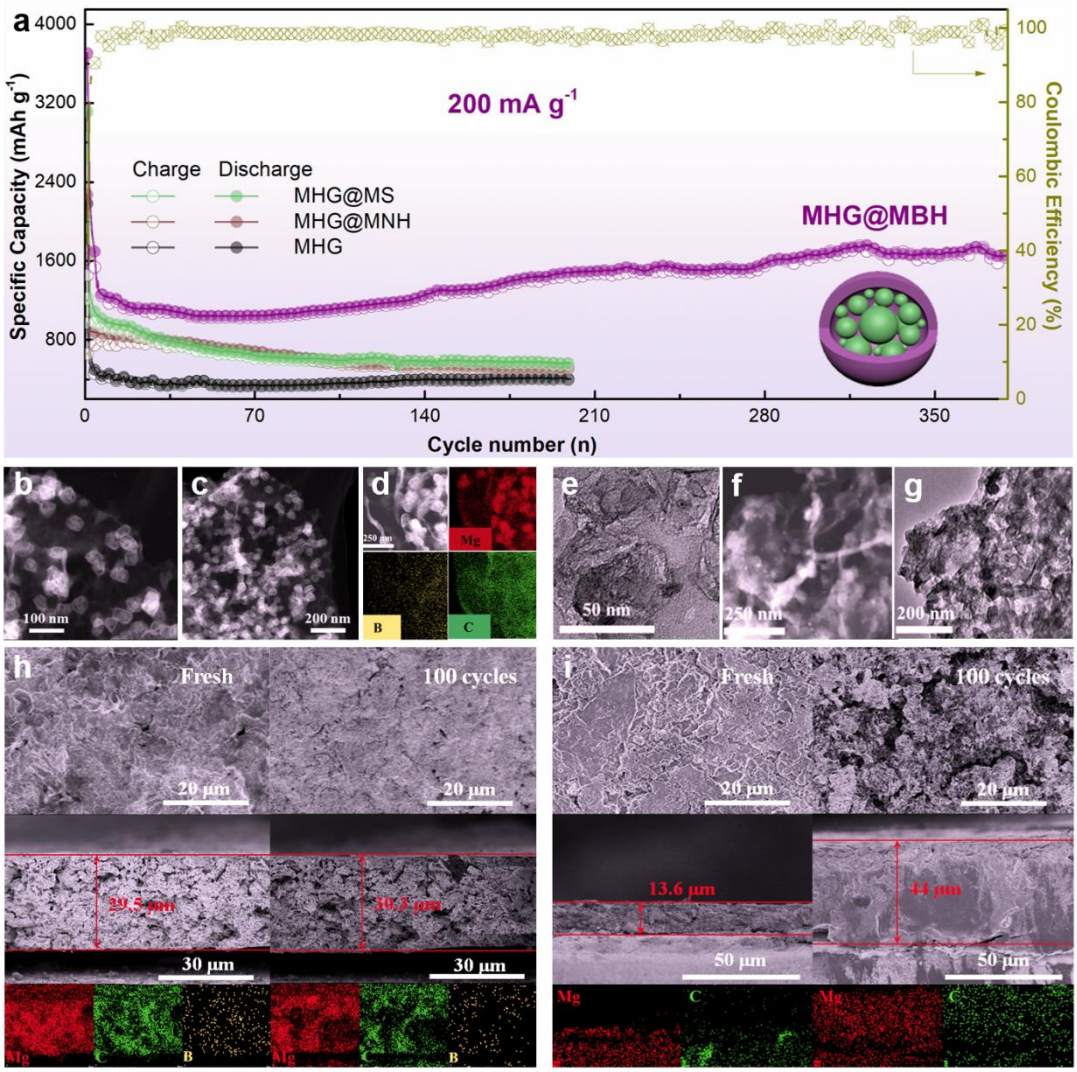

Figure 6.15 (a) Cycling performance of MHG@MBH, MHG@MS, MHG@MNH, and MHG electrodes at 200 mA g^{-1}. (b, c) STEM images of MHG@MBH in the charged state after 100 cycles at 200 mA g^{-1}. (d) Elemental mapping images of MHG@MBH in the charged state after 100 cycles. (e-g) TEM images of MHG in the charged state after 100 cycles at 200 mA g^{-1}. Top-view, cross-sectional SEM images, and the corresponding elemental mapping of (h) MHG@MBH, and (i) MHG electrode before and after 100 cycles at 200 mA g^{-1}.

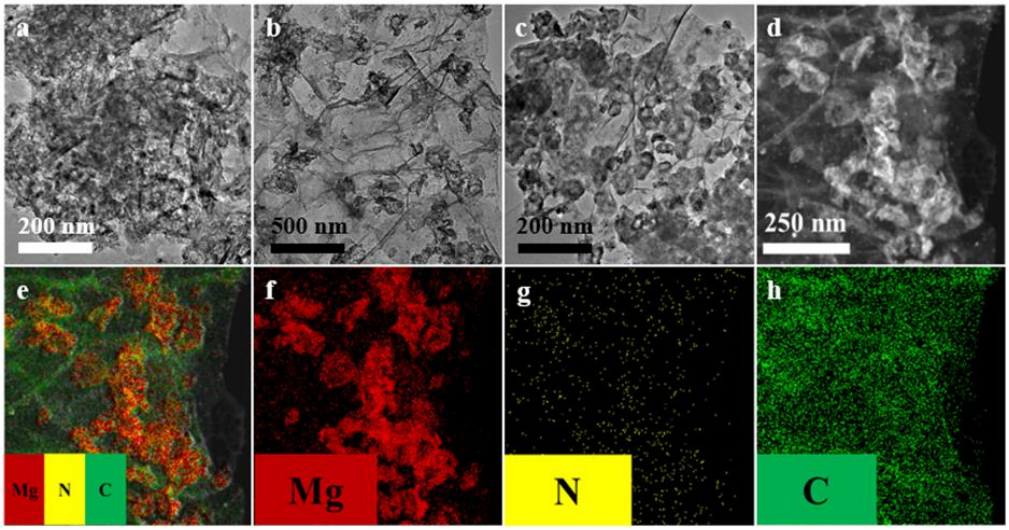

Figure 6.16 (a-c) TEM and (d) STEM images of MHG@MNH in the charged state after 100 cycles at 200 mA g^{-1}. (e-h) Elemental mapping images of MHG@MNH in the charged state after 100 cycles at 200 mA g^{-1}.

In comparison with MHG@MBH and MHG@MNH (**Figure 6.16 and 6.17**), the trend towards aggregation and particle growth is more obvious for MgH_2 NPs after coating with MgS (**Figure 6.18**). Additionally, obvious cracks on the surface of MHG@MS electrode could be observed with a large thickness expansion rate of 64% after 100 cycles of charge-discharge process (**Figure 6.19**). In strong contrast, (**Figures 6.15h**), the MHG@MBH electrode maintains its flat surface with few visible cracks and the thickness expansion rate is limited to be only 3% even after 100 cycles. In order to unravel the reason behind this phenomenon, the electrochemical performances of pure $Mg(BH_4)_2$, MgS, and $Mg(NH_2)_2$ as electrodes were tested. Only neglectable electrochemical capacity could be observed for $Mg(BH_4)_2$ and $Mg(NH_2)_2$ electrodes under the adopted experimental condition (**Figure 6.20 and 6.21**).

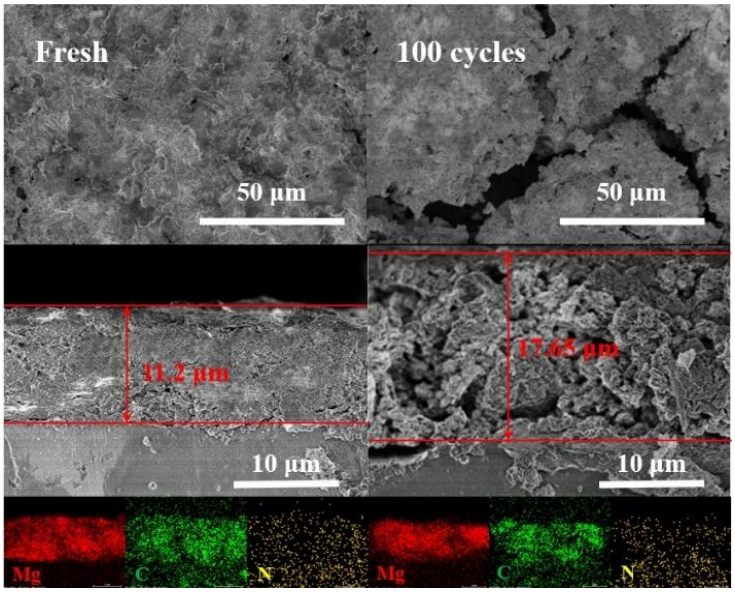

Figure 6.17 Top-view, cross-sectional SEM images, and the corresponding element mapping of MHG@MNH electrode at fresh state and after 100 cycles at 200 mA g^{-1}.

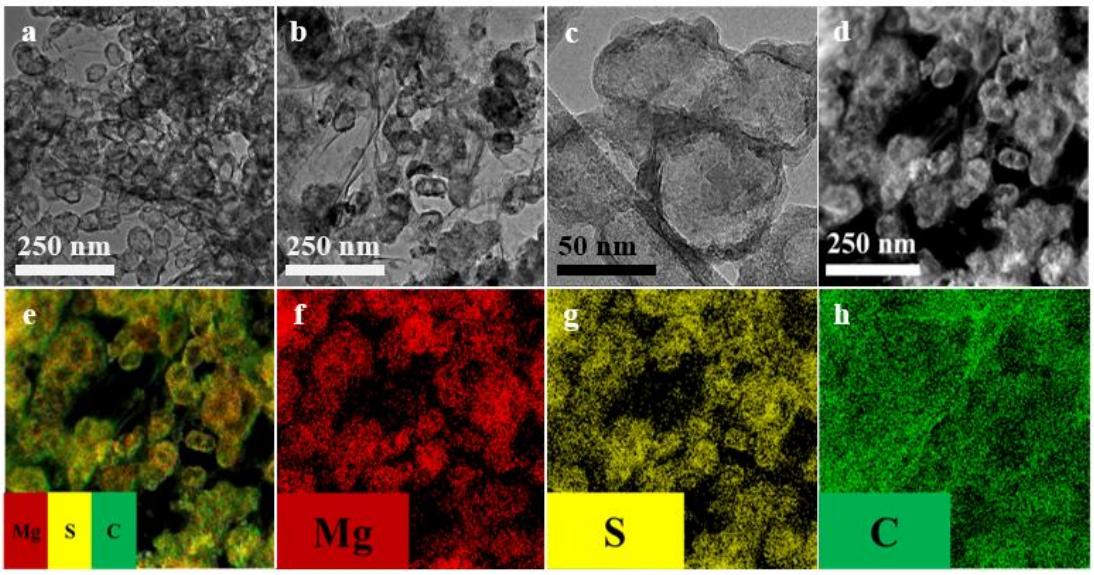

Figure 6.18 (a-c) TEM and (d) STEM images of MHG@MS in the charged state after 100 cycles at 200 mA g^{-1}. (e-h) Elemental mapping images of MHG@MS in the charged state after 100 cycles at 200 mA g^{-1}.

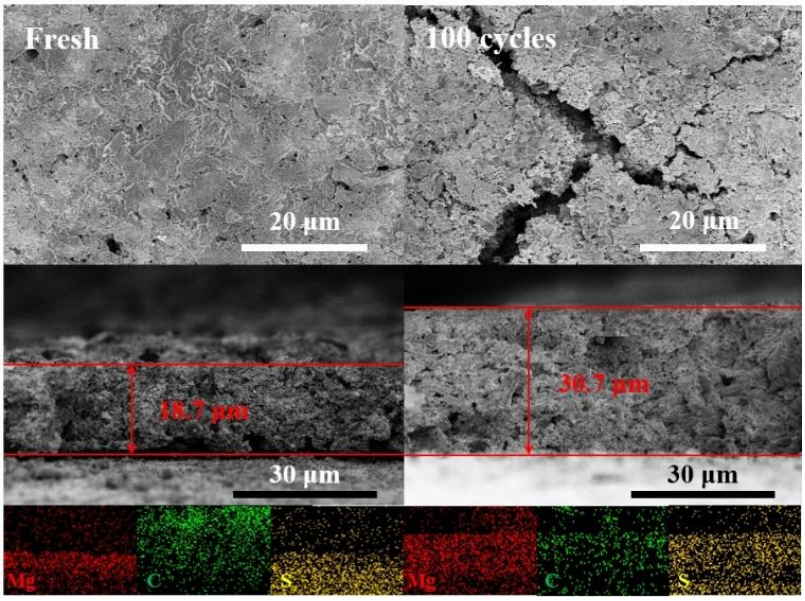

Figure 6.19 Top-view, cross-sectional SEM images and corresponding element mapping of MHG@MS electrode at fresh state and after 100 cycles at 200 mA g^{-1}.

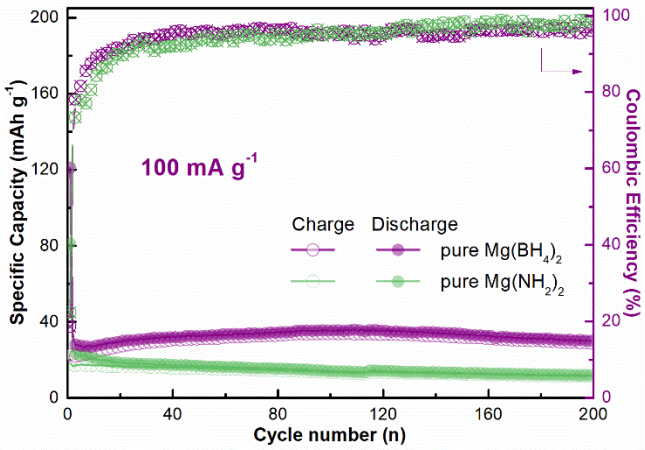

Figure 6.20 Electrochemical performance in half cell. Cycling performance of pure $Mg(BH_4)_2$ and $Mg(NH_2)_2$ at 100 mA g^{-1}.

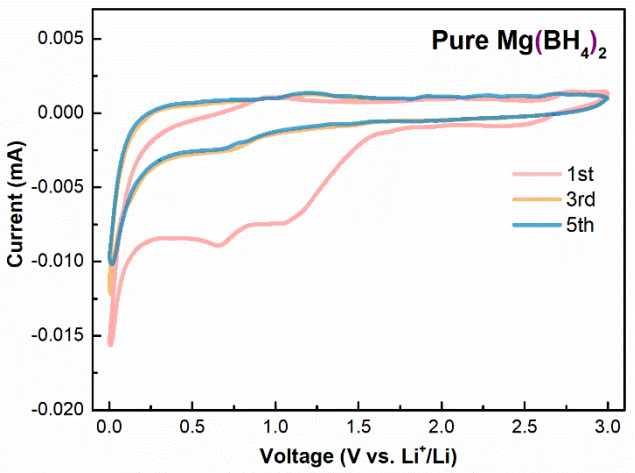

Figure 6.21 Electrochemical performance in half cell. CV curves of pure $Mg(BH_4)_2$ electrode in different cycles.

Moreover, the characteristic peaks of $Mg(BH_4)_2$ and $Mg(NH_2)_2$ in FTIR spectra are well preserved after the first discharge process (**Figure 6.22**), which further demonstrates that they are almost inactive upon the electrochemical reaction. By comparison, a specific discharge capacity about 400 mAh g^{-1} could maintained observed after 100 cycles for bulk MgS electrode (**Figure 6.23**) and the corresponding CV result (**Figure 6.24**) exhibit the electrochemical reaction process between lithium and MgS [46], which leads to the rupture and collapse of the shell upon charge-discharge cycling process and hence the fast decay of specific capacities upon cycling. Meanwhile, the shell composed of $Mg(BH_4)_2$ and/or $Mg(NH_2)_2$, which is electrochemically inactive, could generally maintain their stable structure during repeated lithiation and delithiation process, resulting in a superior cycling stability than MHG@MS.

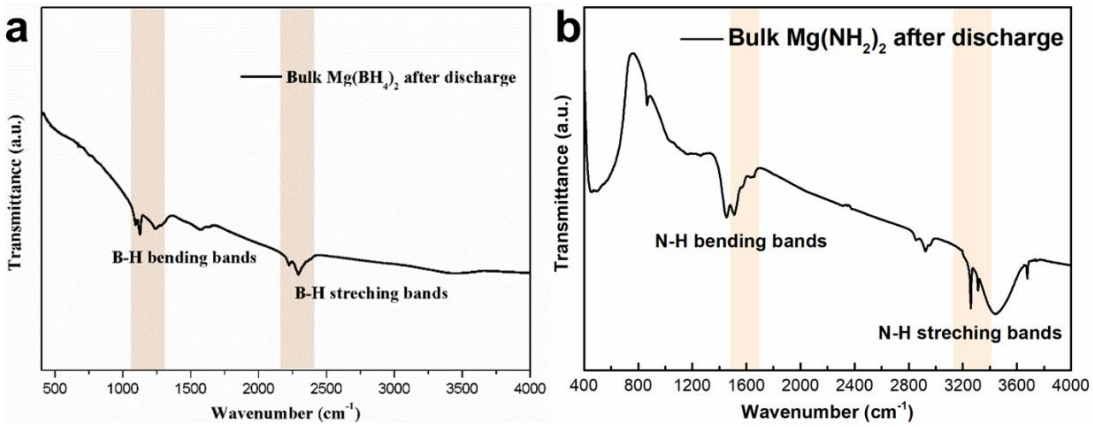

Figure 6.22 FTIR spectra of (a) MHG@MBH and (b) MHG@MNH after the first lithium insertion reaction at 200 mA g^{-1}.

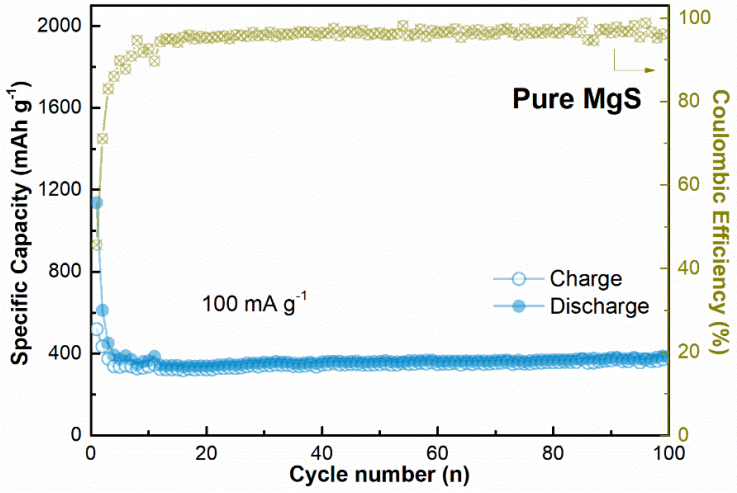

Figure 6.23 Electrochemical performance in half cell. Cycling property of pure MgS at 100 mA g^{-1}.

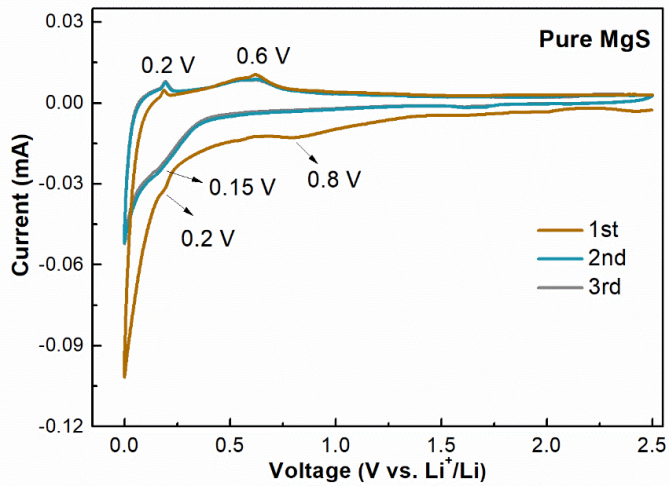

Figure 6.24 Electrochemical performance in half cell. CV curves of pure MgS electrode in first three cycles.

Interestingly, although bearing the comparable structure, the electrochemical capability of MHG@MBH, particularly the specific capacity, is much better than that of MHG@MNH. Hence, in addition to the structural effect, the impact of the coating material, *i.e.*, $Mg(BH_4)_2$ and $Mg(NH_2)_2$, on improving the electrochemical performance of MgH_2 was further investigated by adopting DFT calculations. In order to initiate the electrochemical reaction of MgH_2 with a yolk-shell-like structure, Li^+ ions should be able to intercalate into the coating layers first, followed by their diffusion towards the active materials. Therefore, the Li^+ insertion behaviour into MgH_2, $Mg(BH_4)_2$, and $Mg(NH_2)_2$ was subsequently examined. As illustrated in **Figure 6.25a-c**, the intercalation behaviour of Li^+ into each compound could be evaluated quantitatively by the formation energy (E_f). After structural modification, the E_f for the lithium ions intercalation into MgH_2 is calculated to be 0.16 eV. In strong contrast, the E_f that represent for the Li-inserted $Mg(NH_2)_2$ or $Mg(BH_4)_2$ (*i.e.*, -1.91 eV or -0.87 eV, respectively) is verified to be thermodynamically favourable, indicating the facile lithium insertion into both $Mg(NH_2)_2$ and $Mg(BH_4)_2$, which could significantly decrease the energy required for lithium ions diffusion through the coating layers and hence promote the lithium storage performance of MgH_2.

Subsequently, the diffusion barrier of Li^+ inside $Mg(BH_4)_2$ and $Mg(NH_2)_2$ were calculated using CI-NEB method [47] and the optimized transmission channel of Li^+ ions diffusion between two equivalent sites and corresponding energy profiles were plotted in **Figure 6.25d-f**. Obviously, the diffusion barrier of Li^+ in $Mg(BH_4)_2$ is calculated to be only 0.3 eV, while this value approaches 0.5 eV for $Mg(NH_2)_2$, which provides direct evidence to the faster ion-diffusion performance inside $Mg(BH_4)_2$ compared with

$Mg(NH_2)_2$, kinetically promoting the lithium storage performance of MgH_2. Therefore, in comparison with $Mg(NH_2)_2$, the building of $Mg(BH_4)_2$ as the shell could not only physically relieve the volume variation of MgH_2 during cycling process, but also effectively facilitate the intercalation and diffusion of lithium ions into MgH_2, leading to superior electrochemical properties of MgH_2 with ultra-high lithium storage capacity.

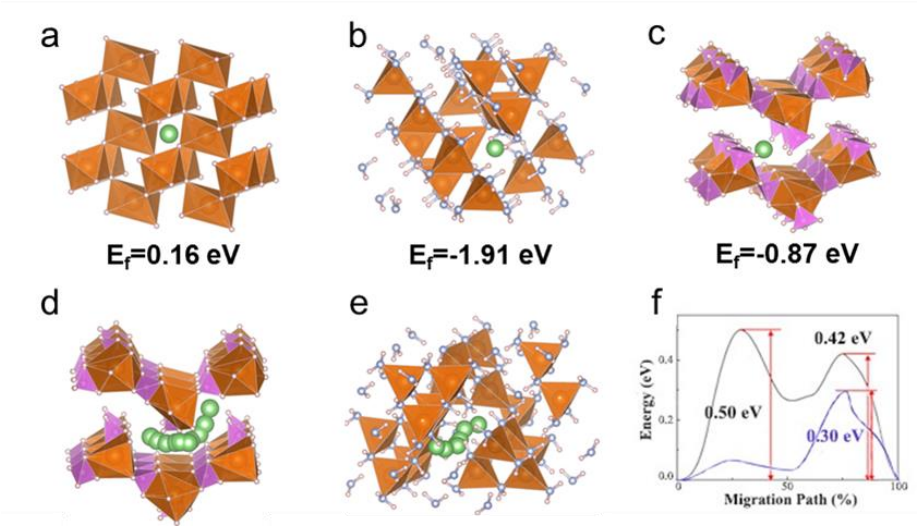

Figure 6.25 The intercalation behaviour of Lithium ion into each compound are described quantitatively via the Li-inserted stable structure and the corresponding formation energy (E_f) when Li^+ inserted into (a) MgH_2, (b) $Mg(NH_2)_2$, and (c) $Mg(BH_4)_2$. Diffusion paths of Li^+ inside (d) $Mg(BH_4)_2$, and (e) $Mg(NH_2)_2$ between two equivalent sites and (f) the corresponding energy profiles (the blue line corresponds to the $Mg(BH_4)_2$, and the black line corresponds to the $Mg(NH_2)_2$).

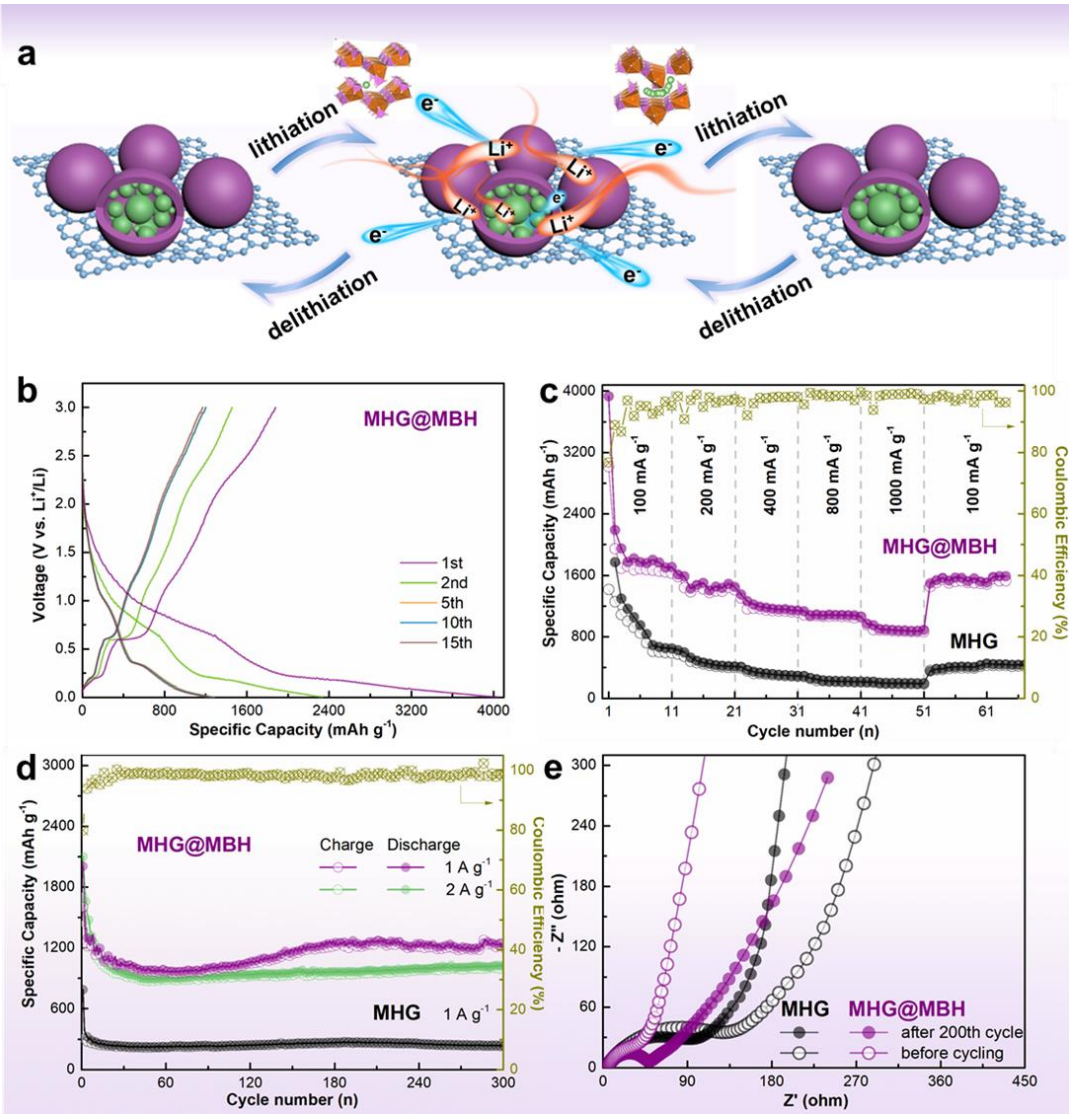

Figure 6.26 Electrochemical performance in half cell. (a) Schematic illustration of the structural advantages of MBH@MBH as lithium storage materials. (b) Galvanostatic charge-discharge profiles of MHG@MBH at 100 mA g^{-1} at selected cycles. (c) Rate performance of MHG@MBH and MHG electrode. (d) Cycling performance of MHG@MBH and MHG at 1 A g^{-1} and 2 A g^{-1}. (e) Nyquist plots of MHG@MBH and MHG electrodes in the discharged state before and after 200 cycles.

Hence, the lithium storage performance of the as-prepared MHG@MBH was systematically investigated in detail *via* galvanostatic cycling test using coin-type half-cells and the Li-metal as the counter electrode. As shown in **Figure 6.26b**, the

galvanostatic charge-discharge profiles of MHG@MBH in the 0.01-3 V range from the first to 15th cycle at 200 mA g^{-1} is comparable with that of MHG, due to the electrochemically intrinsic performance of $Mg(BH_4)_2$ under the adopted experimental condition.

The initial discharge profile of MHG@MBH consists of a plateau besides 0.75 V, which proved the existence of solid-electrolyte-interphase (SEI) films [16]. Subsequently, along with the gradually voltage reducing, a relatively flat potential plateau appears between 0.18 ~ 0.25 V, corresponding to the transformation from MgH_2 to Mg. Additionally, the plateau below 0.18 V, approaching the cut-off potential, could be ascribed to the formation of Li-Mg alloy. After being discharged to 0.01 V, HRTEM results demonstrate that the *d*-spacings of the crystalline nanodomains in MHG@MBH were measured to be 0.25 nm and 0.26 nm, which belongs to LiH ((200) planes) and Li_xMg ($x \leqq 1.5$) ((002) planes) (**Figure 6.27**), respectively, elucidating the complete lithiation process with the fabrication of LiH and Li-Mg alloys accompanied by the disappearing of MgH_2. Upon the reversible charge process, two plateaus observed at around 0.25V and 0.6 V could be corresponding to the extraction of Li^+ from Li_xMg alloy accompanied with the oxidation of Mg into MgH_2, respectively, as verified by the HRTEM results of fully charged sample. These results validate that the reversible lithiation and delithiation process of MgH_2 in MHG@MBH is derived from the conversion reaction between MgH_2 and Li_xMg alloys and LiH.

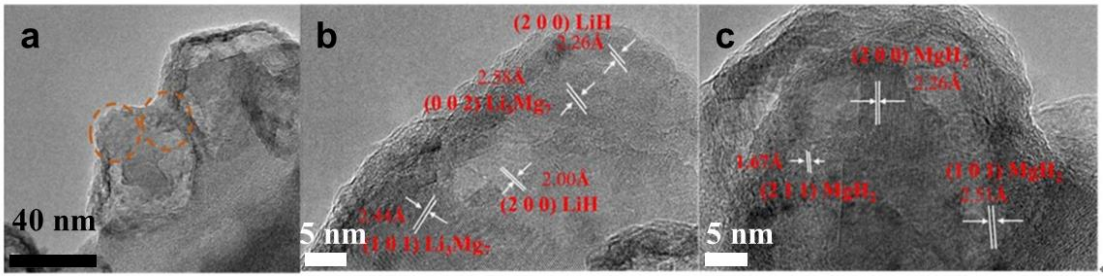

Figure 6.27 HRTEM images of MHG@MBH electrode at the selected (b) discharged and (c) recharged states.

The MHG@MBH electrode delivers a high initial discharge capacity of 3700 mAh g^{-1}, which is slightly higher than the theoretical specific capacity of MgH_2 (2243 mAh g^{-1} based on the conversion reaction to form LiH and the alloying reaction to form hcp-type Li_xMg alloys), as a result of the irreversible formation of the SEI layer and the possible formation of amorphous solid solution of Li-Mg alloys [16]. In the subsequent cycles, the discharge and charge curves of MHG@MBH electrodes are almost overlapping, indicating its good reversibility owing to the protection of $Mg(BH_4)_2$ as the coating shell. By comparison, although MHG electrode exhibits comparable plateaus for charge and discharge curves within the same potential range, the specific capacities decreased rapidly upon cycling (**Figure 6.28**). Besides, the MHG@MBH electrode illustrates superior rate performance than pure MHG electrode (**Figure 6.26c**). In the term of pure MHG, the average reversible specific capacity rapidly fades from 649 mAh g^{-1} to 436 mAh g^{-1}, with the density of the current increasing step by step from 100 mA g^{-1} to 1000 mA g^{-1}. In strong contrast, the reversible capacities of the MHG@MBH electrode could reach 1708, 1450, 1143, 1062, and 890 mAh g^{-1} at 100, 200, 400, 800 mA g^{-1} and finally 1 A g^{-1}, respectively. More importantly, when turned back to 100 mA g^{-1}, a capacity as high as 1588.6 mAh g^{-1} could still be recovered, corresponding to 93% of the initial reversible specific capacity, which corroborates the strong tolerance of MHG@MBH towards fast lithiation/delithiation process due to the protection of $Mg(BH_4)_2$ with low lithium ion diffusion barriers.

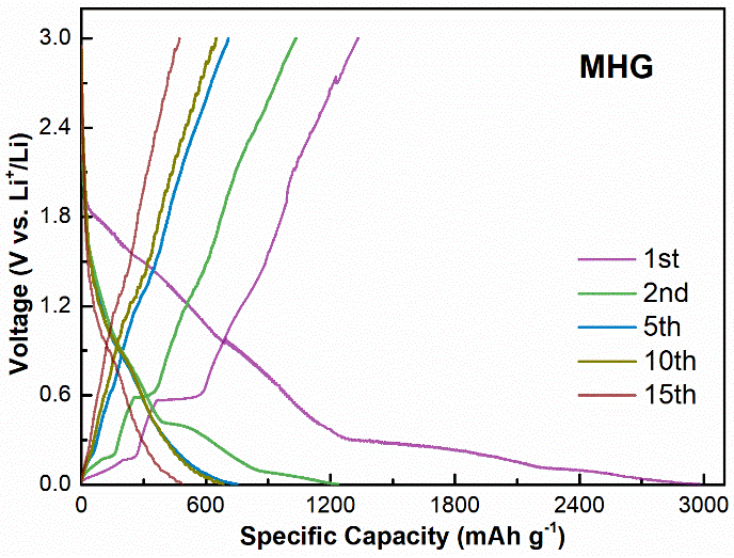

Figure 6.28 Electrochemical performance in half cell. Charging/discharge profiles of MHG electrode at 100 mA g^{-1} at selected cycles.

For the evaluation of the long cycle performance of lithium storage furtherly, the cycling retention of MHG@MBH anode were investigated at 1 A g^{-1} and 2 A g^{-1} (**Figure 6.26d**). Under the current density of 1 A g^{-1}, the MHG@MBH electrode delivers a high reversible capacity of 2005 mAh g^{-1} for the first cycle and still maintains a reversible capacity of 1247 mAh g^{-1} after 300 cycles, corresponding to a capacity maintain of 96% based on that of the 4th cycle. By comparison, the reversible specific capacities of MHG electrode rapidly drop to 235 mAh g^{-1} taking only 23 cycles and remained unchanged after prolonging to 300 cycles under the same testing conditions. Upon increasing the current density to 2 A g^{-1}, a reversible capacity of 1032 mAh g^{-1} could still be achieved for the MHG@MBH electrode after 300 cycles, corresponding to a capacity retention of 85% compared to the specific capacity of the 10th cycle. More importantly, the CEs of MHG@MBH could be preserved at a level over 98.6% through the entire cycling process, which provides further evidence to the excellent reversibility induced by the formation of yolk-shell-like structure homogeneously distributed on graphene with an excellent electrical and ionic conductivity. To illustrate the effects of

the $Mg(BH_4)_2$ as the shell on improving the cycling performance of MgH_2 electrode, the electrochemical impedance spectroscopy (EIS) of MHG@MBH and MHG electrodes were performed (**Figure 6.26e**). All the EIS spectra are composed of a compressed semicircle in the high-to-medium frequency region, corresponding to the charge transfer resistance (R_{ct}), and an inclined straight line in the low-frequency region, corresponding to the typical Warburg behaviour related to the Li ions diffusion within the electrode.[48] According to the fitting results based on the equivalent circuit model (**Figure 6.29**). Here, R_s, R_{ct}, CPE, and W_o represent resistance related to the SEI film, charge-transfer, constant phase element, and typical Warburg behaviour related to the Li ion diffusion within the electrode.[48] The R_{ct} of MHG@MBH electrode extracted from the high-frequency range was calculated to be only 65.8 Ω before cycling, which is much lower than that of the pure MHG (169.1 Ω).

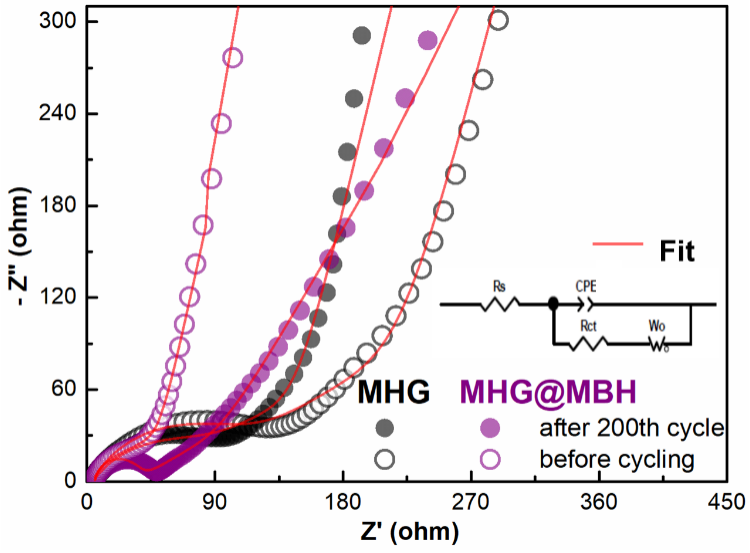

Figure 6.29 Nyquist plots and the corresponding simulated curves of MHG@MBH and MHG electrodes in the discharged state before and after 200 cycles. Inset: the corresponding equivalent circuit (R_s, R_{ct}, *CPE*, and W_o refer to the resistance of the SEI film, the internal resistance, the constant phase element, and Warburg impedance of the tested battery, respectively).

This could be mainly derived from the synergistic effects of the homogeneous distribution of MgH_2 on the graphene with high electronic conductivity and the rapid lithium ion diffusion inside the $Mg(BH_4)_2$, which effectively facilitates both electron and lithium ion transfer throughout the whole electrode and hence decreases the apparent resistance of the electrode. At the 200th cycle, the charge transfer resistance for MHG electrode was as high as 120.6 Ω. The R_{ct} of MHG@MBH electrode, however, exhibited a slight decrease to 50.2 Ω owing to the activation process during cycling, indicating that $Mg(BH_4)_2$, as a protective shell, plays a vital role in facilitating the fast Li ionic transfer and thus enhances the cycling stability and rate capability of the MgH_2-based electrode.

6.4 Conclusion

As a conclusion, facile synthesis of porous MgH_2 NPs with void spaces decorated with a series of Mg-based composites uniformly distributed on graphene has been achieved via the *in-situ* solid-gas reaction using MgH_2 NPs as both the reactants and the structural template. Particularly, the formation of yolk-shell-like structure of MgH_2@$Mg(BH_4)_2$ on graphene could not only physically accommodate the volume change of MgH_2, but also significantly facilitate the transportation of electrons throughout the whole electrode. More importantly, the uniform decoration of ultrathin $Mg(BH_4)_2$ as the shell with thermodynamically favourable intercalation of lithium ions and low kinetic barrier for the lithium ion diffusion contributes to the facile transportation of lithium ions into active MgH_2, which, coupled with the porous structure constructed by flexible graphene, effectively improves the ion conductivity of the electrode. The synergistic improvement on electronic and ionic conductivity leads to outstanding lithium storage properties, including high specific capacity, superior rate

capability, and long cycle life. Therefore, this work offers a new method for developing metal-hydride-based anodes with superior lithium storage performance and this novel strategy could be extended to the fabrication of various types of advanced electrode materials.

6.5 Reference

[1] Scrosati, B.; Hassoun, J.; Sun, Y. K. Lithium-ion batteries. A look into the future. *Energy Environ. Sci.* **2011**, *4*, 3287.

[2] Schmuch, R.; Wagner, R.; Horpel, G. *et al.* Performance and Cost of Materials for Lithium-Based Rechargeable Automotive Batteries. *Nat. Energy* **2018**, *3*, 267.

[3] Sun, Y.; Liu, N.; Cui, Y. Promises and Challenges of Nanomaterials for Lithium-Based Rechargeable Batteries. *Nat. Energy* **2016**, *1*, 16071.

[4] Choi, J. W.; Aurbach, D. Promise and Reality of Post-Lithium-Ion Batteries with High Energy Densities. *Nat. Rev. Mater.* **2016**, *1*, 16013.

[5] Li, M.; Lu, J.; Chen, Z. W. *et al.* 30 Years of Lithium-Ion Batteries. *Adv. Mater.* **2018**, *30*, 1800561.

[6] Liu, N.; Lu, Z. D.; Zhao, J.; McDowell, M. T.; Lee, H. W; Zhao, W. T.; Cui, Y. A Pomegranate-Inspired Nanoscale Design for Large-Volume-Change Lithium Battery Anodes. *Nat. Nanotech.* **2014**, *9*, 187.

[7] Zheng, X. Y.; Yang, C. K.; Chang, X. H.; Wang, T.; Ye, M.; Lu, J.; Zhou, H. H.; Zheng, J.; Li, X. G. Synergism of Rare Earth Trihydrides and Graphite in Lithium Storage: Evidence of Hydrogen-Enhanced Lithiation. *Adv. Mater.* **2018**, *30*, 1704353.

[8] An, W. L.; Gao, B. A.; Mei, S. X. *et al.* Scalable Synthesis of Ant-Nest-Like Bulk Porous Silicon for High-Performance Lithium-Ion Battery Anodes. *Nat. Commun.* **2019**, *10*, 1447.

[9] Jia, H. P.; Li, X. L.; Song, J. H. *et al.* Hierarchical Porous Silicon Structures with Extraordinary Mechanical Strength as High-Performance Lithium-Ion Battery Anodes. *Nat. Commun.* **2020**, *11*, 1474.

[10] Zhao, Y.; Li, X. F.; Yan, B. *et al.* Recent Developments and Understanding of Novel Mixed Transition-Metal Oxides as Anodes in Lithium-Ion Batteries. *Adv. Energy Mater.* **2016**, *6*, 1502175.

[11] Yang, Y. X.; Liu, Y. F.; Pu, K. C.; Chen, X.; Tian, H.; Gao, M. X.; Zhu, M.; Pan, H. G. Highly Stable Cycling of Amorphous Li_2CO_3-Coated α-Fe_2O_3 Nanocrystalline Prepared via a New Mechanochemical Strategy for Li-Ion Batteries. *Adv. Funct. Mater.* **2017**, *27*, 1605011.

[12] Cao, Y.; Yang, Y. X.; Ren, Z. H.; Jian, N.; Gao, M. X.; Wu, Y. J.; Zhu, M.; Pan, F.; Liu, Y. F.; Pan, H. G. A New Strategy to Effectively Suppress the Initial Capacity Fading of Iron Oxides by Reacting with $LiBH_4$. *Adv. Funct. Mater.* **2017**, *27*, 1700342.

[13] Yan, Y.; Li, S. B.; Yuan, B. *et al.* Flowerlike Ti-Doped MoO_3 Conductive Anode Fabricated by a Novel NiTi Dealloying Method: Greatly Enhanced Reversibility of the Conversion and Intercalation Reaction. *ACS Appl. Mater. Interfaces.* **2020**, *12*, 8240.

[14] Wu, L.; Zheng, J.; Wang, L. *et al.* PPy-Encapsulated SnS_2 Nanosheets Stabilized by Defects on a TiO_2 Support as a Durable Anode Material for Lithium-Ion Batteries. *Angew. Chem. Int. Ed.* **2018**, *57*, 1.

[15] Zhang, Y. P.; Wang, L. L.; Xu, H. *et al.* 3D Chemical Cross-Linking Structure of Black Phosphorus@CNTs Hybrid as a Promising Anode Material for Lithium Ion Batteries. *Adv. Funct. Mater.* **2020**, *30*, 1909372.

[16] Oumellal, Y.; Rougier, A.; Nazri, G. A.; Tarascon, J. M.; Aymard, L. Metal Hydrides for Lithium-Ion Batteries. *Nat. Mater.* **2008**, *7*, 916-921.

[17] Brutti, S.; Mulas, G.; Piciollo, E.; Panero, S.; Reale, P. Magnesium Hydride as A High-Capacity Negative Electrode for Lithium-Ion Batteries. *J. Mater. Chem.* **2012**, *22*, 14531-14537.

[18] Deng, J. J.; Yu, X. L.; Qin, X. Y. Co-B Nanoflakes as Multifunctional Bridges in $ZnCo_2O_4$ Micro-/Nanospheres for Superior Lithium Storage with Boosted Kinetics and Stability. *Adv. Energy Mater.* **2019**, *9*, 1803612.

[19] Cheng, D. L.; Yang, L. C.et al. Nano-Spatially Confined and Interface-Controlled Lithiation-Delithiation in an In Situ Formed (SnS-SnS_2-S)/FLG Composite: A Route to an Ultrafast and Cycle-Stable Anode for Lithium-Ion Batteries. *J. Mater. Chem. A.* **2019**, *7*, 15320.

[20] Liu, Z. L.; Yang, S. L.; Sun, B. X.; Yang, P. P.; Zheng, J.; Li, X. G. Low-Temperature Synthesis of Honeycomb CuP_2@C in $ZnCl_2$ Molten Salt for High-Performance Lithium-Ion Batteries. *Angew. Chem., Int. Ed.* **2020**, *59*, 1975.

[21] Aymard, L.; Oumellal, Y.; Bonnet, J. P. Metal Hydrides: An Innovative and Challenging Conversion Reaction Anode for Lithium-Ion Batteries. *Beilstein J. Nanotechnol.* **2015**, *6*, 1821.

[22] Kharbachi, A. E.; Hu, Y.; Sørby, M. H. *et al.* Understanding Capacity Fading of MgH_2 Conversion-Type Anodes via Structural Morphology Changes and Electrochemical Impedance. *J. Phys. Chem. C* **2018**, *122*, 8750.

[23] Oumellal, Y.; Zlotea, C.; Bastide, S.; Cachet-Vivier, C.; Leonel, E.; Sengmany, S.; Leroy, E.; Aymard, L.; Bonnet, J. P.; Latroche, M. Bottom-Up Preparation of MgH_2 Nanoparticles with Enhanced Cycle Life Stability During Electrochemical Conversion in Li-Ion Batteries. *Nanoscale* **2014**, *6*, 14459.

[24] Zeng, L.; Ichikawa, T.; Kawahito, K.; Miyaoka, H.; Kojima, Y. Bulk-Type All-Solid-State Lithium-Ion Batteries: Remarkable Performances of a Carbon Nanofiber-Supported MgH_2 Composite Electrode. *ACS Appl. Mater. Interfaces* **2017**, *9*, 2261.

[25] Zhang, B. P.; Xia, G. L.; Sun, D. L.; Fang, F.; Yu, X. B. Magnesium Hydride Nanoparticles Self-Assembled on Graphene as Anode Material for High-Performance Lithium-Ion Batteries. *ACS Nano* **2018**, *12*, 3816.

[26] Zhang, B. P.; Si, Y. S.; Gu, Q. F.; Chen, M.; Yu, X. B. Hydrangea-Shaped 3D Hierarchical Porous Magnesium Hydride-Carbon Framework with High-Rate Performance for Lithium Storage. *ACS Appl. Mater. Interfaces* **2019**, *11*, 28987.

[27] Zeng, L.; Ichikawa, T.; Kawahito, K.; Miyaoka, H; Kojima, Y. Bulk-Type All-Solid-State Lithium-Ion Batteries: Remarkable Performances of a Carbon Nanofiber-Supported MgH_2 Composite Electrode. *ACS Appl. Mater. Interfaces.* **2017**, *9*, 2261.

[28] Xia, G. L.; Tan, Y. B.; Chen, X. W.; Sun, D. L.; Guo, Z. P.; Liu, H. K.; Ouyang, L. Z.; Zhu, M.; Yu, X. B. Monodisperse Magnesium Hydride Nanoparticles Uniformly Self-Assembled on Graphene. *Adv. Mater.* **2015**, *27*, 5981

[29] Xia, G. L.; Zhang, B. P.; Chen, X. W.; Sun, D. L.; Guo, Z. P.; Liang, F. X.; Zou, W. D.; Yang, Z. Z.; Yu, X. B. Molecular-Scale Functionality on Graphene to Unlock the Energy Capabilities of Metal Hydrides for High-Capacity Lithium-Ion Batteries. *ACS Nano* **2018**, *12*, 8177.

[30] Zhang, H. Y.; Xia, G. L.; Zhang, J.; Sun, D. L.; Guo, Z. P.; Yu, X. B. Graphene-Tailored Thermodynamics and Kinetics to Fabricate Metal Borohydride Nanoparticles with High Purity and Enhanced Reversibility. *Adv. Energy Mater.* **2018**, *8*, 1702975.

[31] Wang, Y. R.; Chen X. W.; Zhang, H. Y.; Xia, G. L.; Sun, D. L.; Yu, X. B. Heterostructures Built in Metal Hydrides for Advanced Hydrogen Storage Reversibility. *Adv. Mater.* **2020**, *32*, 2002647.

[32] Huang, Y. Q.; Xia, G. L.; Chen, J.; Zhang, B. P.; Li, Q.; Yu, X. B. One-Step Uniform Growth of Magnesium Hydride Nanoparticles on Graphene. *Prog. Nat. Sci.* **2017**, *27*, 87.

[33] Kresse G., Hafner J. Ab Initio Molecular Dynamics for Liquid Metals. *Phys. Rev. B.* **1993**, *47*, 558.

[34] Kresse G., Furthmüller J. Efficient Iterative Schemes for Ab Initio Total-Energy Calculations Using a Plane-Wave Basis Set. *Phys. Rev. B.* **1996**, *54*, 11169.

[35] Blöchl P. E. Projector Augmented-Wave Method. *Phys. Rev. B.* **1994**, *50*, 17953.

[36] Perdew J. P., Burke K., Ernzerhof, M. Generalized Gradient Approximation Made Simple. *Phys. Rev. Lett.* **1996**, *77*, 3865.

[37] Henkelman G., Jonsson H. A Climbing Image Nudged Elastic Band Method for Finding Saddle Points and Minimum Energy Paths. *J. Chem. Phys.* **2000**, *113*, 9978.

[38] Z. Rong, R. Malik and P. Canepa, et al. Materials Design Rules for Multivalent Ion Mobility in Intercalation Structures. *Chem. Mater.* **2015**, *27*, 6016.

[39] R. Malik, D. Burch, M. Bazant and G. Ceder. Particle Size Dependence of the Ionic Diffusivity. *Nano Lett.*, **2010**, *10*, 4123.

[40] Fan, M. M.; Liao, D. K.; Aboud, M. F. A.; Shakir, I.; Xu, Y. X. A Universal Strategy toward Ultrasmall Hollow Nanostructures with Remarkable Electrochemical Performance. DOI:10.1002/anie.202000352.

[41] D'Anna, V.; Spyratou, A.; Sharma, M.; Hagemann, H. FT-IR Spectra of Inorganic Borohydrides. *Spectrochimica Acta Part A: Molecular and Biomolecular Spectroscopy* **2014**, *128*, 902.

[42] Cao, H.; Wang, H.; He, T.; Wu, G. T.; Xiong, Z. T.; Qiu, J. S.; Chen, P. Improved Kinetics of the $Mg(NH_2)_2$–2LiH System by Addition of Lithium Halides. *RSC Adv.* **2014**, *4*, 32555.

[43] Zhang, J. X.; Liu, Y. F.; Zhang, X.; Yang, Y. X; Zhang, Q. H; Jin, T.; Wang, Y. X.; Gao, M. X.; Sun, L. X.; Pan, H. G. Synthesis of CsH and Its Effect on the Hydrogen Storage Properties of the $Mg(NH_2)_2$-2LiH System. *Int. J. Hydrogen Energy.* **2016**, *41*, 11264.

[44] Avril, C.; Malavergne, V.; Caracas, R. *et al.* Raman Spectroscopic Properties and Raman Identification of CaS-MgS-MnS-FeS-Cr_2FeS_4 Sulfides in Meteorites and Reduced Sulfur-Rich Systems. *Meteoritics & Planetary Science* **2013**, *4*8, 1415.

[45] Luong, D. X., Bets, K. V., Algozeeb, W. A. *et al.* Gram-Scale Bottom-Up Flash Graphene Synthesis. *Nature* **2020**, *577*, 647.

[46] Yu, X. Y.; Yu, L.; Lou, X. W. Metal Sulfide Hollow Nanostructures for Electrochemical Energy Storage. *Adv. Energy Mater.* **2016**, *6*, 1501333.

[47] Henkelman, G.; Jonsson H. A. Climbing Image Nudged Elastic Band Method for Finding Saddle Points and Minimum Energy Paths. *J. Chem. Phys.* **2000**, *113*, 9978.

[48] Geng, X.; Zhang, Y.; Han, Y.; Li, J.; Yang, L.; Benamara, M.; Chen, L.; Zhu, H. Two-Dimensional Water-Coupled Metallic MoS_2 with Nanochannels for Ultrafast Supercapacitors. *Nano Lett.* **2017**, *17*, 1825.

CHAPTER 7 IN-SITU CONSTRUCTED DOUBLE IONIC-ELECTRONIC TRANSFER INTERFACE BETWEEN MgH_2 AND $LiBH_4$ BOOSTING SOLID-STATE LITHIUM BATTERIES

7.1 Introduction

Incessant growth in energy demand and urgent desire to shift into the "green" electricity in the global world have put forward constant new requirements on the materials side [1-2]. As one of the most widely used energy storage technologies in numerous fields from small personal electronic devices to grid-scale energy storage, lithium-ion batteries (LIBs) are also in great demand to develop new electrode materials with high energy density, fast charge/discharge rate and good cycle life [3]. In order to make up the gap between LIBs (200-300 Wh kg^{-1}) and gasoline (12000 Wh kg^{-1}) in terms of specific energy density. Intensive research has been devoted to find new electrode and electrolyte system and improve its electrochemical performance [3]. Recently, abundant potential candidates have been deeply explored such as carbides [4–6], Si based materials [7–9], hydrides [10,11], sulfides [12,13], phosphides [14], and transition-metal oxides [15, 16].

Among the myriad of available materials, hydrides which was conceptually proposed by Oumellal et al. in 2008, can be used as negative electrode, owing to the conversion reaction with lithium ions ($MHx + xLi+ + xe- \rightleftharpoons M + xLiH$) [10]. Owing to the attracting theoretical gravimetric and volumetric capacity which is as high as 2038 mAh g^{-1} and 2878 mAh L^{-1}, respectively, low polarization, as well as a low and safe potential window of an average voltage of 0.5 V versus Li^+/Li, magnesium hydride (MgH_2) has been paid much attention. However, the intrinsic poor electricity conductivity and volume expansion/shrinkage, which is inevitable for conversion reaction, limits the

application of MgH_2 in LIBs. Furthermore, the capacity rapidly decreases from 1480 mAh g^{-1} in the first cycle to less than 200 mAh g^{-1} after only 10 cycles. Tremendous efforts and attempts have been devoted to solving the above issues and improving performance of MgH_2 electrode. It has been proved recently, nanostructured materials display enhanced performance as an anode in LIBs, with larger specific surface area, sufficient active sites and shorter pathway of lithium mass diffusion and charge transport. Oumellal et al. has synthesized the MgH_2 nanoparticles benefit for alleviating the pulverization of bulk MgH_2 upon cycling and improving cycle life stability, with a bottom-up method [17]. More recently, a seize of magnesium hydride-carbon framework composite (graphene, Mxene, HPCs) with uniform and stable dispersion of MgH_2 nanoparticles has been investigated through continuous efforts [18-20]. An exceptional high discharge capacity of 884 mAh g^{-1} was retained after 500 cycles at 2 A g^{-1}. Taking advantage of the robust architecture of carbon supports, the MgH_2 nanoparticles demonstrates improved electricity conductivity, closed interfacial contact between electrolyte and electrode, sufficient channels for fast electron/Li+ transfer, which contribute to prevent agglomeration and provide buffer for electrode expansion/shrinkage. However, along with the increasing number of discharge/charges cycling, the capacity depression induced by side reaction between organic liquid electrolyte and electrode become serious gradually. Hence, introducing relatively stable solid-state electrolyte (SSE) into the battery system was an effective strategy for deeply improving the electrochemical performance of MgH_2 [1,25–28]. $LiBH_4$ firstly used as a kind of solid-state electrolyte by Orimo et al. in 2007, showing wide electrochemical window (0-5 V) and high lithium ionic conductivity (10^{-3} S cm^{-1}) at high temperature (390 K) [21,22]. Simultaneously, as a well-known hydrogen storage system, MgH_2-$LiBH_4$ composite has been reported to have superior hydrogen exchange effect between

the two materials [23], which indicates the stability of the mixture when applying these materials as anode electrode and electrolyte for LIBs, respectively. For instance, many efforts have been made to develop this system, CoO and Nb_2O_5 have been used as catalysts to improve the solid-state lithium-ion battery (SSLIB) performance of MgH_2 anode with $LiBH_4$ electrolytes [23]. Nevertheless, SSLIBs system have several constrains, such as high interfacial resistance and unstable solid-electrolyte interphase formation, hindered their widespread application [24]. To solve the issues, many approaches has been employed including electrodes coating [25], buffer layer construction [26] and constructing multifunctional solid electrolyte interface [27]. Therefore, stable and compatible interfacial layers with low contact resistance between electrode and electrolyte are much desired.

Combining these above effects, the yolk-shell-liked nanostructure MHG@MBH fabricated in the previous chapter may be the best candidate as the anode electrode materials for SSLIB. We choose two MgH_2 nanospheres with a particle size of 50 and 10 nanometers as nanoreactor, in-situ coating the layer of $Mg(BH_4)_2$ outside via gas-solid reaction. Besides, the MgH_2@$Mg(BH_4)_2$ particles uniformly separated on the graphene nanosheets. After the first lithiation, the coating layer of $Mg(BH_4)_2$ reacts with lithium ions to produce lithium borohydride, magnesium hydride and Li_2B_6, so that the magnesium hydride is in situ coated with a layer of electrolyte ($LiBH_4$). Li_2B_6 acts as a good lithium ion and electronic conductor and is also coated outside the electrode (MgH_2). Therefore, we design a in situ electrochemical method to produce double conductive Li_2B_6 Layers which are principally formed at anode-electrolyte interface. The Li_2B_6 Layers of the York-shell structure could reduce the contact resistance and improve interface stability, which benefit for long cycle life and fast charging. More importantly, the in-situ growth of the mixed ionic-electronic transfer layer at the

electrode-electrolyte interface facilitate Li^+ immigration which are contribute to high specific capacity and favorable rate performance.

7.2 Experimental Section

7.2.1 Material Synthesis

All the materials were purchased from Sigma-Aldrich and used as received. All the operations were carried on in the purified argon gas filled glove box (MIKROUNA) to avoid oxidation and moisture. On a content of 60 wt.%, MgH_2 nanospheres uniformly grown on graphene nanosheets via the hydrogenation of $MgBu_2$ the same as the last chapter. And the in situ coating of $Mg(BH_4)_2$ by the solid-gas reaction is also introduced in details at last chapter. The working electrode powder was mixed by ball milling of MHG@MBH, $LiBH_4$ and conductive carbon (Ketjen black) in a weight ratio of 1: 1: 2 with no further optimization.

7.2.2 Materials Characterization

The identification of phase structure of MHG@MBH electrode was conducted by XRD, Raman and FT-IR. The morphological characterization of the samples was performed by FE-SEM and TEM. Elemental analysis was performed with an Element Tar Vario EL3 Elemental Analyser.

7.2.3 Electrochemical Measurements

The MHG@MBH electrode was assembled in a sleeve made of poly (ether-ether ketone) with an inside diameter of 10 mm. firstly, the solid electrolyte $LiBH_4$ (70 mg) was loaded into the sleeve. Secondly, the working electrode mixture with a quantity of 4 mg was placed on the upside of the $LiBH_4$ layer and pressed at 100 MPa as well, then, a lithium foil was placed on the downside of electrolyte layer as counter electrode.

Finally, the whole cell was settled into a steel mould, and the screws are tightened with a torque of 10 N/cm. All the procedure were conducted in an Ar-filled glovebox with concentrations of moisture and oxygen below 1 ppm. EIS were performed using a Biologic VMP-3 electrochemistry workstation at 120 ℃, from 7 M Hz to 1 Hz. The cycling performance and rate stability of cells were tested using a NEWARE Battery Test System between 0.25 V and 1.3 V (vs. Li^+ /Li) at different constant current densities.

7.3 Results and Discussion

The synthesis process of MgH_2 nanoparticles (NPs) decorated with $Mg(BH_4)_2$ with diameters of 47 nm and 11 nm is schematically illustrated in **Figure 7.1**. In the first place, graphene confined MgH_2 NPs (MHG) were fabricated via a hydrogenation-induced decomposition of $(C_4H_9)_2Mg$ according to the previous work.[28] The size of the synthesized particles can be controlled by the amount of added solvent. The thus-formed MgH_2 NPs uniformly separated on the graphene with strong adsorption energy, due to the favorable adsorption energy between $(C_4H_9)_2Mg$ and graphene [29]. Subsequently, MHG composite was adopted as the nanoreactor for *in-situ* solid-gas reaction between MgH_2 NPs and B_2H_6 gas. After heat preservation process, a layer of $Mg(BH_4)_2$ shell with 2 nm thick fabricated outside the MgH_2 NP. The MgH_2 NPs with a diameter of 11 nm grows to 13 nm (13-MHG@MBH) **Figure 7.2a**, while the MgH_2 NPs with a diameter of 47.7 nm becomes 49.6 nm (50-MHG@MBH) **Figure 7.2g.** During which, the graphene with flexible and porous structure not only acts as the structural support to inhibit the aggregation and growth of MgH_2 NPs, but also shorten the diffusion tunnels for the transportation of gases to facilitate the uniform reaction with MgH_2 NPs [29]. The morphology of the synthesized MHG@MBH is characterized

through SEM and TEM. **Figure 7.2** demonstrates the morphology of MgH_2 NPs and their homogeneous distribution on graphene are well preserved after the *in-situ* solid-gas reaction, owing to the presence of graphene as the robust structural support. Moreover, characteristic lattice fringes of 4.3 and 4.2 Å, related to the (100) and (002) planes of $Mg(BH_4)_2$, respectively, could be clearly observed on the surface of MgH_2 NPs, indicating the successful formation of $Mg(BH_4)_2$.

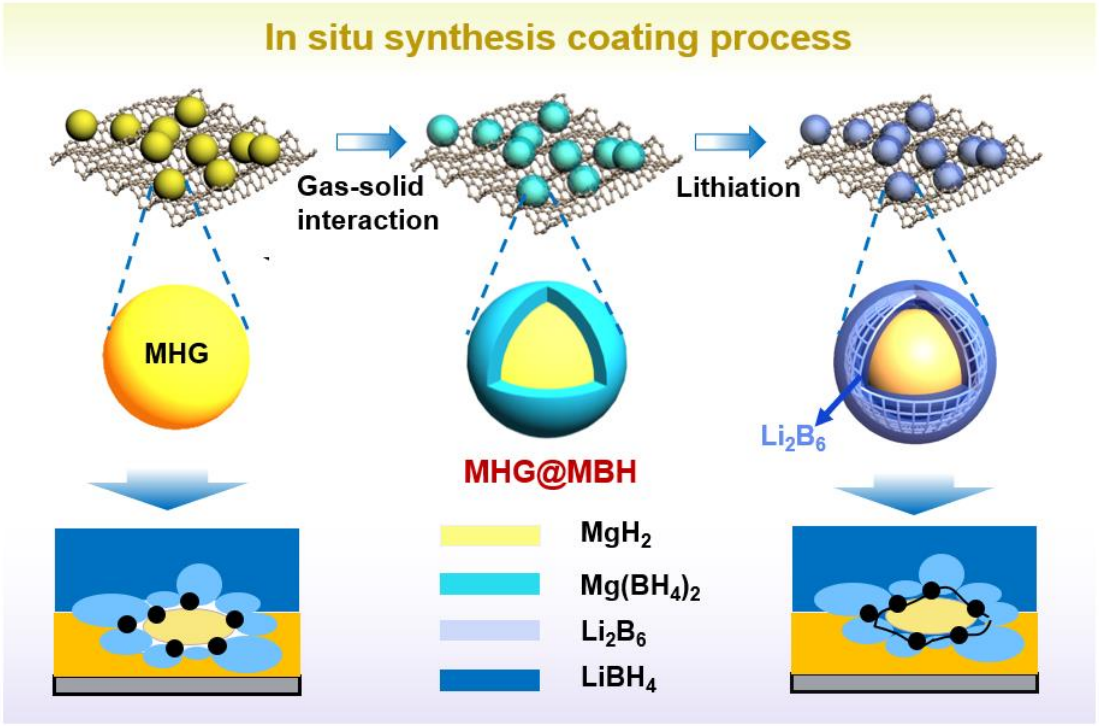

Figure 7.1 Schematic diagram of the preparation procedure of MHG@MBH, and the lithiation process of $Mg(BH_4)_2$.

As discussed in the last chapter. scanning TEM images (**Figure 7.2e and k**) reveal that, owing to the Kirkendall effect, original MgH_2 NPs break up into several smaller nanoparticles, inducing the simultaneous synthesis of $Mg(BH_4)_2$ as the shell and the porous structure of MgH_2 inside.[30] The void spaces between smaller MgH_2 crystals inside the shell benefit for alleviating the volume expansion of MgH_2 NPs during the cycling charge-discharge process, while the cracked MgH_2 NPs provide more active sites and shorter diffusion pathway for the lithiation/delithiation reaction. The

elemental line-scan profile furtherly proved the yolk-shell-like structure of MHG@MBH (**Figure 7.2e**). The intensity of signal B which related with the amount of B element, in the fringe of MgH_2 NPs is higher than that in the center area, indicating the existence of $Mg(BH_4)_2$ on the surface of MgH_2 NPs. Furthermore, no matter in MHG@MBH with 13 nm or 50 nm, the distribution of Mg, B, and C elements matches well with each other, being strong evidences for the uniform formation of the $Mg(BH_4)_2$ shell outside the yolk of MgH_2 NPs (**Figure 2f and l**). The $Mg(BH_4)_2$ has well attachment with $LiBH_4$, for the same chemical group of $[BH_4]^-$, and the graphene not only acted as a supporter but also largely promote the electronic conductivity of the whole electrodes. Hence, the nanostructure of this rational designed system is benefit for the magnesium hydride, as an anode, to reach its full potential on lithium storage.

The structure of the synthesized samples 50-MHG, 50-MHG@MBH, and 13-MHG 13MHG@MBH are determined by PXRD. As illustrated in **Figure 7.3** all the diffraction peaks matched well with patterns of β-MgH_2 (PDF 12-0697), indicating the compose single MgH_2 phase with high purity. In addition, the diffraction peaks become weaker and broader in the order of 50-MHG, 50-MHG@MBH,13-MHG 13MHG@MBH as a result of the nanocrystalline size nature. Especially, the diffraction peaks of 13MHG@MBH are almost invisible. Alternatively, Raman and FTIR are conducted to characterize the chemical composition of 13MHG@MBH sample.

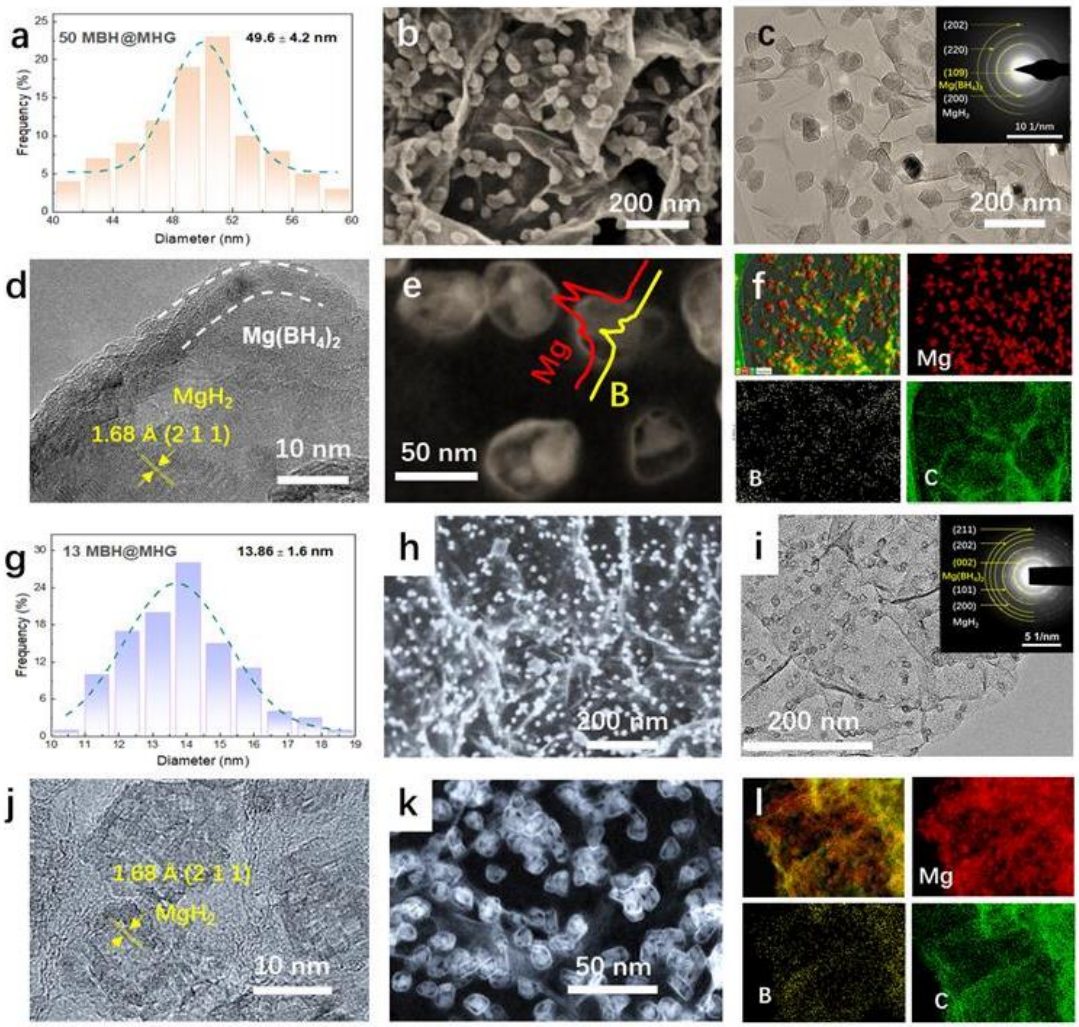

Figure 7.2 Morphological characterization of the as synthesized 50-MHG@MBH and 13-MHG@MBH. (a, g) The particle size distributions of 50-MHG@MBH and 13-MHG@MBH, respectively. The corresponding SEM images (b, h), TEM images (c, i), HRTEM images (d, j), STEM images (e, k), the elemental mapping (f, l). The insets of (c, i) is the SAED patterns.

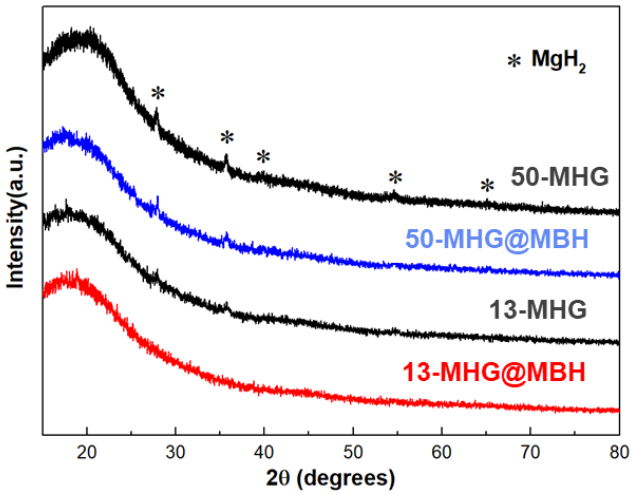

Figure 7.3 PXRD patterns of the synthesized samples 50-MHG, 50-MHG@MBH, 13-MHG, and 13MHG@MBH.

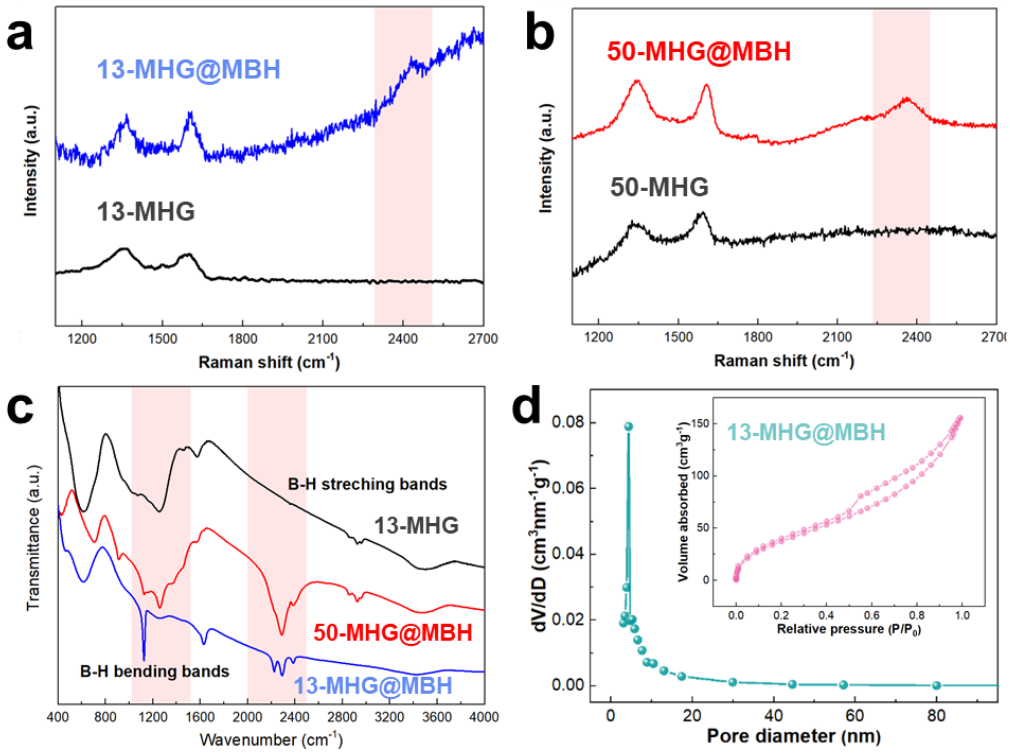

Figure 7.4 Raman spectra of as-prepared (a) 13-MHG@MBH and 13MHG, (b) 50-MHG@MBH and 50MHG, and FTIR spectra of (c) MHG@MBH and MHG. Pore-size distribution of 13-MHG@MBH (d). The inset of (d) is the corresponding nitrogen adsorption/desorption isotherm.

In **Figure 7.4a and b**, the broad peak at around 2400 cm^{-1} observed in the Raman spectra of the as-synthesized 13-MHG@MBH and 50-MHG@MBH composites are Raman characteristic peak of $Mg(BH_4)_2$ [31, 32], and the strong peak at ~ 2300 cm^{-1} and 1175 cm^{-1} assigned to the stretching of B-H bonds is obviously observed in FTIR spectra in **Figure 7.4c.** which provides additional evidence proving the regeneration of $Mg(BH_4)_2$ after the reaction between MgH_2 and B_2H_6 [33-35]. The two broad peaks at around 1338 and 1600 cm^{-1} observed in the Raman spectra of all the as-synthesized composites could be indexed to the typical D and G bands of graphene. [36] The Brunauer-Emmett-Teller (BET) surface of 13-MHG@MBH is calculated to be 150.8 m^2 g^{-1}, with a pore size distribution from 2 to 30 nm, indicating the mesoporous structure.

To evaluate the performance of 13-MHG@MBH and 50-MHG@MBH work as an anode of SSLIBs, the charge-discharge performance of the as-synthesized 13-MHG@MBH, and 50-MHG@MBH electrodes were firstly investigated at a current density of 200 mA g^{-1}, with the corresponding pure MHG included for comparison. As shown in **Figure 7.5a**, an initial discharge/charge capacity of 1234/872 mAh g^{-1}, with a Coulombic efficiency (CE) of 70.7%, and the maintained capacity is 780 mAh g^{-1} after 150 cycle. When worked as an electrode 50-MHG delivers obviously higher capacity and more stable cycling performance in SSLIBs than that in traditional liquid electrolyte, strongly supports the fact that solid state electrolyte $LiBH_4$ are more fit for magnesium hydride electrodes. However, the capacity deterioration is still rapid, the discharge/charge capacity decreased to 748/746 mAh g^{-1} at the second cycle. The phenomenon has been relieved after being coated by $Mg(BH_4)_2$. With the initial discharge/charge capacity of 1375/1128 mAh g^{-1}, and a CE of 82.1%, 50-MHG@MBH electrodes shows better cycling stability at first several cycles. The reversible capacity

is still 1000 mAh g^{-1} at the 10^{th} cycle, after which, the capacity dropped to 843 mAh g^{-1} gradually and maintained over 150 cycles. The coating effect of $Mg(BH_4)_2$ proved to be effective. To enhance the lithium storage capacity, the 13-MHG and 13-MHG@MBH with smaller size are tested. Apparently, MgH_2 NPs with diameter of 10 nm shows significantly higher reversible capacity. Under the same current density with 50-MHG, a stable capacity of 960 mAh g^{-1} is maintained over 150 cycles, corresponding to a high CE of 99.8% which may be attributed to the smaller size of MgH_2 NPs with better electrical and ionic conductivity. Moreover, the capacity fading could be significantly alleviated with $Mg(BH_4)_2$ coating layer, the 13-MHG@MBH exhibits a first discharge capacity of 2054 mAh g^{-1} with a high CE of 98%, and it remains a high capacity of 1415 mAh g^{-1} after 150 cycles at 200 mA g^{-1}. As a result of the outstanding electrochemical performance, the other lithium storage behaviors of 13-MHG@MBH were furtherly studied. The galvanostatic discharge/charge curves illustrated in **Figure 7.5b**, testing at 200 mA g^{-1}. Herein, differential patterns based on the calculation of galvanostatic dis/charge curves have been thoroughly discussed as presented in **Figure 7.5c and e**. On one hand, the first three cycle curves of 13-MHG@MBH are overlapped well, which indicates the stable cycling stability, while the discharging (charging) peak of 13-MHG is become weaker along with the cycling longer, corresponding with the decline of capacity. On the other hand, for 13-MHG@MBH, the discharging (charging) peak is located at around 0.45 V (0.55 V). The peak which located at 0.45 V is owing to the formation of Mg along with the lithiation of electrode, the charge peak at ~0.55 V refers to the conversion of Mg and LiH accompanied by the resynthesized MgH_2 of the composite. For 13-MHG, the first discharging (charging) peak is located at around 0.46 V (0.56 V) which indicate the conversion and regeneration of MgH_2, the second discharging (charging) peak is

located at around 0.82 V (0.84 V) may contribute to the activation and size effect of MgH_2 NPs, which become weaker during three cycles. Furthermore, the 13-MHG@MBH electrodes also display comparable excellent rate capabilities particularly when cycling at high current densities (**Figure 7.5f**). Specifically, 13-MHG@MBH delivers a reversible capacity of 1652, 1495, 1345, 1228, and 1080 mAh g^{-1} at current densities ranging from 100 mA g^{-1} to 2 A g^{-1}. Consequently, a high capacity of 1566 mAh g^{-1} can be retained when returns to 100 mA g^{-1}. As comparison, the capacity and stability of 13-MHG@MBH are all better than that of 13-MHG, when the current density is increased to 2000 mA g^{-1}, the reversible capacity of 13-MHG rapidly fades to 650 mAh g^{-1}, and only a capacity of about 950 mAh g^{-1} was increased back to 100 mA g^{-1}. Moreover, when cycled at a high current density of 2 A g^{-1}, 13MHG@MBH exhibits an admirable capacity of 800 mAh g^{-1} can be maintained over 300 cycles (**Figure 7.5g**). The advanced performances of 13-MHG@MBH electrodes can be mainly ascribed to the York-shell nanostructure of MgH_2 on graphene, which demonstrate fast reaction kinetics, high-capacity utilizations, and electrochemical stabilities during cycling.

Figure 7.5h indicates the electrochemical impedance spectra (EIS) of 13-MHG@MBH before and after 50 cycles compared with 13-MHG electrode. The Nyquist plots of 13-MHG@MBH shows apparently much smaller depressed semicircle at the middle-to-high frequency region, than that of 13-MHG, indicating an obvious superiority in reducing interfacial resistance and stabilizing interface.

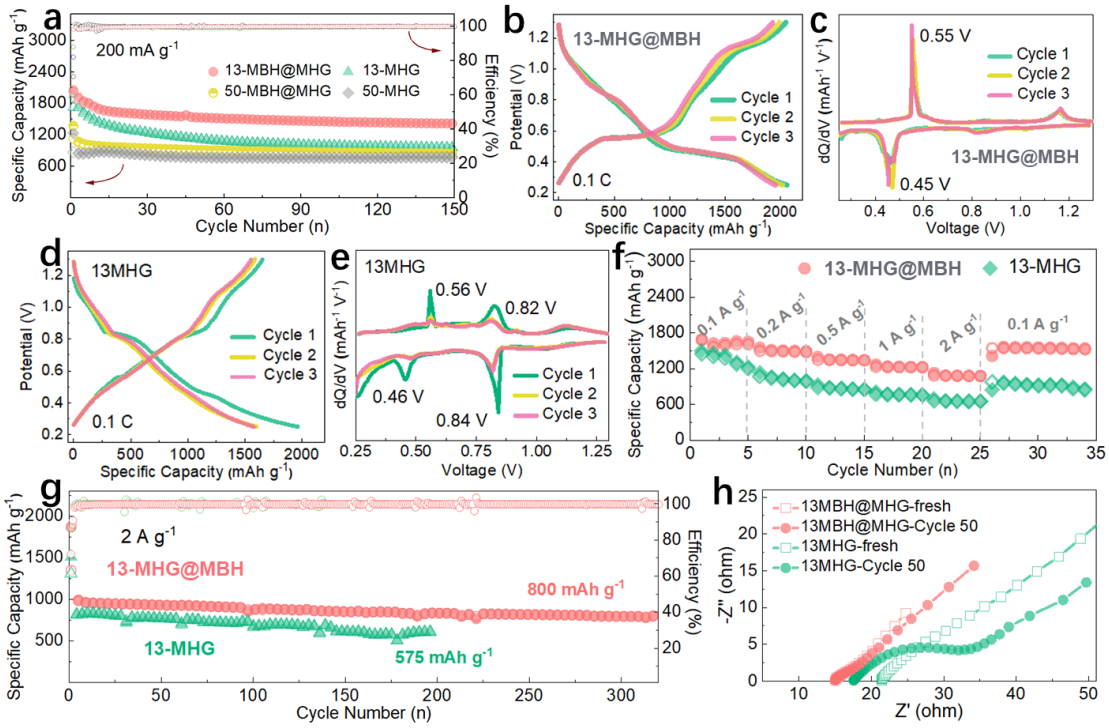

Figure 7.5 Electrochemical performance. (a) Cycling performance of 50-MHG@MBH, 13-MHG@MBH, and MHG electrodes at 200 mA g^{-1}. (b, d) Galvanostatic charge-discharge profiles of 13-MHG@MBH, and 13-MHG at 200 mA g^{-1} at first 3 cycles, respectively. (c, e) The corresponding derivative curves (dQ/dE) of assembled half-cell. (f) Rate performance of 13-MHG@MBH and 13-MHG electrodes from 100 to 2000 mA g^{-1}. (g) Cycling performance of 13-MHG@MBH and 13-MHG electrodes at 2 A g^{-1}. (h) Nyquist plots of 13-MHG@MBH and 13-MHG electrodes in the discharged state before and after 50 cycles.

Hence, to understand the role of $Mg(BH_4)_2$ composites during the lithium storage process, and reveal the mechanism of lithium storage, the structure and phase evolution of 13-MHG@MBH was explored through XRD and XPS during the first cycle. As illustrated in **Figure 7.6a and b**, in discharge process, the intensity of XRD pattern peaks belongs to MgH_2 gradually decreases, and disappeared at the fully discharged state, however the change of peaks for Mg phase is reversed. The peaks of Mg appeared

during the whole discharge process. When it comes to the fully discharged state, all the peaks belong to MgH_2 disappear, instead of which, the peak sign ascribed to Mg becomes stronger, and the peak corresponding to LiH start to be detected. Finally, in the charge state, the peak intensity of MgH_2, recovers along with the disappear of Mg and LiH. The XRD patterns elucidated a good reversibility of the electrochemical cycling in potential window of 0.25~1.3 V. Simultaneously, the structure and phase change during cycling was detected by X-ray photoelectron spectroscopy (XPS) of 13-MHG@MBH with the presence of Li and B, before which, we analyzed the possible reaction between $Mg(BH_4)_2$ and Li via literature research and confirmed our conclusions through experimental results. As shown in **Figure 7.7**, the Inoishi's group [37] has firstly applied bulk $Mg(BH_4)_2$ as anode, and Li metal as reverse electrode with $LiBH_4$ as electrolyte. The electrochemical tests were performed between 0.3~1.5 V. Through the analysis of the discharge/charge capacity and the exhibited electrochemical plateau, they assessed the reaction mechanism of the lithiation of $Mg(BH_4)_2$ anode, and designed experiments to confirm that the products of the lithiation of $Mg(BH_4)_2$ are magnesium and $LiBH_4$ during the discharge process through solid state NMR and ex situ XRD. The electrochemical performance of bulk $Mg(BH_4)_2$ was also conducted with a voltage range of 0.25~1.3 V and MgH_2 as the comparison sample in this thesis. As shown in **Figure 7.7a and b**, the initial discharge capacity of bulk $Mg(BH_4)_2$ is as high as 1680 mAh g^{-1}, far more higher than that of 664 mAh g^{-1} tested by Inoishi. And the nanosized $Mg(BH_4)_2$@G composite synthesized through the same gas-solid reaction, shows ultrahigh capacity of 2750 mAh g^{-1} with an obvious discharge/charge plateau of 0.45 V/0.55 V which could be ascribed to the conversion of MgH_2 **(Figure 7.7c and d)**. Moreover, the capacity of $Mg(BH_4)_2$@G is maintained 900 mAh g^{-1} after 20 cycles at current density of 200 mA g^{-1} which cloud be ascribed

to the discharge/charge cycling of MgH_2, so the MgH_2 could be determined as one of the products of lithiation of $Mg(BH_4)_2$. However, the high capacity is still too far to reach with only two products of MgH_2 and $LiBH_4$, other reaction mechanism with boron as product was considered. Hence, the electrochemical performance of amorphous boron powder was tested under the same conditions with $Mg(BH_4)_2$. As shown in **Figure 7.7e and f**, the amorphous powder displays a steady capacity of 300 mAh g^{-1} with an initial capacity of 732 mAh g^{-1}. And the lithiation product at fully discharged state was characterized through PXRD (**Figure 7.7g**), the phase of Li_2B_6 and LiOH are observed, LiOH may attributed to the oxidation of Li metal during testing process, which indicates that Li_2B_6 was the product of the lithiation of boron under this electrochemical testing conditions. Furtherly, XPS is also used to verify the existence of Li_2B_6, the discharged /charged samples of boron sample are tested (**Figure 7.7h and i**). As comparison, the XPS spectrum of synthesized pure Li_2B_6 was presented. The peak of 187.2 eV in the B 1s spectrum and the peak of 53.5 eV in the Li 1s spectrum are related to the formation of Li_2B_6 which always exists during the charge and discharge process of amorphous B. In summary, the lithiation products of nanosized $Mg(BH_4)_2$ are verified to be MgH_2, $LiBH_4$ and Li_2B_6. By virtue of both good electric conductivity and ionic conductivity, Li_2B_6 [38, 39] is suitable for acting as an interface buffer material between electrode and electrolyte which could improve the lithium-ion transport kinetics of the electrode materials and the conductivity of the electrode material at the same time.

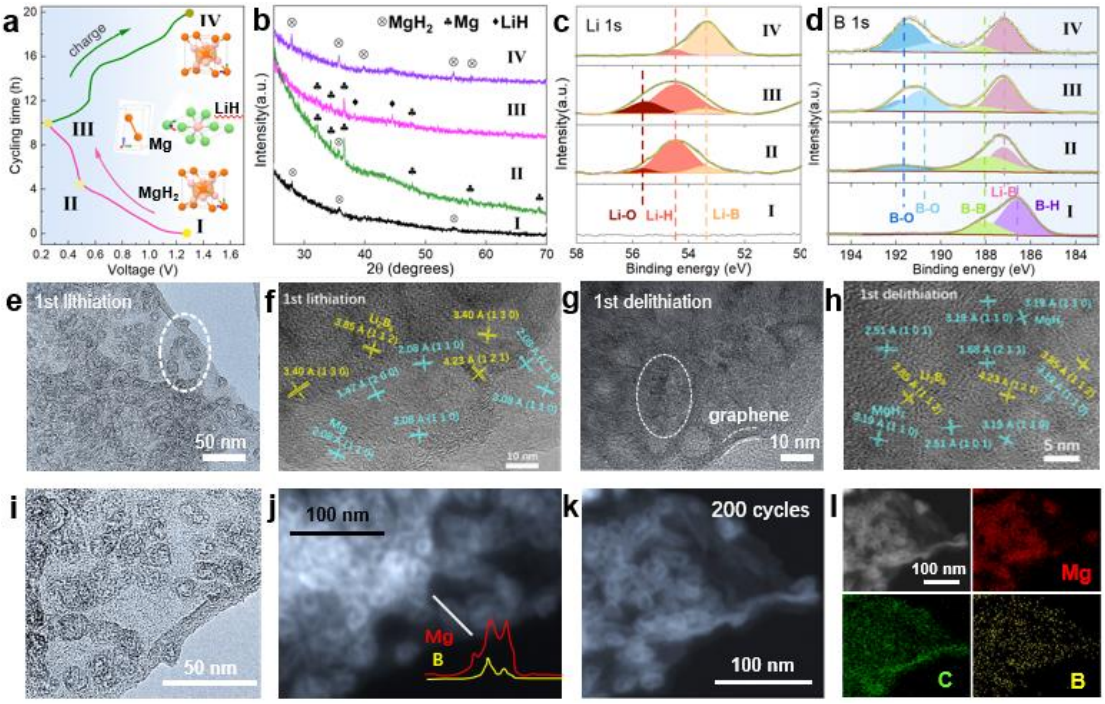

Figure 7.6 (a) Evolution of the potential (V) along with cycling time for the 13-MHG@MBH electrode at 200 mA g^{-1} in the first cycle., (b) XRD patterns of 13-MHG@MBH at different cycle states. And XPS spectra of high resolution of Li 1s (c) and B 1s (d) of 13-MHG@MBH at different cycle states. (e–f) HRTEM images of 13-MHG@MBH collected at the first lithiation state and (g-h) the delithiation state. (i) TEM images and (j) the EDS line scan on a STEM image of 13-MHG@MBH at the first delithiation state. (k) STEM image and (l) the elemental mapping of 13-MHG@MBH after 200 cycles at 2 A g^{-1}.

Come back to the XPS analysis of 13-MHG@MBH, in **Figure 7.6c and d**. At initial state of 13-MHG@MBH, the peak of 186.7 eV in the B 1s spectrum indicate the existence of $Mg(BH_4)_2$, [40, 41] and during the discharge process, the peak of 186.7 eV shift to 187.3 eV, which ascribed to Li-B bonds, which always exists even come back to the fully charge state, which means the irreversibility of $Mg(BH_4)_2$. On consideration of Li 1s spectrum, the Li-H bonds of 54.5 eV appears during discharge, which coincidence well with the result of xtests, and almost weakened to barely seen in the

fully charged state. However, the peaks of 53.5 eV could be observed during the whole discharge/charge process.

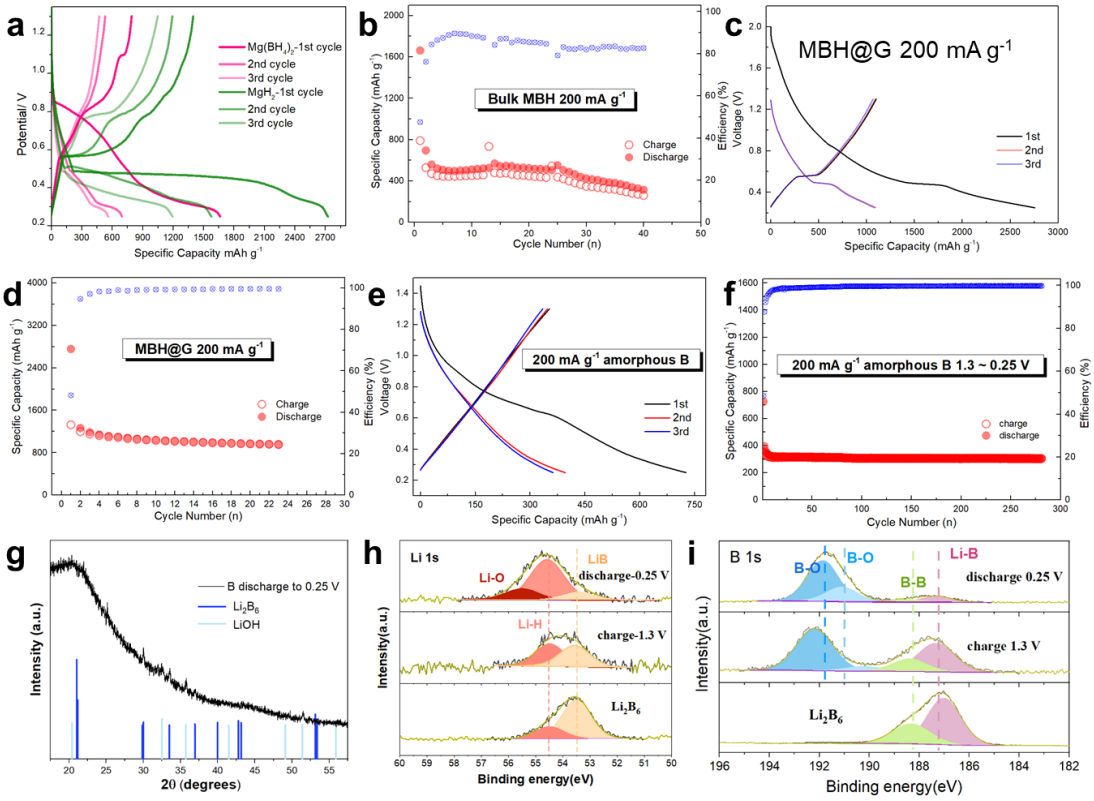

Figure 7.7 Galvanostatic charge-discharge profiles of (a) bulk MgH_2 and $Mg(BH_4)_2$, (c) nano MBH@G, (e) amorphous B at 200 mA g^{-1} at selected cycles. Cycling performance of (b) bulk $Mg(BH_4)_2$, (d) nano MBH@G and (f) amorphous B at 200 mA g^{-1}. PXRD patterns of delithiation products of amorphous B samples (g). And XPS spectra of high resolution of Li 1s (c) and B 1s (d) of amorphous B samples at different cycle states.

As multiple nanocrystalline phases have been generated during cycling, the structure and morphological evolution of 13-MHG@MBH was detected by TEM. The HRTEM images at the fully lithiation state (**Figure 7.6e-f**) demonstrate the lattice fringes with d-spacing of 3.85, 3.4 and 4.23 Å correspond to the (112), (130) and (121) planes of generated Li_2B_6 alloys. Besides, the lattice fringes with d-spacing of 2.08 and 1.47 Å correspond to the (110), (200) planes of formed Mg crystals. **Figure 7.6g and h** shows

the reformation of MgH_2 and the maintained Li_2B_6. The HRTEM results are coincidence well with that of XRPD patterns. It can be seen in **Figure 7.6i-l**, 13-MHG@MBH nanoparticles still retains its original structure with uniform separation anchored on graphene nanosheets. The STEM images after 200 cycles at 2 A g^{-1} and the corresponding elemental mapping indicating the excellent structure stability of 13-MHG@MBH nanoparticles with 12.08 diameter grown on the graphene sheet without any aggregation.

The interface between electrolyte and electrode is investigated by SEM with energy dispersive X-ray spectrometry (EDS) to gain further information of the interfacial conditions. Shown in **Figure 7.8a-b2**, in contrast to the 13-MHG‖$LiBH_4$ interface, the 13-MHG@MBH‖$LiBH_4$ interface demonstrates better connection and compact without obvious boundary even after 100 cycles at current density of 2 A g^{-1}. The signs that small pores and fractures start to spread could be observed on the 13-MHG‖$LiBH_4$ interface after 300 cycles. However, there is apparent interspace and gap generated on the 13-MHG‖$LiBH_4$ interface after 100 cycles at the same current density. At 200th cycle, the interface becomes porous and obvious folds and fractures appear at it. The results presents the good compatibility of 13-MHG@MBH electrode and $LiBH_4$ electrolyte was achieved, not only the $Mg(BH_4)_2$ coating lays but also as-synthesized Li_2B_6 are benefit for the interface contact and stability.

Figure 7.8c and d shows the EIS comparison of 13-MHG@MBH and 13-MHG. The interface between the electrode and SE can become an ion transport "bottleneck" due to chemical reactions [42]. It is important to study the evolution of interfacial properties with cycling, so we conducted the EIS measurement during the first stepwise discharging/charging for 13-MHG@MBH and 13-MHG anodes. It is well-known that the semi-circle at high frequency region corresponds to extremely fast process such as

SE ionic conductivity. [43] The resistance value extracted from this region does not vary over cycling. With the coating layer, the ion conductivity of the cell system of 13-MHG@MBH is higher than that of 13-MHG; Mid frequency (10 kHz-10 Hz) region are the most significant portion in this study which is correspond to charge transfer through electrode/electrolyte interface. [44] In contrast to 13-MHG in **Figure 7.8f and g**, the 13-MHG@MBH shows lower interface resistance of $R_{13\text{-}MHG@MBH|LBH,}$ which are calculated to be only 2.8 Ω before cycling, which is much lower than that of the 13-MHG (20 Ω). During the cycling process, the $R_{13\text{-}MHG@MBH|LBH,}$ are generally remained unchanged, indicating the interfacial stability, while the $R_{13\text{-}MHG|LBH}$ of interfacial resistance of 13-MHG are changing along with the cycling, the charged state shows higher interfacial resistance than that of discharged state. The EIS results reveal that the 13-MHG interface suffers from substantial instability. The existence of the double ionic-electronic interface Li_2B_6, significantly enhanced the stability and connection of the electrode/SE interface. Thus, effectively facilitates both electronic and lithium-ion transfer throughout the whole electrode and hence decreases the apparent resistance of the electrode. Upon the proceeding of cycling lithiation and delithiation to 200 cycles, the interface resistance for 13-MHG@MBH electrode exhibits a gently decrease from 5 Ω to only 2.2 Ω owing to the interface stability during cycling charge and discharge process, while this value is sharply changed for 13-MHG electrode, indicating the presence of $Mg(BH_4)_2$ as the protective shell could effectively stabilize the interface between MgH_2 and $LiBH_4$, which contributes to enhancing the cycling stability of MgH_2-based electrode.

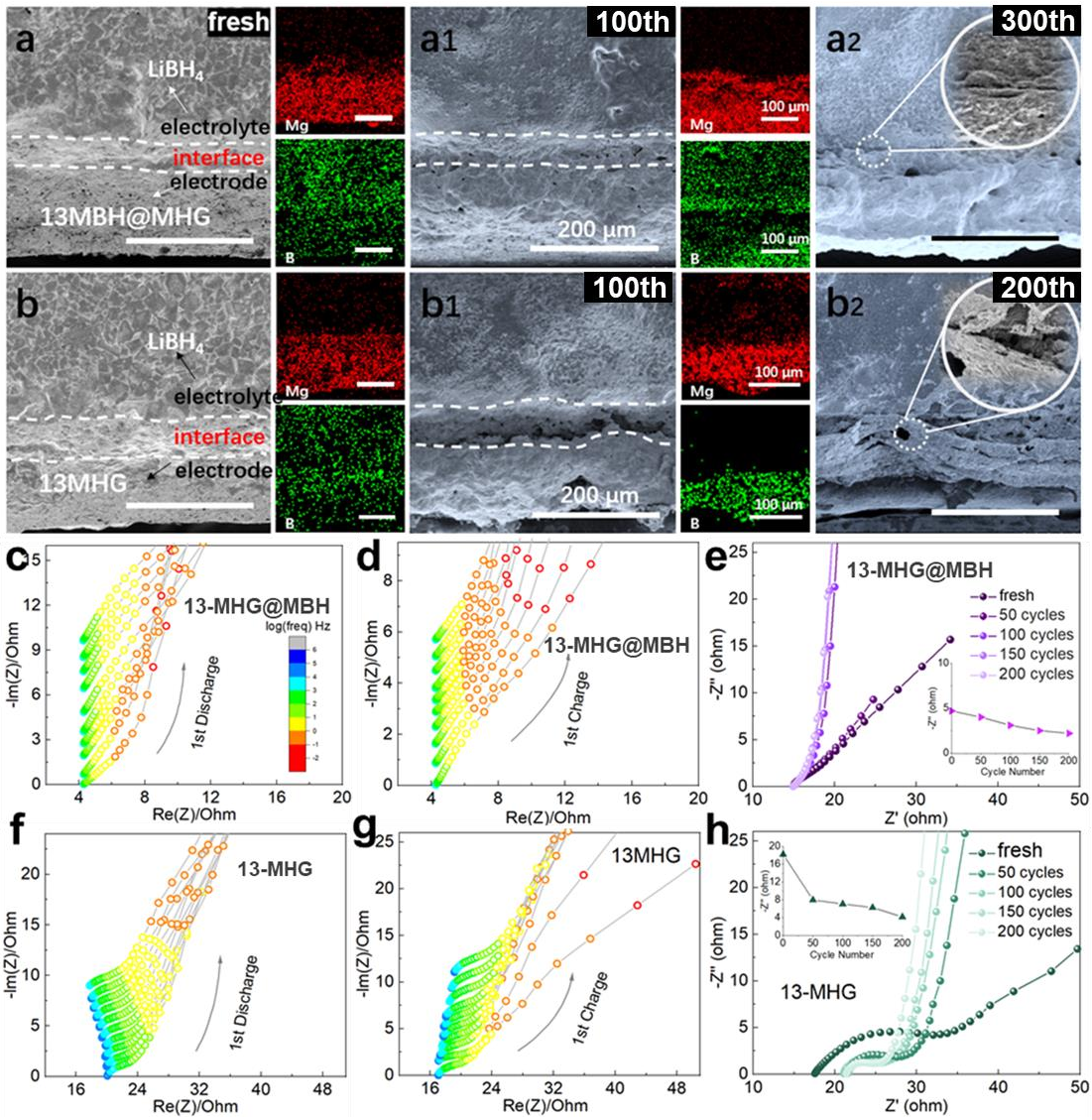

Figure 7.8 Cross-sectional SEM image of electrode−electrolyte interface. SEM images of $LiBH_4$/13-MHG@MBH interface (a) after 100 cycles (a1) and 300 cycles (a2). SEM images of $LiBH_4$/13-MHG interface (b) after 100 cycles (b1) and 200 cycles (b2) at 2 A g^{-1}. Impedance measurement during the initial discharge and charge cycle for 13-MHG@MBH (c-d) and MHG electrodes (f-g). Nyquist plots of MHG@MBH (e) and MHG (h) electrodes in the charged state before and after 50,100,150, 200 cycles.

To accurately characterizing potential polarization, the potentiation intermittent titration technique (PITT) is adopted to understand the electrode kinetics and reaction pathways of the diffusion coefficient of Li^+ ions [45,46]. In the PITT measurement, the

voltage steps do not go on to next step until the current decays to < 2 mA g^{-1} (C/1000). Only the potential range of conversion reaction has been considered since the single-phase region is very narrow. For the 13-MHG@MBH sample, the lithiation reaction proceeds through several 10 mV steps at the potential range from 0.25 to 1.1 V. As illustrated in **Figure 7.9a and a_1**, the $D_{(Li+)}$ obtained from PITT are plotted versus the voltage. In this case, the diffusion coefficient of Li^+ for 13-MHG@MBH and 13-MHG process were 1.5 x 10^{-15} cm^2 s^{-1} at 0.5 V and 3.65 x 10^{-17} cm^2 s^{-1} at 0.5 V, respectively. The diffusion coefficients of 13-MHG@MBH for all the whole conversion steps were calculated to be higher than that of 13-MHG, indicating the fast Li^+ ions diffusion and electrode kinetics for the improved rate cycling performance of 13-MHG@MBH electrode. In addition, morphology of various electrodes after 50 cycles at 2 A g^{-1} was systematically investigated using SEM measurement (**Figure 7.9b-d2**). As presented, after 50 cycles at high current density, MgH_2 NPs of pure MHG suffers from serious aggregation and pulverization due to the large volume change of MgH_2 and the lack of the physical protection upon cycling process, which corresponds well with its fast decay of specific capacities. After 200 cycles, the size of the particles increased from 11 nm to 14.91 nm. In comparison, under the identical conditions, the size of 13MHG@MBH decreased from 13.86 nm to 12.02 nm, which could be attributed to the transformation of $Mg(BH_4)_2$. As proved above, the $Mg(BH_4)_2$ was transformed to Li_2B_6 surrounding MgH_2 NPs after the first discharge process. As a result, the maintenance of the size of MgH_2 NPs could attributed to the existence of Li_2B_6, which not only alleviated the volume change but also prevented aggregation of MgH_2 NPs during cycles of lithiation and delithiation processes.

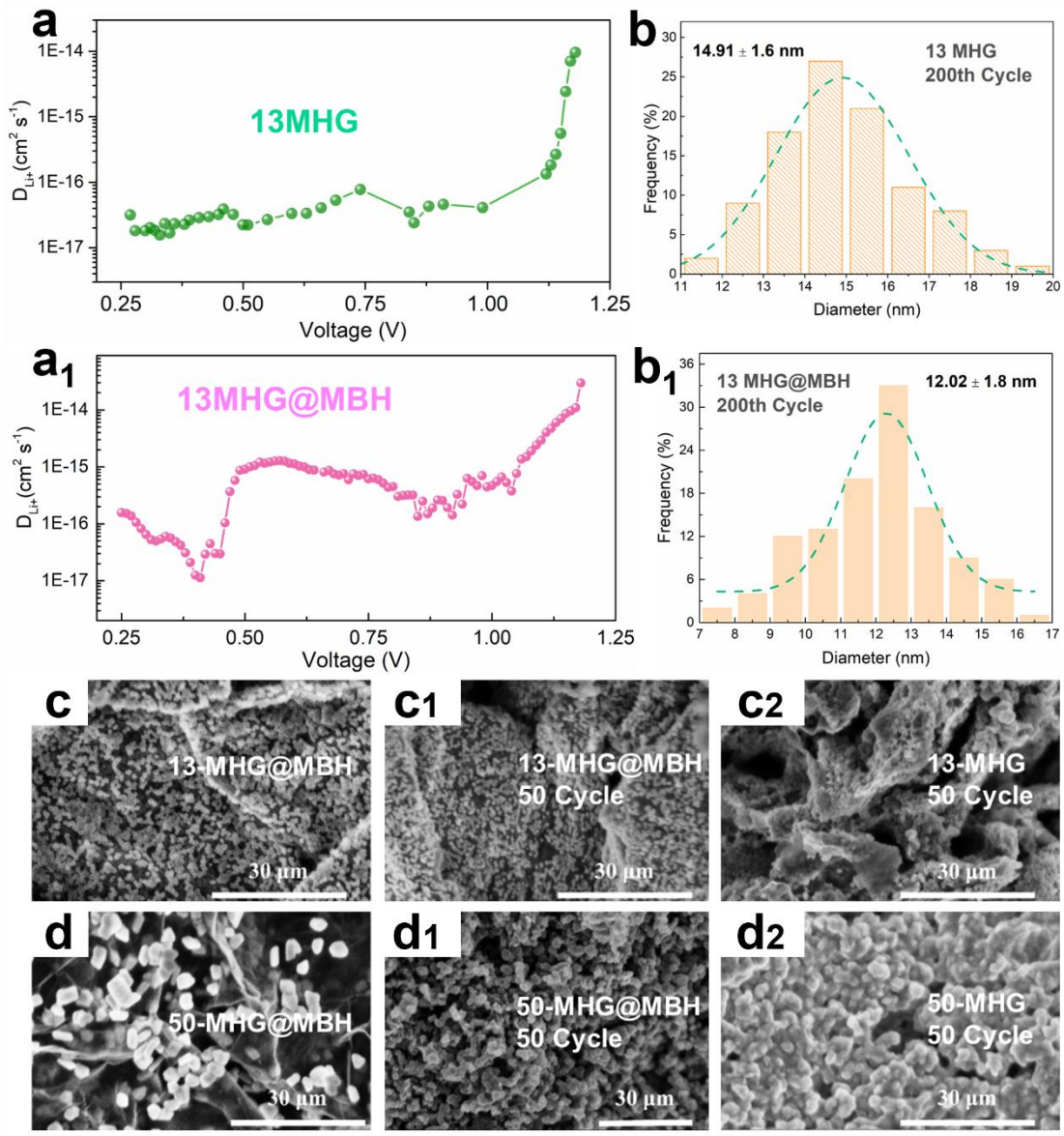

Figure 7.9 Diffusion coefficients of 13-MHG (a) and 13-MHG@MBH (a_1) extracted from high resolution PITT characterization. The particle size distributions of 13-MHG (b) and 13-MHG@MBH (b_1) after 200 cycles at 2 A g^{-1}. SEM images of 13-MHG@MBH before and after 50 cycles at 2 A g^{-1} (c-c1), SEM images of 50-MHG@MBH before and after 50 cycles at 2 A g^{-1} (d-d1), SEM images of 13-MHG (c2) and 50-MHG (d2) after 50 cycles at 2 A g^{-1}.

7.4 Conclusion

In summary, based on the formation of yolk-shell-like structure of $MgH_2@Mg(BH_4)_2$ on graphene, a new coating layer Li_2B_6 which is double ionic-electronic transfer interface outside the MgH_2 NPs was synthesized through further lithiation. Particularly, the formation of yolk-shell-like structure of $MgH_2@Li_2B_6$ on graphene could not only physically accommodate the volume change of MgH_2, but also significantly facilitate the transportation of electrons and ions throughout the whole electrode, which are benefit for the superior rate capability. More importantly, not only the ultrathin $Mg(BH_4)_2$ layer, but also the layer of Li_2B_6 has the advantage of increasing interfacial contact between the electrode and SE, thus decreasing the interface resistance, and the Li_2B_6 shell also has the ability to maintain the interface stability which leads to a long cycle life at high current density. The synergistic effects of Li_2B_6 leads to outstanding lithium storage properties, including high specific capacity, superior rate capability, and long cycle life. Therefore, this work offers a new methodology for developing metal-hydride-based anodes with superior solid state lithium storage performance and this novel strategy could be extended to the fabrication of various types of advanced electrode materials.

7.5 Reference

[1] Manthiram, A.; Yu, X.; Wang, S. Lithium Battery Chemistries Enabled by Solid-State Electrolytes. *Nat. Rev. Mater.* **2017**, *2*, 1.

[2] Bruce, P. G.; Scrosati, B.; Tarascon, J.-M. Nanomaterials for Rechargeable Lithium Batteries. *Angew. Chemie Int. Ed.* **2008**, *47*, 2930.

[3] Manthiram, A. An Outlook on Lithium-Ion Battery Technology. *ACS Cent. Sci.* **2017**, *3*, 1063.

[4] Anasori, B.; Lukatskaya, M. R.; Gogotsi, Y. 2D Metal Carbides and Nitrides (MXenes) for Energy Storage. *Nat. Rev. Mater.* **2017**, *2*, 16098.

[5] Wang, C. D.; Chen, S. M. et al. Atomic Sn^{4+} Decorated into Vanadium Carbide MXene Interlayers for Superior Lithium Storage. *Adv. Energy Mater.* **2019**, *9*, 1802977.

[6] Naguib, M.; Halim, J.; Lu, J.; Cook, K. M.; Hultman, L.; Gogotsi, Y.; Barsoum, M. W. New Two-Dimensional Niobium and Vanadium Carbides as Promising Materials for Li-Ion Batteries. *J. Am. Chem. Soc*. **2013**, *135*, 15966.

[7] Liu, J.; Zhang, Q. et al. A Robust Ion-Conductive Biopolymer as a Binder for Si Anodes of Lithium-Ion Batteries. *Adv. Funct. Mater*. **2015**, *25*, 3599.

[8] Son, I. H.; Hwan Park, J. et al. Silicon Carbide-Free Graphene Growth on Silicon for Lithium-Ion Battery with High Volumetric Energy Density. *Nat. Commun.* **2015**, *6*. 7393.

[9] Jin, Y.; Zhu, B.; Lu, Z.; Liu, N.; Zhu, J. Challenges and Recent Progress in the Development of Si Anodes for Lithium-Ion Battery. Adv. Energy Mater. 2017, 7, 1700715.

[10] Oumellal, Y.; Rougier, A.; Nazri, G. A.; Tarascon, J.-M.; Aymard, L. Metal Hydrides for Lithium-Ion Batteries. *Nat. Mater*. **2008**, *7*, 916.

[11] Zhang, B.; Xia, G.; Sun, D.; Fang, F.; Yu, X. Magnesium Hydride Nanoparticles Self-Assembled on Graphene as Anode Material for High-Performance Lithium-Ion Batteries. *ACS Nano* **2018**, *12*, 3816.

[12] Bai, S.; Liu, X.; Zhu, K.; Wu, S.; Zhou, H. Metal–Organic Framework-Based Separator for Lithium–Sulfur Batteries. Nat. Energy 2016, 1 (7), 16094.

[13] Seh, Z. W.; Sun, Y. et al. Designing High-Energy Lithium–Sulfur Batteries. *Chem. Soc. Rev.* **2016**, *45*, 5605

[14] Xia, Q.; Li, W.; Miao, Z.; Chou, S.; Liu, H. Phosphorus and Phosphide Nanomaterials for Sodium-Ion Batteries. Nano Res. 2017, 10 (12), 4055.

[15] Zheng, M.; Tang, H.; Li, L.; Hu, Q.; Zhang, L.; Xue, H.; Pang, H. Hierarchically Nanostructured Transition Metal Oxides for Lithium-Ion Batteries. Adv. Sci. 2018, 5 (3), 1700592.

[16] Zhao, Y.; Li, X. et al. Recent Developments and Understanding of Novel Mixed Transition-Metal Oxides as Anodes in Lithium-Ion Batteries. *Adv. Energy Mater*. **2016**, *6*, 1502175.

[17] Oumellal, Y.; Zlotea, C. et al. Bottom-up Preparation of MgH_2 Nanoparticles with Enhanced Cycle Life Stability during Electrochemical Conversion in Li-Ion Batteries. *Nanoscale*, **2014**, *6*, 14459.

[18] Xia, G. L.; Tan, Y. B.; Chen, X. W.; Sun, D. L.; Guo, Z. P.; Liu, H. K.; Ouyang, Uniformly Self-Assembled on Graphene. *Adv. Mater.* **2015**, *27*, 5981.

[19] Zhong, S.L.; Ju, Shunlong, Magnesium Hydride Nanoparticles Anchored on MXene Sheets as High Capacity Anode for Lithium-Ion Batteries, *J. Energy Chem.* **2021**, *62*, 431.

[20] Zhang, B. P.; Si, Y. S. et al. Hydrangea-Shaped 3D Hierarchical Porous Magnesium Hydride−Carbon Framework with High Rate Performance for Lithium Storage. *ACS Appl. Mater. Interfaces*, **2019**, *11*, 28987.

[21] Matsuo, M.; Nakamori, Y. et al. Lithium Superionic Conduction in Lithium Borohydride Accompanied by Structural Transition. *Appl. Phys. Lett.* **2007**, *91*, 224103.

[22] Kim, S.; Oguchi, H. et al. A Complex Hydride Lithium Superionic Conductor for High-Energy Density All-Solid-State Lithium Metal Batteries. *Nat. Commun.* **2019**, *10*, 1081.

[23] a) Kharbachi, A. E.; Uesato, H. et al. MgH_2–CoO: a Conversion-Type Composite Electrode for $LiBH_4$-Based All-Solid-State Lithium-Ion Batteries, *RSC Adv.*, **2018**, *8*, 23468. b) Zeng, L.; Kawahito, K. et al. Metal Hydride-Based Materials towards High Performance Negative Electrodes for All-Solid-State Lithium-Ion Batteries, *Chem. Commun.*, **2015**, *51*, 9773.

[24] Wu, N.; Chien, P. H.; et al. Enhanced Surface Interactions Enable Fast Li^+ Conduction in Oxide/Polymer Composite Electrolyte. *Angew. Chem. Int. Ed.* **2020**, *59*, 4131.

[25] Xu, H.; Li, Y.; Zhou, A.; Wu, N.; Xin S.; Li, Z. Y.; Goodenough, J. B., Li_3N-Modified Garnet Electrolyte for All-Solid-State Lithium Metal Batteries Operated at 40 °C. *Nano Lett.* **2018**, *18*, 7414.

[26] Zhao, Q.; Liu, X.; Stalin, S. et al. Solid-State Polymer Electrolytes with in-Built Fast Interfacial Transport for Secondary Lithium Batteries. *Nat. Energy* **2019**, *4*, 365.

[27] Mu, S.; Huang, W. L. et al. Heterogeneous Electrolyte Membranes Enabling Double-Side Stable Interfaces for Solid Lithium Batteries. *J. Energy Chem.* **2021**, *60*, 162.

[28] Huang, Y. Q.; Xia, G. L.; Chen, J.; Zhang, B. P.; Li, Q.; Yu, X. B. One-Step Uniform Growth of Magnesium Hydride Nanoparticles on Graphene. *Prog. Nat. Sci.* **2017**, *27*, 87.

[29] Liu R, Zhao Y, Chu T. Theoretical Exploration of MgH_2 and Graphene Nano-Flakes in Cyclohexane: Proposing a New Perspective toward Functional Hydrogen Storage material. *Chem. Commun.*, **2015**, *51*, 2429.

[30] Bryan, D. A. and Joseph. B. T., Nanoparticle Conversion Chemistry: Kirkendall Effect, Galvanic Exchange, and Anion Exchange. *Nanoscale.* **2014**, *6*, 12195.

[31] Hagemann, H.; Danna, V.; et al., New Fundamental Experimental Studies on α-$Mg(BH_4)_2$ and other Borohydrides. *J. Alloys Compd.* **2011**, *509*, S688.

[32] A. G. D. Colognesi, L. U. M. Zoppi et al. High Resolution Raman and Neutron Investigation of $Mg(BH_4)_2$ in an Extensive Temperature Range. *J. Phys. Chem A.* **2010**, *114*, 2788.

[33] J. G. Zheng, H. Cheng, X. Z. Xiao, M. Chen, L. X. Chen. Enhanced Low Temperature Hydrogen Desorption Properties and Mechanism of $Mg(BH_4)_2$ Composited with 2D MXene. *Int. J. Hydrogen Energy.* **2019**, *44*, 24292.

[34] J. G. Zheng, Z. D. Yao, X. Z. Xiao et al. Enhanced Hydrogen Storage Properties of High-Loading Nanoconfined $LiBH_4$–$Mg(BH_4)_2$ Composites with Porous Hollow Carbon Nanospheres. *Int. J. Hydrogen Energy.* **2021**, *46*, 852.

[35] J. G. Zheng, X. C Wang, X. Z. Xiao et al. Improved Reversible Dehydrogenation Properties of $Mg(BH_4)_2$ Catalyzed by Dual-Cation Transition Metal Fluorides K_2TiF_6 and K_2NbF_7. *Chem. Eng. J.* **2021**, *412*, 128738.

[36] A. C. Ferrari, D. M. Basko. Raman Spectroscopy as A Versatile Tool for Studying the Properties of Graphene. *Nat. Nanotechnol*. **2013**, *8*, 235.

[37] H. Sato, R. Sakamoto, H. Minami, H. Izumi, K. Ideta, A. Inoishi and S. Okada. The In Situ Formation of an Electrolyte via the Lithiation of $Mg(BH_4)_2$ in an All-Solid-State Lithium Battery. *Chem. Commun.* **2021**, *57*, 2605.

[38] Q. Y. Zhou, H. F. Zhan, B. Chen, H. Li, Z. D. Huang, Y. W. Ma, H. Zhang, S. Z. Li, X. Huang and W. Huang. Imparting Boron Nanosheets with Ambient Stability through Methyl Group Functionalization for Mechanistic Investigation of Their Lithiation Process. *ACS Appl. Mater. Interfaces* **2020**, *12*, 23370.

[39] W. J. Dong, Y. T. Zhao, X. Wang, X. T. Yuan, K. J. Bu, C. L. Dong, R. Q. Wang and F. Q. Huang. Boron Embedded in Metal Iron Matrix as a Novel Anode Material of Excellent Performance. *Adv. Mater.* **2018**, *30*, 1801409.

[40] C. Du, W. Younas, Z. Wang. *et al.* Constructing Sheet-Assembled Hollow CuSe Nanocubes to Boost the Rate Capability of Rechargeable Magnesium Batteries. *J. Mater. Chem. A.* **2021**, *9*, 3648.

[41] Z. Y. Li, T. Diemant, Z. Meng, Y. L. Xiu, A. Reupert, L. P. Wang, M. Fichtner and Z. Zhao-Karger. Establishing a Stable Anode–Electrolyte Interface in Mg Batteries by Electrolyte Additive. *ACS Appl. Mater. Interfaces.* **2021**, *13*, 33123.

[42] J. G. Zheng, C. G. Sun, Z. X. Wang, S. J. Liu, B. G. An, Z. H. Sun and F. Li. Double Ionic-Electronic Transfer Interface Layers for All Solid-State Lithium Batteries. *Angew. Chem. Int. Ed.* **2021**, *60*, 18448.

[43] T. Deng, X. Ji, Y. Zhao. *et al.* Tuning the Anode–Electrolyte Interface Chemistry for Garnet-Based Solid-State Li Metal Batteries. *Adv. Mater.* **2020**, *32*, 2000030.

[44] B. Zahiri, A. Patra, C. Kiggins, A. X. B. Yong, E. Ertekin, J. B. Cook and P. V. Braun. Revealing the Role of the Cathode–Electrolyte Interface on Solid-State Batteries. *Nat. Mater.* **2021**, *20*, 1392.

[45] D. Renz, M. Cronau and B. Roling. Determination of Lithium Diffusion Coefficients in Single Battery Active Material Particles by Using an AFM-Based Steady-State Diffusion Depolarization Technique. *J. Phys. Chem. C.* **2021**, *125*, 2230.

[46] J. Y. Liu, J. X. Wu, S. W. Fan and G. D. Li. CoS_2/N-Doped Hollow Spheres as an Anode Material for High-Performance Sodium-Ion Batteries. *Chem. Eur. J.* **2021**, *27*, 9820.

CHAPTER 8 SUMMARY

8.1 General Conclusions

This doctoral thesis mainly focuses on improving the lithium storage performance of metal hydride materials represented by sodium aluminum hydride and magnesium hydride as anode materials for lithium-ion batteries. Metal hydride is regarded as one of the potential anode materials for lithium-ion batteries due to its high lithium storage capacity, low voltage platform, and low polarization. Unfortunately, metal hydrides often have defects such as instability of electrode structure and short cycle life due to poor conductivity, volume expansion, and high chemical activity, which are easily oxidized during applications. In this thesis, the metal hydride is modified in a targeted manner from four aspects: carbon doping, nano crystallization, surface modification and process modification through the methodology of structural design. By way of self-assembly, gas-solid reaction and other synthesis methods, the multi nanostructure of metal hydride-based anode materials ($NaAlH_4$ and MgH_2) were designed, and a variety of composite materials of metal hydride and graphene with different structures were successfully prepared, which not only successfully improved the conductivity of the metal hydride anode material and effectively alleviated the volume effect, and also improve the lithium storage performance of the sodium aluminum hydride and magnesium hydride systems. This paper also conducted a series of detection and analysis on the physical and chemical properties of the synthesized composite materials and performed a complete and reliable electrochemical performance characterization of the lithium-ion battery systems. The following parts concluded the outcomes of this doctoral work.

A robust nanostructure composed of homogeneous $NaAlH_4$ nanoparticles with an average size of ~ 12 nm encapsulated in graphene nanosheets has been developed via a facile solvent evaporation induced deposition method with a tunable loading and distribution. The SAH@G-50 electrode exhibits an initial discharge and charge capacity of 1995 and 1710 mAh g^{-1} at 100 mAh g^{-1}, respectively corresponding to a coulombic efficiency (CE) of 85.7%. The specific discharge capacity slowly decayed and then was stabilized at ~698 mAh g^{-1} after 200 cycles. The rate capability test of SAH@G-50 electrode at current densities ranging from 50 to 500 mA g^{-1} demonstrates that this electrode could deliver average capacities of 1495, 1273, 924, 620, and 529 mAh g^{-1} at 50, 100, 200, 300, and 500 mA g^{-1}, respectively. When switching back to 100 mA g^{-1} after the high-rate cycling, the capacity can return to 950 mA h g^{-1}. This validates the strong tolerance of SAH@G-50 electrode toward rapid lithium ion insertion and extraction. Furthermore, the SAH@G-50 electrode delivered an impressive discharge capacity of 522 mAh g^{-1} after 200 cycles at a high current density of 500 mA g^{-1}, with a high CE of around 100% through the whole cycling process, which further demonstrates its superior reversibility. It has been founded in this thesis, graphene could act as an effective platform to tailor the metal-hydrogen bonds of $NaAlH_4$ through their favorable molecular interaction. Theoretical and experimental results confirm that graphene is capable of weakening the Al-H bonds of $NaAlH_4$, thus facilitating the breaking and recombination of Al-H bonds towards advanced lithium storage performance. In addition, The synergistic effects of the favorable molecular interaction between graphene and $NaAlH_4$, and the noticeable decrease in particle size significantly boost the lithium storage performances of $NaAlH_4$. This method provides new avenues to tailor the molecular bonds of metal hydrides for a new range of applications in various fields.

An facile synthesis strategy has been reported towards the precise construction and morphology controllable of MgH_2@G for advanced performance in LIBs. A series of magnesium hydride-graphene nanostructures with different morphologies (nanospheres, nanorods and nanosheets) were achieved through the self-assembly of MgH_2 growing uniformly on the graphene nanosheets, under the hydrogenolysis of $(C_4H_9)_2Mg$. Not only the shape, but also the size and loading ratio of MgH_2 could be precisely controlled via parameters regulation. Compared with the nano MgH_2, the MgH_2@G demonstrates better lithium storage performance benefiting from the graphene supported nanostructure with better electronic conductivity. Among the different morphologies, the nanospheres delivers higher capacity utilization and more stable cycling performance (a reversible capability around 520 mAh g^{-1} under 200 mA g^{-1} after 50 cycles) than the MgH_2@G nanorods and nanosheets, as a result of the higher specific surface area and more sufficient active sites. Acted as structure director and scaffold, graphene plays a vital role in maintaining the structure stability. Additionally, the MgH_2@G could also serve as an attractive basic model for further construction of more complex structures in various applications.

Based on the nanosturcture of MHG, a series of yolk-shell-like structures, composed of porous MgH_2 nanoparticles (NPs) decorated with Mg-based composites (MHG@MBH, MHG@MS, MHG@MNH) through *in-situ* solid-gas reaction using MgH_2 as both the reactant and the structural template, have been fabricated and uniformly dispersed on electronically conductive graphene. In strong contrast with MHG, MHG@MS and MHG@MNH, the MHG@MBH electrode exhibits highest specific capacity at first cycle, 1454.6 mAh g^{-1}, much higher than the capacity of both MHG@MS (1186.4 mAh g^{-1}) and MHG@MNH (1195 mAh g^{-1}). More importantly, a reversible capability 1629.4 mAh g^{-1} could be maintained for the MHG@MBH

electrode even after 380 cycles with a Coulombic efficiency of approximately 99.1%. Under the current density of 1 A g^{-1}, the MHG@MBH electrode shows a high specific capacity of 2005 mAh g^{-1} for the first cycle and still maintains a reversible capacity of 1247 mAh g^{-1} after 300 cycles, corresponding to a capacity retention of 96% calculated based on that of the 4th cycle. When the current density was increased as high as 2 A g^{-1}, a reversible capacity of 1032 mAh g^{-1} could still be kept for the MHG@MBH electrode after 300 cycles, corresponding to a capacity retention of 85% compared to the specific capacity of the 10th cycle. More importantly, the CEs of MHG@MBH could be preserved at a level over 98.6% through the entire cycling process, which provides further evidence to the excellent reversibility induced by the formation of yolk-shell-like structure homogeneously distributed on graphene with an excellent electrical and ionic conductivity. It could not only physically accommodate the volume change of MgH_2 owing to the physical protection of Mg-based composites and the formation of void space inside MgH_2 NPs, but also effectively facilitate the transportation of electrons throughout the whole electrode. Particularly, the uniform decoration of ultrathin $Mg(BH_4)_2$ as the shell with thermodynamically favorable intercalation of lithium ions and low kinetic barrier for the lithium-ion diffusion promotes facile transportation of lithium ions into active MgH_2, which, coupled with the porous structure constructed by flexible graphene, effectively improves the ion conductivity of the electrode. This work may provide new guidance for preparing advanced conversion-type anodes towards practical energy storage application.

To furtherly solve the side reaction between MHG@MBH electrode and traditional liquid electrolyte, the yolk-shell-like structure of MgH_2@$Mg(BH_4)_2$ separated on graphene has been used in solid-state battery as an anode with $LiBH_4$ as an electrolyte. Compared with the MHG@MBH with diameter of 50 nm, the 13-MHG@MBH with

diameter of 13 nm displays better charge-discharge performance. At 200 mA g^{-1}, the 13-MHG@MBH displays discharge capacity about 2054 mAh g^{-1} at first cycle with a high CE of 98%, and it keeps a high capacity, 1415 mAh g^{-1} after 150 cycles. 13-MHG@MBH also delivers outstanding rate performance. When cycled at a high current density of 2 A g^{-1}, 13MHG@MBH exhibits an admirable capacity of 800 mAh g^{-1} can be maintained over 300 cycles. The advanced performance for lithium storage should be ascribed to the coating layer Li_2B_6 which is double ionic-electronic transfer interface outside the MgH_2 NPs was synthesized through further lithiation of $Mg(BH_4)_2$. Particularly, the formation of yolk-shell-like structure of MgH_2@Li_2B_6 on graphene could not only physically accommodate the volume change of MgH_2, but also significantly facilitate the transportation of electrons and ions throughout the whole electrode, which are benefit for the superior rate capability. More importantly, not only the ultrathin $Mg(BH_4)_2$ layer, but also the layer of Li_2B_6 has the advantage of increasing interfacial contact between the electrode and SE, thus decreasing the interface resistance, and the Li_2B_6 shell also has the ability to maintain the interface stability which leads to a long cycle life at high current density. The synergistic effects of Li_2B_6 leads to outstanding lithium storage properties, including high specific capacity, superior rate capability, and long cycle life.

8.2 Outlook

For $NaAlH_4$-based electrode, although we have developed a facile SEID method to build the nanostructure with graphene as structrual support. The enhanced lithium storage performance with high specific capacity, superior rate capability, and long cycle life has been realized, due to the improved conductivity and the declined energy barrier for both the insertion and extraction of Li ions which all could be attributed to the

graphene. However, the capacity decay, partial irreversibility, and side reactions between metal hydrides and the liquid electrolyte are still key issues that need to be solved. More efforts should be devoted to understanding the mechanism of capacity degradation, including theoretical calculations and experimental observations. Only under the joint guidance of theory and practice can we find the right direction to realize a more ideal $NaAlH_4$-based electrode with better cyclability and higher reversible capacity. Replacing liquid electrolyte with solid-state electrolyte is also a worthwhile approach. In addition to borohydrides, other solid-state electrolytes, including LISICON, perovskites, and garnet-type oxides, are also worth trying.

In the case of MgH_2-based electrodes, although we have devoted efforts to investigating them in solid-state batteries with $LiBH_4$ as the electrolyte and achieved some good results in terms of advanced electrochemical performance when they were tested as anodes in SSLIBs, the operating temperature of the batteries was still somewhat high, which may be limited by the nature of $LiBH_4$. Other solid electrolytes, such as $LiBH_4$•LiI or some stable composite solid-state electrolytes that work well at room temperature, could be selected and further expand the range of practical applications for MgH_2-based electrode. In terms of materials design, catalyst doping and reduction of the content of supporting materials are also feasible approaches to further enhance the rate capability and reversible capacity of the magnesium hydride-based anodes.

There are many other light metal hydrides with high specific capacity, which have good potentials in the field of lithium-ion battery. It must be interesting to explore their applications in the field of electrochemical energy storage fields.

APPENDIX A: LIST OF PUBLICATIONS

1. **Yuqin Huang**, Guanglin Xia, Jian Zhang, Zaiping, Guo, Xuebin Yu, Graphene tailored molecular bonds for advanced hydrogen and lithium storage performance, ***Energy Storage Materials***, 2019, 17: 178.